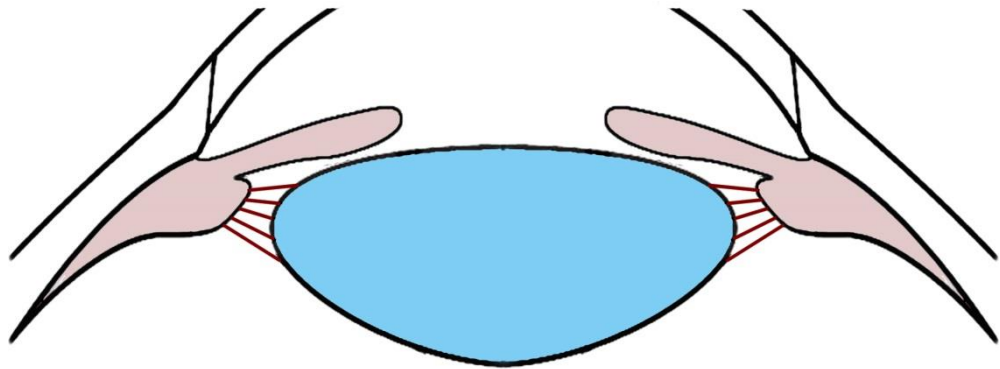


Finite Element Modelling of Human Eye Lens



Kehao Wang

Faculty of Science Engineering and Computing

Kingston University

A Thesis submitted for the degree of

Doctor of Philosophy

May 2017

I dedicate this Thesis to my parents, Mr. Mingzhong Wang and Mrs. Xiaojuan Ke, for your unconditional love and endless support to me over the past 26 years. I hope the achievement of this PhD will make you proud of your daughter, to whom you have given the strongest courage to fulfil her dream.

ABSTRACT

The human lens provides one-third of the ocular focussing power and is responsible for altering focus over a range of distances. This ability, termed accommodation, defines the process by which the lens changes its shape, in response to the movement of ciliary body, to adjust the refractive power. The accommodative ability gradually decreases with age such that around the fifth to sixth decades of life it is lost rendering the eye unable to focus on near objects. Current technologies are unable to effectively restore the requisite optical powers and accommodative ability of a presbyopic eye as the mechanism of accommodation is not fully understood. Plausible explanations, which are contradicted to each other, require definitive supports. Nevertheless, experimental evidences are difficult to obtain from living eye.

Computational modelling serves as an alternative solution for the understanding of the physiological process of accommodation. An accurate and detailed model can closely simulate the *in vivo* behaviour of the eye lens. To date, the relevance of available models to the physiology needs to be further explored. The accuracy of any computational model highly depends on the input parameters. To build up a complete lens model one needs to seek resources from different studies and to assemble parameters of lenses from different subjects, which bring great challenges to this research field.

The present work utilizes the Finite Element Analysis as the fundamental approach for investigating the mechanical and optical performances of lens models built at various ages based on input parameters from both *in vivo* and *in vitro* studies. The contributions of different ocular parameters to the accommodative loss are investigated i.e. the lens geometries, material properties, capsular thickness, capsular elasticity, zonular angles. Relations between two seemingly contradicting accommodative theories are demonstrated and possible explanations for the presbyopia are proposed.

ACKNOWLEDGEMENTS

Undertaking this PhD is a life-challenging experience for me and I would not be able to get through without the guidance and support I received from many people.

First and foremost I would like to express my sincerest gratitude to my first supervisor Professor Barbara Pierscioneck, for continuously supporting my PhD study through the past 2.5 years, for her patience and encouragement when I am depressed, for guiding me in each sentence I wrote in my papers and thesis, and most importantly for leading me into the scientific world. Her strong scientific spirit, passion in research and acute insight in this field has greatly inspired me and will have life-long impacts to my attitude toward research. I could not imagine having a better supervisor for my PhD. What I have learnt from her is more than worded in this thesis.

My deep appreciation goes to my second supervisor Dr. Demetrios Venetsanos, without whom I would not be able to achieve so much during my PhD study. I am particularly indebted to his selfless help and immense time devotion building various models and solving different problems with me. Starting from drawing a single line in SOLIDWORKS and writing a single command in ANSYS input file to the methodologies adopted in my project, he taught me lots of engineering skills. Specially, I am thankful to him for all the cookies and desserts he gave me for encouragement.

My great thanks also go to my supervisor Professor Jian Wang, whose wisdoms in scientific methodology and experience in mechanics have supported me all the way through my PhD journey. His profound knowledge in physics and mathematics has inspired me to explore the deep nature of engineering. In addition, I really enjoyed listening to his working experiences in both UK and China. From those stories I broadened my vision in the research world.

I am really thankful to Professor Andy Augousti for giving me the chance to work on this project as he was the interviewer of my PhD application and also offered significant help and guidance to my research work in the later stage of my study.

Last, but by no means least, I would like to thank my Mom and Dad for their unconditional love and endless support to me. You are always there with me no matter what happens, sharing my happiness and my sadness, believing in me and encouraging me to carry on to fulfil my dream. Specifically, I would like to give a big hug to my husband for his endless support to my research work and daily life.

CONTENTS

ABSTRACT	i
ACKNOWLEDGEMENTS.....	iii
CONTENTS.....	v
LIST OF FIGURES	ix
LIST OF TABLES	xvii
1 INTRODUCTION.....	1
1.1 Anatomy and physiology.....	1
1.1.1 The crystalline lens	1
1.1.1.1 Location and constituents of the lens	2
1.1.1.2 Dimensions of the lens	3
1.1.1.3 Lens refractive power.....	4
1.1.1.4 Discontinuity zones.....	5
1.1.2 The ciliary body and zonule.....	6
1.2 Mechanism of accommodation	8
1.2.1 Accommodative theory by Helmholtz.....	8
1.2.2 Accommodative theory by Schachar	9
1.2.3 Other accommodative theories	10
1.3 Presbyopia	11
1.3.1 Theories of development of presbyopia.....	12
1.3.2 Restoring accommodation	13
1.4 Finite Element Analysis in biomechanics	15
1.5 Aim and objectives	16
1.6 Structure of the thesis	17
2 LITERATURE REVIEW.....	19
2.1 Elastic properties of the lens.....	19
2.1.1 Spinning	19

Contents

2.1.2 Indentation	21
2.1.3 Bubble-based acoustic radiation force	23
2.1.4 Compression	24
2.1.5 Brillouin light scattering	24
2.2 Dynamic mechanical properties of the lens	27
2.2.1 Dynamic mechanical analysis.....	28
2.2.2 Biomechanical model	31
2.3 Material properties of the lens capsule.....	32
2.3.1 Inflation test of human anterior capsule	32
2.3.2 Uniaxial stretching test	33
2.4 Material properties of the zonular fibres	34
2.5 Computational modelling of the lens	36
2.5.1 Modelling accommodative mechanisms.....	38
2.5.2 Sensitivity analysis	41
2.5.3 Modelling zonular forces	43
2.5.4 Modelling gradient material properties	44
2.5.5 Modelling stress and strain of the internal lens	45
2.6 Summary of the state of FEA models	47
3 DEVELOPMENT OF GRADIENT MODULI MODELS	49
3.1 Modelling the lens and the capsule	49
3.1.1 Geometry: discontinuity zones	49
3.1.2 Finite Element model: element selection and mesh generation.....	51
3.1.3 Gradient material properties	53
3.2 Direct generation of zonular fibres.....	55
3.3 Boundary conditions.....	57
3.4 Stress distributions of the models.....	58
3.4.1 Single cortex models.....	58
3.4.2 Multi-layered models.....	60

3.5 Deformations of the models	63
3.5.1 Polar displacements	63
3.5.2 Sagittal deformations	66
3.5.3 Central radius of curvature of the outer lens surface and internal layers	68
3.6 Verification and validation of models	73
3.6.1 Mesh checking	73
3.6.2 Comparing to experimental measurements.....	74
3.7 Discussion	75
3.8 Summary	77
4 ZONULAR STRUCTURES: INFLUENCE ON LENS OPTICAL PERFORMANCE	79
4.1 Modelling different configurations of the zonule.....	79
4.2 Model A: Comparison to <i>in vivo</i> lens.....	81
4.3 Model B: Altering the stretching angles.....	83
4.4 Model C: split zonular fibres	86
4.4.1 Changing the zonular angles.....	86
4.4.2 Changing the ratio of the displacements applied to the three zonular fibres..	87
4.5 Comparison between models with different sets of material properties	90
4.6 Discussion	92
4.7 Summary	93
5 ZONULAR ANGLES: EXHAUSTIVE SEARCH SCHEME.....	95
5.1 Model development.....	95
5.2 Applied procedure: exhaustive search.....	97
5.3 Fits to clinical values	100
5.3.1 Models with uniform capsular thickness	100
5.3.2 Models with spatially varying capsular thickness	105
5.3.3 Zonular angle triplets providing the optimal fits	110
5.3.4 Models with mixed geometry and material properties	111
5.4 Optical Performances	114

Contents

5.5 Changes in radius of curvature	119
5.6 Discussion and conclusion	120
5.6.1 The geometry and material properties of the lens models	120
5.6.2 The influence of zonular angles	121
5.6.3 The importance of spatially varying capsular thickness	122
5.6.4 Comparing between accommodative theories	123
5.7 Summary	124
6 MODELS WITH LINEARLY VARYING MODULI.....	125
6.1 Geometry of the lens models	125
6.2 Model development	127
6.2.1 Element selection and mesh generation	127
6.2.2 Modelling the capsule and the zonule	128
6.2.3 Modelling the linearly changing moduli	129
6.2.4 Boundary conditions	131
6.3 Stress distributions of models with a single stretching point	132
6.4 Models with three different stretching points	136
6.4.1 Stress distributions	136
6.4.2 Change in radii of curvature	140
6.4.3 Deformations of the model in sagittal and equatorial directions	144
6.5 Discussion	146
6.6 Summary	147
7 DISCUSSION AND FUTURE WORK.....	149
7.1 Discussion	149
7.2 Future directions	152
APPENDIX I	155
APPENDIX II.....	157
LIST OF PUBLICATIONS	171

LIST OF FIGURES

Figure 1.1 (a) sagittal view of the human eye's anatomy, (b) structure of the human lens.	2
Figure 1.2 Schematic drawing of the lens shape.....	3
Figure 1.3 Discontinuity zones.	6
Figure 1.4 Illustration of main components of zonular apparatus.	6
Figure 1.5 Drawings of (a) posterior zonule (PZ) and anterior hyaloid membrane (AHM) share the attachment on the lens via Weiger's ligament and (b) posterior zonule anchored on hyaloid membrane.	7
Figure 1.6 Illustration of the Helmholtz's accommodative mechanism.	9
Figure 1.7 Illustration of the Schachar's accommodative mechanism.	10
Figure 1.8 Variation in capsular thickness.	10
Figure 1.9 Comparison of normal and presbyopic eye.	12
Figure 2.1 Young's modulus of lens nucleus and cortex with age reproduced from Fisher ⁶²	20
Figure 2.2 Shear modulus of lens nucleus and cortex with age reproduced from Wilde et al. ⁶⁵	21
Figure 2.3 Shear modulus of the nucleus and the cortex with age reproduced from Heys et al.	22
Figure 2.4 Spatially varying Young's moduli of lenses reproduced from Hollman et al.	23
Figure 2.5 The bulk modulus of the nucleus and cortex with age reproduced from Bailey <i>et al.</i> ¹⁰³	26
Figure 2.6 Longitudinal modulus across the lens at age 19, 43 and 61 years reproduced from Besner <i>et al.</i> ⁷¹	27
Figure 2.7 Shear storage and shear loss modulus of all measured lenses with age reproduced from Weeber <i>et al.</i> ⁶⁷	29
Figure 2.8 Spatially varying shear storage modulus of all measured lenses reproduced from Weeber <i>et al.</i> ⁶⁴	30
Figure 2.10 Young's modulus of anterior lens capsule with age reproduced from Fisher ¹¹⁹	33
Figure 2.11 Young's modulus less than 10% strain of both the anterior and posterior capsule with age reproduced from Krag and Andreassen ¹²³	34

List of figures

Figure 2.12 Basic mechanism of stretching test for measuring the elastic properties of zonular fibres.....	35
Figure 2.13 The deformed lens shape obtained from geometrical (a) linear and (b) nonlinear analysis with 6.25% of equatorial strain from Burd <i>et al.</i> ¹³³	37
Figure 2.14 (a) Assembled lens geometry and (b) deformed mesh of the 29-year-old lens model from Burd <i>et al.</i> ⁹⁹	39
Figure 2.15 The lens models developed by Ljubimova <i>et al.</i> ¹³⁹ for the cases: (a) with and (b) without vitreous.	40
Figure 2.16 Deformed lens models under three configurations of zonular forces from Hermans <i>et al.</i> ¹⁰⁰	43
Figure 2.17 Zonular forces using three sets of material properties estimated by Hermans <i>et al.</i> ¹⁴⁵	44
Figure 2.18 Change in COP with age of lens models using three different set of material properties reproduced from Weeber and van der Heijde ¹²⁸	45
Figure 2.19 The strain along the central axis of three lens models aged 20, 40 and 60 years reproduced from Weeber and van der Heijde ¹³⁰	46
Figure 2.20 The internal von Mises stress of the 27-year-old model under the stretching force of (a) 0.65N and (b) 0.100N from Belaidi and Pierscionek ¹²⁹	46
Figure 3.1 Dimensions of lenses aged (a) 16, (b) 35 and (c) 48 years of age fitted from Bahrami <i>et al.</i> ³⁷	50
Figure 3.2 3D solid lens model developed in SOLIDWORKS (ver.2014).....	51
Figure 3.3 FE models of lenses aged (a) 16, (b) 35 and (c) 48 years of age.....	52
Figure 3.4 Elements used for lens model: (a) SOLID186, (b) SHELL281, (c) LINK180.	53
Figure 3.5 Distributions of Young's moduli in 35-year-old lens model.....	54
Figure 3.6 The anchorage of the zonular fibres on the lens capsule.	56
Figure 3.7 The boundary conditions of the quarter lens models demonstrated in (a) oblique view and (b) top view.....	57
Figure 3.8 Nodal coordinate system of the stretching point.	58
Figure 3.9 Stress distributions of the (a) 16-year-old, (b) 35-year-old and (c) 48-year-old lens models with a single cortical modulus using the material properties of Fisher ⁶² under a stretching force of 0.08N.....	59
Figure 3.10 Stress distributions of the (a) 16-year-old, (b) 35-year-old and (c) 48-year-old lens models with flipped single cortical modulus using the material properties of Fisher ⁶² under a stretching force of 0.08N.....	59

Figure 3.11 Stress distributions of the (a) 16-year-old, (b) 35-year-old and (c) 48-year-old lens models with single cortical modulus using the material properties of Wilde <i>et al.</i> ⁶⁵ under a stretching force of 0.08N.....	60
Figure 3.12 Stress distributions of the multi-layered models aged (a, d) 16-year-old, (b, e) 35-year-old and (c, f) 48-year-old using the material properties of Fisher ⁶² under a stretching force of 0.08N.....	61
Figure 3.13 Stress distributions of the flipped multi-layered models aged (a, d) 16-year-old, (b, e) 35-year-old and (c, f) 48-year-old lens models using the material properties of Fisher ⁶² under a stretching force of 0.08N.....	62
Figure 3.14 Stress distributions of the multi-layered models aged (a, d) 16-year-old, (b, e) 35-year-old and (c, f) 48-year-old lens models using the material properties of Wilde <i>et al.</i> ⁶⁵ under a stretching force of 0.08N.....	62
Figure 3.15 Diagrammatic representations of lens displacements at the equator, anterior and posterior poles.	63
Figure 3.16 The displacements of anterior pole, posterior pole and equator of the whole lens and the nucleus in the three lens models of different ages with a single cortical modulus and modulus values from Fisher ⁶² and Wilde <i>et al.</i> ⁶⁵	64
Figure 3.17 The displacements of the anterior pole, posterior pole and equator of the whole lens and the nucleus in models of different cortical layers of lenses 16 years old.	65
Figure 3.18 The comparison of sagittal deformations in the nucleus and the cortex for models using (a-c) the material properties of Fisher ⁶² , (d-f) the flipped material properties of Fisher ⁶² and (g-i) the material properties of Wilde <i>et al.</i> ⁶⁵	67
Figure 3.19 The relationship between the (a) anterior and (b) posterior radius of curvature and the vertex locations of different layers of the undeformed lens models. .	71
Figure 3.20 The radius of curvature as a function of the vertex location of different layers for both the anterior and posterior part of the models using (a,b) the material properties of Fisher ⁶² , (c,d) Flipped material properties of Fisher ⁶² and (e,f) the material properties of Wilde <i>et al.</i> ⁶⁵	72
Figure 3.21 FE models of the 16-year-old lens with a (a) lower and a (b) higher mesh density.	73
Figure 3.22. The comparison of displacements at anterior pole, posterior pole and the equator for the 16-year-old model with two mesh densities.	74

List of figures

Figure 4.1 A 35-year-old model (a) with anterior, equatorial and posterior zonular fibres bound to a single point and applied with horizontal stretching, (b) with bound zonular fibres shifted anteriorly and (c) with split zonular fibres in three different directions. ..	80
Figure 4.2 The deformed lens models together with undeformed lens shape under the accumulated force levels of (a) 0.08N, (b) 0.16N, (c) 0.24N, (d) 0.32N, (e) 0.40N and (f) 0.48N.....	81
Figure 4.3 The change in anterior and posterior radii of curvature plotted against accommodative amplitude for the 35-year-old model with horizontal zonular stretching.	82
Figure 4.4 The change in anterior and posterior radii of curvature plotted against accommodative amplitude for the 35-year-old model with bound zonular fibres shifted to different angles.....	85
Figure 4.5 The change in anterior and posterior radii of curvature plotted against accommodative amplitude for the 35-year-old model with 20° anterior, 0° equatorial and 35° posterior zonular angles.	86
Figure 4.6 The change in anterior and posterior radii of curvature plotted against accommodative amplitude for a selective 35-year-old model with 20° anterior, 15° equatorial and 40° posterior zonular angles.	89
Figure 4.7 The change in anterior and posterior radii of curvature plotted against accommodative amplitude for the 35-year-old model with horizontal zonular stretching using both sets of material properties.	91
Figure 4.8 The change in anterior and posterior radii of curvature plotted against accommodative amplitude for the 35-year-old model with zonular fibres shifted anteriorly by 15 degrees using both sets of material properties.....	91
Figure 4.9 The change in anterior and posterior radii of curvature plotted against accommodative amplitude for a selective 35-year-old model with 20° anterior, 15° equatorial and 40° posterior zonular angles using both sets of material properties	92
Figure 5.1 The flow diagram of the applied methodology.	97
Figure 5.2 The 16-year-old lens model with -20 degree anterior, 4 degree equatorial and 34 degree posterior zonular angles at six deformed states (dashed line: undeformed shape).	98
Figure 5.3 The optimum fittings provided by the 16-year-old lens model using both sets of material properties.	99

Figure 5.4 The p-value contours of (a) anterior lens surface and (b) posterior lens surface of the 16-year-old lens model with uniform capsular thickness using the material properties of Fisher ⁶²	101
Figure 5.5 The p-value contours of (a) anterior lens surface and (b) posterior lens surface of the 35-year-old lens model with uniform capsular thickness using the material properties of Fisher ⁶²	102
Figure 5.6 The p-value contours of (a) anterior lens surface and (b) posterior lens surface of the 16-year-old lens model with uniform capsular thickness using the material properties of Wilde <i>et al.</i> ⁶⁵	103
Figure 5.7 The p-value contours of (a) anterior lens surface and (b) posterior lens surface of the 35-year-old lens model with uniform capsular thickness using the material properties of Wilde <i>et al.</i> ⁶⁵	104
Figure 5.8 The p-value contours of (a) anterior lens surface and (b) posterior lens surface of the 16-year-old lens model with spatially varying capsular thickness using the material properties of Fisher ⁶²	106
Figure 5.9 The p-value contours of (a) anterior lens surface and (b) posterior lens surface of the 35-year-old lens model with spatially varying capsular thickness using the material properties of Fisher ⁶²	107
Figure 5.10 The p-value contours of (a) anterior lens surface and (b) posterior lens surface of the 16-year-old lens model with spatially varying capsular thickness using the material properties of Wilde <i>et al.</i> ⁶⁵	108
Figure 5.11 The p-value contours of (a) anterior lens surface and (b) posterior lens surface of the 35-year-old lens model with spatially varying capsular thickness using the material properties of Wilde <i>et al.</i> ⁶⁵	109
Figure 5.12 The p-value contours of (a) anterior lens surface and (b) posterior lens surface of the model with uniform capsular thickness mixing the 16-year-old geometry and 35-year-old material properties of Fisher ⁶²	112
Figure 5.13 The p-value contours of (a) anterior lens surface and (b) posterior lens surface of the model with uniform capsular thickness mixing the 35-year-old geometry and 16-year-old material properties of Fisher ⁶²	113
Figure 5.14 Scatter plots of Accommodative Amplitude provided by the 16-year-old model using the material properties of Fisher ⁶²	115
Figure 5.15 Scatter plots of Accommodative Amplitude provided by the 35-year-old model using the material properties of Fisher ⁶²	116

List of figures

Figure 5.16 Scatter plots of Accommodative Amplitude provided by the 16-year-old model using the material properties of Wilde <i>et al.</i> ⁶⁵	117
Figure 5.17 Scatter plots of Accommodative Amplitude provided by the 35-year-old model using the material properties of Wilde <i>et al.</i> ⁶⁵	118
Figure 5.18 Histograms of accommodative amplitude compared between the uniform capsular thickness model and the spatially varying capsular thickness model for (a) 16-year-old lens and (b) 35-year-old lens using the material properties of Fisher ⁶² , (c) 16-year-old lens and (d) 35-year-old lens using the material properties of Wilde <i>et al.</i> ⁶⁵	119
Figure 5.19 The changes in radii of curvature (R) in mm and Central Optical Power (COP) in dioptres (D) for progressive stretching steps of the 16-year-old lens model using the material properties of (a) Fisher ⁶² and of (b) Wilde <i>et al.</i> ⁶⁵ and of the 35-year-old lens model using the material properties of (c) Fisher ⁶² and of (d) Wilde <i>et al.</i> ⁶⁵	120
Figure 6.1 Dimensions of the lenses with the nuclear sizes fitted from corresponding refractive index profile measured by Pierscioneck <i>et al.</i> ¹⁴⁹	126
Figure 6.2 The FE lens model aged (a) 16, (b) 35, (c) 40, (d) 57, (e) 62, (f) 74, (g) 86 and (h) 91 years of age.	128
Figure 6.3 Illustration of the model (a) with three zonular fibres attached to a single endpoint showing the radius of ciliary body and (b) with three zonular fibres attached to three different endpoints.	129
Figure 6.4 Illustration of the linearly varying moduli within the lens cortex with colour bar shown on the right side demonstrating the decreasing moduli from the nuclear boundary to the outer lens surface.	130
Figure 6.5 Stress distributions of the models aged 16 and 35 years of age for models with a single stretching point under a stretching force of 0.08N.	133
Figure 6.6 Stress distributions of the models aged 40 and 57 years of age for models with a single stretching point under a stretching force of 0.08N.	133
Figure 6.7 Stress distributions of the models aged 62 and 74 years of age for models with a single stretching point under a stretching force of 0.08N.	134
Figure 6.8 Stress distributions of the models aged 86 and 91 years of age for models with a single stretching point under a stretching force of 0.08N.	134
Figure 6.9 The (a) maximal and (b) minimal von Mises stresses of all lens models with a single stretching point plotted against age.	135
Figure 6.10 Stress distributions of the models aged 16 and 35 years of age for models with three stretching points under a displacement of 0.2mm applied to each zonular fibre.	137

Figure 6.11 Stress distributions of the models aged 40 and 57 years of age for models with three stretching points under a displacement of 0.2mm applied to each zonular fibre.	137
Figure 6.12 Stress distributions of the models aged 62 and 74 years of age for models with three stretching points under a displacement of 0.2mm applied to each zonular fibre.	138
Figure 6.13 Stress distributions of the models aged 86 and 91 years of age for models with three stretching points under a displacement of 0.2mm applied to each zonular fibre.	138
Figure 6.14 The (a) maximal and (b) minimal von Mises stresses of all lens models with three stretching points plotted against age.	139
Figure 6.15 The central radius of curvature of the (a) anterior and (b) posterior lens surfaces plotted against age for all three types of models.	142
Figure 6.16 The central radius of curvature of the (a) anterior and (b) posterior nuclear surfaces plotted against age for all three types of models.	143
Figure 6.17 The sagittal and equatorial deformations of the nucleus and the cortex plotted against age for models with (a) a uniform cortical modulus and a uniform capsular thickness, (b) linearly changing cortical moduli and a uniform capsular thickness and (c) linearly changing cortical moduli and spatially varying capsular thickness.	145

List of figures

LIST OF TABLES

Table 3.1 Dimensions of the lenses aged 16, 35 and 48 years of age from Bahrami et al. ³⁷	50
Table 3.2 Material properties of the lens components.	53
Table 3.3 The distances of the anterior and posterior zonular attaching points to the lens equator.....	56
Table 3.4 Displacements of anterior pole, posterior pole and equator of the whole lens and the nucleus.....	66
Table 3.5 Sagittal deformations of the nucleus and cortex	68
Table 3.6 Central radius of curvature (R) of models using the material properties of Fisher ⁶²	69
Table 3.7 Central radius of curvature (R) of flipped models using the material properties of Fisher ⁶²	70
Table 3.8 Central radius of curvature (R) of models using the material properties of Wilde <i>et al.</i> ⁶⁵	70
Table 4.1 Anterior and posterior slopes of the linear relationships between radius of curvature and accommodative amplitude for models with bound zonular fibres and shifting angles.	83
Table 4.2 Anterior and posterior slopes of the models with different zonular angle triplets under the 0.5mm displacements applied to all three zonular fibres.....	87
Table 4.3 Anterior and posterior slopes provided by the model with a zonular angle triplet of [20°, 0°, 35°] under different amount of displacements.....	88
Table 4.4 Anterior and posterior slopes provided by the model with a zonular angle triplet of [20°, 5°, 35°] under different amount of displacements.....	88
Table 4.5 Anterior and posterior slopes provided by the model with a zonular angle triplet of [20°, 10°, 40°] applied with different combinations of displacements.	88
Table 4.6 Anterior and posterior slopes of the model with a zonular angle triplet of [20°, 15°, 40°] applied with different combinations of displacements.....	89
Table 5.1 Zonular angle triplets resulting in the optimal fittings to <i>in vivo</i> data ²⁷ for 16 year old geometries and material properties.	110
Table 5.2 The anterior and posterior zonular angles that provide the top three highest accommodative amplitudes for each model.....	110
Table 6.1 Dimensions of the lenses.	127

List of tables

Table 6.2 The capsular thickness taken from Fisher ¹¹⁹ for uniform capsular thickness models.	128
Table 6.3 The central radii of curvature of undeformed models.	140
Table 6.4 The central radii of curvature of models with a uniform cortical modulus and a uniform capsular thickness.	140
Table 6.5 The central radii of curvature of models with linearly varying cortical moduli and a uniform capsular thickness.	141
Table 6.6 The central radii of curvature of models with linearly varying cortical moduli and a spatially varying capsular thickness.	141

1 INTRODUCTION

1.1 Anatomy and physiology

The human eye is a well-designed optical and biological system consisting of a series of ocular components that work together to meet the visual demands of the individual. The light reflected from an object in the field of view firstly passes through the cornea, which provides two thirds of the refractive power of the eye, then through the aqueous humour, pupil, crystalline lens, vitreous and is finally focused onto the retina. The retina converts the light into electro-chemical signals that can be recognized by the brain. The lens serves as a tuneable component responsible for adjusting the refractive power of the eye to focus over a range of distances; this capacity diminishes with age. The other condition that can affect the lens as it ages is cataract which is a loss of transparency. The current treatment for cataract is removal of the lens and replacement with an intraocular implant. To date no implant can mimic the image quality and the focus changing capacity of the biological lens. A deeper understanding of both the mechanics and physiology of the lens is required not just to better understand age-related diseases and conditions that affect it but also for design of better implant lenses.

1.1.1 The crystalline lens

Accommodation refers to the process by which the lens increases or decreases its optical power to bring near or far objects into focus by altering its shape. With age, this accommodative ability gradually diminishes^{1, 2} such that around the fifth to sixth decades of life the eye is unable to focus on near objects^{3, 4}; this condition is known as

presbyopia. Currently, theories describing the physiological process of accommodation are controversial and explanations for causes of the development of presbyopia are inconclusive⁵⁻⁷.

1.1.1.1 Location and constituents of the lens

The human lens, located between the iris and vitreous, is in an ellipsoidal shape axisymmetric about its central optical axis (Figure 1.1a). It consists of 65% of water and 35% of protein⁸. The crystalline lens is a unique organ in that it contains long thin cells solely of a single type known as lens fibre. The lens fibres are enclosed by a transparent semi-elastic basement membrane named the capsule⁹ (Figure 1.1b), with a thickness that is approximately 10µm but has localised variations⁹. The lens is held in place by a ring of fibrous ligaments collectively called the zonule. Zonular fibres are attached to the lens capsule at its equatorial zone and connect the lens equator with ciliary body (Figure 1.1b). The lens equator, defined as the conjunction of anterior and posterior lens surfaces, shows a number of dentations corresponding to the position of zonular attachment^{10, 11}.

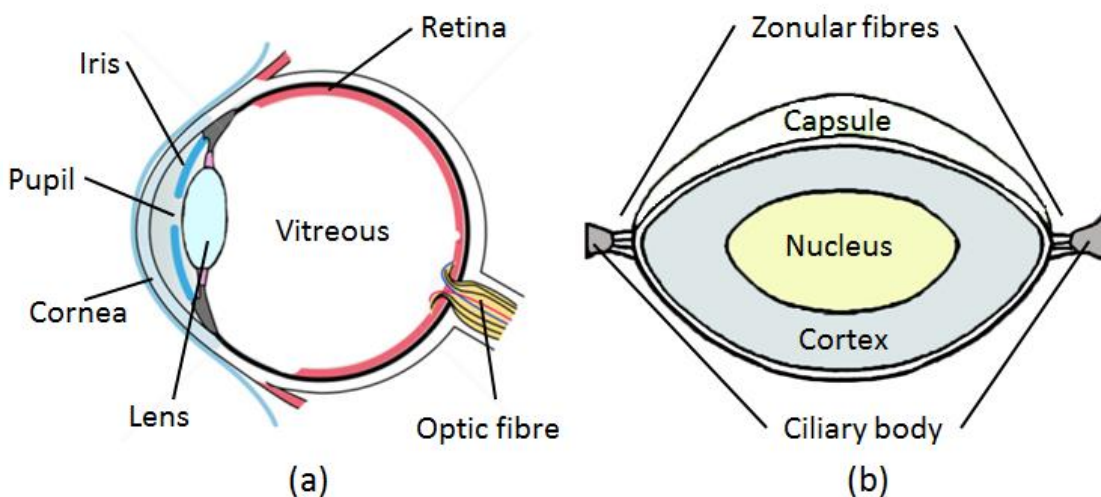


Figure 1.1 (a) sagittal view of the human eye's anatomy, (b) structure of the human lens.

Lens fibres within the exterior capsular surface are arranged in concentric shells forming a lamellar structure. Each fibre cell runs from the anterior to the posterior pole. Most of the fibres from a same shell meet with each other at positions near the poles forming a 'Y' pattern and called the 'lens suture'. The sutures at the anterior and posterior poles become more branched as newer layers of cells are added¹². The lens

fibre cells are developed at various stages of life, with the oldest ones compacted in the centre and the most recently synthesised cells on the lens surface with no concomitant cellular loss throughout life. Newly added lens fibres lose their nuclei and organelles and therefore their metabolic ability retaining their proteins. Although there is no clear demarcation, the lens is considered to have two regions: the central part, with a diameter of approximately two thirds of the lens, which is known as the lens nucleus and the remaining peripheral zones which are collectively called the cortex^{13, 14} (Figure 1.1b).

1.1.1.2 Dimensions of the lens

The lens dimensions have been characterized as a function of both age and accommodation using different *in vivo* and *in vitro* techniques, such that varying findings have been reported¹². The *in vivo* lens interacts with other ocular components and is more suitable for revealing functional information. The *in vitro* lens can be completely observed, i.e. no part is hidden behind other components of the eye such as the iris and is invaluable for assessing and characterizing lens growth. The lens sagittal thickness and equatorial diameter commonly used for describing lens size are illustrated in Figure 1.2.

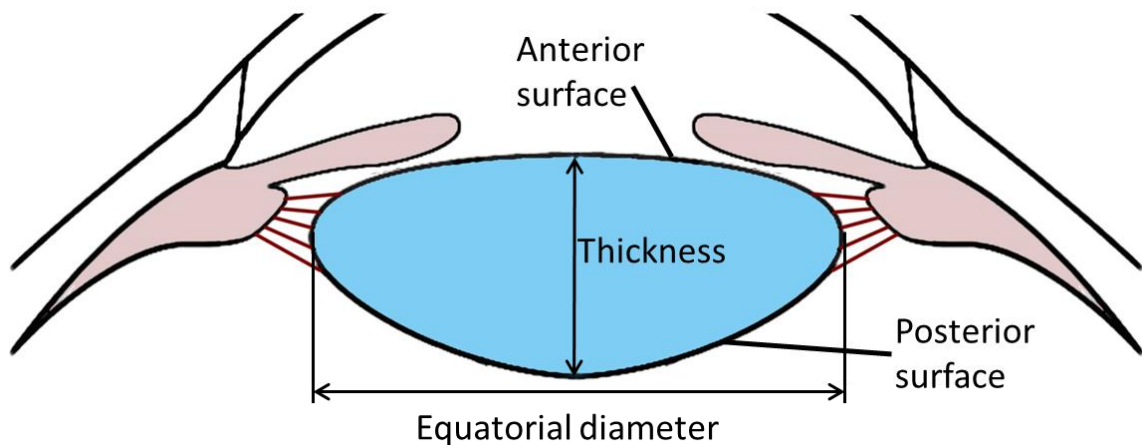


Figure 1.2 Schematic drawing of the lens shape.

The *in vitro* lens measured at birth has a diameter and thickness of around 6mm and 4mm respectively¹². Both increase with age but the ageing patterns differ. The equatorial diameter continuously increases with age until it reaches the maximal value of around 9-10mm^{10, 12}. The lens thickness, however, firstly decreases from 4mm to 3.3mm in the late teenage years¹², which was thought to be because of the compaction

Chapter 1. Introduction

of lens fibres in a remodelling process¹⁵, and gradually increases with age in later life roughly at a speed of 0.012mm/year¹⁶ reaching 4.75-5.0mm in old age¹⁰. The increase in thickness and diameter of the lens are related in that, from adulthood, they maintain a constant aspect ratio of around 2.2^{16, 17}. It needs to be pointed out there are significant variations in reported lens dimensions and the data from various observations are hard to reconcile^{12, 15-17}. This could be attributed to the different methods used, individual variations and the different conditions of lens samples¹².

The *in vivo* equatorial diameter is reported to behave in a different manner. MRI measurements suggest it is around 9.2-9.3mm in an unaccommodated lens and varies little with increasing age^{18, 19}. The equatorial diameter of an accommodated lens increases until middle age when it becomes equal to the diameter of an unaccommodated lens¹⁹. The increase of the lens thickness is evidenced by the forward movement of the anterior pole^{13, 20} and the constant distance of the posterior pole to the cornea^{13, 20, 21} with age. The thickening of the sagittal lens size measured *in vivo* is at a speed of 0.013 to 0.025mm/year in adulthood^{12, 18-20, 22, 23}. The age-related increase of the lens thickness is mainly due to the increase in cortical sizes^{13, 14, 21}, more pronounced in the anterior cortex than the posterior portion^{14, 17}. The nucleus shows no change in size with age^{13, 21}. The anterior surface, with a radius of curvature around 8.0-14.0mm, is less convex than the posterior surface, the radius of curvature of which is 4.5-7.5mm¹⁰. The anterior radius of curvature has been found to decrease with age at a faster rate than the posterior radius of curvature²²⁻²⁵.

It is widely agreed that during accommodation, the lens thickness increases^{18, 26-28} and the lens diameter decreases^{18, 29, 30}. The nucleus has significantly higher amount of thickness change than the cortex^{13, 26, 31} and the cortical thickness changes are mainly concentrated in the posterior portion^{13, 14, 31}. Many studies have reported that both central anterior and posterior radii of curvature decrease with accommodation^{13, 27, 29, 32}, with higher amounts of decreases seen in the anterior than in the posterior surface³³. Opposing evidence for steeper central lens curvatures in the accommodated lens were seen^{8, 34} and will be explained in further detail in section 1.2.

1.1.1.3 Lens refractive power

The precise arrangement of the lens fibres and their homogeneity provide the lens with a high degree of transparency. The lens surface shape together with the refractive indices

of the lens, and the lens surrounding aqueous and vitreous humours determine the lens refractive power. The eye lenses of all measured species so far have a Gradient Refractive Index (GRIN)³⁵. A lens with homogeneous refractive index refracts the light only at the surface while a lens with gradient refractive index continuously refracts the light within the medium³⁵ and provides a better image quality. The GRIN eye lens contributes to the sharpness of focus and reduces spherical aberrations. The distribution of the GRIN profile varies among different subjects³⁶ and the amount of contribution to the lens refractive power is determined by the magnitude of the refractive index and the steepness of the gradient³⁵. In the human lens the refractive index distribution shows two distinct regions: a central region where the refractive index is relatively constant with a value of approximately 1.42 and an outer 0-1mm zone with rapid changes of the refractive index that decreases outward to a value of approximately 1.35 near the lens surface³⁷. The width of the central plateau increases continuously with age¹². The surrounding aqueous that bathes the anterior surface, and the vitreous have slightly lower refractive indices of approximately 1.336³⁸. The refractive contribution of the lens in a normal adult eye is about 15 out of a total of 40 dioptries. The profile of the GRIN in the eye lens is created by the varying distribution of the proteins with different physicochemical properties³⁵. The magnitude of the refractive index is linearly related to the protein concentration according to the Gladstone-Dale formula³⁹.

1.1.1.4 Discontinuity zones

The proteins contained within the fibre cells of the lens are distributed in different concentrations throughout the lens to form discrete light and dark optical regions when viewed using *in vivo* slit lamp microscopy, termed 'zones of discontinuity'¹². Different zones are thought to have developed at different periods of growth, the radius of curvature and location of the zones of discontinuity are linearly related^{32, 40}. Four cortical zones are commonly identified in an adult lens, namely C1, C2, C3 and C4 successively from the outermost layer beneath the capsule to the innermost layer surrounding the nucleus^{41, 42} (Figure 1.3). The growth of the lens dimensions mainly occurs at cortical zones and especially in C2^{12, 14}. [Such nomenclature is described using the Oxford system which defines the nucleus as the lens substance formed at birth⁴¹].

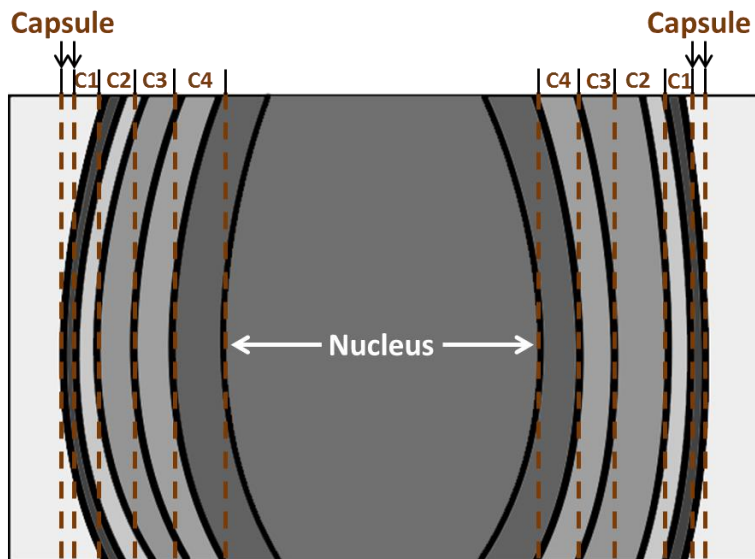


Figure 1.3 Discontinuity zones.

1.1.2 The ciliary body and zonule

The zonular section consists of a series of fibres connecting the lens with the ciliary body¹⁰, which contains an anterior folded portion named ‘pars plicata’ and a flattened posterior part named ‘pars plana’ (Figure 1.4). Zonular fibres transmit the force from the ciliary body to control the lens shape changes during accommodation. When seen under the microscope, the zonular fibres appear as straight glassy rods with diameters of 5 to 30 μm ⁴³. Each fibre is composed of highly oriented and closely aggregated microfibrils averaging 10nm (8 to 12nm) in diameter^{10, 43}.

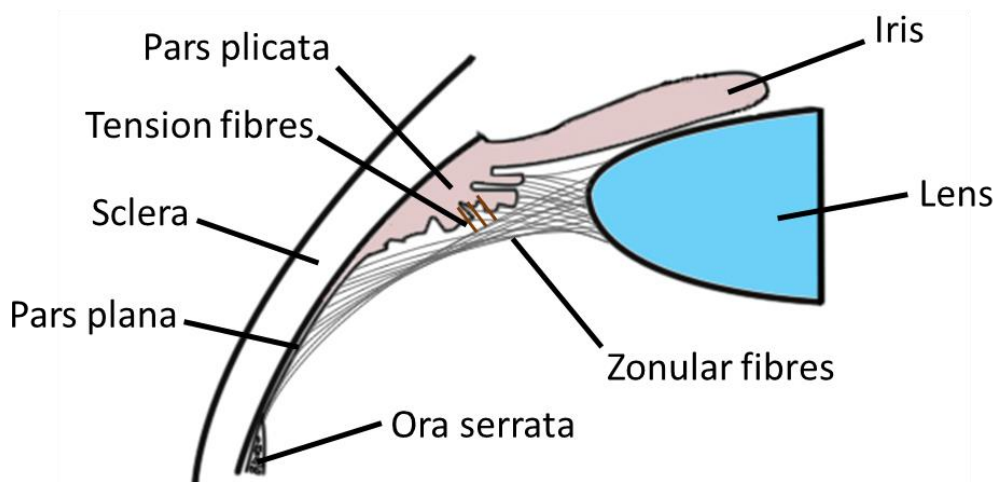


Figure 1.4 Illustration of main components of zonular apparatus.

The vast majority of the zonular fibres originate from the posterior end of the pars plana about 0.5 to 1.5mm anterior to the ora serrata^{10, 43, 44} (Figure 1.4). The fibres pass anteriorly forward to the posterior margin of the pars plicata where they segment into zonular plexuses¹⁰, which consist of broad flattened fibre strands crossing and joining each other in regular patterns, pass through the valleys between ciliary processes and are closely attached to the bases of ciliary processes through tension fibres^{10, 44}. Each plexus then further divides into three groups of zonular fibres going to the anterior, equatorial and posterior lens capsule⁴⁴. The anchorage of the zonular plexuses to the ciliary processes through tension fibres is thought to explain how the equatorial force, partly from pars plana and partly from ciliary processes, is exerted on the lens⁴⁴.

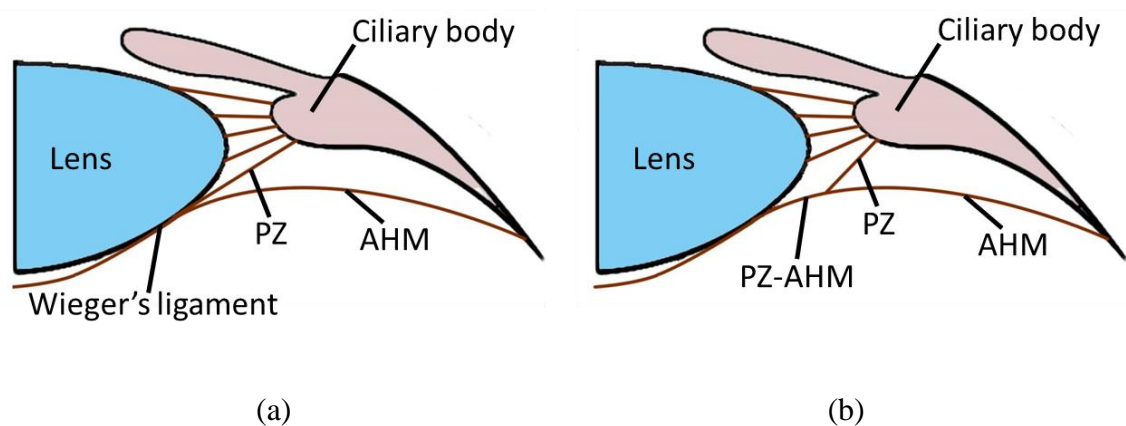


Figure 1.5 Drawings of (a) posterior zonule (PZ) and anterior hyaloid membrane (AHM) share the attachment on the lens via Weiger's ligament and (b) posterior zonule anchored on hyaloid membrane.

The relatively dense insertions of anterior zonular section on the lens capsule are approximately 1.5mm from the equator^{10, 43}. The bundles of anterior zonular fibres spread over a zone of 0.3 to 0.4mm meridional length¹⁰. The insertion of posterior zonular fibres, which spread over a zone of 0.4 to 0.5mm wide¹⁰, extends to about 1.25mm from the equator^{10, 43}. The sparse equatorial fibres insert into the capsule almost perpendicular to the lens surface and merge with the meridional fibres that arch over the equatorial capsule¹⁰. In addition to this, a delicate structure, called the anterior hyaloid membrane, runs from the pars plana to the posterior lens with its attachment shared with the posterior zonule via Weiger's ligament⁴⁵ (Figure 1.5a). A recent study, opposing this classical description, suggests that the majority of posterior zonules are anchored on hyaloid membrane instead of attaching directly to posterior lens capsule⁴⁶ (Figure 1.5b). With age, both the anterior and posterior zonular attachments become broader and move

more centrally^{10, 47}. The diameter of the anterior zonular free area of the capsule decreases from 8mm at the first and second decades of life, to 5.5-6.5mm in the eighth decade⁴⁸. The equatorial zonule becomes finer and sparser, and has been known to rupture in very old age⁴⁷.

1.2 Mechanism of accommodation

The ability of the eye to alter focus over different distances was firstly demonstrated by Scheiner^{49, 50} in 1619 using his classic double-pinhole. When looking through a card, containing two pinholes at a distance less than the diameter of the pupil, to focus on a needle, a single needle can only be observed at a right distance; two needles are seen if the distance is nearer or farther. The concept of relating the accommodative process to lens shape changes was proposed at a very early date^{5, 51}. The first complete description of accommodative theory, postulated by von Helmholtz⁵² in 1840s, has been supported by many studies and still remains to be the most widely supported theory. Alternative theories⁵³⁻⁵⁵ with different considerations about the behaviour of the zonule and lens shape changes during accommodation have also been suggested^{34, 53, 54, 56}.

1.2.1 Accommodative theory by Helmholtz

The accommodative theory proposed by Helmholtz states that the unaccommodated lens is in a flattened shape while the accommodated lens is in a more spherical shape. During unaccommodation, the ciliary muscle relaxes providing a relatively large radius and causing increased tensions in all the zonular fibres in such a way that the lens is pulled into a flattened shape; the lens equatorial diameter increases and the thickness decreases. This process brings far objects into focus with reduced optical power of the lens. During accommodation, the ciliary muscle contracts with a decrease in its radius to reduce the tensions in the zonular fibres enabling the lens to return to a more spherical shape. The increased lens thickness and central curvatures of lens surfaces increase the optical power, bringing near objects into focus. The comparison between the unaccommodated and accommodated lens as explained in the Helmholtz accommodation theory is shown in Figure 1.6.

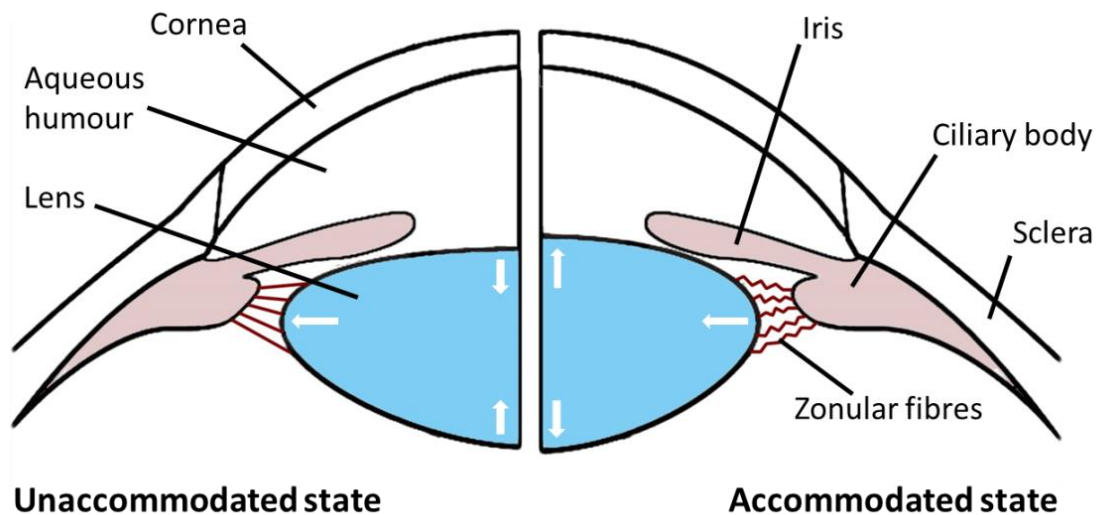


Figure 1.6 Illustration of the Helmholtz's accommodative mechanism.

1.2.2 Accommodative theory by Schachar

Schachar⁵⁶ proposed a different theory to the one by Helmholtz and the difference arises from the zonular behaviour during accommodation. Schachar argues that the equatorial zonular section, originated from the anterior end of the ciliary muscle at the root of iris, is the only active component during the change of lens shape in the accommodative process⁵⁶ (Figure 1.7). The anterior and posterior zonular fibres, inserted into the posterior end of the ciliary body, which have a different origin from the equatorial part, are relaxed because of the anterior movement of pars plana⁸. The anterior and posterior zonules thus contribute less to the accommodative changes in lens shape and provide functional support to maintain the lens in position⁸. According to Schachar, with accommodation, the central lens surfaces steepen, the peripheral lens surfaces flatten, both the lens thickness and equatorial diameter increase such that the accommodated lens takes on a spindle shape⁵⁷. During unaccommodation, the equatorial zonular fibre relaxes while the anterior and posterior zonular fibres become tauter causing the radii of curvature at the central lens surface to increase and at the peripheral lens surface to decrease. Both the thickness and equatorial diameter decrease.

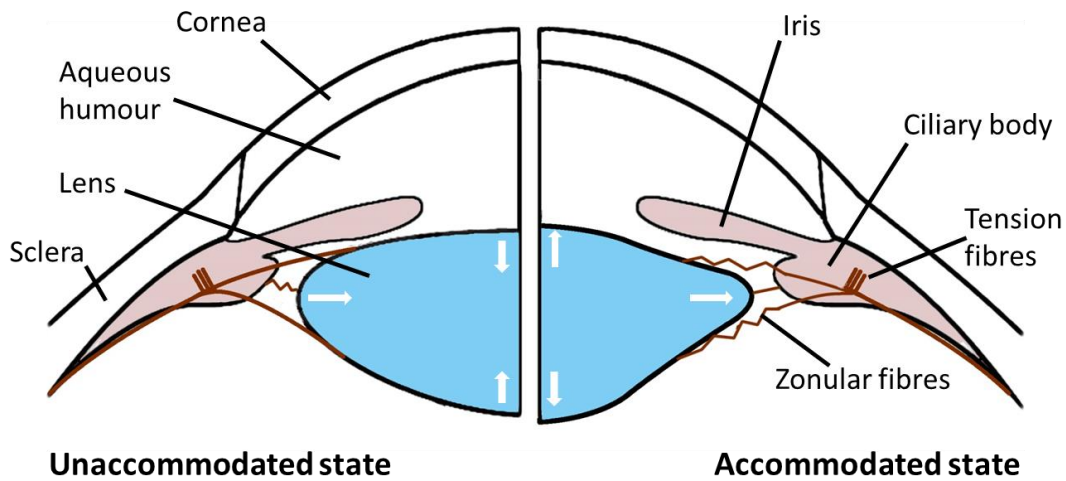


Figure 1.7 Illustration of the Schachar's accommodative mechanism.

1.2.3 Other accommodative theories

Tscherning^{53, 58} was an early opponent to Helmholtz introducing a theory that relied on increased zonular forces in response to the contraction of ciliary muscle which he suggested further causes the lens to flatten at its periphery and to steepen at the centre during accommodation. Tscherning⁵⁹ attributed such changes to the different mechanical properties between the lens nucleus and cortex as he believed the nucleus was more curved and more resistant to external forces. The lens diameter would increase and the lens thickness would decrease due to the bulging of lens created by compression from the vitreous during accommodation⁷.

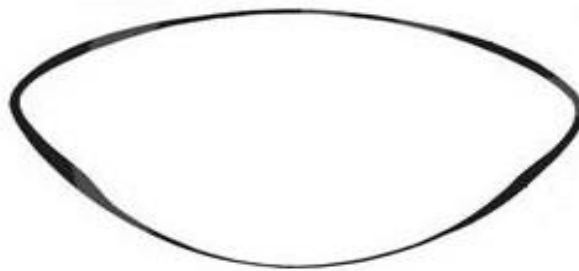


Figure 1.8 Variation in capsular thickness.

Fincham³⁴ described similar curvatures of accommodated lens surfaces, especially for the anterior surface. Contrary to Tscherning⁵⁹, Fincham thought that such lens shape changes were due to the spatial variation of the capsular thickness³⁴. The lens capsule is thicker in the anterior than in the posterior portion, with the thickest part at lens

periphery^{34, 60}(Figure 1.8). The application of tension would flatten the peripheral part where the capsule is the thickest and strongest, but steepen the central axial region where the capsule is weaker³⁴. The changes in lens curvature with accommodation described by Schachar⁵⁶ are essentially the same as the one proposed by Fincham³⁴. The difference between these two theories is whether such steeper central lens curvature and flatter peripheral lens curvature is induced by the different zonular behaviours or the spatially varying capsular thickness.

Coleman's catenary hydraulic suspension theory considered the influence from the vitreous that was suggested to impose a pressure force on the lens posterior surface⁵⁴. In this theory the lens, zonular fibres and anterior vitreous formed a diaphragm between the anterior and posterior chambers of the eye. Contraction of the ciliary muscle was thought to induce a pressure difference between the aqueous humour and the vitreous. The anterior lens capsule, supported by the aqueous humour, together with the zonules would form the shape of a catenary or a trampoline⁶¹. The lens in such a state would have a steep anterior central curvature but a flattened peripheral curvature. The ciliary body would not be providing any equatorial stretching forces to the lens. A very early theory dating back to 1611 was proposed by Kepler (reviewed by Werner 2000⁵) and this states that the lens changes focus by anterior and posterior movement. Most of the *in vivo* visualizations of the ciliary body and zonules are hampered by the presence of the iris, therefore more evidence is needed for a fuller understanding of the accommodative process.

1.3 Presbyopia

Accommodative amplitude defines the capacity of the lens to change focus and it is calculated by the difference in optical power of the lens in fully accommodated and fully unaccommodated states. The optical power of the fully accommodated lens gradually decreases with age such that the reduction of the focus in the near range becomes pronounced in middle age. The ability of the lens to focus on far objects is preserved with age and the optical power of the unaccommodated lens remains relatively constant. The difference between the optical powers of these two states, i.e. the accommodative amplitude, therefore gradually decreases throughout lifetime and was found to follow a linear trend until the fifth to sixth decades of life^{1, 2}. Such a loss of accommodative ability is commonly known as presbyopia. Figure 1.9 shows the

comparison between a normal eye (Figure 1.9a) and a presbyopic eye (Figure 1.9b) when focusing on near objects.

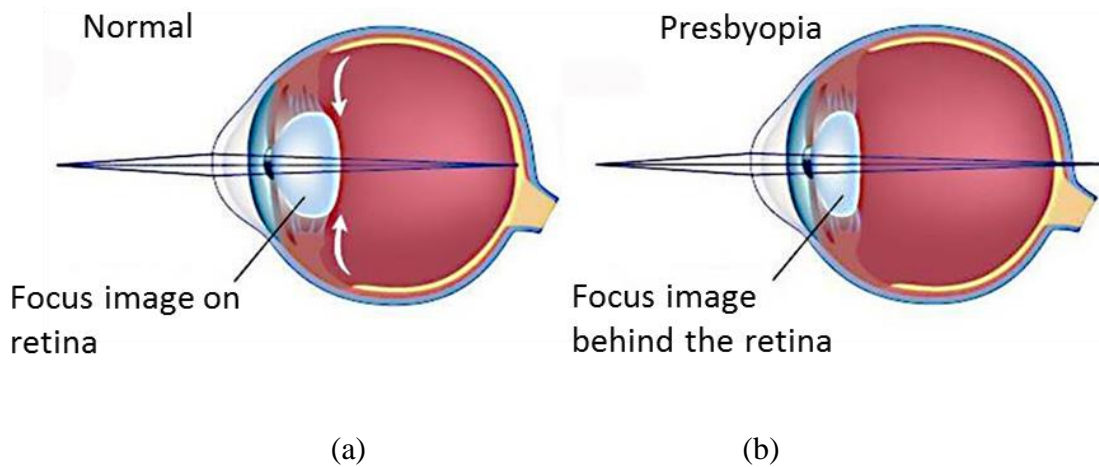


Figure 1.9 Comparison of normal and presbyopic eye.

1.3.1 Theories of development of presbyopia

Several potential causes are thought to contribute to the development of presbyopia and can be broadly divided into two categories: one considering the changes in mechanical properties and one considering the changes in geometries. In addition to the lens, other ocular components involved in accommodation, such as the capsule, zonules and ciliary muscle have all been considered to contribute to the presbyopic process.

Changes in mechanical properties can be attributed to the lens substance as well as to the capsule. The age-related sclerosis of the lens substance has been widely reported⁶²⁻⁶⁵. The continuous addition of lens fibres with age is thought to cause the lens to become more compact and stiff⁵, especially in the nucleus^{62, 66, 67}. The lens stiffness increases with age such that the degree to which the lens alters its shape in response to the accommodative stimulus is reduced. Although different studies have reported large variations in the mechanical properties, and this can be at least partially attributed to different measuring techniques^{62-65, 68}, there is a general trend of an increasing mechanical modulus and increasing resistance to external deformation⁶⁹. In addition, the lens capsule was thought to become less able to mould the hardened lens into the accommodated form as proposed by Fincham³⁴. Such a hypothesis is evidenced by experimental measurements of the capsular elasticity conducted by Fisher, who found that the Young's modulus of the lens capsule decreases with age and, by 60 years of age,

the value is almost half of that in younger years⁷⁰. Recently, changes in the distribution of material properties within the lens have been reported by Besner *et al.*⁷¹. Using Brillouin analysis they found a stiff central plateau region in all measured lenses and the width of this region increases steadily with age. As the peak value of measured longitudinal modulus in each lens does not change with age, the expansion of the central stiff region may account for presbyopia⁷¹.

The second consideration which relates to the change in lens geometries⁷² considers the relative morphology between the lens and the zonule. Both the cross sectional area and the thickness of the lens increase throughout life^{19, 28} and it is believed that presbyopia results from the continuous growth of lens dimensions especially with regard to the equatorial diameter⁷³. The apex of the ciliary muscle moves anteriorly and inwards with age, suggesting a thickening of the ciliary body⁷⁴. Such an increase in equatorial dimension and decrease in the ciliary ring diameter will leave less space for zonular fibres and thereby decrease the zonular tension with age^{75, 76}. Another geometrical possibility is related to the angle of zonular forces exerted on the lens. The anterior zonular attachment positions shift anteriorly as the lens grows with age⁴⁸. This further influences the relative angles of the zonular forces applied on the lens capsule, causing the anterior zonules to become more tangent to the lens surface^{72, 77} and thereby less able to change the lens shape.

Other factors that have been considered to be involved in the loss of accommodative amplitude include: the reduced contractibility of the ciliary muscle^{1, 2, 78} and the reduced support by the vitreous as it becomes more liquid with age^{53, 79}. There was once a lack of data describing the *in vivo* morphology and function of the ciliary muscle due to the blockage by the iris^{80, 81}. Recently the contractibility of the ciliary muscle was demonstrated to be retained long after the onset of presbyopia using *in vivo* MRI observations⁷⁴, giving support for the aforementioned lenticular theories. Whether some or all those factors work mutually to account for presbyopia or one of them acts predominantly requires further investigation.

1.3.2 Restoring accommodation

The restoration of accommodative ability to the presbyopic eye is of major research interest because all people develop presbyopia. Traditional ways for treating presbyopia are by using reading glasses, either designed as mono-vision, bi-vision or multi-vision⁸².

Chapter 1. Introduction

Reading glasses aid the lens to focus on predefined fixed distances but do not give back true active accommodative ability to the lens. Various surgical treatments have been proposed to restore the accommodative ability of the lens in a presbyopic eye.

Scleral expansion is an approach based on Schachar's theory of accommodation^{56, 57} and presbyopia⁷⁵. The sclera is expanded to increase the diameter of the inner ciliary ring to restore the space between the lens equator and ciliary muscle, such that the slackened zonular fibres, induced by the lens equatorial growth with age, can regain the required tensions during accommodation. However, scleral expansion did not achieve the proposed expectations^{83, 84} with complications reported, such as thin scleral pockets, extraction of bands, axial myopia etc^{85, 86}.

A method using pharmacological intervention has also been proposed⁸⁷, i.e. eye drops are developed to selectively act on the lens and destroy molecular and cellular bonds that are thought to soften the lens and preserving the shape changing ability of the lens to restore the accommodative ability^{82, 88}. Such eye drops need to be applied for many years, preferably before the onset of presbyopia⁸². Most of the pharmacological compounds include a combination of different drugs and it is currently unclear how much contribution was played by each of the drug⁸⁷.

An alternative way is to soften the lens substance using a laser. The lens is left in place and treated using a femtosecond laser, which causes ablation of the lens substance and thereby changes the mechanical properties⁸⁹. Studies incorporating this non-invasive approach on animal and human cadaver lenses have proved its ability in restoring accommodation in the presbyopic eye⁸⁹⁻⁹¹, but efforts are still required to avoid induced opacities.

Replacing the lens substance with an artificial intraocular lens (IOL) is a possible way to restore accommodative ability. This is a typical treatment for cataract surgery, in which an incision is made to the anterior capsule to remove the cloudy lens and to place an IOL in the empty capsular bag⁹². An accommodative IOL restores the accommodation by forward and backward movement in response to the ciliary muscle contraction⁹². Reported complications of the IOL surgery, which are relatively rare, include proliferation of lens epithelial cell, capsular shrinkage and opacification of posterior capsule⁸². Reports of successful accommodating IOLs are not conclusive^{92, 93}.

It has been proposed that accommodation could be restored by refilling the empty capsule with a suitable inert medium⁸². The material used to refill the lens would need

to be able to behave mechanically akin to a young lens and produce the required optical properties. The challenge of such a treatment is mainly on the development of materials with expected behaviours and the precise control of the refilling process⁹⁴. Posterior capsular opacification is also a potential complication⁹⁵.

1.4 Finite Element Analysis in biomechanics

Finite Element Analysis (FEA) is a numerical method for solving engineering problems, which deal with complex mathematical problems, for analysing stress and strain patterns, heat transfer, electromagnetism, fluid flow etc⁹⁶. Real world engineering structures usually have complicated geometries, loadings and material properties that are not easily solved by an analytical mathematical method. Most engineering problems can be described numerically using differential equations with initial and boundary conditions. For complex problems such as those involving nonlinearities, the number of differential equations can be huge. With the evolution of high performance computational technology, FEA has become an ideal choice for addressing problems that are otherwise intractable.

As a numerical tool, FEA divides a complicated structure into a large number of divisions with regular shapes such as triangles or rectangles for 2-dimensional problems and tetrahedrons or hexahedrons for 3-dimensional problems, which are given the name elements. Elements are connected with each other through nodes in a manner such that adjacent elements share common nodes at their common boundary. Equations describing the geometrical continuities and mechanical behaviour for each element are formulated. All equations of the elements in the whole problem domain are combined and analysed to provide solutions for the whole body⁹⁷. High performance computing provides the FEA approach with the ability to solve complex geometries, complex material properties and complex tissue interactions especially in the biomechanical field.

Most of the biomechanical studies related to the human body, such as investigating the natural behaviours of body structures and load-bearing implants, deal with the analysis of stresses and strains. FEA models have proved useful in various fields especially for bone mechanics, muscle and soft-tissue mechanics. This technique offers the possibility of analysing behaviours through simulations that may not be easily performed experimentally, which is especially the case for the crystalline lens. Other applications

of FEA in ophthalmology include testing the feasibility of implant devices such as IOLs and prediction of lens behaviour after surgery⁹⁸.

1.5 Aim and objectives

The present thesis aims to provide an improved understanding of the physiological process of accommodation and the development of the loss of accommodative ability with age through the utilization of FEA. The research reported in this thesis endeavours to provide the most physiologically accurate lens models by using the most up-to-date input data to enhance the model performances.

The step by step objectives of the present dissertation include:

1. To develop Finite Element (FE) lens models incorporating the lens geometries measured using synchrotron interferometric X-ray analysis³⁷, which provides the complete dimensions of the external geometries as well as the internal continuity zones from intact lenses. The uncertainties brought by assembling lens shapes using parameters from different sources^{99, 100} can be avoided.
2. To overcome the limitations related to coupling the zonular fibres to the capsule. The existing FE models consider the attachment of the zonular fibre to the lens capsule as a single point coupling, a consideration which yields discontinuous curvatures of the lens shape^{99, 101, 102}. The present research has created lens models with continuous smooth lens curvatures by introducing multiple nodal coupling mechanisms to the lens models.
3. To validate the accuracy of the developed FEA lens models by comparing the results obtained from simulations with both *in vivo* clinical measurements and *in vitro* experimental data. The predicted changes in the dimensions, thickness and curvature of the lens models, should match those from experimental measurements to prove the accuracy of the lens models developed and their physiological relevance.
4. To investigate the influence of different distributions of material properties on the performance of FEA lens models. Gradient distributions of material properties within the cortical region reflect the physiological importance of spatially varying mechanical properties of the lens.
5. To propose possible configurations of the zonular fibres and examine the impact of different zonular angles on accommodation. To try and resolve differences between the

theories of accommodation as well as to determine the contribution of zonular fibres to age-related accommodative loss.

6. To evaluate the sensitivities to various parameters of different ocular components in accommodation, including lens geometries, the positions of zonular-capsular attachment and capsular thickness variations. The lens is a complex organ with the morphology and properties of almost all of its consisting components changing with age and with accommodation.

1.6 Structure of the thesis

In this Chapter, an overview of the anatomy and physiology of the crystalline lens, how it functions during accommodation and how it changes with age has been presented. The interaction of the lens with the surrounding ciliary body and zonules are also discussed. These have provided a basic understanding of the concept and clinical problems to be studied in this work.

In Chapter 2, a comprehensive review of previous work on measuring the material properties of the lens, the lens capsule and the zonular fibres are firstly presented. These are to understand the sources of the various values induced by different measuring techniques and lens preparation procedures and to select appropriate values as input data for our developed models. Lens models developed by previous FEA studies are reviewed. Those studies provide the stepping stone of this discipline hence the review mainly focuses on their methodologies.

In Chapter 3, the complete procedure for developing three dimensional lens models is presented, including extraction of the lens geometries from optical images, generation of three dimensional CAD solid models and conversion into FE models. Material properties obtained from two previous spinning lens studies^{62, 65} were used for the lens models. Models with gradient distributions of cortical moduli are examined and compared to models with a uniform distribution of cortical modulus, with respect to stress and displacement fields. The curvatures of the major lens surfaces determined and analysed which accommodative theories to support.

In Chapter 4, three different types of zonular configurations are modelled and simulated with higher levels of stretching forces. The changes this obtained in lens deformations in relation to changes in optical power are compared to *in vivo* data. The alterations in

Chapter 1. Introduction

zonular angles are investigated and how they affect the comparison with the *in vivo* data is determined.

In Chapter 5, an exhaustive search scheme is developed and a sensitivity analysis is conducted based on axisymmetric models with three sets of zonular fibres pointing in three different and uncoupled directions. The correlations between these three angles and the contribution of the anterior, equatorial and posterior zonular angles to accommodation are reported. Variations in capsular thickness were also considered.

In Chapter 6, eight new lens models, covering the age range from 16 to 91 years, are developed. Material properties according to *in vivo* Brillouin light scattering analysis⁷¹ were used for these models. The distribution of the elastic modulus within each examined lens is linearly related to the profile of the respective refractive index⁷¹. The lens stresses and deformations resulting from these models are presented.

In Chapter 7, i.e. the last chapter of this PhD Thesis, an overall discussion of the present work is demonstrated, while guidelines and ideas for future work are stated.

2 LITERATURE REVIEW

2.1 Elastic properties of the lens

A good knowledge of the lens mechanical properties is not only essential in understanding the physiological process of accommodation and the development of presbyopia, but also of crucial importance in conducting computer simulations as they determine the accuracy of the FE lens models. Previous studies concerning mechanical properties of the lens were conducted *in vitro* as the measuring procedures required dealing with the isolated lens directly^{62, 63, 68}. Recently it has become possible to perform *in vivo* measurements of lens mechanical properties using Brillouin light scattering analysis⁷¹. Similarly to the optical properties, the mechanical properties of lenses vary between different individuals and alter with age. Various approaches developed in previous work were able to map the spatially varying distribution of elastic modulus across the lens but the reported values and ageing trends were not consistent given the range of diverse methods^{63, 65, 68, 103}. The different approaches and their reported mechanical properties of the human lens are reviewed below.

2.1.1 Spinning

Fisher (1971)⁶² firstly proposed the method of spinning the lens around its central axis at a fixed speed so that the induced centrifugal forces deformed the lens in a manner similar to the lens shape change during accommodation. The deformed profile of the lens during spinning was monitored by a high speed camera allowing the determination

of the lens shape parameters. The sagittal thickness and equatorial diameter of the lens, as well as the specimen density were used to calculate Young's moduli for both the nucleus and the cortex of each lens. The nucleus is determined from a central spherical region with a radius equal to the anterior thickness of the lens. All 40 measured lenses, aged from 4 months to 67 years, were kept with intact capsules and were freed from zonular fibres. The reported Young's modulus of the cortex, found to range from 0.5kPa to 4.0kPa, is higher than that of the nucleus, which ranged from 0.5kPa to 3.5kPa, in all measured ages. In both parts the Young's modulus increased continuously throughout the lifespan, with a higher rate of growth seen in the nucleus than that of the cortex after 40 years of age (Figure 2.1). The spinning method has the advantage of maintaining the lens intact thus inducing fewer disturbances to the lens fibre cells⁶².

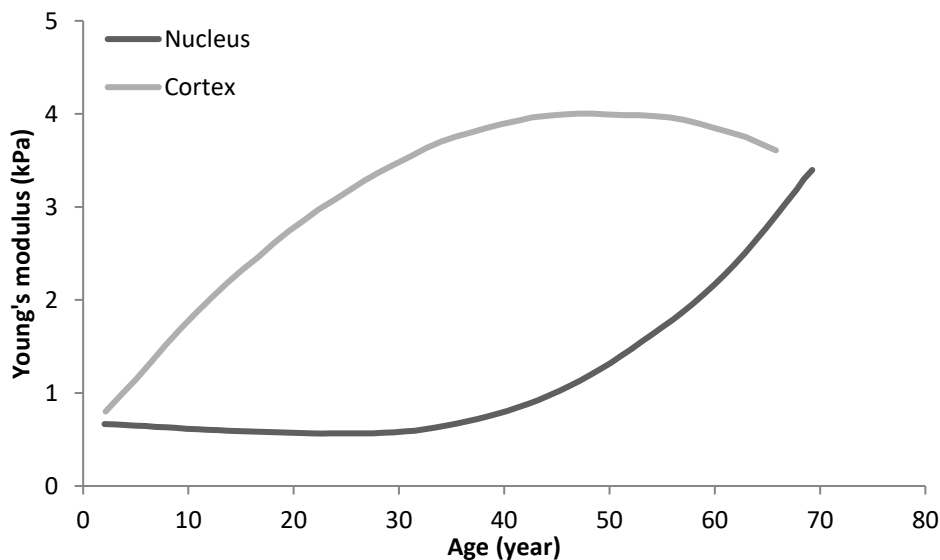


Figure 2.1 Young's modulus of lens nucleus and cortex with age reproduced from Fisher⁶².

The spinning method was repeated by Wilde *et al.*⁶⁵ using 29 lenses aged from 12 years to 58 years old; these lenses were decapsulated. Different procedures were introduced to correct the systematic errors made by Fisher (1971)⁶² noted by Burd *et al.* (2006)¹⁰⁴: a camera recording the lens deformations was synchronized with the lens orientation to reduce motion blur; an iterative optimization procedure was introduced to reduce the approximation during calculations. The shear modulus determined in the nucleus and the cortex plotted against age is shown in Figure 2.2. The ageing trend of the shear modulus in the nucleus is in accordance with Fisher⁶² in that the older lens has a higher elastic modulus than the younger lens. The shear modulus in the nucleus is lower than that of the cortex in young lens but grows at a faster speed with age and becomes higher

than that of the cortex in the old lens. The age at which the nuclear modulus becomes greater than the cortical modulus is around 45 years of age, after which the cortical shear modulus demonstrates a slightly decreasing trend. The validity of this measurement also remains questionable as reported moduli are solely from lenses from which capsules were removed. Decapsulated lenses are at risk of dehydration especially during the spinning process as the induced centrifugal forces can drive out a significant amount of the water content.

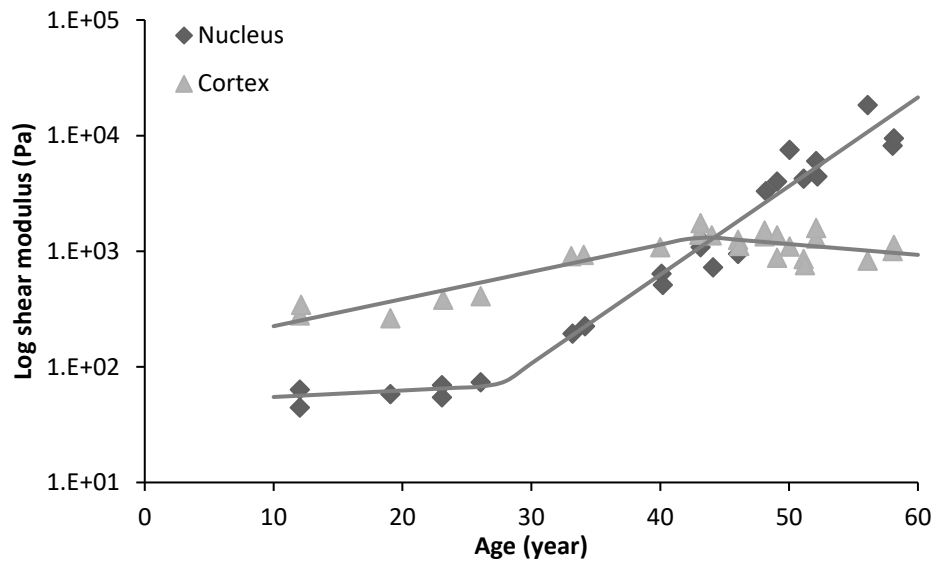


Figure 2.2 Shear modulus of lens nucleus and cortex with age reproduced from Wilde et al.⁶⁵.

2.1.2 Indentation

Heys *et al.* (2004)⁶³ carried out indentation tests on 18 *post-mortem* lenses aged from 14 to 78 years using a custom made cylindrical probe. All the lenses were stored at -80°C and were cut along the equatorial plane before being measured. During the test, the probe was penetrated into each sectioned lens for a series of measurements across the lens equatorial plane using a slowly ramped force from 0 to 3mN. The shear modulus G was calculated using equation 2.1:

$$P = 4RdG/(1 - \nu) \quad (2.1)$$

where P and d is the total load and recorded maximal depth of indentation respectively, $R = 0.2\text{mm}$ is the radius of the probe, $\nu = 0.5$ is Poisson's ratio. The reported modulus shows a continuously increasing trend with age in both the nucleus and the cortex. The

cortical shear modulus increases approximately 53 fold from 48.5Pa (in a 14-year-old lens) to 2577Pa (in a 76-year-old lens) while the nuclear shear modulus demonstrates a more pronounced 930 fold increase from 25.7Pa (in a 20-year-old lens) to 23954Pa (in a 73-year-old lens). Lenses younger than 30 years have shear moduli in the nucleus lower than those in the cortex. Lenses older than 60 years, on the contrary, have higher shear moduli in the nucleus than in the cortex. The crossover age, at which the moduli of the nucleus become higher than that of the cortex is around 30 to 35 years (Figure 2.3). However, the accuracy of an indentation test was limited by the freezing and sectioning procedures that may disturb the water content and fibres alignment within the lens.

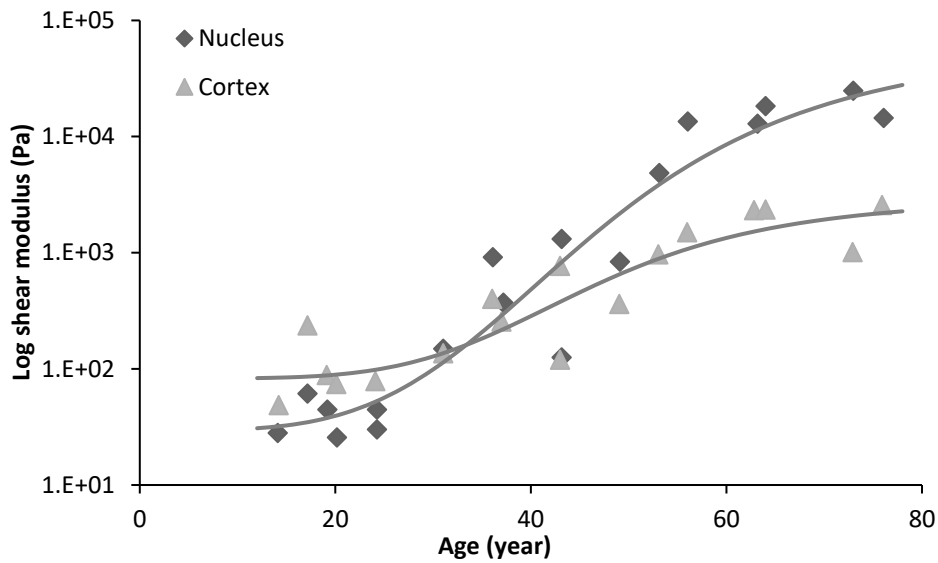


Figure 2.3 Shear modulus of the nucleus and the cortex with age reproduced from Heys et al.⁶³.

To evaluate whether the freezing process during lens storage has a significant influence on the measured values, Heys *et al.* (2007)¹⁰⁵ performed the indentation test again on 40 fresh human lenses aged from 0 to 88 years less than 48 hours after death but measurements in this experiment were only conducted at the lens centre. The difference between measured elastic moduli of fresh and frozen lenses is more pronounced in young lenses as the young fresh lenses had shear moduli about 5 to 6 times higher than their counterpart frozen lenses; in old lenses the moduli were similar. In addition, the shear moduli of fresh lenses displayed less scatter compared to those of frozen lenses but both demonstrated 500 fold increases over the age range between 20 to 60 years. Excluding the freezing process, the results reported by indentation tests are still less reliable than those using non-destructive approaches as lenses measured using such

invasive methods need to be thawed and penetrated and therefore destruction to the lens fibres and the loss of water content are unavoidable.

2.1.3 Bubble-based acoustic radiation force

Hollman *et al.*⁶⁸ implemented a bubble-based acoustic radiation force to measure human lenses by keeping fresh lenses in collagenous gelatin with ultrasound access from the top and laser access from the bottom of the sample container. The laser created micro-bubbles within the lens tissue at 1mm intervals from the lens centre to the lens periphery. The ultrasound transducer applied an acoustic radiation force to the laser-induced bubbles and tracked their resultant displacements. As the displacement of each bubble is proportional to the local compliance of the lens substance¹⁰⁶, a map of spatially varying Young's moduli can be determined using a constant of proportionality⁶⁸ and the inverse of the displacements of bubbles at different locations. Three middle-age (40 to 41 year old) and 9 older-age (63 to 70 year old) human lens specimens were measured. Young's modulus in the lens centre was found to be higher than that of the surrounding parts: it decreases from 5.2kPa in the centre to 1.1kPa at the periphery in middle-age lenses and from 10.6kPa to 1.4kPa in old-age lenses (Figure 2.4). Bubble-based acoustic radiation has the potential to be performed *in vivo*; however large scatter was observed in both age groups by Hollman *et al.*⁶⁸.

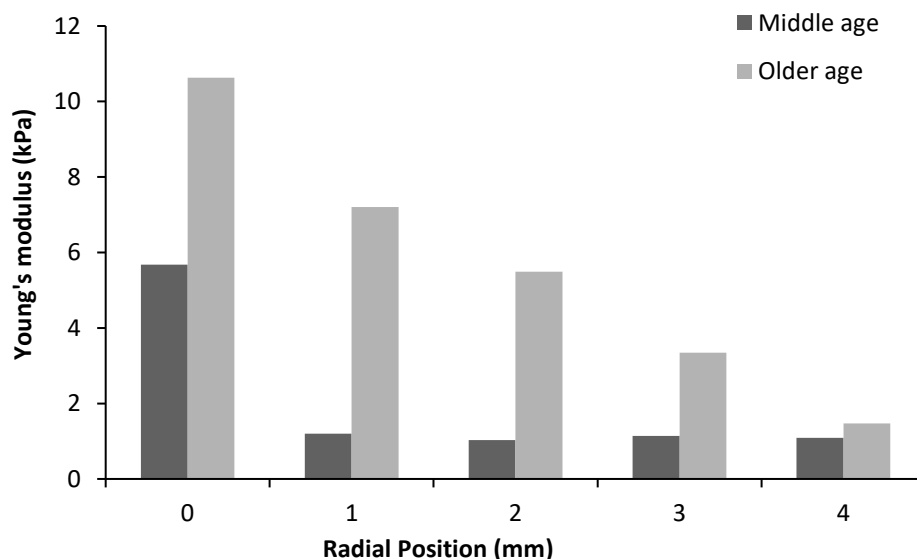


Figure 2.4 Spatially varying Young's moduli of lenses reproduced from Hollman *et al.*⁶⁸.

2.1.4 Compression

The compression method is only applicable for determining the overall mechanical behaviour of the lens as it requires squeezing of the intact lens. Glasser and Campbell⁶⁹ compressed 19 lenses aged from 5 to 96 years old using a custom designed squeezing apparatus that can apply compression forces along the optical axis of the lens. Only the relative resistance of the lens to the same amount of compression was recorded and it is shown to increase with age. The compression method is limited by the difficulty in converting the measured parameters into an elastic modulus, as this would involve the consideration of lens shape as well as the contact area between the compressor and the lens. Further investigations are needed to take full advantage of the compression technique in the determination of the lens mechanical properties.

2.1.5 Brillouin light scattering

Brillouin light scattering is a type of inelastic scattering that makes use of two interaction types between optics and acoustics: acoustic waves can modulate optical photons and the optical field can induce acoustic waves¹⁰³. In more detail, the propagation of acoustic waves can spatially and temporally modulate the material density by creating expansions and contractions of the medium. The refractive index of the medium is related to the density and therefore serves as an indication of the acoustic modulation¹⁰³. Conversely, an incident light beam can initiate acoustic waves from the material by creating spatially and temporally variations of elastic strain in the medium¹⁰³. These two interacting mechanisms cause the incident light to either gain energy from existing acoustic waves in a medium or to transfer energy to the material to induce acoustic waves. Therefore the scattered light from the medium will be associated with both upshift (anti-Stokes scattering) and downshift (Stokes scattering) frequencies, namely the characteristic Brillouin doublets¹⁰³. It is possible to detect the elastic properties of a medium using the Brillouin Light Scattering (BLS) technique by monitoring the propagation of a well-defined acoustic wave, as it is coupled with the mechanical properties of the material.

Bailey *et al.*¹⁰³ measured the bulk modulus of 29 intact *post-mortem* capsulated human lenses, aged from 30 to 70 years, using the BLS technique. The BLS frequency shifts were measured using a laser of 2-10mW radiation along the central axis of the lens from the anterior pole to the posterior pole in $25\pm 1\mu\text{m}$ steps. The propagation speed U of an

acoustic wave through a medium of density ρ is defined by the shear modulus G and bulk modulus K of the materials:

$$U^2 = \left(K + \left(\frac{4}{3} \right) G \right) / \rho \quad (2.2)$$

The bulk modulus K is related to G and Poisson's ratio ν in an isotropic material through the equation 2.3:

$$K = 2G(1 + \nu) / 3(1 - 2\nu) \quad (2.3)$$

The lens, with a high water concentration, is nearly incompressible and has a Poisson ratio $\nu \sim 0.5$, which contributes to a very large K compared to G . Therefore the relation between U and K can be described as equation 2.4:

$$K = U^2 \rho \quad (2.4)$$

The speed of acoustic wave in Brillouin scattering is related to the wavelength of incident light λ , the refractive index of the medium n , and the average of the Stokes and anti-Stokes frequency shift f as given by equation 2.5:

$$U = \lambda f / 2n \quad (2.5)$$

Therefore the bulk modulus is directly obtained from the Brillouin measurement of frequency shift f with knowledge of n , λ and ρ from equation 2.6:

$$K = \rho \lambda^2 f^2 / 4n^2 \quad (2.6)$$

The calculated bulk modulus of the lens nucleus, 2.79 ± 0.14 GPa, was larger than that of the lens cortex, 2.36 ± 0.09 GPa with no age dependence in both parts (Figure 2.5). The BLS technique is superior to other approaches in that it provides non-destructive measurements suitable for characterizing the spatial variations of lens mechanical properties with high resolution¹⁰³. However, Bailey *et al.* used a refractive index of $n=1.42$ for the nucleus, 1.37 for the cortex and a density of 1085 kg/m^3 for all the lenses¹⁰³ without considering the spatially changing refractive index^{35, 37} across the lens and the individual variations in sample densities.

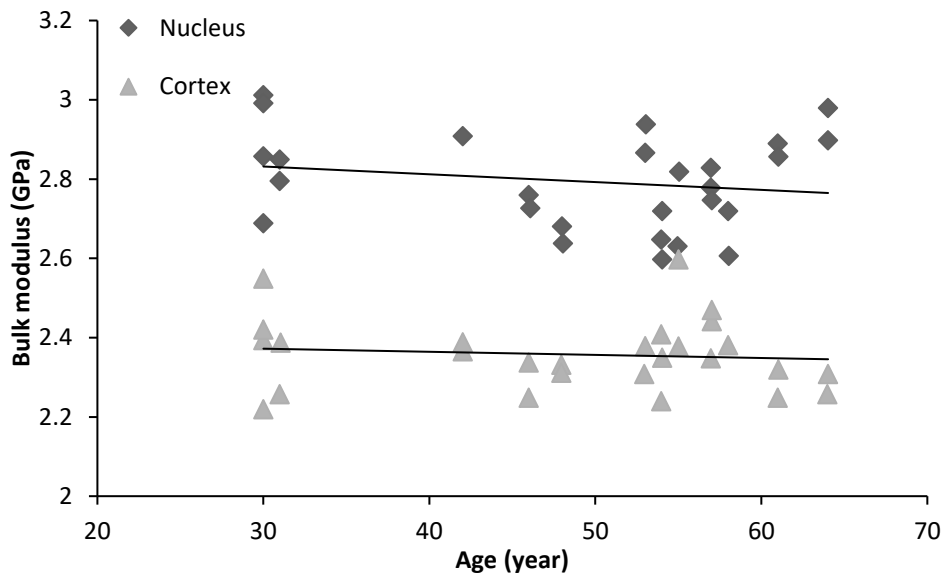


Figure 2.5 The bulk modulus of the nucleus and cortex with age reproduced from Bailey *et al.*¹⁰³.

Not long after Bailey *et al.*¹⁰³, Scarcelli and Yun¹⁰⁷ successfully constructed a BLS optical scanner safe for *in vivo* human use. The laser power of this new device using a continuous-wave laser of 780nm wavelength is only 0.7mW, about 46 times lower than the clinical safety threshold of 32mW Maximum Permissible Exposure (MPE) calculated using a 1mm aperture¹⁰⁸ (0.79mm² area) of cornea-lens and 4W/cm² safety limit according to the International Commission on Non-ionizing Radiation Protection (ICNIRP)¹⁰⁹. Scarcelli and Yun¹⁰⁷ performed the first *in vivo* BLS measurement on a 42-year-old healthy man and reported the lens longitudinal modulus to be within the range of 2.38 to 3.1GPa. The longitudinal modulus M is related to the bulk modulus K by Poisson's ratio ν as described by equation 2.7:

$$M=3K(1-\nu)/(1+\nu) \quad (2.7)$$

The lens with $\nu \sim 0.5$ thus has the same values of longitudinal modulus and bulk modulus, such that the results by Scarcelli and Yun (2012)¹⁰⁷ are consistent with the bulk moduli reported by Bailey *et al.* (2010)¹⁰³.

Recently, Besner *et al.*⁷¹ conducted a wider aged *in vivo* BLS measurement using a 780nm wavelength laser of 2mW radiation to characterize the longitudinal moduli in 56 eyes from 30 healthy human subjects aged from 19 to 63 years old. The longitudinal modulus M was determined from the measured Brillouin frequency shift f using equation 2.8:

$$M = \rho f^2 \lambda^2 / (4n^2 \sin^2(\frac{\theta}{2})) \quad (2.8)$$

where ρ is the density of the sample, $\lambda=780\text{nm}$ is the wavelength of the laser, n is the refractive index, and $\theta=180^\circ$ is the angle between the incident and scattered light, the ratio $\rho/n^2 = 0.5636\text{g/cm}^3$ is constant although both ρ and n are varying across the lens. The measured longitudinal modulus increases from the lens periphery to a central plateau at all ages. The width of the central plateau region increases steadily with age over the tested age range as can be seen from the longitudinal moduli of three selected lenses aged 19, 43 and 61 years from Besner *et al.*⁷¹ replotted in Figure 2.6. No age dependence was found for the peak modulus at the central plateau in human lenses aged from 19 to 45 years but a slightly decreasing trend was observed in lenses aged from 45 to 64 years. These findings add to the knowledge of the development of presbyopia, which can be attributed to the increasing width of the central stiff plateau with age⁷¹.

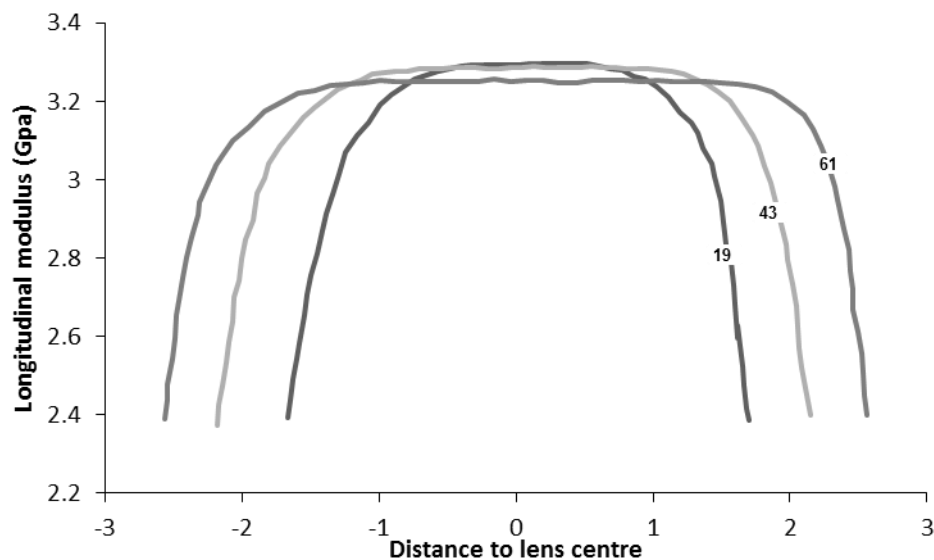


Figure 2.6 Longitudinal modulus across the lens at age 19, 43 and 61 years reproduced from Besner *et al.*⁷¹.

2.2 Dynamic mechanical properties of the lens

The methods described in previous sections were mainly to measure the elastic properties of lenses in the quasi-static state i.e. the observation time scale was in minutes or hours¹¹⁰. The lens, however, exhibits viscoelastic behaviour^{69, 110-112} due to the coupling of elasticity of lens fibre membrane and cytoskeleton^{112, 113} and the cytoplasmic movement^{114, 115}, which therefore cannot be fully described using a single

elastic modulus. It was found previously that *in vitro* lenses deform rapidly in response to compression but recover slowly after unloading^{110, 111}. The dynamics of accommodation, which relates to the rate of lens deformation in response to accommodative stimuli, were found to change with age as well¹¹⁵. The viscoelastic behaviour of the lens is dependent on frequency⁶⁷ and should also be included in the description. Studies that employed dynamic mechanical methods, allowing the characterization of the viscoelastic properties at different frequencies, are reviewed below.

2.2.1 Dynamic mechanical analysis

The general principle for performing dynamic mechanical analysis is to provide the lens specimen with oscillatory deformations, either in the normal or shear directions, at different frequencies. The relation between the oscillatory force and deformation will provide information about both the elastic and viscous properties of the lens. Itoi *et al.*¹¹⁰ applied oscillatory compressions using an electromagnetic transducer to a *post-mortem* female human lens aged 85 years over the frequency range of 0.01-25Hz. The resultant stress and strain formed a hysteresis loop, the shape parameters of which were used to determine the elastic modulus and the loss tangent. However, Itoi *et al.*¹¹⁰ did not factor the real lens shape into the calculation but used a cylinder instead with equivalent length to the lens thickness and equivalent disk area to the lens cross-sectional area. The equivalent Young's modulus of the lens was reported to be 10^4 to 10^5 Pa which slightly increases with oscillatory frequency. The loss tangent is between 0.3-0.4 and shows little dependence on frequency.

Weeber *et al.* (2005)⁶⁷ applied shear oscillatory deformations to 39 *post-mortem* human lenses aged from 18 to 90 years old which were stored at -70 °C before being measured. The oscillatory deformations at 18 different frequencies at equal intervals on a logarithmic scale within the range of 0.001 to 30Hz were provided. During the measurement, each intact lens sample was held between two surfaces with sinusoidal shear displacement $x^*(t) = x_0 e^{i\omega t}$ applied to one side of the lens and a reaction force measured at the other side. The reaction force $F^*(t) = F_0 e^{i(\omega t + \delta)}$ has the same frequency as the applied displacement but is added with a phase shift δ . All measurements were taken within the linear viscoelastic range and this was ensured by

the proportional relations between the amplitudes of the applied displacement x_0 and the resulting force F_0 . Complex shear compliances were determined using equation 2.9:

$$J^* = x^*(t)/(g_0 F^*(t)) \quad (2.9)$$

where g_0 is a constant geometrical factor. The complex shear compliance J^* consists of a storage compliance and a loss compliance. Both the storage and the loss compliance decrease with age and the values measured at a 1Hz frequency are shown in Figure 2.7. Conversion of compliances into elastic moduli needs to take account of the lens shapes, which were not reported, making direct comparison with other studies difficult. Both compliances decrease with increasing frequency, such is a common behaviour of viscoelastic material. Weeber *et al.* (2005)⁶⁷ also demonstrated the influence of freezing on the measured results using porcine lenses: higher storage and loss compliances in fresh lenses were found compared to frozen lenses.

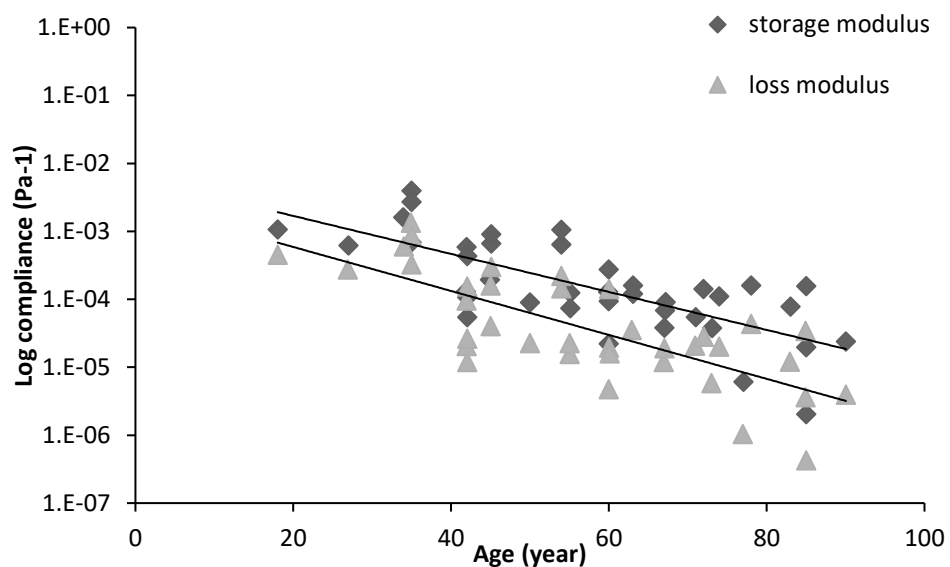


Figure 2.7 Shear storage and shear loss modulus of all measured lenses with age reproduced from Weeber *et al.*⁶⁷.

A further dynamic mechanical analysis by Weeber *et al.* (2007)⁶⁴, applying oscillatory indentation instead of shear deformation to the specimens, took into account the lens shape and calculated the shear moduli of 10 human lenses aged from 19 to 78 years old. The sample preparation procedures were similar to the indentation tests carried out by Heys *et al.*^{63, 105}: the lenses were frozen and sectioned before being measured. A cylindrical probe with 0.5mm diameter was inserted into the lens equatorial plane from the lens centre to the periphery with a 0.5mm interval applying oscillatory displacements ranging from 0.1 to 20Hz to the specimen in the vertical direction. The

applied sinusoidal displacements, resultant force and a shape factor, determined using theoretical finite element analysis, were used to calculate the complex shear modulus of the lens $G=G'+iG''$, which consists of a real part called the storage shear modulus G' and an imaginary part called the loss shear modulus G'' . Results at only three frequencies: 0.10, 0.17 and 0.30 Hz were reported. The storage moduli were higher than the loss moduli at all three frequencies, as seen in two reported lenses aged 40 and 64 years. This is consistent with viscoelastic behaviour in that the materials are more elastic than viscous at low frequencies. The storage shear modulus increases with age at all measured positions but the rate of increase differs: the lens centre increases by a factor of 10^4 over the measured age range while at lens periphery this increase is only 10^2 . The shear storage modulus at the lens centre is lower than the periphery for young ages and becomes nearly uniformly distributed in middle age around 45 to 50 years but is higher than the periphery at older ages (Figure 2.8).

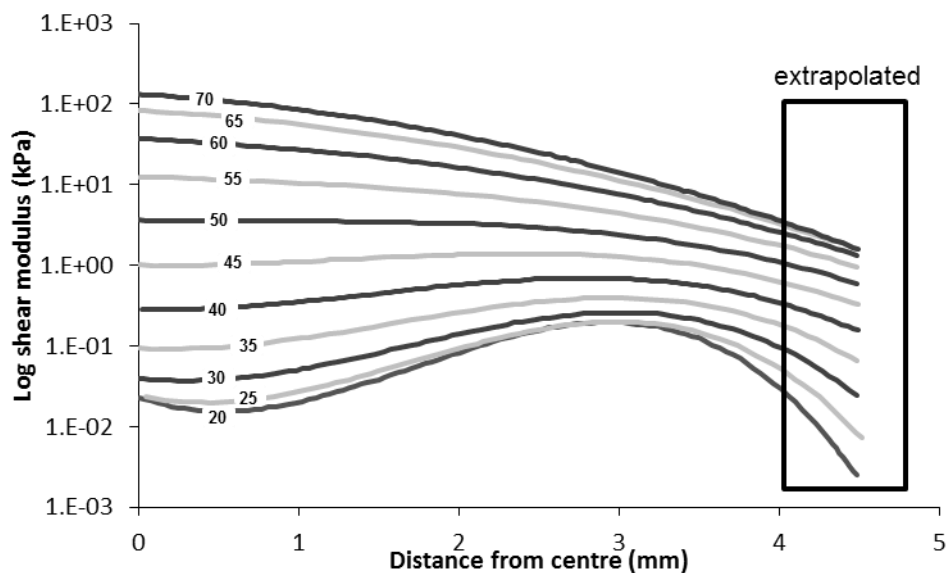


Figure 2.8 Spatially varying shear storage modulus of all measured lenses reproduced from Weeber *et al.*⁶⁴.

Schachar *et al.* (2011)¹¹⁶ employed simple-shear rheometry on 52 human lenses all under 40 years of age with a mean age of 17.5 ± 9.2 years. Two 0.5mm thick mid-sagittal sections of nucleus and of cortex were removed from each lens. Each lens section was then placed between two parallel plates of the rheometer and subjected to small-amplitude (1% shear strain) sinusoidal shear deformations at three frequencies of 75Hz, 100Hz and 150Hz. The determined viscous shear modulus was reported to be higher than the elastic shear modulus under all three frequencies, demonstrating that the lens behaves as a more viscous than an elastic medium at higher frequencies. A small

age-related increase was found in the elastic shear modulus but not in the viscous shear modulus.

2.2.2 Biomechanical model

Beer and van der Heijde^{112, 115}, uniquely, proposed a biomechanical model using springs and dashpot to describe the whole accommodative apparatus. The lens was modelled using the Voigt model consisting of a spring and a dashpot in parallel, with the spring providing the elasticity and the dashpot providing the viscosity. The idea of representing the lens with a Voigt model was firstly shown in Ejiri *et al.*¹¹⁷ for analysing the dynamic behaviour of lenses from cats and dogs. The Voigt model was a set of three springs of different spring constants in series representing the peripheral and axial zonular fibres and choroid (Figure 2.9). Beer and van der Heijde^{112, 115} measured the *in vivo* responses of accommodative process in healthy human subjects and fitted those responses with the developed biomechanical model so that two time constants describing the far-to-near and near-to-far response were determined. The far-to-near accommodating dynamics are dominated by the viscoelastic properties of the lens alone, while near-to-far unaccommodating dynamics are dependent on the properties of the lens as well as on the elasticity of zonular fibres and the choroid. The two time constants were then used to calculate two ratios that give useful predictions of the accommodative dynamics.

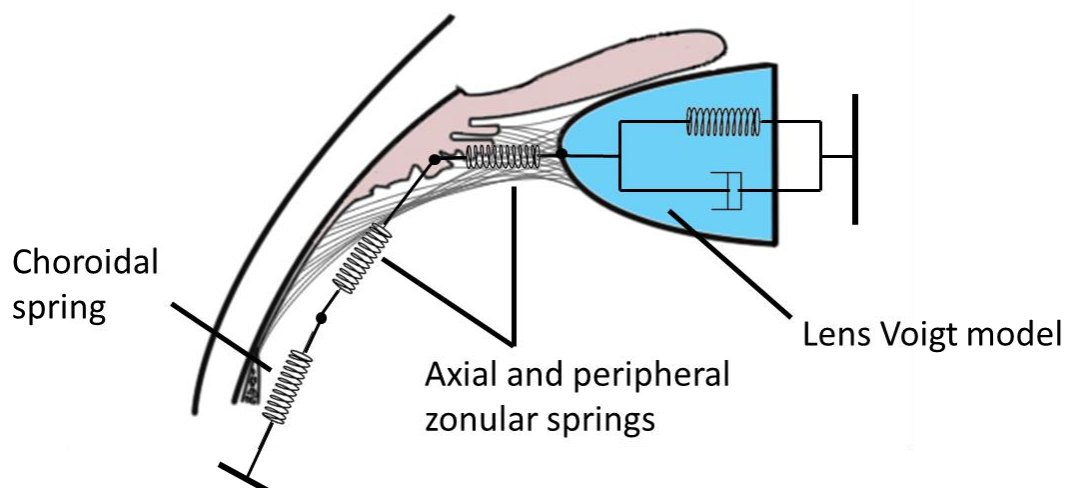


Figure 2.9 The biomechanical model reproduced from Beer and van der Heijde^{112, 115} consists of springs and a dashpot.

2.3 Material properties of the lens capsule

The lens capsule functions as a deformable part during accommodation through which the ciliary body applies forces to the lens. The elasticity of the capsule has long been of interest not only because it maintains the lens shape but also because it affects the lens surface curvatures during accommodation. The importance of the mechanics of the capsule is also seen in cataract treatment which is required to hold in place an artificial IOL. More knowledge of the mechanical properties of the lens capsule can help to improve the design of IOLs. Currently, there are two main types of approaches employed by different studies that the capsule is subjected to inflation or to uniaxial stretching. The capsule exhibits nonlinear elasticity when the strain is above 15% during uniaxial stretching¹¹⁸. However the capsular strain during accommodation is much smaller than this limit as indicated by Hermans *et al.*²⁹: the surface area of an unaccommodated lens capsule was on average 5% higher than that of the accommodated lens capsule. Therefore the elastic properties within the linear range, usually less than 10% strain, are of major concern.

2.3.1 Inflation test of human anterior capsule

Fisher (1969)¹¹⁹ designed a special apparatus with two chambers connected to a number of glass tubes and taps. The whole apparatus was filled with isotonic saline and the pressure between the two chambers was controlled through taps. A glass plate with a central 4mm diameter hole clamping a disk of specimen cut from the anterior lens capsule was placed between the two chambers. The pressure in the lower chamber was then increased to deform the lens capsule to form an upward spherical cap. Young's modulus of the capsule specimen was calculated using the applied pressure and the induced cap volume. In childhood Young's modulus is about 6MPa which decreases to 3MPa at around 60 years old and further decreases to 1.5MPa in extreme old age (Figure 2.10). The Poisson's ratio of the capsule was determined to be 0.47, indicating the volume was almost conserved during the capsular deformation. Danielsen¹²⁰ applied a similar method to that of Fisher (1969)¹¹⁹ on anterior human lens capsules using a plate with a 3mm diameter hole and the measured Young's modulus at 10% strain was 2.40MPa for specimens obtained from human subjects aged from 58 to 96 years. In these two inflation tests the capsule was treated as an isotropic material.

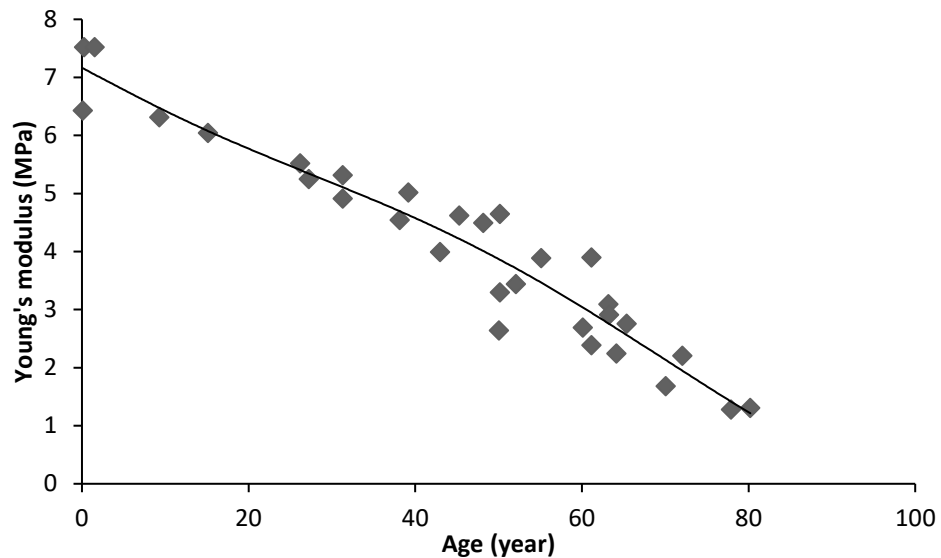


Figure 2.10 Young's modulus of anterior lens capsule with age reproduced from Fisher¹¹⁹.

The regional multiaxial behaviour was investigated by Pedrigi *et al.*¹²¹ using the anterior capsule from both normal and diabetic human lenses aged from 29 to 81 years old. During the test the cornea and iris were removed from an enucleated eye to expose the anterior capsule, which was then penetrated with a needle injecting solutions both to separate the capsule from the lens and to apply pressure. A number of video tracking markers were arranged on the exposed lens capsule to allow the deformations to be measured by a video system consisting of two cameras so that the 3D locations of each marker could be determined. An inverse FE model was used to analyse the material properties of the capsule but the exact values of the elastic modulus were not calculated. The anterior lens capsule was found to exhibit a nonlinear mechanical behaviour and to be regionally anisotropic. The stiffness along the circumferential direction was shown to be increasingly higher than along the meridional direction. The diabetic lens capsules were stiffer than normal lens capsules in both directions.

2.3.2 Uniaxial stretching test

Cutting a ring of capsule with a 3.2mm outer diameter and 100 μ m width from the anterior lens capsule and then slipping the capsular ring over two pins for uniaxial stretching, Krag *et al.*¹²² and Krag and Andreassen¹²³ examined capsular specimens from both the anterior and posterior human lenses respectively over a wide age range from birth until the 10th decade of life. The two pins were connected to a motor and a

force transducer respectively and stretched the capsule ring at a constant speed with the elongation and forces monitored until the capsule ruptured. The mechanical behaviour of the capsule within the whole range of strains from 0 to the rupture point was recorded and the nonlinearity of the lens capsule was found. The ultimate strain, ultimate stress and ultimate tangent modulus all decreased with age. Elastic moduli at less than 10% strain were determined by Krag and Andreassen¹²³. For the posterior lens capsules they were found to range from 0.3 to 2.3 MPa, differing by 0.25 ± 0.1 MPa from the anterior lens capsule (reanalysed from Krag *et al.*¹²²). The Young's moduli of both anterior and posterior lens capsules increased from birth until middle age and decreased thereafter (Figure 2.11).

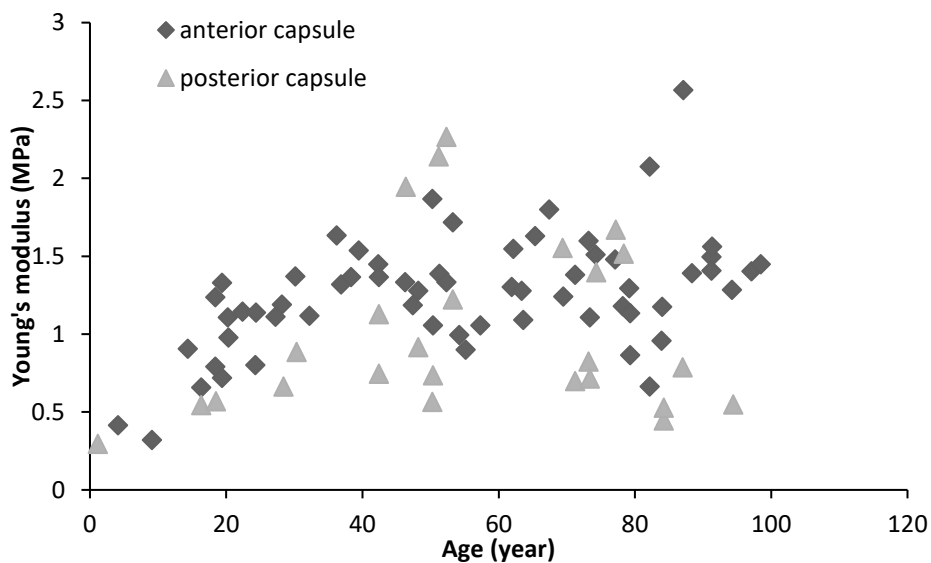


Figure 2.11 Young's modulus less than 10% strain of both the anterior and posterior capsule with age reproduced from Krag and Andreassen¹²³.

2.4 Material properties of the zonular fibres

The zonule is in a long thin cylindrical form with uniform cross-sectional area and it can stand tensional forces only. Therefore the Young's modulus, E , of zonular fibres has been commonly measured using a uniaxial stretching test. The stress is determined by dividing the applied stretching force F by the cross-sectional area A ($\sigma = F/A$) and strain is the ratio between the elongation ΔL and the original length L ($\epsilon = \Delta L/L$) (Figure 2.12) so that Young's modulus is determined by the ratio between stress σ and strain ϵ :

$$E = \sigma / \epsilon \quad (2.10)$$

Currently there is no such technique to allow the direct measurement of the *in vivo* zonular force. The stretching tests reviewed below all determined Young's modulus using the measured stretching force, original length and elongation of the tested zonular fibres with the cross-sectional area values obtained from the literature.

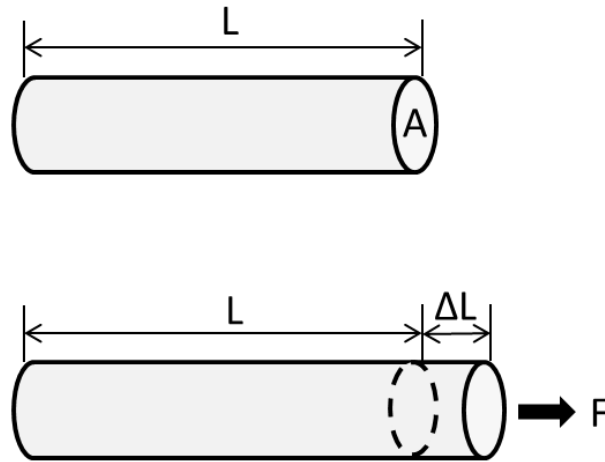


Figure 2.12 Basic mechanism of stretching test for measuring the elastic properties of zonular fibres.

The measurement conducted by Fisher (1986)¹²⁴ on 12 *post-mortem* lens specimens determined the zonular force using a previously proposed method¹²⁵ combining the stretching test with the spinning test. The lens, together with zonular fibres and ciliary body, were firstly removed from the eyeball and subjected to radial stretching forces mediated by the ciliary body deforming the lens in a manner similar to that found during *in vivo* accommodation. The lens was removed from the surrounding zonular fibres and ciliary body after the stretching test and was spun around its central axis (as done in Fisher (1971)⁶²). The spinning induced centrifugal force was regarded as having the same magnitude of zonular force during the stretching test when the same changes in lens thickness were seen for the two tests. Fisher (1986)¹²⁴ did not indicate directly the cross-sectional area used for the calculation, but 0.1225mm^2 can be estimated through an inverse estimation using the constant ratio of $F/\Delta L=1.75\text{Grms/mm}$ as presented in Fig 4b of Fisher (1986)¹²⁴ and a typical length of 2.5mm for the zonular fibre. The resultant Young's modulus was 350kPa which did not vary with age from 15 to 45 years old. Radial stretching and spinning deforms the lens in different ways therefore it is not accurate enough to only compare the thickness change since the shape changes in peripheral regions may differ depending on the method used.

The stretching force was measured directly by van Alphen and Gaebe¹²⁶ who investigated the mechanical properties of zonular fibres from 71 human specimens aged from 0 to around 70 years. The lens with the zonular fibres and ciliary body were treated as a unit and fitted between two clamps providing stretching forces along two opposite directions. The magnitude of the force was measured using a force sensor hooked to one of the clamps and the elongation of the zonular fibre was recorded by a camera. The Young's moduli at 10% strain were 1.0MPa for specimens around 16 years old and 1.5MPa for old specimens with a mean age of 52 years.

Michael *et al.*¹²⁷ applied radial instead of uniaxial stretching to 13 lenses aged from 47 to 97 years old in eight different directions. The section cut kept the sclera with the lens, zonular fibres and ciliary body. The sclera and ciliary body were segmented into eight parts attached to eight hooks equally radially spaced, to avoid circumferential tension. A force sensor was connected to the hooks to measure the stretching force. Linear relationships were found between the recorded force and elongation of zonular fibres within 10% strain. Michael *et al.*¹²⁷ used 0.427mm^2 as the cross-sectional area of the zonule, with the data from Weeber and van der Heijde (2007)¹²⁸, by assuming 100 anterior zonular fibres for each $50\mu\text{m}$ of diameter, 50 equatorial and 135 posterior zonular fibres for each $40\mu\text{m}$ of diameter. Young's modulus was 340kPa among the specimens aged from 47 to 60 years and 270kPa in older ages from 83 to 97 years, at the same magnitude to that obtained by Fisher (1986)¹²⁴.

2.5 Computational modelling of the lens

Computational models provide the possibility of revealing important features that are not feasible or readily obtained through *in vivo* or *in vitro* experiments, such as the internal stress¹²⁹ and strain¹³⁰ of the lens. It is also possible to investigate the contribution of different ocular components involved in accommodation^{131, 132} through computer simulations. The validity and accuracy of computational models are directly related to the input parameters i.e. geometrical shapes and material properties. However, lens models to date have been limited by the available resources of the input data. Complete descriptions of intact lens shapes were rare in early times such that the geometries of developed lens models were usually assembled using parameters from several studies on different lenses using different approaches⁹⁹. The *in vivo* and *in vitro* lenses are in different stress states therefore their dimensions differ (as has been

reviewed in section 1.1.1.2). Coupling the geometries using parameters from different sources would alter the model from the natural lens shape. In addition, the zonular fibres that surround the lens equatorial region are hardly seen through *in vivo* imaging therefore the exact locations of zonular attachment to the lens capsule as well as the directions of forces applied to the lens are not known. In addition, diversities exist in the measurements of elastic properties of the lens substance (as has been reviewed in section 2.1) adding to the obstacles that need to be overcome to construct physiologically accurate models. Current available lens models are able to characterize certain main features of accommodation, such as the changes in central surface curvatures, thickness or central optical powers, which are reviewed below.

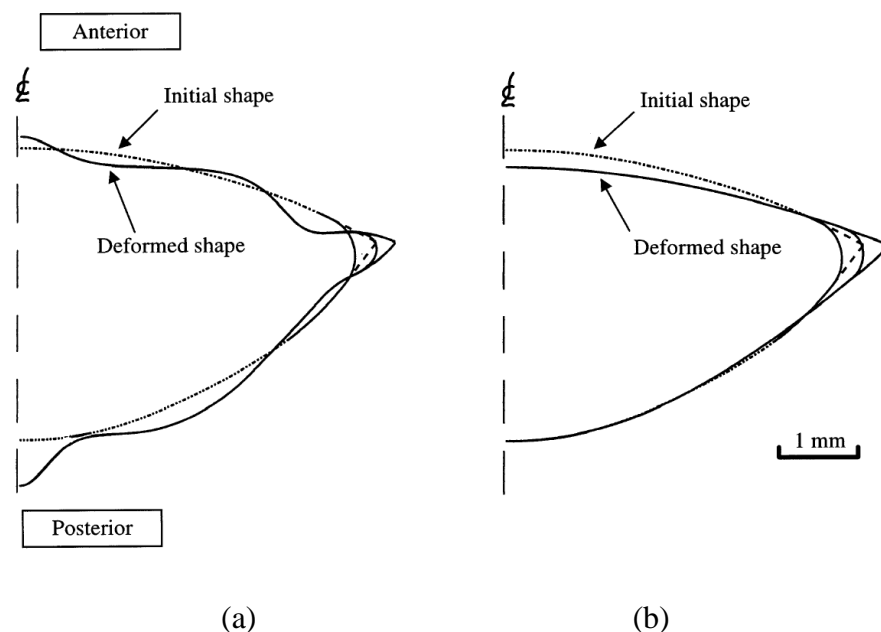


Figure 2.13 The deformed lens shape obtained from geometrical (a) linear and (b) nonlinear analysis with 6.25% of equatorial strain from Burd *et al.*¹³³.

An early mathematical modelling study by Schachar *et al.* (1993)¹³⁴ reported support for the accommodative theory of Schachar⁵⁶ by showing that the Central Optical Power (COP) of the lens model increases with increasing zonular tension. The lens capsule was modelled as an axisymmetric membrane and the influence of the lens substance was treated as that of a fluid with no volumetric change. It was later pointed out by Burd *et al.* (1999)¹³³ that Schachar's model showed an unrealistic deformation of lens shape because a linear-elastic formulation was used. Burd *et al.* (1999)¹³³ then demonstrated the difference between the linear and nonlinear geometrical behaviours of a spherical membrane under expansion using a mathematical calculation. Burd *et al.* (1999)¹³³ developed FE models with only the lens capsule keeping the enclosed volume

conserved during deformation and showed that the COP decreases with increasing equatorial strain when nonlinear geometrical behaviour is considered, supporting the accommodative theory of Helmholtz⁵². The comparison between the deformed lens shape using linear-elastic and nonlinear-elastic formulation is shown in Figure 2.13. These early models were too simplistic to provide a full description of the lens behaviour. The FEA studies reviewed below evaluated various aspects of the complex behaviour of the whole accommodative apparatus, including the zonular forces, gradient material properties and lens internal stress and strain.

2.5.1 Modelling accommodative mechanisms

Schachar and Bax¹³⁵ compared the accommodative theories by Schachar⁵⁶ and by Helmholtz⁵² using an FEA study on 19 and 29 year old lens models. Different values of the lens thickness and radii of curvatures were selected from Brown¹³ to model the two theories such that the initial COPs for the 19 and 29 year old lenses respectively were set to 18 and 15 dioptres, for simulating the accommodative theory of Schachar⁵⁶, and 30.5 and 33 dioptres for simulating the accommodative theory of Helmholtz⁵². Only equatorial zonular tension was applied to Schachar's theory model and continuous increase of the COP with stretching was demonstrated. For modelling of Helmholtz's theory no matter which type of zonular tensions were applied by all three zonules or by anterior and posterior zonules, the COP was found to initially increase for the first 65 μ m of stretching and decrease with further stretching. Different locations of zonular attachments on the capsule obtained from the literature^{48, 136} were modelled: the anterior attaching point varied from 0.37mm to 1.42mm away from the equator and the posterior attaching point varied from 0.25mm to 1.0mm away from the equator. An increasing trend of COP with zonular traction was seen regardless of the zonular attaching positions on the capsule. A greater increase in COP was seen with closer locations of the zonular attaching positions to the equator. The accommodative theory of Schachar⁵⁶ was found to be supported according to the modelling results.

Burd *et al.* (2002)⁹⁹ built three axisymmetric FE lens models based on lenses aged 11, 29 and 45 years old and the input parameters of these models were assembled from a series of clinical studies for both the geometries^{13, 19, 34, 48, 137} and the material properties^{62, 119, 122, 138}. Burd *et al.* (2002)⁹⁹ demonstrated the capabilities of modelling procedures by capturing the main feature of presbyopia i.e. that the 45-year-old lens

model was less effective than the 29-year-old model for accommodation. In support of the accommodative theory of Helmholtz⁵², the central lens surface was shown to flatten on stretching. Most of the later modelling studies have adopted the lens models in this study as the detailed parameters for building these three models were presented and an input file for building the 29-year-old model is freely available online. It should be noted that the nucleus was defined by two circular arcs and the position where these two arcs were connected is seen as a sharp point which is not physiological (Figure 2.14a). In addition, the three zonules were connected to the lens capsule through three single points which resulted in discontinuous curvatures of the deformed lens shapes (Figure 12.14b). These cannot exist in real physiological conditions and should therefore be avoided in lens models.

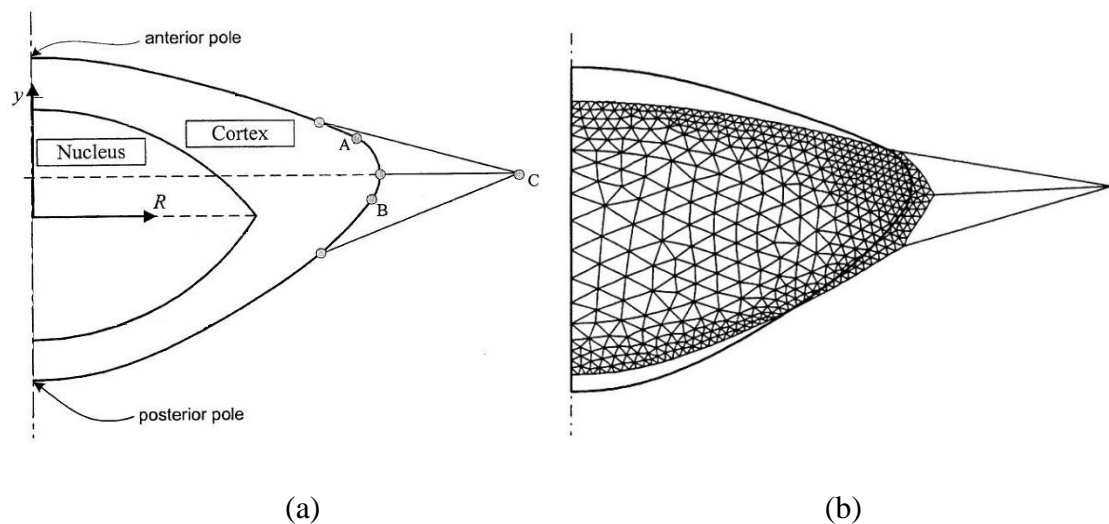


Figure 2.14 (a) Assembled lens geometry and (b) deformed mesh of the 29-year-old lens model from Burd *et al.*⁹⁹.

The lens models aged 29 and 45 years from Burd *et al.* (2002)⁹⁹ were adopted by Martin *et al.*¹⁰¹ to compare the accommodative theories of Helmholtz⁵² and that of Coleman⁵⁴. Lens models were subjected to radial displacements taken from Strenk *et al.*¹⁹ to simulate the accommodative theory of Helmholtz⁵². A static pressure up to 225Pa was applied to the posterior surface of the lens model in addition to the radial displacements to simulate the accommodative theory of Coleman⁵⁴. Martin *et al.*¹⁰¹ concluded that Coleman's theory did not contribute to accommodation as the model with applied posterior pressure could not provide the requisite physiological change of COP. The capsule in this study was modelled using linear shell elements that neither excluded the bending stiffness from the capsule nor considered the accuracy of low order elements for modelling highly curved capsular geometries.

Ljubimova *et al.*¹³⁹ used the 29-year-old lens geometry from Burd *et al.* (2002)⁹⁹ and added support from the vitreous to balance the posteriorly sloped zonular force such that the lens was kept in an equilibrium state. When the vitreous was present (Figure 2.15a) it was modelled as an incompressible body encapsulated with a membrane of the same elasticity as the lens capsule. A coefficient of friction of 0.01 was used between the posterior lens surface and the vitreous to mimic the existence of Wieger's ligament (as shown in Figure 1.5a of chapter 1). When the vitreous was not modelled, a rigid pin was created to allow the posterior zonular fibre gliding from it to maintain the equilibrium state (Figure 2.15b). The influence of the vitreous on accommodation was shown by the smaller changes in sagittal thickness, anterior and posterior surface curvatures of the lens model with vitreous support compared to those found in the model without the vitreous support. Ljubimova *et al.*¹³⁹ also developed models without the equatorial zonular force and found a definitive movement of the lens equator toward the ciliary body in models with or without equatorial zonular force and providing support for the accommodative theory of Helmholtz⁵².

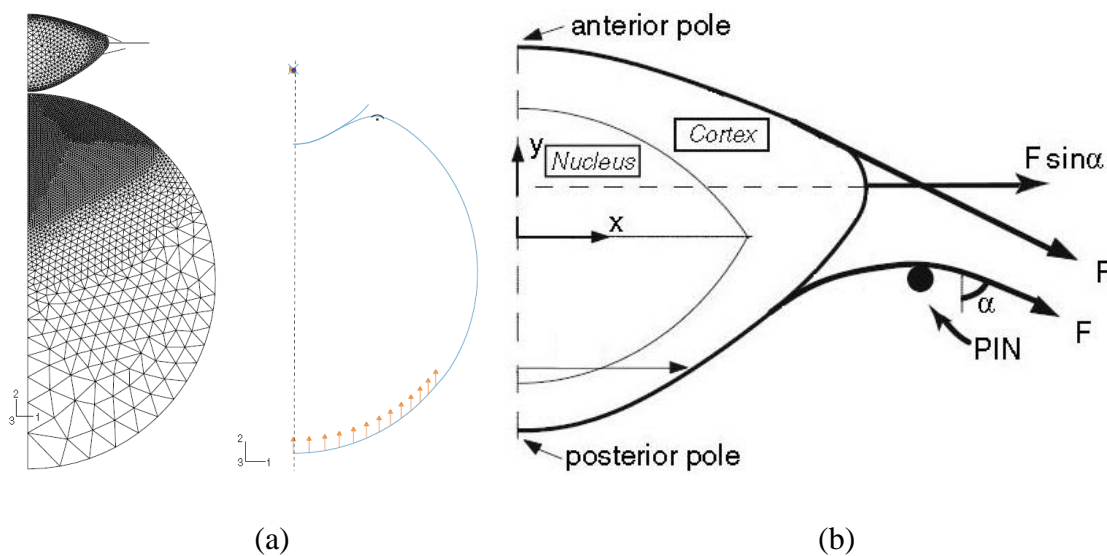


Figure 2.15 The lens models developed by Ljubimova *et al.*¹³⁹ for the cases: (a) with and (b) without vitreous.

Although Liu *et al.*¹⁰² did not use the lens models from Burd *et al.* (2002)⁹⁹, the geometries and material properties of the assembled lens models used by these researchers were from the same sources. The three zonular fibres were modelled as three springs of spring stiffness 0.6N/mm, 0.2N/mm and 0.6N/mm for the anterior, equatorial and posterior zonules respectively. The three zonular fibres were either modelled to attach to the ciliary body at a single point or to attach at three different

points to simulate either the accommodative theory by Helmholtz⁵² or by Schachar⁵⁶, respectively. In the former case the influence from both the radial displacements and the posterior surface pressure were considered and the resultant COP decreased linearly with stretching, supporting Helmholtzian theory⁵², but increased with increasing pressure. In the latter case, the anterior and posterior zonular fibres were moved in opposite directions to the equatorial zonular fibre. The resultant lens model demonstrated increased thickness and steeper anterior surface when the equatorial zonular fibre was away from the lens equator, supporting the accommodative theory of Schachar⁵⁶. Liu *et al.*¹⁰² made a successful attempt to model different equatorial zonular behaviour from that of the anterior and posterior zonular fibres. However, when a zonular fibre was moved toward the lens equator, a compression force was induced on the lens by the zonular spring elements. This is not accurate in physiological conditions as the zonular fibres can only mediate tensional force. Therefore the supporting results for Schachar's theory remain questionable.

2.5.2 Sensitivity analysis

Sensitivity analysis has been used to investigate the relative contributions of certain components to the accommodative process or to the development of presbyopia. Weeber¹⁴⁰ showed that there is little influence of the stress-free lens shapes on accommodation using two models with one taking the initial lens shape from a fully accommodated lens and the other from an unaccommodated lens. For both models to achieve 3 dioptres of accommodative change, the required stretching forces were identical. Stachs *et al.*¹⁴¹ modelled the complex zonular structure using ten sets of zonular fibres and this was compared with the commonly simplified configuration using three zonular fibres. With same amount of displacement applied, little difference was seen in the resultant COP between the two models. However, the accuracy of this study was questioned by Schachar *et al.*¹⁴² regarding the geometries, material properties and elements of the lens models.

Schachar *et al.* (2006)¹³² determined the critical material properties and lens geometries that contribute to accommodative loss through a comprehensive sensitivity analysis. Five axisymmetric lens models were built with lens profiles fitted from published MRI images^{19, 143}, including a 20-year-old and a 40-year-old lens in their accommodated and unaccommodated states as well as a 60-year-old lens in its unaccommodated state. All

Chapter 2. Literature review

analysed parameters were assigned a baseline value and a variation range, and each of the analysed parameters was then varied between the defined minimum and maximum values while the other parameters remained at their baseline. Examined parameters included: the thickness and stiffness of the lens capsule, the strength of attachment between the lens capsule and its underlying cortex, stiffness of the zonular fibres and the elastic moduli of the lens nucleus and cortex. Amongst all the tested parameters, the decrease in changes of COP was found to be related only to the increase in the elastic modulus of the lens substance. Lens profiles that would affect the change in COP were also not consistent with the aetiology of presbyopia as 20-year-old accommodated and 40-year-old unaccommodated shapes displayed similar responses with zonular tractions.

To further investigate the source of the main contribution to presbyopia, Abolmaali *et al.*¹³¹ conducted an extended study of Schachar *et al.* (2006)¹³² adding into consideration three types of zonular tractions: by equatorial zonular fibre alone, by the anterior and posterior zonules together or by all three sets of zonules. The three types of zonular tractions all relied on the stretching point being at the same position and were applied with displacement along the equatorial direction. The locations of the attachment of anterior and posterior zonules on the capsule were also included in the sensitivity analysis. With increasing zonular tension, the COP increases no matter what type of zonular traction is applied, the central anterior surface steepens and the peripheral surface flatten, supporting the accommodative theory of Schachar⁵⁶. Closer location of the zonular attachment to the lens equator results in greater change in COP. Abolmaali *et al.*¹³¹ attributed the cause of presbyopia to the normal growth in lens equatorial diameter as such growth reduces the distance between the ciliary body and the lens equator causing a reduction in zonular tension. The lens equatorial growth also increases the distance between the zonular attaching position and the equator. Both would contribute to the declining change in COP with age according to the modelled results.

The analysis conducted by Sompel *et al.*¹⁴⁴ again investigated the roles of lens geometries and material properties in the development of presbyopia. The analysis was based on the 29 and 45 year old lens models from Burd *et al.* (2002)⁹⁹. Sompel *et al.*¹⁴⁴ considered the lens GRIN profile in the calculation of optical powers using a ray-tracing algorithm. Among the two new models developed by reshaping the surface or replacing the material properties of the 45-year-old lens model with those of the 29 years old lens, the reshaped model retained 72% to 94% of the accommodative amplitude of the

original 45-year-old model. A wider range of geometries and material properties were then simulated and the changes in lens geometry were thought to be the predominant contributors to the development of presbyopia.

2.5.3 Modelling zonular forces

Hermans *et al.* (2006)¹⁰⁰ adopted the 29-year-old lens model from Burd *et al.* (2002)⁹⁹ and updated the lens geometry with new *in vivo* measurements^{14, 22, 27} but excluded the zonular fibres. Instead of applying concentrated force on separate nodes, a uniformly distributed body force was applied to the equatorial capsular bag to avoid the singularities that appeared in previous models^{99, 101}. The lens model was subjected to an equatorial force only, anterior and posterior zonular force together or all three sets of zonular forces (Figure 2.16). An iterative process was used, minimizing the relative errors between the deformed lens shape and reference lens geometry at 0 dioptres with respect to four parameters: the thickness, anterior surface curvature, anterior surface asphericity and posterior surface curvature of the lens. A total net force of 0.08N was calculated for the whole lens no matter which type of zonular force was applied. Hermans *et al.* (2006)¹⁰⁰ proposed a solution for the discontinuities in curvatures of the deformed lens seen at the zonular attachment points^{99, 101} but did not avoid the sharp point at the nuclear equator as seen in the geometries of the lens models in Figure 2.16.

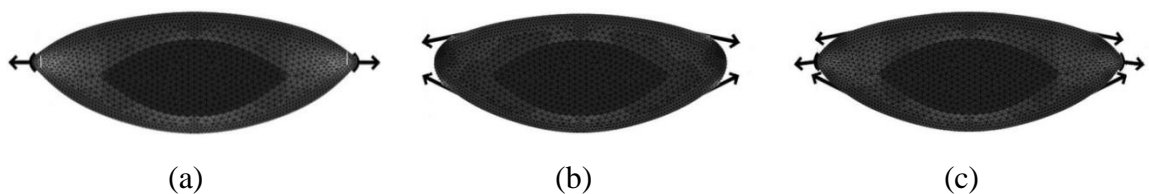


Figure 2.16 Deformed lens models under three configurations of zonular forces from Hermans *et al.*¹⁰⁰.

A following study by Hermans *et al.* (2008)¹⁴⁵ included all three lenses models aged 11, 29 and 45 years from Burd *et al.* (2002)⁹⁹ to investigate the age-related changes in zonular forces. Among the three sets of simulated material properties, namely from Fisher⁶², Heys *et al.*⁶³ and Weeber *et al.*⁶⁴, the difference between the simulated results and a clinical reference shape was the lowest when using the material properties of Fisher⁶². The averaged net force for stretching the lens into the unaccommodated state increases slightly with age: 0.041N for 11 years, 0.056N for 29 years, 0.056N for 45 years. The estimated net force using each set of material properties is shown in Figure

2.17. The forces estimated by these two studies are more likely to be the same as the centrifugal force estimated by Fisher (1977)¹²⁵, which do not replicate the forces exerted by the zonular fibres or ciliary muscle in the living eye. However the zonular force reported by Fisher (1977)¹²⁵ is around 0.013N, which is far less than that estimated by Hermans *et al.*^{100, 145}.

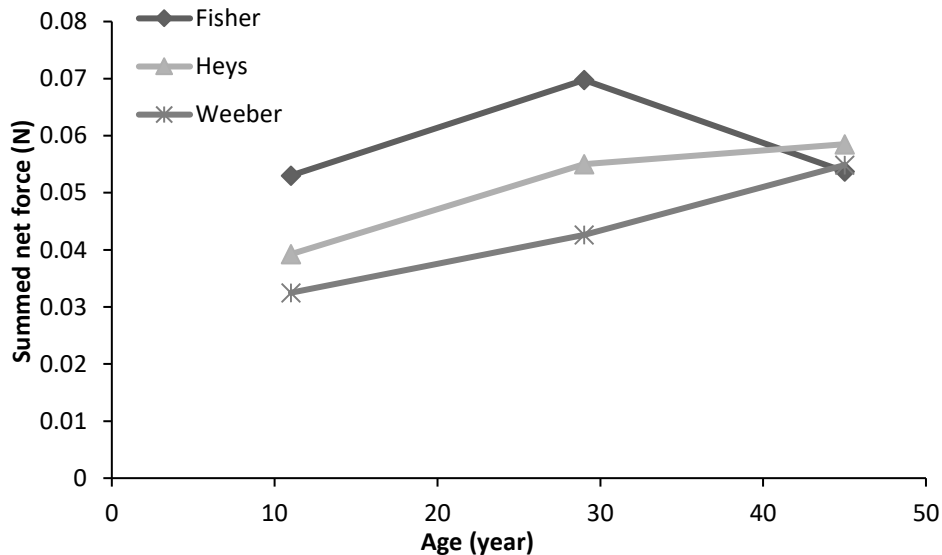


Figure 2.17 Zonular forces using three sets of material properties estimated by Hermans *et al.*¹⁴⁵.

2.5.4 Modelling gradient material properties

The contributions of the changing gradient material properties to the age-related loss of accommodative ability were investigated by Weeber and van der Heijde (2007)¹²⁸ using three axisymmetric lens models at age 20, 40 and 60 years old with equatorial diameters from Strenk *et al.*¹⁹, anterior and posterior surface curvatures from Dubbelman *et al.*²⁷. Each model was divided into concentric regions of equal intervals and the number of regions made equal to the number of measurements conducted by Weeber *et al.* (2007)⁶⁴. The material properties were either modelled as uniformly distributed across the lens using elastic moduli from Fisher (1971)⁶² and Weeber *et al.* (2005)⁶⁷, or modelled as gradient distributed elastic moduli according to Weeber *et al.* (2007)⁶⁴. The force applied to all the models was the amount that could stretch the 40-year-old lens to a point where the equatorial strain was 7% of the original equatorial diameter. Lens models with uniformly distributed elastic moduli showed linear decreases in accommodative amplitude with age whilst models with material properties distributed

along a gradient showed an accelerated decrease after 40 years of age (Figure 2.18). The accelerated decrease in lens accommodative ability after middle age concurs with Duane¹⁴⁶ indicating the contribution of a changing gradient of elastic modulus with age to the accommodative loss.

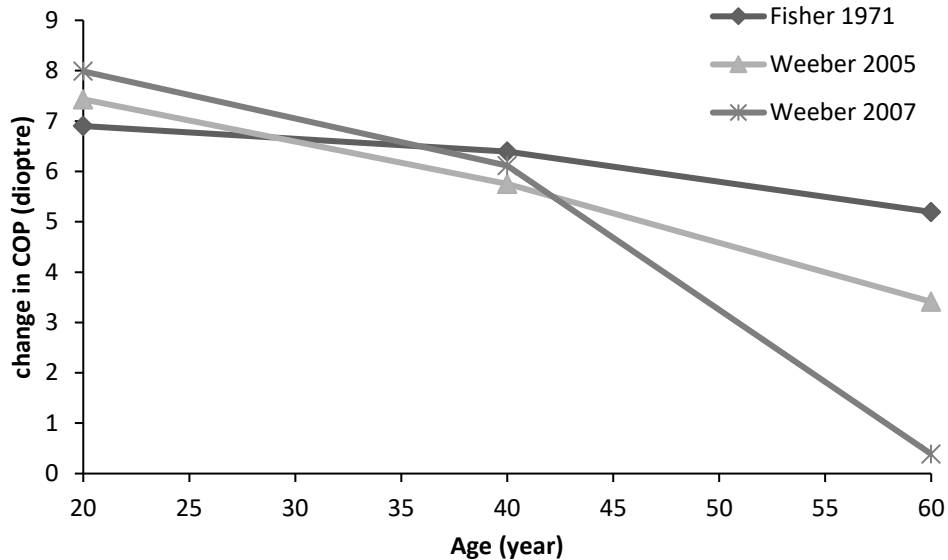


Figure 2.18 Change in COP with age of lens models using three different set of material properties reproduced from Weeber and van der Heijde¹²⁸.

2.5.5 Modelling stress and strain of the internal lens

The internal lens strain was analysed by Weeber and van der Heijde (2008)¹³⁰ using the same lens models and gradient material properties as Weeber and van der Heijde (2007)¹²⁸. With 7% strain of the original equatorial diameter 7.1D, 6.2D and 0.7D of accommodative change were achieved by the models aged 20, 40 and 60 years respectively. The two younger lens models had the greatest change of thickness in the nucleus and a much smaller change in the cortex (Figure 2.19). The 60-year-old model, on the contrary, showed minimal change of thickness in the nucleus, whilst the deformations were mainly concentrated in the equatorial region. The strains shown in Figure 2.19 are produced by models¹³⁰ having similar settings as those demonstrating accelerated decrease of change in COP after 40 years of age as shown in Figure 2.18¹²⁸. The oldest model producing the minimal strain in the lens nucleus (Figure 2.18) also demonstrated the minimal accommodative change. The nucleus was thus thought to be the most active part of the lens during accommodation as it caused the main

deformation in young pre-presbyopic lenses but had little impact on the central curvatures in the older non-accommodating lens.

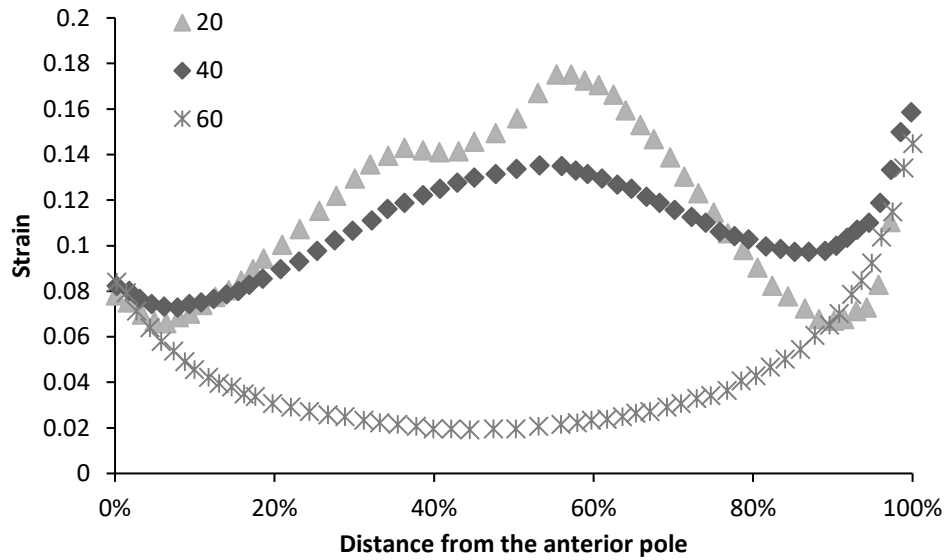


Figure 2.19 The strain along the central axis of three lens models aged 20, 40 and 60 years reproduced from Weeber and van der Heijde¹³⁰.

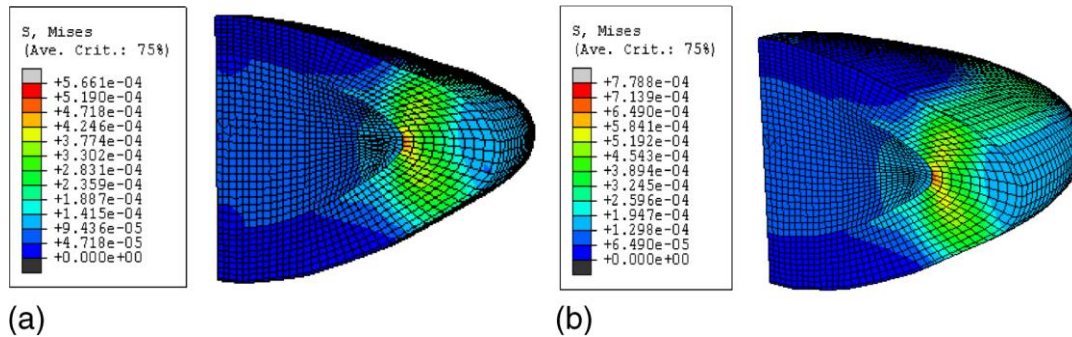


Figure 2.20 The internal von Mises stress of the 27-year-old model under the stretching force of (a) 0.65N and (b) 0.100N from Belaidi and Pierscionek¹²⁹.

Belaidi and Pierscionek¹²⁹ created three dimensional models using outer lens shapes taken from an *in vitro* study by Pierscionek¹⁴⁷ from 17 and 46 year old lenses and the nucleus was constructed to be two thirds of the lens. Models with a single elastic modulus and different elastic moduli in the nucleus and cortex according to those measured by Fisher (1971)⁶² were simulated. Stretching forces of 0.065N and 0.120N were applied to the single modulus models, 0.065N and 0.100N to the models with different moduli in the nucleus and cortex. A high stress concentration region was

demonstrated by all the models in the equatorial region near the boundary between the nucleus and cortex (Figure 2.20). A flattening of the peripheral lens curvatures with stretching was seen in all models. The central lens curvatures, however, either steepen or flatten dependent on different lens geometries, distributions of material properties and applied forces. Therefore both accommodative theories by Helmholtz⁵² and by Schachar⁵⁶ were supported.

2.6 Summary of the state of FEA models

Various FEA studies have been reviewed and the capability of FEA in investigating various aspects of accommodative process and development of presbyopia has been demonstrated. The lenses modelled by different studies were similar in that these were developed using axisymmetric models consisting of lens nucleus, cortex, capsule and zonule. The majority of modelling studies relied on the same three lens models⁹⁹. The vitreous support was included in some studies either by modelling the vitreous as a sphere or by applying a pressure to the posterior lens surface. The ciliary body as a component of the accommodative apparatus physiologically was not presented in these models but its function was simulated by the outward stretching of the zonular fibres. Some studies excluded the zonular fibres from the model applying stretching forces of different directions to the lens directly and the sensitivity of zonular angles has not been analysed. Spatially varying material properties have been considered only by a limited number of studies and further efforts are needed.

The current FEA models are limited in a number of aspects. First of all, computational models rely highly on the quality of the input data and a full description of the dynamic response of lenses during accommodation. This is currently unavailable and there still remain diversity and uncertainties in experimental results. Secondly, some simplification in modelling the zonules occurs because of restrictions caused by current computational resources and simulation times. In the biological lens the zonular complexity is far greater than the computational models. As models are further refined and computational resources advance, more sophisticated models should be constructed. Thirdly, the crystalline lens is a delicate structure consisting of proteins and water, the material properties and concentrations of the proteins as well as the interactions between these components are currently not fully understood^{35, 148}. A more comprehensive description of material behaviour is needed to more accurately construct the FE model.

Chapter 2. Literature review

In recent years, new studies using advanced techniques have shown improvements in lens geometry and material properties for lenses over a wide age range serving as a good basis for FEA studies. New models that are closer to the physiological condition are needed to help provide improved insight into accommodation.

3 DEVELOPMENT OF GRADIENT MODULI MODELS

This chapter aims to elucidate how material properties can affect accommodation using FE models based on interferometric measurements of refractive index made on human lenses³⁷. In this chapter, the detailed procedures for building three FE lens models aged 16, 35 and 48 years with gradient material properties are presented. The gradient distribution of the materials is set to be linearly related to the distribution of the refractive index within the lens. The models are simulated in a manner similar to the accommodative process *in vivo* and the results are compared across ages to provide improved understanding for the ageing process. The effect of changes in elastic moduli of the lens substance are analysed to determine how they affect the anterior and posterior curvatures of the lens approximated by spheres to determine which theory of accommodation is supported, and how the model results compare to studies on living eyes.

3.1 Modelling the lens and the capsule

3.1.1 Geometry: discontinuity zones

The geometries of three human lenses aged 16, 35 and 48 years of age were created in SOLIDWORKS (ver.2014) based on the optical measurements conducted by Bahrami *et al.*³⁷ using advanced synchrotron interferometric X-ray analysis. This technique enabled the observation of subtle fluctuations in refractive index that had not been

Chapter 3. Development of gradient moduli models

shown before^{37, 149}. The measured gradient index profiles of the three human lenses were used in mathematical modelling recreating the images of lenses as seen in the living human eye³⁷. The darkest regions in the lens centres corresponding to the central plateau region of the refractive index profile were modelled as the lens nucleus and the surrounding brighter regions corresponding to the steep regions of the refractive index profile were modelled as the lens cortex³⁷ (Figure 3.1). The zones of discontinuity are clearly identified in the reported images especially in cortical regions as bright and dark bands and the geometries of which were fitted together with the nucleus (Figure 3.1).

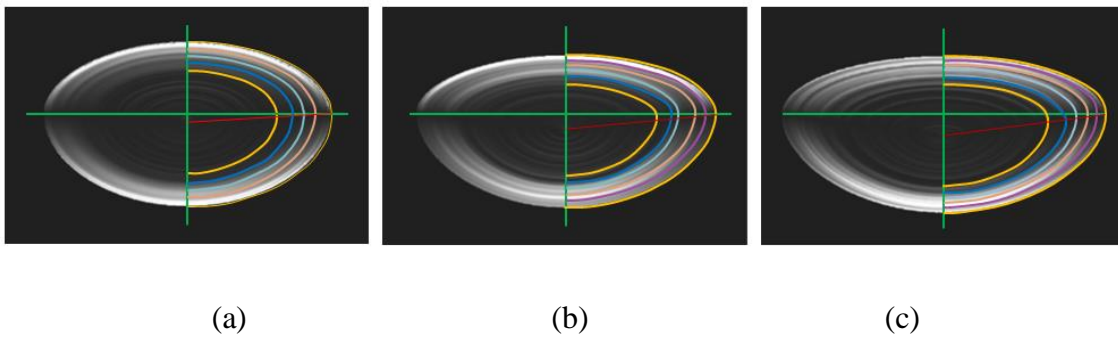


Figure 3.1 Dimensions of lenses aged (a) 16, (b) 35 and (c) 48 years of age fitted from Bahrami *et al.*³⁷.

Table 3.1 Dimensions of the lenses aged 16, 35 and 48 years of age from Bahrami *et al.*³⁷.

	16-year-old (mm)	35-year-old (mm)	48-year-old (mm)	
Thickness	Nucleus	2.91	2.75	2.87
	Cortical layer1	3.39	3.15	3.33
	Cortical layer2	3.77	3.53	3.63
	Cortical layer3	4.15	3.85	3.93
	Cortical layer4	4.64	4.17	4.22
	Cortical layer5	-	4.54	4.51
Diameter	Nucleus	5.06	5.40	6.20
	Cortical layer1	5.90	6.23	6.92
	Cortical layer2	6.66	6.97	7.59
	Cortical layer3	7.31	7.63	8.19
	Cortical layer4	8.06	8.31	8.85
	Cortical layer5	-	8.94	9.43

The extracted sagittal thicknesses and equatorial diameters of the nuclear and cortical layers from the three lenses are listed in Table 3.1. Four cortical layers for the 16-year-old model and five layers for the 35-year-old and 48-year-old models were fitted according to the images shown in Figure 3.1. The equatorial diameter of the outer lens shapes increases with age while the sagittal thickness slightly decreases with age (Table 3.1). The 35-year-old and 48-year-old lenses are more asymmetric in that the equatorial plane slightly shifted toward the anterior lens surface compared to the 16-year-old model.

3.1.2 Finite Element model: element selection and mesh generation

A quarter lens solid model (Figure 3.2) was created for each age in SOLIDWORKS (ver. 2014) by rotating the fitted geometry as shown in Figure 3.1 around the lens central axis over 90 degrees. The solid models were then imported into ANSYS mechanical APDL (ver.16.0) for conversion into FE models (Figure 3.3). Each model consists of six different parts: lens nucleus, lens cortex, capsule, anterior zonular fibre, equatorial zonular fibre and posterior zonular fibre. The lens capsule was modelled as the exterior surface surrounding the quarter lens model with thicknesses of 13 μm , 15 μm and 17 μm from Fisher¹¹⁹ for the models of lenses aged 16, 35 and 48 years of age respectively.

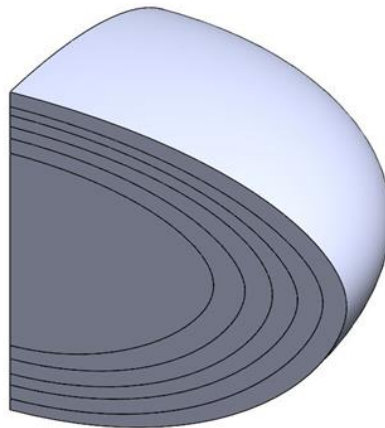


Figure 3.2 3D solid lens model developed in SOLIDWORKS (ver.2014).

The lens nucleus and cortex were considered as solid bodies and were meshed using 20-node brick elements (ANSYS element type: SOLID 186). Mixed u-p element formulation method was employed to avoid the volumetric locking phenomenon for nearly incompressible material behaviour. The capsule was treated as a membrane and was meshed using 8-node shell elements (ANSYS element type: SHELL 281). The

Chapter 3. Development of gradient moduli models

zonular fibres were modelled as 2-node 3D spar elements, with three translational degrees of freedom at each node and with the ability to carry uniaxial tension only (ANSYS element type: LINK 180). The total numbers of elements for the examined models were 23523, 17683 and 16923 while the total numbers of nodes were 139718, 105338 and 100632 for the 16-year-old, 35-year-old and 48-year-old respectively. Non-linear geometrical analyses were performed for all models.

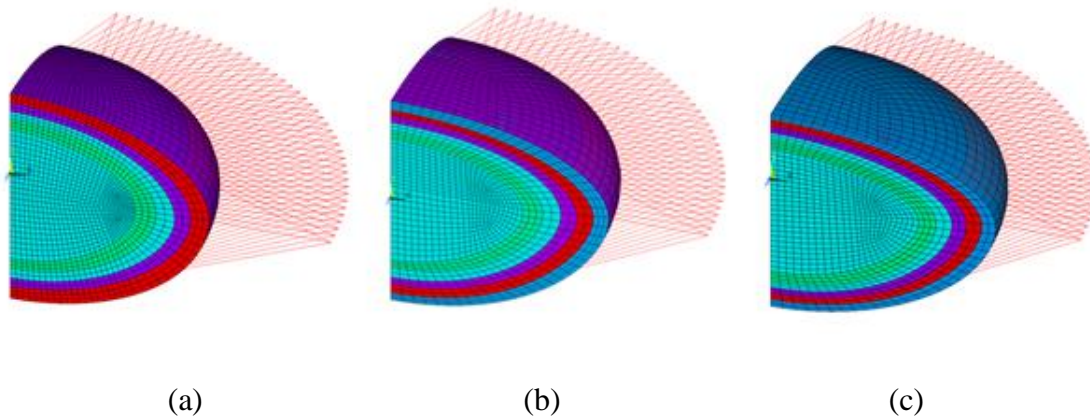


Figure 3.3 FE models of lenses aged (a) 16, (b) 35 and (c) 48 years of age.

The elements used to convert the solid model into the FE model are shown in Figure 3.4. The selected elements for modelling the nucleus and the capsule are in quadratic form with a mid-node at each boundary as they provide more accurate results for highly curved geometries than lower order linearly formed elements. To obtain a more accurate solution for a given model one can either increase the number of elements used or increase the orders of the used elements. However, additional degrees of freedom caused by increasing the number of elements would bring additional constraints imposed by incompressibility. The 20 nodes defining the SOLID186 element each has three degrees of freedom: translations along the three axes of the nodal coordinate. The 8 nodes defining the SHELL281 element each has 6 degrees of freedom, 3 translational and 3 rotational, with both the bending stiffness and membrane stiffness included. In the present study the capsule was modelled as a membrane therefore bending stiffness was excluded resulting in only three translational degrees of freedom for each node. The LINK180 element for modelling the zonular fibres has only 2 nodes with three translational degrees of freedom each. All the three selected elements are included with large strain capabilities which are suitable for the models in the present study.

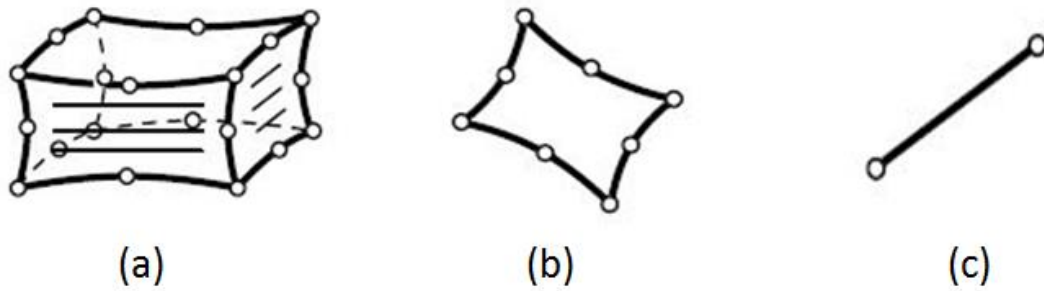


Figure 3.4 Elements used for lens model: (a) SOLID186, (b) SHELL281, (c) LINK180.

3.1.3 Gradient material properties

The material properties of each part constituting the lens models were assumed to be linear elastic, isotropic and homogenous. The elastic moduli of the nucleus and cortex were taken from two measurements that have spun the lenses, namely of Fisher⁶² and of Wilde *et al.*⁶⁵; Poisson's ratio for both parts was 0.49 assuming the nearly incompressible behaviour of the lens substance^{29, 130}. The elastic modulus and Poisson's ratio used for each part are listed in Table 3.2. Fisher⁶² reported Young's modulus and Wilde *et al.*⁶⁵ reported shear modulus for the nucleus and the cortex. Both sets of material properties were simulated. Young's moduli for the capsule were 5.87 MPa, 4.90 MPa and 4.20 MPa for the 16, 35 and 48 aged lenses¹¹⁹ respectively, and 0.35 MPa for the zonular fibres¹²⁴ at all three ages. The lens nucleus and cortex having elastic moduli in the kilopascal scale are much more flexible than the lens capsule and zonular fibres. Poisson's ratio for both the capsule and zonular fibres was 0.47^{126, 150}.

Table 3.2 Material properties of the lens components.

		16-year-old (kPa)	35-year-old (kPa)	48-year-old (kPa)	Poisson's ratio
Fisher (E)	Nucleus	0.5	0.6	1.1	0.49
	Cortex	2.4	3.7	4	
Wilde <i>et al.</i> (G)	Nucleus	0.06	0.26	2.67	0.47
	Cortex	0.32	0.89	1.22	
Capsule		5.87×10^3	4.9×10^3	4.2×10^3	0.47
Zonular fibre			0.35×10^3		

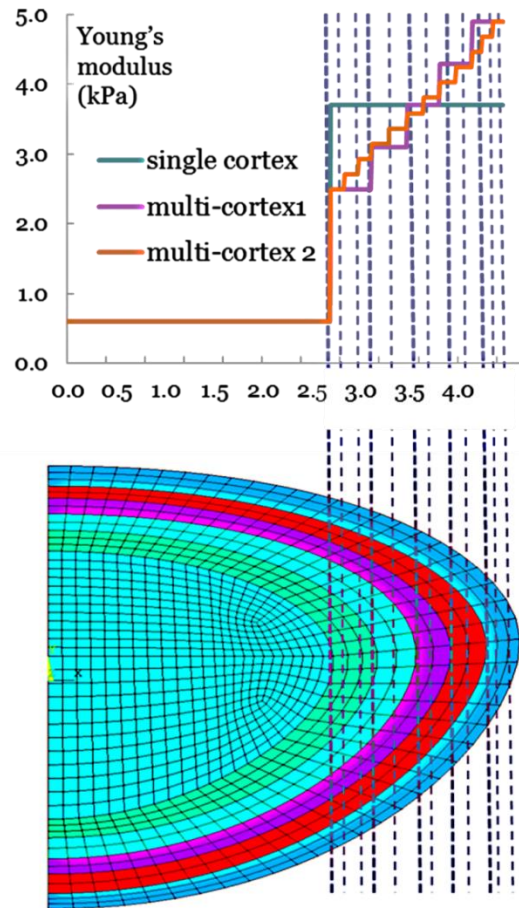


Figure 3.5 Distributions of Young's moduli in 35-year-old lens model.

Lens models were created either with a single modulus value or with two gradient distributions of moduli in the cortex. The number of the cortical layers of multi-layered models is based on the contours of refractive index of each particular lens³⁷. The single cortex models incorporate the moduli exactly as those reported by Fisher⁶² and Wilde *et al.*⁶⁵ (Table 3.2). The 35 year-old-lens model using material properties of Fisher⁶² is selected as a representative case in Figure 3.5 for the demonstration of the three distributions of elastic moduli. The multi-layered models with gradient distribution of elastic moduli in the cortex increase from the innermost to the outermost layer, as with the moduli values, maintaining a mean value of all the cortical layers in accordance with that used for the single cortex model. Young's moduli for the innermost layer and the outermost layer are the same in the two multi-layered models with the same set of material properties but the intervals of moduli values between adjacent layers are different. The material properties used for each layer in the two levels of multi-layered models were shown in Tables I.1 to I.3 of Appendix I.

3.2 Direct generation of zonular fibres

In ANSYS there are two approaches for developing FE models. The one described in section 3.1, in which the geometries were firstly established and were meshed using elements with the desired size and shape, is the solid modelling method. The zonular fibres were modelled using the direct generation method in which the location of each node and the shape of each element were defined directly. The LINK180 element used for the zonular fibre is defined by two nodes with one node from the lens capsule and the other one defined manually. The accumulated force applied to the whole lens was evenly distributed and applied to the lens models by 160 sets of zonular fibres that encircle the lens equator. Each set consists of an anterior, an equatorial and a posterior zonular fibre connecting to the equatorial region of the lens capsule. The quarter lens models developed in the present study were modelled with 41 sets of zonular fibres, with the two sets at the boundaries having half the cross-sectional areas of the rest of the zonular fibres. The cross-sectional area of each zonular fibre was set to 0.12mm^2 as estimated from Fisher¹²⁴ and was 0.06mm^2 for the fibres at the boundary of the models. A number of manually defined nodes representing the stretching point connecting the anterior, equatorial and posterior zonular fibres were set with distances to the lens equator of 2.5 mm, 2.0 mm and 1.8 mm for the lenses aged 16, 35 and 48 years old respectively as taken from Strenk *et al.*¹⁹.

Previous FEA models have anchored the zonular fibre to a single point^{99, 101, 102, 131, 139, 144} on the lens capsule resulting in non-physiological discontinuities in curvature as shown in section 2.5 of Chapter 2. In order to model the complex anchorage of the zonules on the lens capsule, a master-slave nodes mechanism was introduced by applying a number of constraint equations to zonular-capsular attaching points. This mechanism couples the degrees of freedom of the neighbouring nodes so that they follow the movement of each anchorage point, yielding smooth curvatures on deformed lens shapes. This coupling is shown in Figure 3.6 in which the neighbouring nodes coupled to the three zonular anchorage points on the capsule were marked in a purple colour.

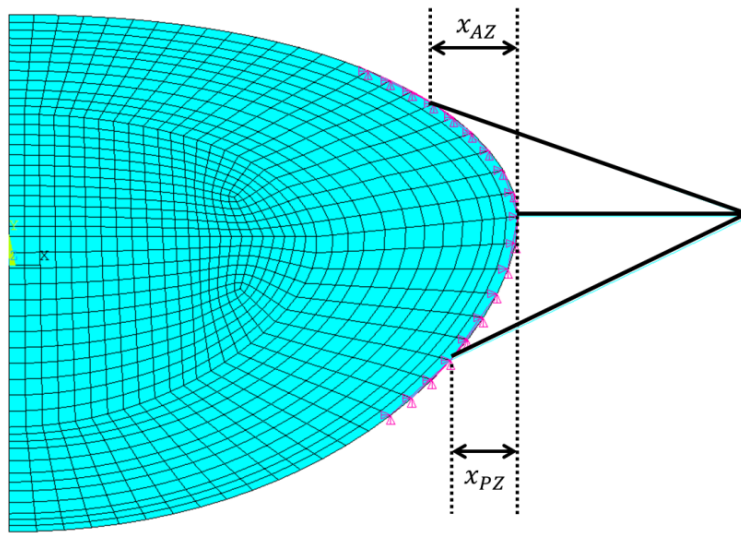


Figure 3.6 The anchorage of the zonular fibres on the lens capsule.

The attaching locations of the zonular fibres to the peripheral region of the lens capsule are not easily imaged during *in vivo* measurements, which hamper the determination of the location of the zonular-capsular attachment point as well as the width of the attachment of each zonular section on the lens capsule along the meridional direction. In models developed in the present study, the equatorial zonular fibre was attached to the lens equator while the attaching points of the anterior and posterior zonular fibres were arbitrarily selected. The distance of the attaching points of both the anterior and posterior zonular fibres on the lens capsule to the lens equator are listed in Table 3.3 for all three aged lens models. To determine the number of neighbouring nodes coupled to each zonular anchorage points, a series of models in which different numbers of nodes were coupled to the three zonular anchorage points were simulated. The model shown in Figure 3.6 with 6 nodes coupled to the anterior and posterior zonular anchorage points each and 4 nodes coupled to the equatorial zonular anchorage point was selected as it provided the smoothest curvatures.

Table 3.3 The distances of the anterior and posterior zonular attaching points to the lens equator.

	16-year-old (mm)	35-year-old (mm)	48-year-old (mm)
x_{AZ}	0.56	0.74	0.80
x_{PZ}	0.49	0.59	0.56

3.3 Boundary conditions

The boundary conditions applied to the quarter lens models are shown in Figure 3.7. The nodes on the central axis are restricted to have only translational movements in the vertical direction along the y-axis of the global coordinates system. The two cross-sectional areas (indicated as B and C in Figure 3.7b) were applied with symmetrical boundary conditions such that the nodes on these two surfaces cannot have out-of-plane movements. The accumulated force applied to the whole lens is 0.08N which, divided by 160, gives $500\mu\text{N}$ for each set of zonular fibres. The two sets in line with the cross-sectional areas B and C were applied with a force of $250\mu\text{N}$ each which is half of the force applied to the rest of the zonular fibres to maintain correspondence with the symmetry boundary conditions.

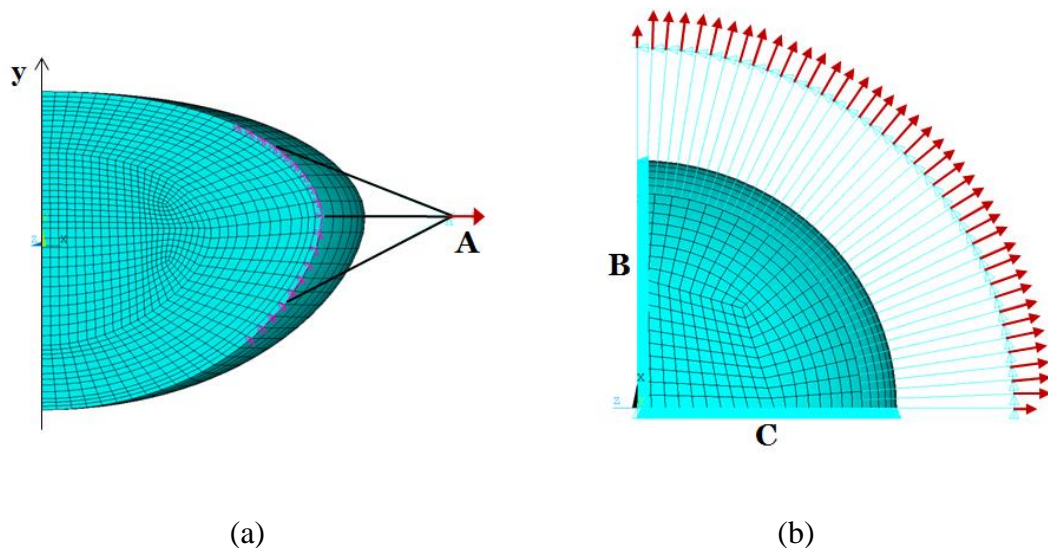


Figure 3.7 The boundary conditions of the quarter lens models demonstrated in (a) oblique view and (b) top view.

The degrees of freedom of the 41 stretching nodes (representative node A is shown in Figure 3.7a) of the quarter model were constrained in the nodal coordinate system. The nodal coordinate system of each node was positioned with the x-axis in alignment with the radial direction of the corresponding set of zonular fibres, the y-axis parallel to the global y-axis and the z-axis tangential to the lens equator. The stretching force was applied along the direction of the x-axis in the nodal coordinate system of each node (Figure 3.7b). The movement of each node along the y-axis and z-axis of each nodal coordinate system was restricted. Two representative nodal coordinate systems are shown in Figure 3.8.

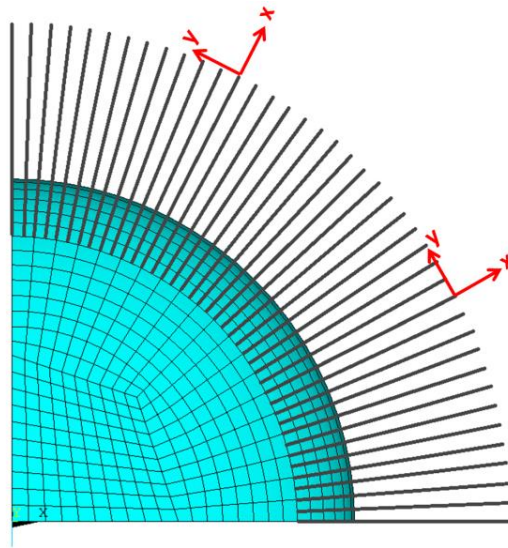


Figure 3.8 Nodal coordinate system of the stretching point.

3.4 Stress distributions of the models

3.4.1 Single cortex models

The material properties measured by Fisher⁶² indicate that the lens nucleus is more flexible than the cortex while others have suggested the contrary i.e. that the nucleus is stiffer than the cortex¹⁰³. To make a full comparative analysis Young's modulus reported by Fisher⁶² for the nucleus and the cortex were flipped and applied to each aged lens model; these models were designated with the name 'flipped models'. Young's moduli of the nucleus are lower than that of the cortex in all three aged models using the original material properties of Fisher⁶²; in the flipped models the nucleus has a higher Young's modulus than the cortex. The accumulated force of 0.08N applied to the total lens for all the models is of the same magnitude as estimated by Hermans *et al.*¹⁰⁰ and is within the range of 0.06N to 0.1N by Burd *et al.*⁹⁹.

Stress patterns for the three aged lens models with a single value of the cortical modulus using the material properties of Fisher⁶² are shown in Figure 3.9. The corresponding stress values (as von Mises stress in MPa) of each model are indicated using colour coding with the colour bar on the left side. The lens nucleus indicated in dark blue has minimal stress values for each age model. There is a high stress region indicated in green and yellow concentrated near the nuclear region of the equator, which is especially marked in the 16-year-old lens. The anterior cortical stress is higher than the

posterior cortical stress for all three models. The general stress pattern becomes asymmetric with increasing age.

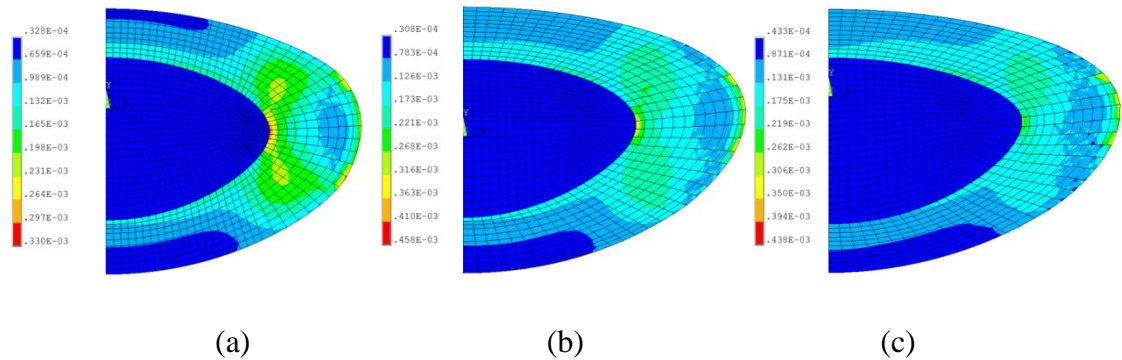


Figure 3.9 Stress distributions of the (a) 16-year-old, (b) 35-year-old and (c) 48-year-old lens models with a single cortical modulus using the material properties of Fisher⁶² under a stretching force of 0.08N.

In Figure 3.10 the stress patterns of the flipped models at all three ages are shown. For these flipped models, high stress regions appeared in the lens nucleus shown in red, which shifted toward the equatorial region of the nucleus in the 48-year-old model. The stresses decrease from the centre toward the lens surface. The minimal stresses near the lens poles are in dark blue. The higher stress region shifts slightly anteriorly with increasing age contributing to more asymmetric stress patterns in older lens models.

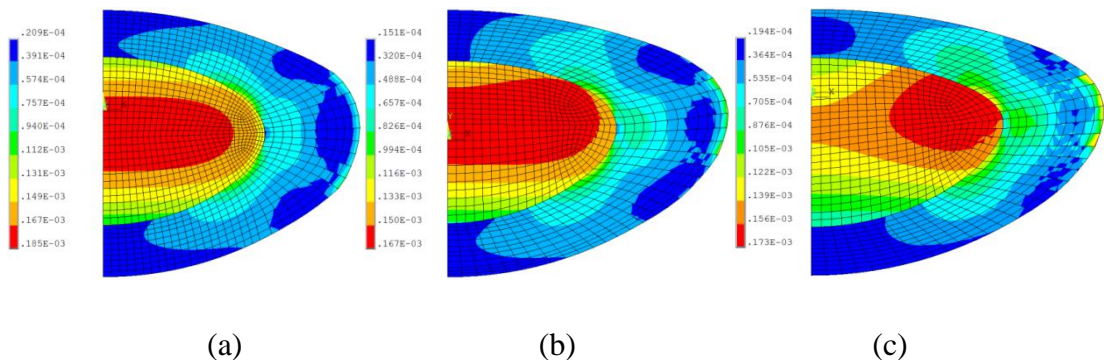


Figure 3.10 Stress distributions of the (a) 16-year-old, (b) 35-year-old and (c) 48-year-old lens models with flipped single cortical modulus using the material properties of Fisher⁶² under a stretching force of 0.08N.

The study by Wilde *et al.*⁶⁵ indicated that the nucleus is more flexible than the cortex in the 16-year-old and 35-year-old models but is stiffer than the cortex in the 48-year-old model. The stress patterns of the three lens models using the material properties of Wilde *et al.*⁶⁵ are displayed in Figure 3.11. The 16-year-old lens model and the 35-year-old lens model display similar stress patterns to those using the material properties of

Fisher⁶² as shown in Figure 3.9. The 48-year-old lens model, however, shows greater differences with a high stress region in the equatorial region of the nucleus, shown in green; minimal stresses appearing in the posterior cortex, shown in dark blue. The stress pattern of the 48-year-old model using the material properties of Wilde *et al.*⁶⁵ is similar to the same age flipped model (Figure 3.10c) but with different magnitudes of stress.

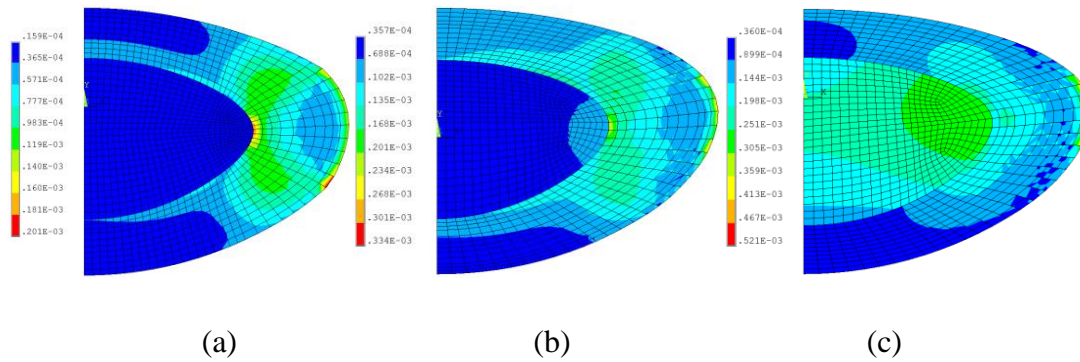


Figure 3.11 Stress distributions of the (a) 16-year-old, (b) 35-year-old and (c) 48-year-old lens models with single cortical modulus using the material properties of Wilde *et al.*⁶⁵ under a stretching force of 0.08N.

3.4.2 Multi-layered models

Figure 3.12 show the stress patterns of multi-layered models using the material properties of Fisher⁶². The cortex in the smallest of these lens models, based on the 16-year-old lens³⁷, is divided into four layers; the cortical regions in the other two lenses have five layers. Young's moduli for each model increase incrementally by 0.6 MPa from the innermost to the outermost layers, maintaining a mean value for all layers that is in accordance with the values reported by Fisher⁶²; Young's moduli of the nucleus is constant. Layered stress patterns are observed in the anterior and posterior cortical regions of the 16-year-old lens model (Figure 3.12a) and largely in the posterior cortical region for the 35-year-old (Figure 3.12b) and the 48-year-old lens (Figure 3.12c). The stresses at the equatorial cortical region are more evenly distributed than in the single cortex models and the stress concentration region shown in the single cortex modulus model has been eliminated.

Dividing the cortex further into more layers whilst maintaining the same mean value as reported by Fisher⁶²: ten layers for the 16-year-old lens model, twelve layers for the 35-year-old lens model and eleven layers for the 48-year-old lens model, in accordance

with the contours of refractive index³⁷ gives results shown in the second row of Figure 3.12. The increment of Young's moduli is reduced between two adjacent layers so that the innermost and outermost layers in the second row of Figure 3.12 have the same value. Young's moduli with the second level of multi-layered models are shown in the second row of Figure 3.12. The number of steps in the stress patterns of the cortex increases with the increasing number of cortical layers. The stresses are more evenly distributed in all three lens models from this set (Figure 3.12d-e) than in the models with the single value of cortical modulus (Figure 3.9) and in those with fewer layers (Figure 3.12a-c).

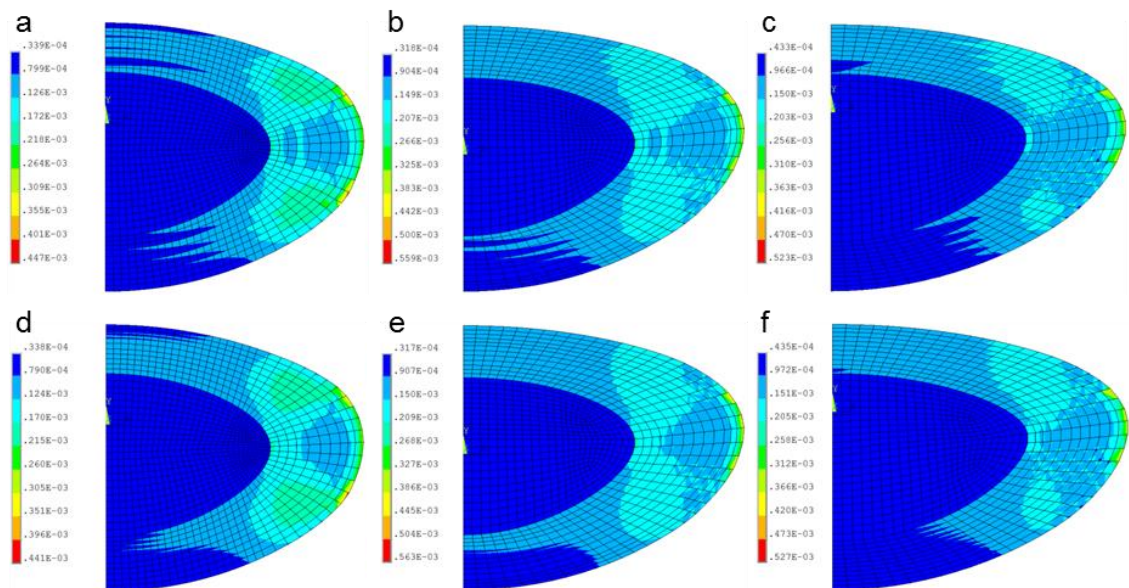


Figure 3.12 Stress distributions of the multi-layered models aged (a, d) 16-year-old, (b, e) 35-year-old and (c, f) 48-year-old using the material properties of Fisher⁶² under a stretching force of 0.08N.

In the flipped multi-layered models, the nucleus is the stiffest part of the model and Young's moduli in the cortex decreases from the innermost layer to the outermost layer while maintaining mean values equal to those measured by Fisher⁶² for the nucleus. Stepped stress patterns are also seen in the flipped multi-layered models in both the anterior and posterior cortex as displayed in Figure 3.13 with the most pronounced case appearing in the 48-year-old lens. The stepped shape is different from those shown in Figure 3.12 which is more like a 'Christmas tree' pattern. Compared to the flipped models with single cortex modulus shown in Figure 3.10, the cortical stresses are again more evenly distributed. More steps in the cortex are seen for the models with the greater number of cortical layers (Figure 3.13d-e).

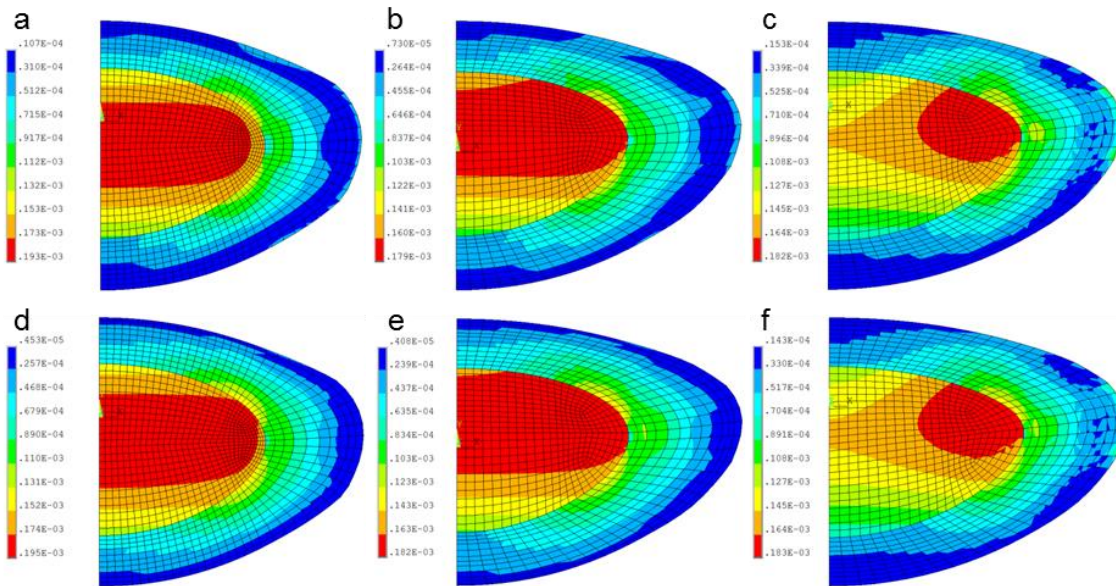


Figure 3.13 Stress distributions of the flipped multi-layered models aged (a, d) 16-year-old, (b, e) 35-year-old and (c, f) 48-year-old lens models using the material properties of Fisher⁶² under a stretching force of 0.08N.

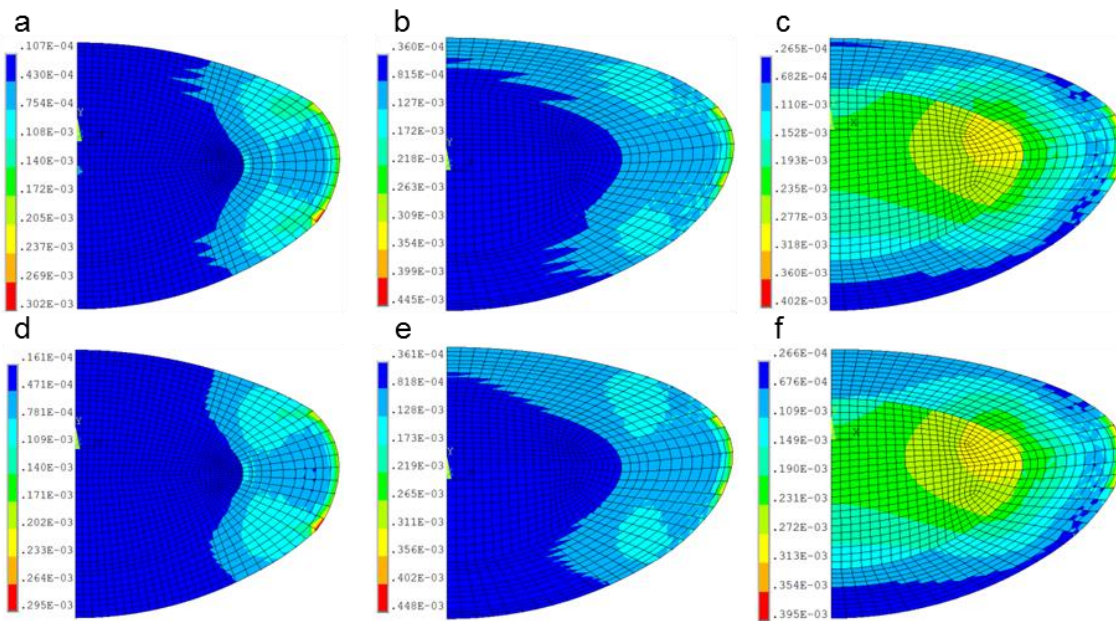


Figure 3.14 Stress distributions of the multi-layered models aged (a, d) 16-year-old, (b, e) 35-year-old and (c, f) 48-year-old lens models using the material properties of Wilde *et al.*⁶⁵ under a stretching force of 0.08N.

For the multi-layered models using the material properties of Wilde *et al.*⁶⁵ (following the same layered format used to apply the material properties measured by Fisher⁶²), the resulting stress patterns are shown in Figure 3.14. The 16-year-old and 35-year-old lens models do not show the jagged edged stress patterns in the posterior cortex that are seen

in the models with the material properties of Fisher⁶² (Figure 3.12). The stresses are lower and more diffuse in the models with the material properties of Wilde *et al.*⁶⁵ compared to those of Fisher⁶². Conversely, the two 48-year-old lens models with multiple cortical layers have regions of higher stress, particularly in the nuclear equatorial region shown in yellow, which gradually decrease outward (Figure 3.14c,f), compared to the respective models using the properties measured by Fisher⁶² (Figure 3.12c,f).

3.5 Deformations of the models

3.5.1 Polar displacements

The displacements of the anterior pole, posterior pole and equator of the whole lens are illustrated in Figure 3.15. The displacements at these three positions indicate the extent to which the lens deforms. To compare the influence of different sets of material properties to the lens deformations, the displacements at the anterior pole, posterior pole and the equator of the whole lens as well as of the nucleus are plotted as a function of age in Figure 3.16 and as a function of the number of cortical layers in Figure 3.17.

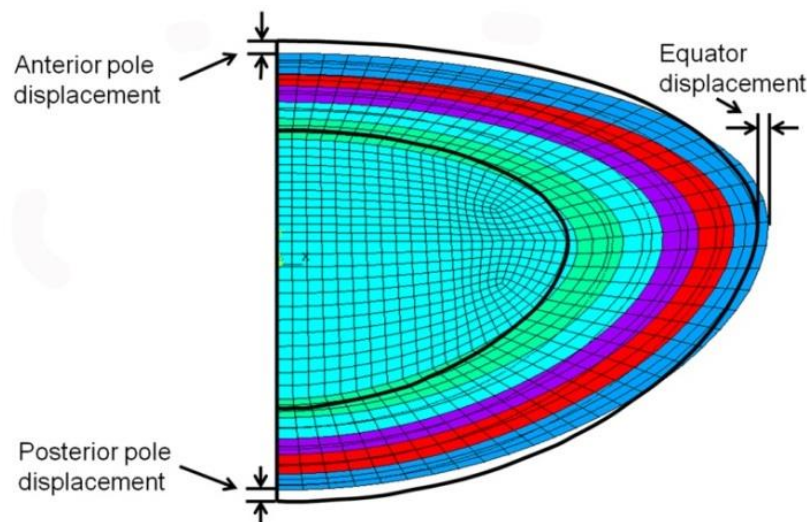


Figure 3.15 Diagrammatic representations of lens displacements at the equator, anterior and posterior poles.

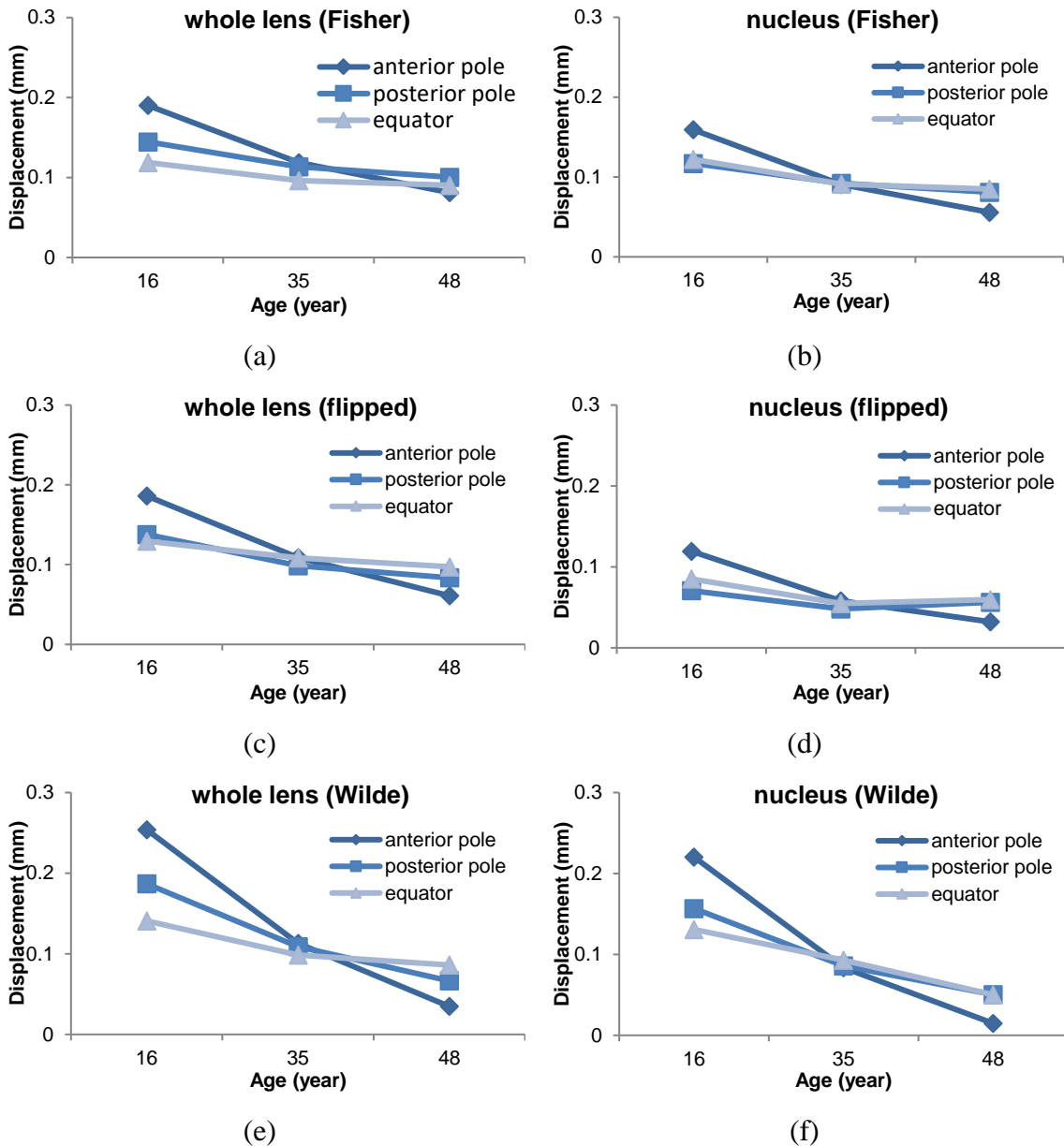


Figure 3.16 The displacements of anterior pole, posterior pole and equator of the whole lens and the nucleus in the three lens models of different ages with a single cortical modulus and modulus values from Fisher⁶² and Wilde *et al.*⁶⁵.

In Figure 3.16, the models shown have a single cortical modulus. Decreasing trends are seen with age for displacements of the anterior pole, posterior pole and the equator for all with the least change seen with the flipped moduli in the nucleus. The decrease is more pronounced in models using the material properties of Wilde *et al.*⁶⁵. The displacements of the anterior pole are higher than the posterior pole in the 16-year-old models but are lower than the posterior pole in the 48-year-old models for all plotted cases.

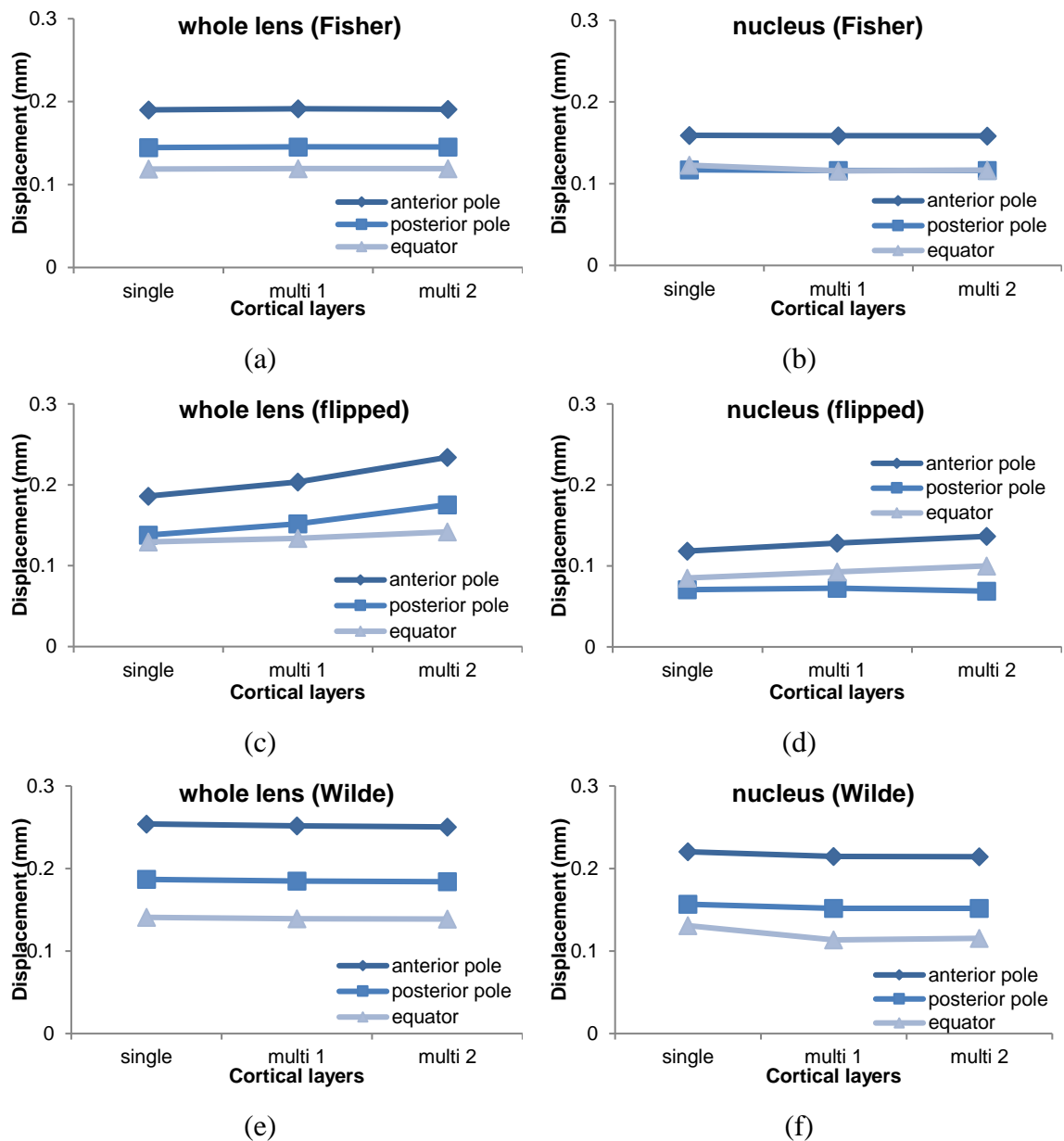


Figure 3.17 The displacements of the anterior pole, posterior pole and equator of the whole lens and the nucleus in models of different cortical layers of lenses 16 years old.

In Figure 3.17, the polar and equatorial displacements of models aged 16 years old with different sets and different distributions of material properties are shown. There are no significant changes in displacement values when comparing between single cortex model and multi-layered models using material properties either of Fisher⁶² or of Wilde *et al.*⁶⁵. For flipped models, there is an increase of anterior and posterior polar displacements with increasing cortical layers of the whole lens, but not for the nucleus. The anterior polar displacement is higher than the posterior displacement for all plotted 16-year-old models. The polar and equatorial displacements of the nucleus are only slightly lower than that of the whole lens, which can be seen in Figures 3.16 and 3.17.

Table 3.4 Displacements of anterior pole, posterior pole and equator of the whole lens and the nucleus.

Unit/mm		16-year-old			35-year-old			48-year-old		
		ant	post	equa	ant	post	equa	ant	post	equa
Whole lens										
Fisher ⁶²	Single	0.1901	0.1446	0.1187	0.1187	0.1135	0.0961	0.0811	0.1003	0.0903
	Multi 1	0.1914	0.1455	0.1193	0.1199	0.1139	0.0964	0.0817	0.1005	0.0906
	Multi 2	0.1909	0.1452	0.1191	0.1197	0.1139	0.0963	0.0817	0.1005	0.0903
flipped	Single	0.1861	0.1379	0.1294	0.1087	0.0987	0.1085	0.0609	0.0835	0.0973
	Multi 1	0.2036	0.1518	0.1338	0.1252	0.1098	0.1125	0.0627	0.0851	0.0974
	Multi 2	0.2340	0.1754	0.1419	0.1496	0.1250	0.1186	0.0639	0.0858	0.0979
Wilde <i>et al.</i> ⁶⁵	Single	0.2540	0.1868	0.1408	0.1128	0.1090	0.0984	0.0347	0.0664	0.0861
	Multi 1	0.2518	0.1849	0.1393	0.1149	0.1096	0.0991	0.0344	0.0668	0.0860
	Multi 2	0.2504	0.1840	0.1388	0.1143	0.1094	0.0988	0.0344	0.0667	0.0862
Lens nucleus										
Fisher ⁶²	Single	0.1592	0.1170	0.1227	0.0908	0.0921	0.0909	0.0558	0.0810	0.0850
	Multi 1	0.1588	0.1162	0.1157	0.0917	0.0913	0.0881	0.0564	0.0806	0.0833
	Multi 2	0.1586	0.1162	0.1166	0.0915	0.0914	0.0885	0.0564	0.0808	0.0834
flipped	Single	0.1183	0.0706	0.0851	0.0580	0.0481	0.0548	0.0321	0.0564	0.0597
	Multi 1	0.1280	0.0725	0.0928	0.0622	0.0524	0.0609	0.0332	0.0581	0.0626
	Multi 2	0.1365	0.0688	0.1000	0.0661	0.0526	0.0622	0.0339	0.0581	0.0626
Wilde <i>et al.</i> ⁶⁵	Single	0.2203	0.1567	0.1308	0.0835	0.0860	0.0929	0.0504	0.0148	0.0501
	Multi 1	0.2145	0.1517	0.1135	0.0852	0.0850	0.0883	0.0511	0.0145	0.0505
	Multi 2	0.2143	0.1518	0.1153	0.0848	0.0851	0.0890	0.0510	0.0145	0.0503

The displacements of the anterior pole, posterior pole and the equator for all the simulated lens models are listed in Table 3.4. In multi-layered models the polar and equatorial displacements decrease with age in a similar way as the single cortex models (Figure 3.16). In 35-year-old and 48-year-old models, the displacements do not change significantly with increasing cortical layers and are similar to those plotted in Figure 3.17 for the 16-year-old models. For both single and multi-layered models, the anterior pole shows more displacement than the posterior pole in the 16-year-old and 35-year-old models. However, in the 48-year-old model the posterior pole has a higher displacement than the anterior pole.

3.5.2 Sagittal deformations

Under the simulated stretching force of 0.08 N, the sagittal deformations of the nucleus and cortex of all three aged lens models using different sets of material properties are listed in Table 3.5 and are plotted in column charts in Figure 3.18 for more intuitive comparisons, for both the single cortex models and multi-layered models. The multi-layered models demonstrate similar changes, in terms of sagittal deformations, to corresponding single cortical modulus models and the changes in thickness of the nucleus are three to six times larger than that of the cortex in all three models using the material properties of Fisher⁶² and the two younger lens models using the material properties of Wilde *et al.*⁶⁵ (Figure 3.18a-c, g-i). These models have lower elastic moduli in the nucleus than in the cortex. All three flipped models of different ages (Figure 3.18d-f) and the 48-year-old model using material properties of Wilde *et al.*⁶⁵ have higher elastic moduli in the nucleus than in the cortex and these stiffer nucleus models show approximately similar amounts of deformations in the nucleus and the cortex. The amounts of deformation decrease with increasing age for all material properties.

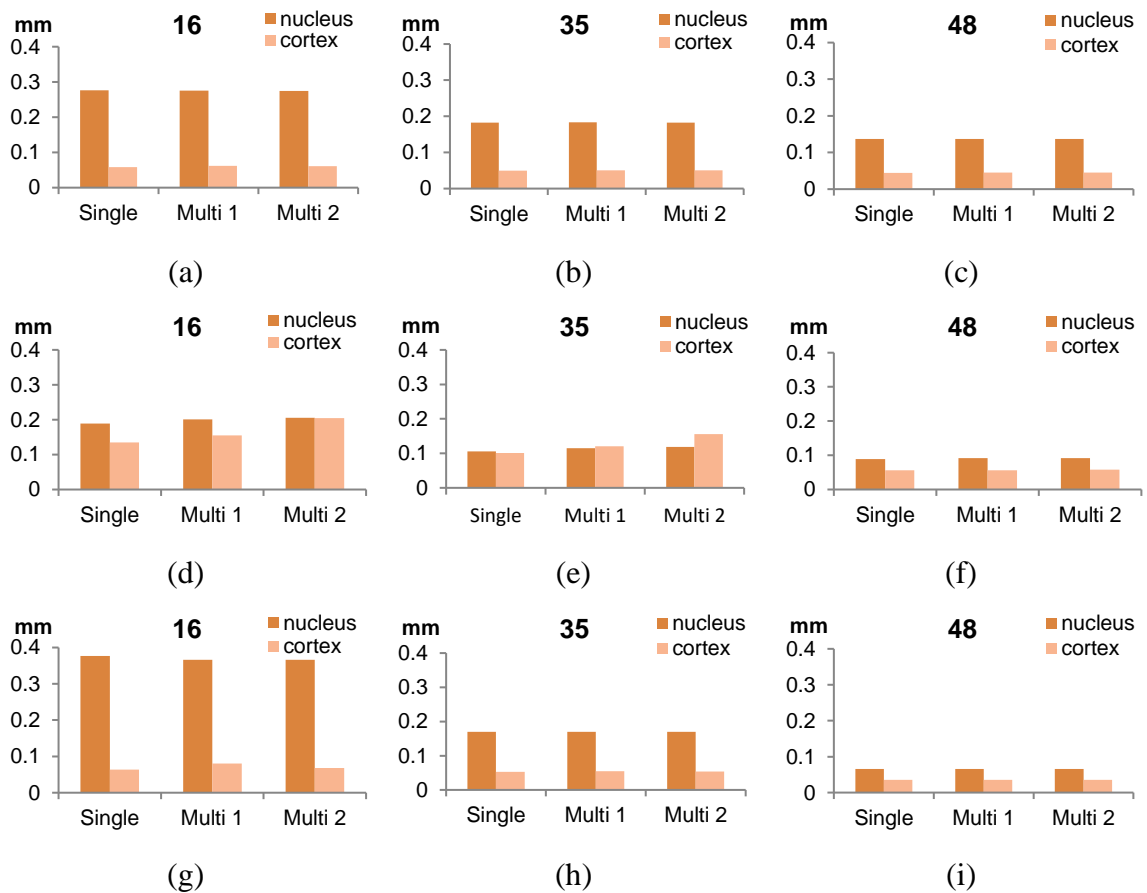


Figure 3.18 The comparison of sagittal deformations in the nucleus and the cortex for models using (a-c) the material properties of Fisher⁶², (d-f) the flipped material properties of Fisher⁶² and (g-i) the material properties of Wilde *et al.*⁶⁵.

Table 3.5 Sagittal deformations of the nucleus and cortex

		16 years old		35 years old		48 years old	
		nucleus	cortex	nucleus	cortex	nucleus	cortex
Fisher ⁸	Single	0.2761	0.0586	0.1829	0.0493	0.1367	0.0447
	Multi one	0.2750	0.0618	0.1830	0.0509	0.1370	0.0452
	Multi two	0.2749	0.0612	0.1829	0.0507	0.1371	0.0451
flipped	Single	0.1889	0.1351	0.1061	0.1013	0.0885	0.0559
	Multi one	0.2005	0.1549	0.1146	0.1204	0.0913	0.0565
	Multi two	0.2053	0.2041	0.1187	0.1559	0.092	0.0577
Wilde <i>et al.</i> ¹²	Single	0.3770	0.0638	0.1694	0.0524	0.0653	0.0358
	Multi one	0.3662	0.0805	0.1701	0.0543	0.0656	0.0356
	Multi two	0.3661	0.0683	0.1699	0.0538	0.0655	0.0356

3.5.3 Central radius of curvature of the outer lens surface and internal layers

The radii of curvature of the external lens surfaces, the inner nuclear surfaces and the surfaces of internal cortical layers for both the anterior and posterior part of each lens model within the central 3mm diameter zone were calculated with a spherical surface approximation circle fitting method¹⁵¹ using MatLab (version 2013b). The calculated radius of curvature of each layer, at the undeformed state as well as for a deformation caused by a cumulative force of 0.08 N, are listed in Tables 3.6-3.8 for all three models of different ages using different sets of material properties. The cortical layers are numbered successively in order from the innermost cortical layer adjacent to the lens nucleus, as cortical layer 1, to the outermost cortical layer, as cortical layer 4 for the 16-year-old model and cortical layer 5 for the two older lens models. The external lens surfaces correspond to the outermost cortical layer of each model.

The two younger lens models constructed with the material properties of Fisher⁶² and the youngest lens model with the material properties of Wilde *et al.*⁶⁵ show increasing anterior central radii of curvature with stretching. For all other models listed in Table 3.6 and Table 3.8 the anterior lens surface becomes steeper as the model is stretched. The posterior surfaces of all the listed models become flatter with stretching. For flipped models both the anterior and posterior radii of curvature of the outer lens surfaces become steeper with stretching (Table 3.7). The changes of radii of curvature

in different layers between the single cortex model and multi-layered models do not show much difference in terms of clinical applicability.

For the 16-year-old and 35-year-old models using both sets of material properties (Table 3.6 and Table 3.8), the radii of curvature of the nuclear surface and all the cortical layers become flatter with stretching. For the 48-year-old model, the anterior radii of curvature of the 3rd and the 4th cortical layers using material properties of Fisher⁶² and the 1st to 3rd cortical layers using the material properties of Wilde *et al.*⁶⁵ become steeper with stretching. For flipped models, steeper surfaces are seen in outer cortical layers, for all three lenses of different age, the number of which increase with age, for both the anterior and posterior parts.

Table 3.6 Central radius of curvature (R) of models using the material properties of Fisher⁶²

		anterior				posterior			
		Un-deformed	Single	Multi1	Multi2	Un-deformed	Single	Multi1	Multi2
		16-year-old							
	Nucleus	4.00	4.53	4.57	4.45	3.25	3.55	3.57	3.57
	Cortical 1	4.95	5.53	5.57	5.56	4.11	4.36	4.38	4.38
	Cortical 2	5.66	6.25	6.27	6.26	4.50	4.72	4.73	4.73
	Cortical 3	6.03	6.64	6.63	6.64	4.93	5.15	5.14	5.14
	Cortical 4	7.15	7.88	7.85	7.86	5.91	6.14	6.11	6.12
		35-year-old							
Fisher ⁶² 2	Nucleus	5.71	6.18	6.21	6.21	3.53	3.77	3.78	3.78
	Cortical 1	6.85	7.21	7.25	7.25	4.30	4.56	4.57	4.57
	Cortical 2	8.60	9.08	9.10	9.10	4.71	4.96	4.96	4.96
	Cortical 3	8.92	9.28	9.28	9.28	5.14	5.40	5.39	5.39
	Cortical 4	10.16	10.55	10.53	10.53	5.61	5.86	5.85	5.85
	Cortical 5	11.81	12.29	12.21	12.23	6.40	6.70	6.71	6.72
		48-year-old							
	Nucleus	7.40	7.63	7.66	7.66	4.19	4.41	4.42	4.42
	Cortical 1	7.95	8.07	8.09	8.10	4.94	5.15	5.16	5.16
	Cortical 2	9.43	9.52	9.52	9.54	5.31	5.53	5.53	5.53
	Cortical 3	10.68	10.61	10.58	10.60	6.15	6.55	6.54	4.42
	Cortical 4	11.41	11.29	11.24	11.27	6.22	6.45	6.44	6.44
	Cortical 5	13.82	13.58	13.50	13.54	6.68	6.91	6.90	6.91

Table 3.7 Central radius of curvature (R) of flipped models using the material properties of Fisher⁶²

		anterior				posterior			
		Un-deformed	Single	Multi1	Multi2	Un-deformed	Single	Multi1	Multi2
		16-year-old							
flipped	Nucleus	4.00	4.57	4.61	4.63	3.25	3.59	3.61	3.62
	Cortical 1	4.95	5.45	5.55	5.61	4.11	4.34	4.41	4.45
	Cortical 2	5.66	5.91	6.04	6.12	4.50	4.61	4.69	4.73
	Cortical 3	6.03	6.13	6.24	6.33	4.93	4.92	5.00	5.05
	Cortical 4	7.15	7.06	7.09	7.09	5.91	5.73	5.74	5.73
	35-year-old								
	Nucleus	5.71	6.18	6.22	6.27	3.53	3.75	3.76	3.77
	Cortical 1	8.60	7.04	7.26	7.35	4.30	4.46	4.51	4.54
	Cortical 2	6.85	8.39	8.64	8.78	4.71	4.77	4.84	4.88
	Cortical 3	8.92	8.33	8.57	8.72	5.14	5.11	5.19	5.23
	Cortical 4	10.16	9.10	9.31	9.48	5.61	5.47	5.54	5.59
	Cortical 5	11.81	10.19	10.28	10.31	6.46	6.20	6.22	6.21
48-year-old									
Nucleus	7.40	7.55	7.57	7.58	4.19	4.38	4.38	4.38	
Cortical 1	7.95	7.91	7.94	7.95	4.94	5.07	5.09	5.09	
Cortical 2	9.43	9.06	9.14	9.16	5.31	5.40	5.42	5.43	
Cortical 3	10.68	9.83	9.93	9.94	6.15	6.26	6.30	6.30	
Cortical 4	11.41	10.27	10.37	10.37	6.22	6.21	6.24	6.24	
Cortical 5	13.94	12.04	12.14	12.12	6.68	6.64	6.67	6.66	

Table 3.8 Central radius of curvature (R) of models using the material properties of Wilde *et al.*⁶⁵

		anterior				posterior			
		Un-deformed	Single	Multi1	Multi2	Un-deformed	Single	Multi1	Multi2
		16-year-old							
Wilde <i>et al.</i> ⁶⁵	Nucleus	4.00	4.57	4.62	4.61	3.25	3.52	3.56	3.54
	Cortical 1	4.95	5.56	5.61	5.59	4.11	4.30	4.33	4.32
	Cortical 2	5.66	6.28	6.30	6.29	4.50	4.65	4.67	4.66
	Cortical 3	6.03	6.68	6.66	6.66	4.93	5.07	5.07	5.07
	Cortical 4	7.15	7.93	7.87	7.88	5.91	6.05	6.02	6.03
	35-year-old								
	Nucleus	5.71	6.10	6.17	6.16	3.53	3.76	3.78	3.77
	Cortical 1	8.60	7.08	7.14	7.13	4.30	4.52	4.53	4.53
	Cortical 2	6.85	8.75	8.85	8.85	4.71	4.91	4.90	4.90
	Cortical 3	8.92	9.00	8.98	8.99	5.14	5.33	5.32	5.32
	Cortical 4	10.16	10.18	10.12	10.13	5.61	5.78	5.75	5.76
	Cortical 5	11.81	11.78	11.68	11.71	6.46	6.63	6.59	6.60
48-year-old									
Nucleus	7.40	7.44	7.44	7.44	4.19	4.32	4.32	4.32	
Cortical 1	7.95	7.87	7.88	7.88	4.94	5.04	5.05	5.05	
Cortical 2	9.43	9.19	9.24	9.23	5.31	5.40	5.42	5.41	
Cortical 3	10.68	10.13	10.20	10.18	6.15	6.31	6.33	6.32	
Cortical 4	11.41	10.70	10.78	10.76	6.22	6.26	6.29	6.28	
Cortical 5	13.94	12.73	12.83	12.80	6.68	6.71	6.73	6.73	

The radii of curvature of different layers vary with the vertex locations of each surface and continuously increase from the nuclear surface to the external lens surface. The vertex location of each layer is linearly related to its central radius of curvature, as shown in Figure 3.19 for lenses in undeformed states. The slope of the linear regression line increases with age for both anterior and posterior sections. The anterior surfaces show steeper slopes than the posterior surfaces (Figure 3.19).

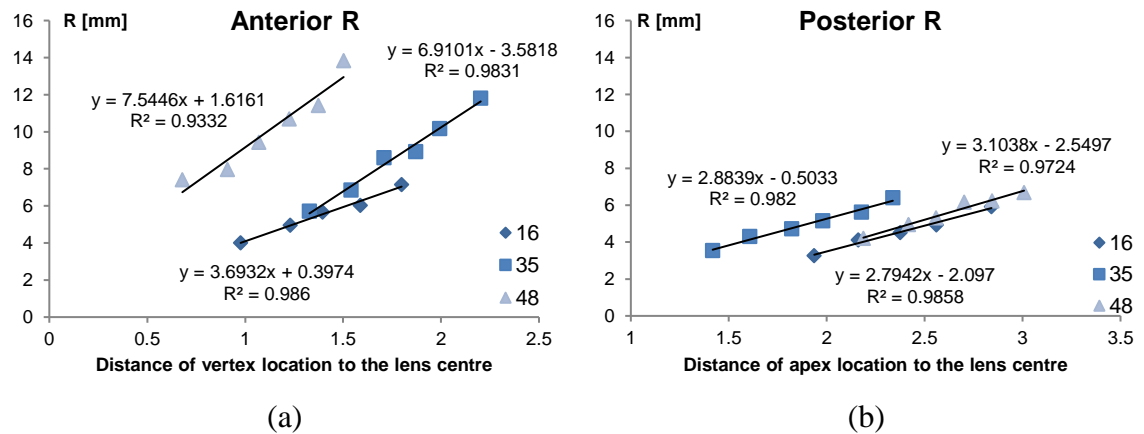


Figure 3.19 The relationship between the (a) anterior and (b) posterior radius of curvature and the vertex locations of different layers of the undeformed lens models.

The radii of curvature as a function of the vertex locations of the deformed lens models, with a single cortical modulus, using different material properties under a stretching force of 0.08N are plotted in Figure 3.20. Multi-layered models are not presented in the figures as they demonstrate similar changes of polar displacements and internal radii of curvatures (Tables 3.4-3.8). The linear relationships are preserved and the slopes of the linear regression line are flatter at young age and steeper in old age during the deformation of lens models. When using the material properties of Fisher⁶², the anterior slope become slightly steeper for the two younger lens models but slightly flatter for the 48-year-old model. The posterior slopes are steeper with stretching for models of all ages. The slopes for both the anterior and posterior section of the lens model at all three ages decrease with stretching for flipped models (Figure 3.20c,d). When using the material properties of Wilde *et al.*⁶⁵, the anterior slopes of the 35-year-old and 48-year-old model become flatter while the other slopes become steeper.

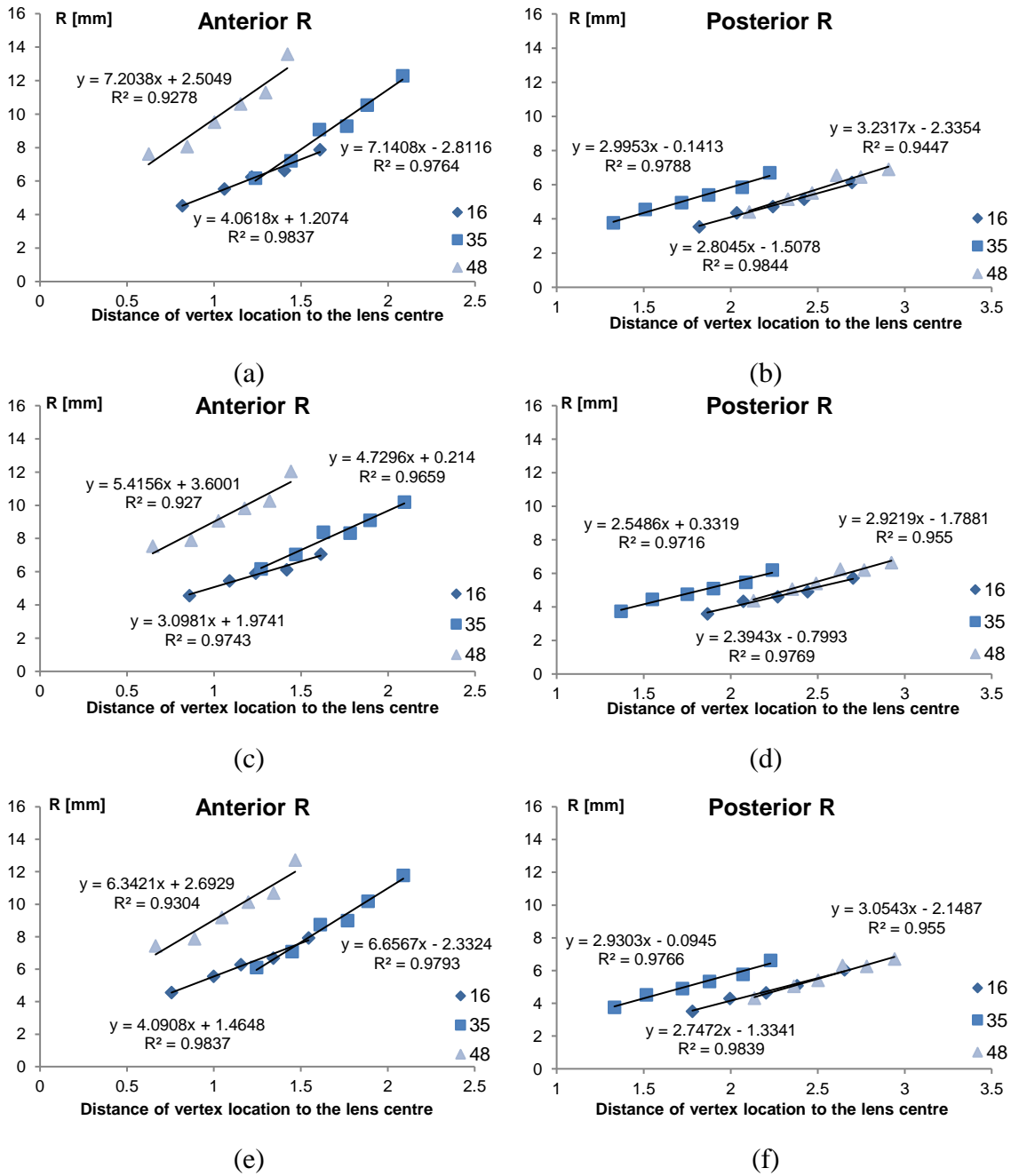


Figure 3.20 The radius of curvature as a function of the vertex location of different layers for both the anterior and posterior part of the models using (a,b) the material properties of Fisher⁶², (c,d) Flipped material properties of Fisher⁶² and (e,f) the material properties of Wilde *et al.*⁶⁵.

3.6 Verification and validation of models

3.6.1 Mesh checking

An additional model with a higher mesh density was created for the 16-year-model using the material properties of Fisher⁶² to check whether the number of nodes and elements was sufficient to produce mesh independent results. The comparison of the model with a higher mesh density (Figure 3.21b) to the model with a lower density (Figure 3.21a) is demonstrated in the figure below. The total number of elements and the total number of nodes for the model displayed in Figure 3.21b were 52467 and 314358 respectively. The number of nodes is roughly two times that of the model displayed in Figure 3.3a.

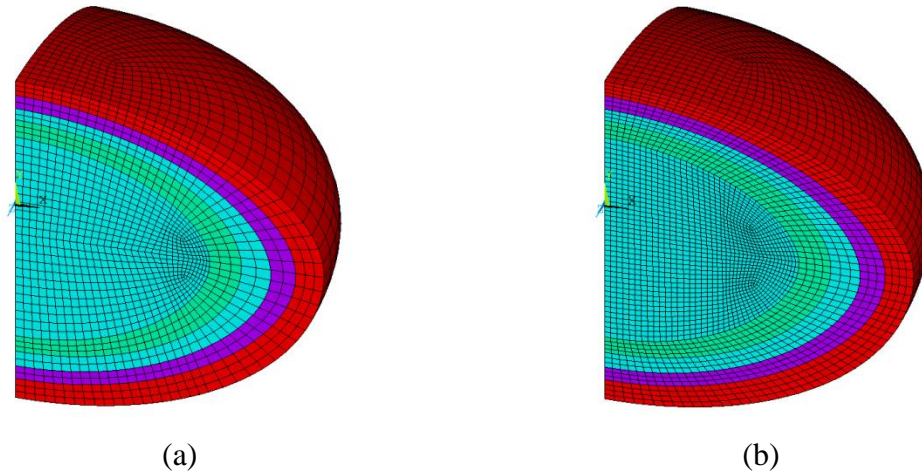


Figure 3.21 FE models of the 16-year-old lens with a (a) lower and a (b) higher mesh density.

Both models were simulated when applied with a total radial stretching force of 0.08N. The displacements taken at the anterior pole, posterior pole and the equator (as illustrated in Figure 3.15) for both models were plotted in Figure 3.22. The displacements between these two models at the three selected positions varies 1-2%, which are optically negligible. The computational time required for the higher mesh density model was much higher and was therefore not selected for further analysis in the present Thesis.

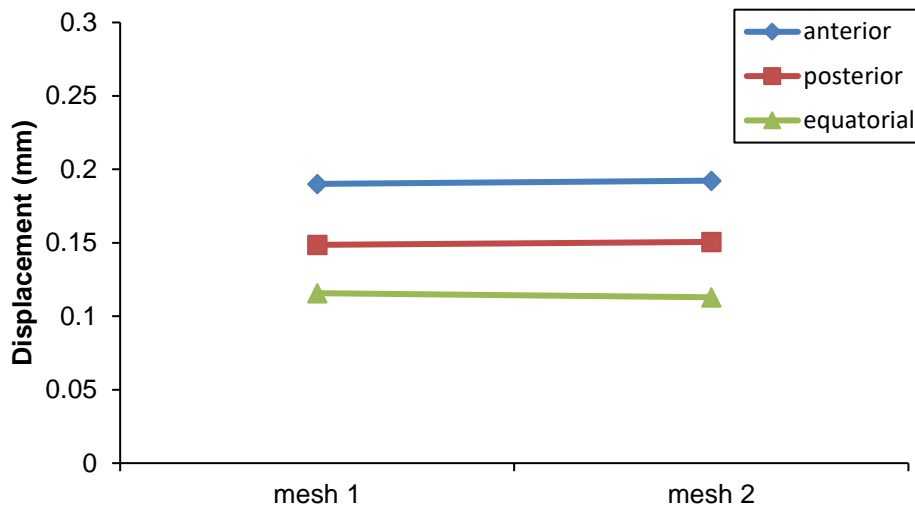


Figure 3.22. The comparison of displacements at anterior pole, posterior pole and the equator for the 16-year-old model with two mesh densities.

3.6.2 Comparing to experimental measurements

The models constructed in the present study combine geometries and material properties measured by different studies and are therefore not representative of specific lenses. It would be worth comparing the general trend, i.e. the ageing behaviour, with those observed by *in vivo* measurements. Under the stretching force of 0.08N all lens models show decreasing trends in displacements with age (Table 3.4 and Figure 3.16), confirming an increased resistance of older lenses to stretching forces^{25, 125} in accordance with the physiological condition of presbyopia.

Deformations in the nucleus are significantly larger than in the cortical region when the lens shape was changed for all the models with a lower elastic modulus in the nucleus than in the cortex (Table 3.5 and Figure 3.18). These include all three models of different ages using the material properties of Fisher⁶² and the two younger lens models using the material properties of Wilde *et al.*⁶⁵. Thickness changes during accommodation have been reported to occur in the nuclear region in several clinical studies^{13, 14, 26, 31}. Furthermore, as lens thickness decreases with stretching, the movement of the anterior pole is greater than that of the posterior pole, for the 16-year-old lens models and the 35-year-old lens models (Table 3.4). Similar changes have been reported in *in vivo* studies^{13, 33}.

The central anterior radii of curvature become flatter with stretching for the two younger lens models using Fisher's material properties and the 16-year-old model using the material properties of Wilde et al, which is also in accordance with previous clinical studies^{13, 27, 29, 30, 32, 33}. Besides, the linear relationship between the radius of curvatures of internal layers and their locations, and the decreasing trend of the slopes with age found in the present study concur with *in vivo* measurements³².

3.7 Discussion

The accuracy of any computational model relies on the data used to construct it, in this case on both geometric parameters of the components of the eye involved in accommodation and on the mechanical properties of the lens. The geometrical parameters of curvature and thickness can be obtained from live eyes using clinical biomicroscopic means^{14, 22, 26, 27}. Since the lens grows throughout life, with age, its thickness increases and the central anterior and posterior radii of curvature decrease^{14, 22, 26, 27}. Individual variations in biological tissues and structures can mask ageing effects given variations in genetics, epigenetics and lifestyle factors. This notwithstanding, eye lens growth with age is well defined^{13, 16, 17, 32}. Material properties have been much harder to ascertain. *In vitro* studies, either with respect to age or across the lens, differ greatly^{62, 63, 65, 67, 68}. The seminal work of Fisher provided values of Young's moduli for the lens substance, the lens capsule and the zonular fibres over a wide age range^{62, 119, 124}. Wilde *et al.*⁶⁵ repeated the spinning method employed by Fisher⁶² but reported different trends of the elastic modulus in the lens nucleus and the cortex to that of Fisher⁶². The material properties from both studies were examined in the present work.

There is a varying protein distribution across the lens resulting in the gradient refractive index that contributes to the high degree of image quality³⁵. The linear relationship between protein concentration and refractive index is well understood^{35, 149}. The material properties across the lens also vary, as experimental studies^{63, 64} have shown, but the correlation between these changes and the protein concentration is still unclear. Recently, *in vivo* studies using Brillouin optical microscopy have reported profiles of elasticity along the lens central axis^{71, 107, 152} that mimic the gradient of refractive index^{35, 37, 149}, suggesting linear relationships may also exist between mechanical and optical properties. Therefore in the present study gradient material properties are introduced

Chapter 3. Development of gradient moduli models

into the lens models assuming a linear relationship with the refractive index distribution³⁷.

Previous FEA models anchored the zonule to a single point^{99, 101, 139, 144} resulting in non-physiological discontinuities in curvature. In this study, a master-slave node mechanism was introduced by applying a number of constraint equations to zonular-capsular attaching points. This mechanism couples the degrees of freedom of the neighbouring nodes so that they follow the movement of each anchorage point, yielding smooth curvatures on deformed lens shapes. Additionally, the lens curvatures and material gradients used to construct the models are based on experimental data³⁷. These characteristics have yielded a model that more closely mimics the physiological condition¹⁵. The FE lens models proposed in the present study are the most biologically accurate to date.

The stress patterns of the single cortex models are similar to the stress patterns found by Belaidi and Pierscionek¹²⁹, showing a high stress region concentrated near the nuclear equatorial pole when the model undergoes simulated stretching. The stiffness variations within the lens only have an effect on internal stress distributions. The more evenly distributed stresses in the cortical regions of multi-layer models, compared with single cortex models, demonstrate that the material property within the cortex is unlikely to be a constant value, as high stress concentrations in biological tissues could be detrimental physiologically.

Further analyses of many more lenses across a wider age range are needed to determine whether there is a cross over point where the elastic modulus in the nucleus becomes higher than in the cortex and at what age this may occur. From the results in our study, as the number of cortical layers increases, there are no significant variations in either deformation changes or in central curvature between the models with different cortical layers (Tables 3.4 to 3.8).

The converse behaviour of the 48-year-old model in terms of anterior and posterior polar movement could be related to the more asymmetric geometry or the anchorage of zonular fibres but it needs to take account of the fact that a lens of this age has very little accommodative capacity left.

With a spherical approximation to curvature fitting, lens central anterior radii of curvature increase with stretching for the two younger lens models using the material properties of Fisher⁶² and for the youngest model using the material properties of Wilde

*et al.*⁶⁵ (Table 3.6 and Table 3.8). This supports the theory of Helmholtz⁵². In the case of the oldest lens using the material properties of Fisher⁶² (Table 3.6), all three aged models with the flipped Young's modulus of Fisher⁶² in the nucleus and the cortex (Table 3.7) and the two older lens models using the material properties of Wilde *et al.*⁶⁵ (Table 3.8), central radii of curvature decrease with stretching and are in support of the theory of Schachar⁵⁶.

3.8 Summary

This chapter presents three-dimensional lens models built at three different ages using geometries taken from optical measurements that include shapes of both external and internal cortical layers. Gradient Young's moduli were modelled in the lens cortical region and were compared to models with a single cortical modulus with respect to changes in stress and displacement fields. The surface curvatures of each lens model were determined and reviewed to see which accommodative theory they support.

4 ZONULAR STRUCTURES: INFLUENCE ON LENS OPTICAL PERFORMANCE

The present chapter investigates different forms of zonular configurations to determine which may most closely mimic the physiological state by comparing displacement fields with simulated shape changes to accommodation in living lenses. In addition to the zonular configurations in models shown in Chapter 3, models with the anterior, equatorial and posterior sections of the zonule bound together with alterations in stretching angles and models with the three zonular sections being stretched independently in different directions are both developed based on the 35-year-old lens³⁷. The effect of changes in different levels of stretching forces provided by zonular fibres and various angles of stretching applied to zonular fibres are analysed to determine how they affect the anterior and posterior curvatures of the lens approximated by spheres and how the model results compare to studies on living eyes.

4.1 Modelling different configurations of the zonule

The contributions of zonular fibres to accommodation have been relatively less investigated as most of the *in vivo* studies on lens deformations during accommodation focused on the changes in the central region^{13, 14, 22, 23, 27, 42, 153, 154}, providing limited information on how the zonular fibres exert forces to alter the lens shape. The majority

Chapter 4. Zonular structures: influence on lens optical performance

of such studies in the literature have modelled the zonular section bound to single stretching points as shown in Figure 4.1a. This simplified version can roughly mimic the physiology in that the lens is stretched into a flattened shape but it cannot capture the influence of the zonular fibres which originate from different parts of the ciliary body (as introduced in Chapter 1). According to the accommodative theory of Schachar⁵⁶, different zonular fibres act differently in altering the lens shape, therefore it is insufficient to fully replicate the behaviour of zonular fibres by the model shown in Figure 4.1a.

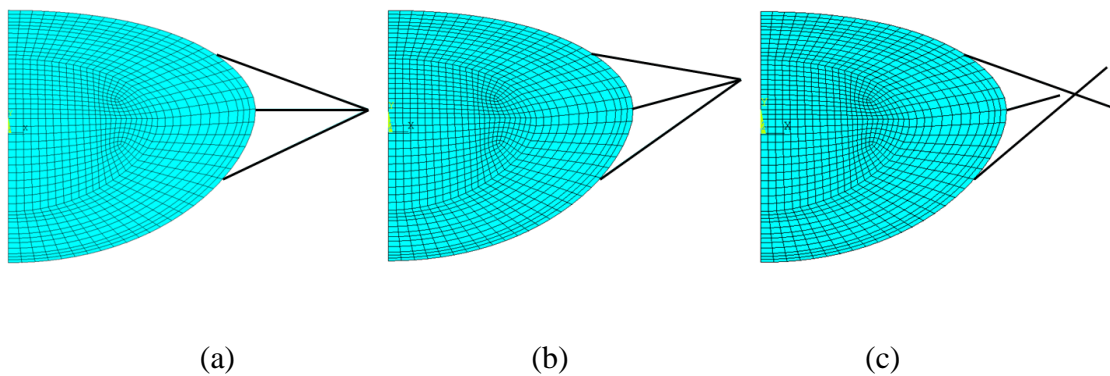


Figure 4.1 A 35-year-old model (a) with anterior, equatorial and posterior zonular fibres bound to a single point and applied with horizontal stretching, (b) with bound zonular fibres shifted anteriorly and (c) with split zonular fibres in three different directions.

To extend the analysis on zonular fibres, two additional types of zonular configurations as shown in Figure 4.1b and Figure 4.1c were proposed based on the 35-year-old lens model. The first type (Figure 4.1b) employs a single stretching point which connects the anterior, equatorial and posterior zonular fibre to the same endpoint. The zonular angle was altered with stretching applied to the endpoint along different directions. In the second type of zonular configuration (Figure 4.1c), the anterior, equatorial and posterior zonular fibres are connected to three different endpoints and are provided with the ability to move independently in different directions.

A number of stretching angles were arbitrarily selected and simulated for newly developed models with both zonular configurations. Stretching was applied to models with zonular structure as shown in Figure 4.1b, for zonular angle shifts of: 5, 10, 15 degrees anteriorly and 10, 20 degrees posteriorly. For the models with zonular structure as represented in Figure 4.1c, a series of combinations of different anterior, equatorial and posterior zonular angles were created with 5 degree alteration in one of the three zonular angles each time. The resultant changes in radius of curvature as a function of

accommodative amplitude of each model were compared to the results obtained from an *in vivo* measurement²⁷. The analyses of the alteration in zonular angles were only based on the single cortex modulus models using the material properties of Fisher⁶² considering computational resources and time consumption. More comprehensive parametric analyses investigating the effect of both the material properties of Fisher⁶² and of Wilde *et al.*⁶⁵ are demonstrated in Chapter 5.

4.2 Model A: Comparison to *in vivo* lens

To make an age-related comparison to the clinical measurement conducted on a living eye of a 29-year-old subject²⁷, the lens models based on a 35-year-old lens³⁷ with the three types of zonular configuration shown in Figure 4.1 were subjected to higher levels of stretching forces than those applied to the models shown in Chapter 3. The reason for the adoption of only single cortex models for the analyses was that the single cortex modulus model and the multi-layered models demonstrate similar changes in terms of curvatures and deformations, as shown in Chapter 3. Six levels of stretching forces are applied to the model shown in Figure 4.1a: 0.08N, 0.16N, 0.24N, 0.32N, 0.40N and 0.48N, resulting in six states of deformed lens shapes (represented in Figure 4.2).

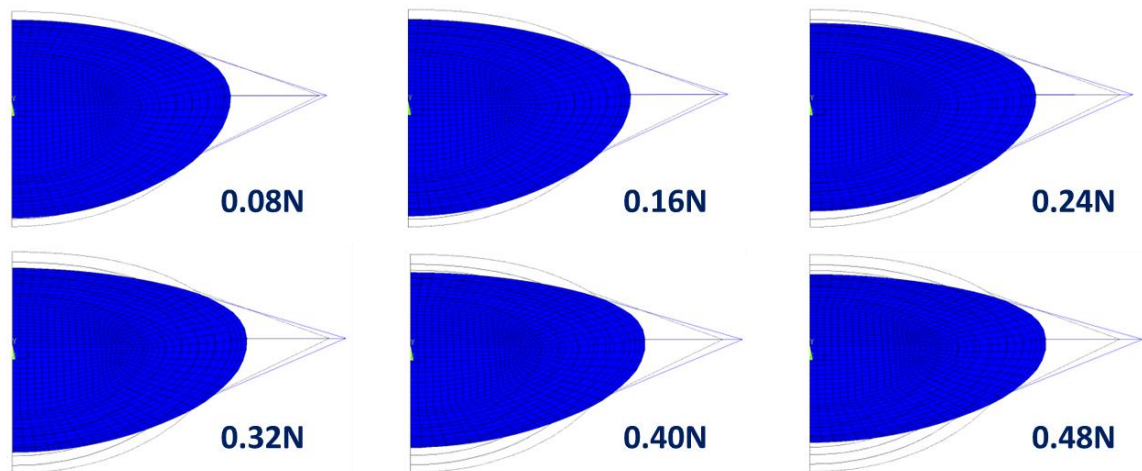


Figure 4.2 The deformed lens models together with undeformed lens shape under the accumulated force levels of (a) 0.08N, (b) 0.16N, (c) 0.24N, (d) 0.32N, (e) 0.40N and (f) 0.48N.

The radii of curvature of the anterior and posterior lens surfaces within the central 3mm diameter zone of the lens and the sagittal thicknesses were extracted from each

deformed lens shape for the calculation of Central Optical Power (COP) based on equation 4.1^{99, 131}:

$$COP = \frac{n_1 - n_a}{r_a} + \frac{n_1 - n_a}{r_p} - \frac{t(n_1 - n_a)^2}{r_a r_p n_1} \quad (4.1)$$

where $n_a = 1.336$, is the refractive index of aqueous humour¹⁸, $n_1 = 1.42$ is the estimated overall refractive index of the lens which is a representative equivalent refractive index, r_a and r_p are the anterior and posterior radii of curvature respectively, t is the sagittal thickness of the lens.

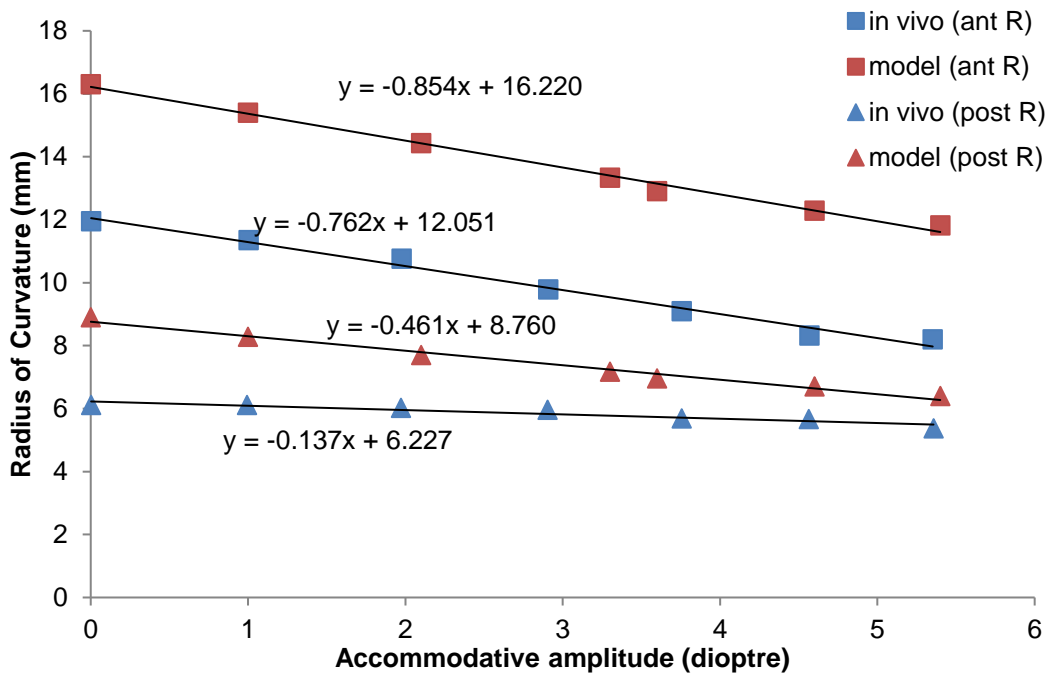


Figure 4.3 The change in anterior and posterior radii of curvature plotted against accommodative amplitude for the 35-year-old model with horizontal zonular stretching.

The changes in both the anterior and posterior radii of curvature as a function of the change in COP, namely the accommodative amplitude, were plotted in Figure 4.3. Linear relationships are found for the simulated lens model, which were compared to results measured from the 29-year-old *in vivo* lens²⁷. The slopes of the linear regression lines were determined and were compared to the clinical data²⁷ using the standard t-test analysis for two independent samples in Excel (ver. 2010). For this model with zonular stretching applied along horizontal direction (Figure 4.1a), the change in anterior radius of curvature as a function of accommodative amplitude fits well with the *in vivo* lens²⁷ as there are no significant differences found ($p = 0.105$). Poor fits are shown for the

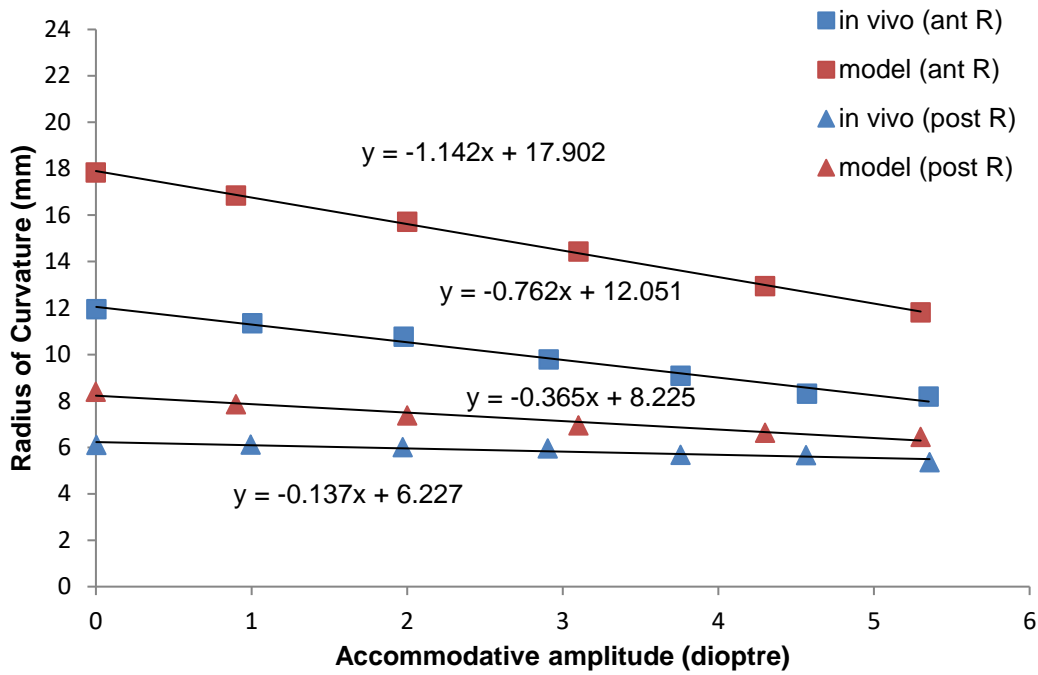
change in posterior radius of curvature and significant differences were found ($p \ll 0.01$).

4.3 Model B: Altering the stretching angles

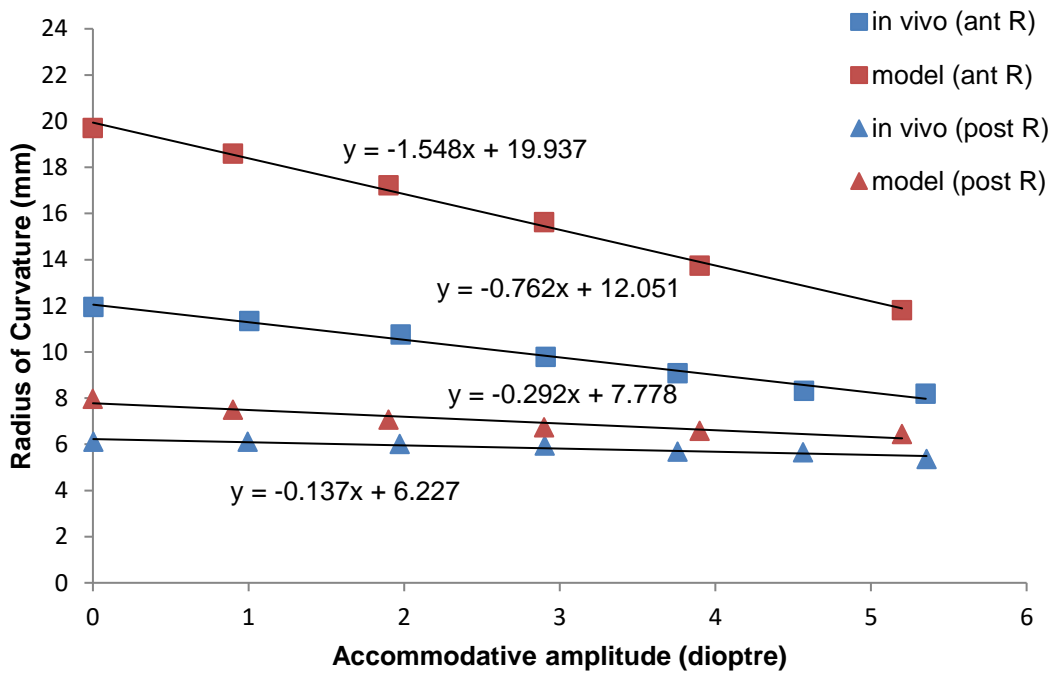
For the model with zonular configuration as shown in Figure 4.1b, the linear relationship between the changes in radius of curvature as a function of accommodative amplitude was preserved when the stretching angle was altered. The anterior and posterior slopes measured *in vivo* are -0.762 and -0.137 respectively (reanalysed from Dubbelman *et al.*²⁷). The models with anteriorly shifted zonular angles resulted in both anterior and posterior slopes that were lower than the clinically derived values. With the increases in the anteriorly shifted angle from 5 degrees to 15 degrees, the anterior slope decreases and deviates further from the *in vivo*²⁷ measured slope; the posterior slope increases and moves close the *in vivo*²⁷ data. The models with posteriorly shifted zonular angles result in a higher anterior slope and a lower posterior slope than that obtained from the *in vivo* lens. The radii of curvature, as a function of accommodation, for models with all simulated angles are plotted in Figure 4.4. The model with zonular fibres shifted posteriorly by 20 degrees was not shown as a convergent solution could not be obtained when the stretching forces were higher than 0.15N. The resulting anterior and posterior slopes, as well as the anterior and posterior p-values, which were calculated using the standard t-test comparison to the *in vivo* lens²⁷, are listed in Table 4.1 for all simulated angles. Significant differences for the anterior slopes are found for models with all simulated zonular angles ($p \ll 0.01$). For the posterior slope, the model with zonular fibres shifted anteriorly by 15 degrees demonstrates good fits ($p = 0.117$) (Figure 4.4c).

Table 4.1 Anterior and posterior slopes of the linear relationships between radius of curvature and accommodative amplitude for models with bound zonular fibres and shifting angles.

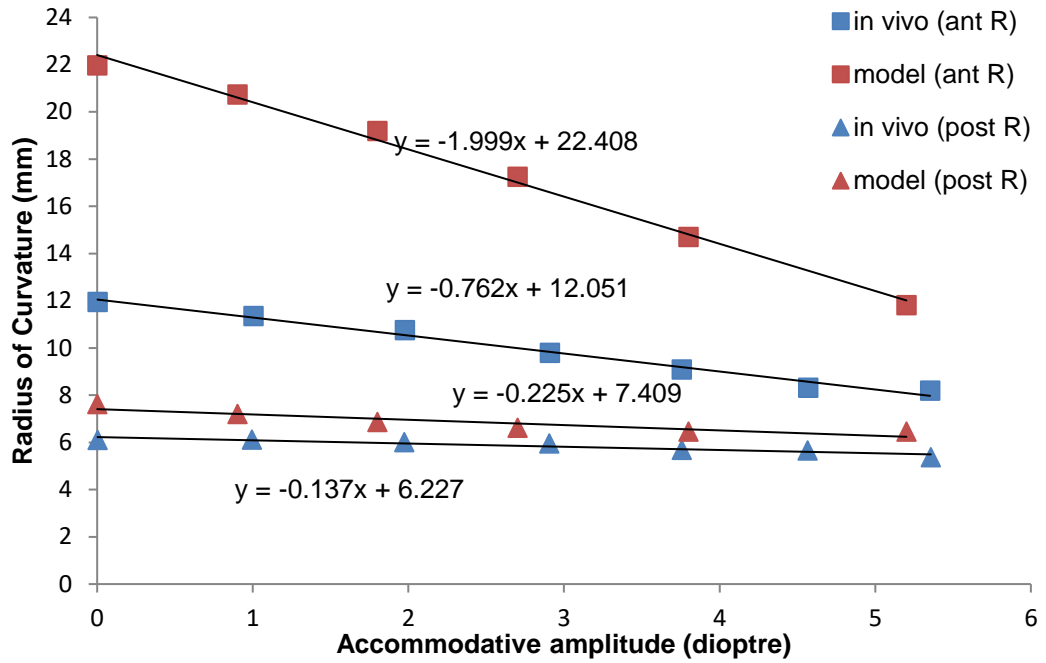
	<i>in vivo</i>	Anteriorly 5°	Anteriorly 10°	Anteriorly 15°	Posteriorly 10°
Anterior slope	-0.762	-1.142	-1.548	-1.999	-0.430
Anterior p	-	$\ll 0.01$	$\ll 0.01$	$\ll 0.01$	$\ll 0.01$
Posterior slope	-0.137	-0.365	-0.292	-0.225	-0.625
Posterior p	-	$\ll 0.01$	0.011	0.117	$\ll 0.01$



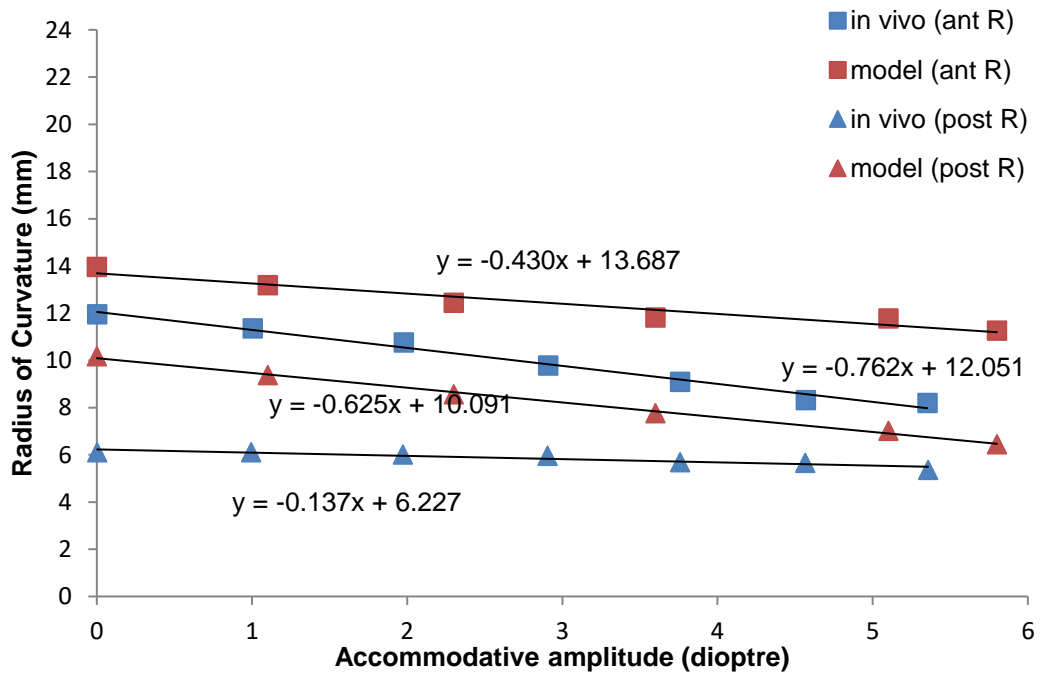
(a) zonular fibres shifted anteriorly by 5 degrees.



(b) zonular fibres shifted anteriorly by 10 degrees.



(c) zonular fibres shifted anteriorly by 15 degrees.



(d) zonular fibres shifted posteriorly by 10 degrees

Figure 4.4 The change in anterior and posterior radii of curvature plotted against accommodative amplitude for the 35-year-old model with bound zonular fibres shifted to different angles.

4.4 Model C: split zonular fibres

4.4.1 Changing the zonular angles

The analysis of models with split zonular fibres started with the zonular angle triplet of $[20^\circ, 0^\circ, 35^\circ]$ for the anterior, equatorial and posterior zonular angles, respectively. The selection of the 20° anterior zonular angle is obtained from the anterior zonular orientation of the model (Figure 4.1a) providing good fits to the *in vivo* lens²⁷ for the anterior lens curvature as shown in Figure 4.3. The selection of a 35° posterior zonular angle was obtained from the posterior zonular orientation of the model (Figure 4.1b) as it demonstrated good fits to *in vivo* data²⁷ for the posterior lens curvatures as shown in Figure 4.4c. Equal amounts of displacement, of 0.5mm, were first applied to the endpoints of the three zonular fibres. Displacements were applied instead of the forces because it was hard to ascertain the ratio of the forces among the three zonules. The linear relationships between the radii of curvature as a function of accommodative amplitude compared to the *in vivo* measurement are plotted in Figure 4.5. Significant differences are found for both the anterior ($p = 0.011$) and posterior ($p \ll 0.01$) surfaces.

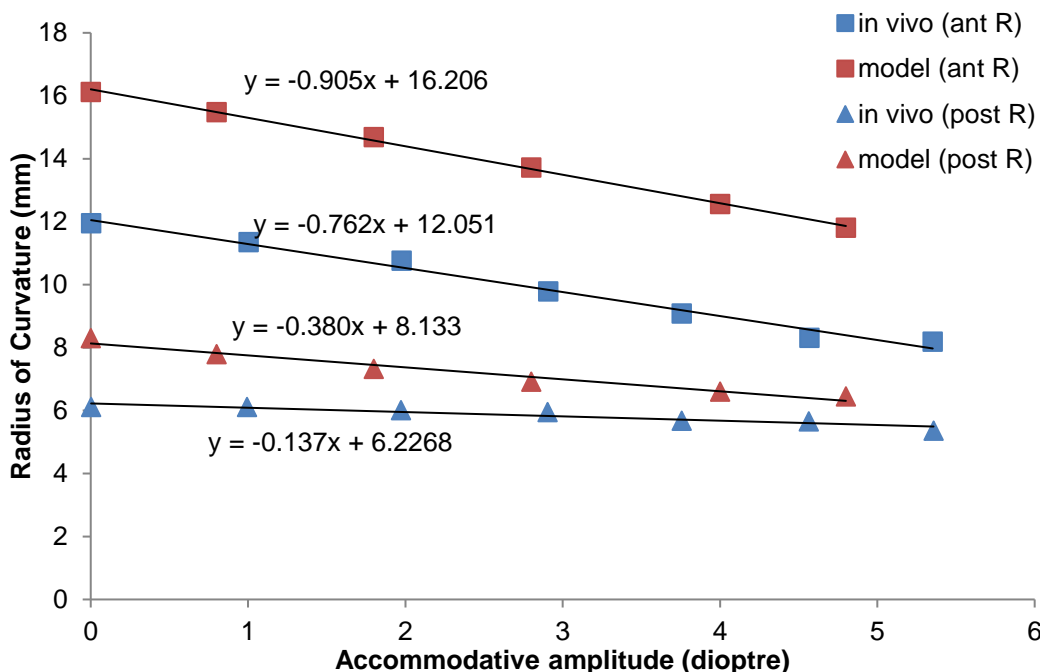


Figure 4.5 The change in anterior and posterior radii of curvature plotted against accommodative amplitude for the 35-year-old model with 20° anterior, 0° equatorial and 35° posterior zonular angles.

Based on the model with a zonular angle triplet of [20°, 0°, 35°], increments of 5° were added to either the equatorial zonular angle or posterior zonular angle each time, contributing to a total number of five developed models with split zonular fibres. Table 4.2 lists the results of these developed models. All three zonular sections in each model had 0.5mm of displacement applied. With the increasing of the equatorial zonular angle or posterior zonular angle (from left to right as listed in Table 4.2), the anterior slope decreases while the posterior slope increases. Significant differences between the modelled results and the *in vivo* measurement²⁷ are found for all cases (all $p < 0.05$). When the anterior slope gets closer to the clinical value of -0.762 the posterior slope deviates further from the clinical value of -0.137. A posterior zonular angle of 45 degrees is considered to be inappropriate as a discontinuity of curvature is seen for the posterior surface with zonular angle triplets of [20°, 10°, 45°]. Such discontinuities are not physiological and therefore the model was discarded and no further analysis conducted.

Table 4.2 Anterior and posterior slopes of the models with different zonular angle triplets under the 0.5mm displacements applied to all three zonular fibres.

	[20°, 0°, 35°]	[20°, 5°, 35°]	[20°, 5°, 40°]	[20°, 10°, 40°]	[20°, 10°, 45°]
Anterior slope	-0.905	-1.057	-1.213	-1.266	-1.462
Anterior p	0.011	<< 0.01	<< 0.01	<< 0.01	<< 0.01
Posterior slope	-0.380	-0.360	-0.300	-0.289	-0.237
Posterior p	<< 0.01	<< 0.01	0.003	0.003	0.034

4.4.2 Changing the ratio of the displacements applied to the three zonular fibres

For each model, different amounts of displacement were further applied to the three zonular fibres and the results for the model with a zonular angle triplet of [20°, 0°, 35°] are listed in Table 4.3. The posterior surfaces of all simulated lens models demonstrate poor fits as significant differences are found between these and the *in vivo* lens²⁷ (all $p << 0.01$). The anterior slopes provided by the first ($p = 0.433$), second ($p = 0.324$) and last ($p = 0.096$) cases, as listed in Table 4.3, demonstrate good fits. For these three cases, the displacement applied to the posterior zonular fibre is less than that applied to the anterior or equatorial zonular fibres. The combination of displacements which consists of 0.5mm, 0.5mm and 0.4mm for the anterior, equatorial and posterior zonular fibres, respectively, was the only case resulting in an anterior slope higher than the *in vivo* data²⁷.

Chapter 4. Zonular structures: influence on lens optical performance

Table 4.3 Anterior and posterior slopes provided by the model with a zonular angle triplet of [20°, 0°, 35°] under different amount of displacements.

Displacements /mm	0.6, 0.5, 0.5	0.5, 0.6, 0.5	0.5, 0.5, 0.6	0.4, 0.5, 0.5	0.5, 0.4, 0.5	0.5, 0.5, 0.4
Anterior slope	-0.808	-0.809	-1.107	-1.081	-0.949	-0.666
Anterior p	0.433	0.324	<< 0.01	<< 0.01	0.005	0.096
Posterior slope	-0.452	-0.369	-0.379	-0.343	-0.390	-0.451
Posterior p	<< 0.01	<< 0.01	<< 0.01	<< 0.01	<< 0.01	<< 0.01

The anterior and posterior slopes resulting from the model with a zonular angle triplet of [20°, 5°, 35°] under different combinations of displacements are listed in Table 4.4. In all cases the posterior surfaces demonstrate poor fits (all $p \ll 0.01$). The simulated model with a displacement combination of 0.6mm, 0.5mm and 0.4mm and a displacement combination of 0.5mm, 0.5mm and 0.4mm demonstrate good fits for the anterior slope ($p = 0.071$ and $p = 0.671$). For these two cases, the displacement applied to the posterior zonular fibre is the lower than that applied to the anterior or posterior zonular fibre.

Table 4.4 Anterior and posterior slopes provided by the model with a zonular angle triplet of [20°, 5°, 35°] under different amount of displacements.

Displacements /mm	0.6, 0.5, 0.5	0.6, 0.5, 0.4	0.5, 0.5, 0.4	0.5, 0.5, 0.45
Anterior slope	-0.897	-0.651	-0.782	-0.921
Anterior p	0.033	0.071	0.671	0.010
Posterior slope	-0.437	-0.470	-0.403	-0.383
Posterior p	<< 0.01	<< 0.01	<< 0.01	<< 0.01

Table 4.5 Anterior and posterior slopes provided by the model with a zonular angle triplet of [20°, 10°, 40°] applied with different combinations of displacements.

Displacements /mm	0.6, 0.5, 0.4	0.55, 0.5, 0.45	0.5, 0.5, 0.45	0.5, 0.55, 0.5	0.45 0.55 0.5
Anterior slope	-0.877	-1.074	-1.162	-1.218	-1.297
Anterior p	0.172	0.002	<< 0.01	<< 0.01	<< 0.01
Posterior slope	-0.369	-0.329	-0.307	-0.300	-0.271
Posterior p	<< 0.01	<< 0.01	0.002	0.003	0.006

The results for the model with a zonular angle triplet of [20°, 10°, 40°] are listed in Table 4.5. Again, the posterior slopes demonstrate poor fits to clinical measurements (all $p < 0.05$). The model with displacements of 0.6mm, 0.5mm and 0.4mm demonstrate good fits for the anterior surface ($p = 0.172$). To continue the search for a model that provides good fits for both surfaces, an additional model with a zonular angle triplet of [20°, 15°, 40°] was developed by further increasing the equatorial zonular angle. The simulated displacements and results are listed in Table 4.6. A model with good fits for both surfaces was not found.

Table 4.6 Anterior and posterior slopes of the model with a zonular angle triplet of [20°, 15°, 40°] applied with different combinations of displacements.

Displacements /mm	0.6, 0.5, 0.4	0.58, 0.5, 0.42	0.72, 0.6, 0.48	0.696, 0.6, 0.504
Anterior slope	-0.923	-1.005	-0.878	-0.971
Anterior p	0.090	0.008	0.137	0.016
Posterior slope	-0.357	-0.341	-0.383	-0.358
Posterior p	$\ll 0.01$	$\ll 0.01$	$\ll 0.01$	$\ll 0.01$

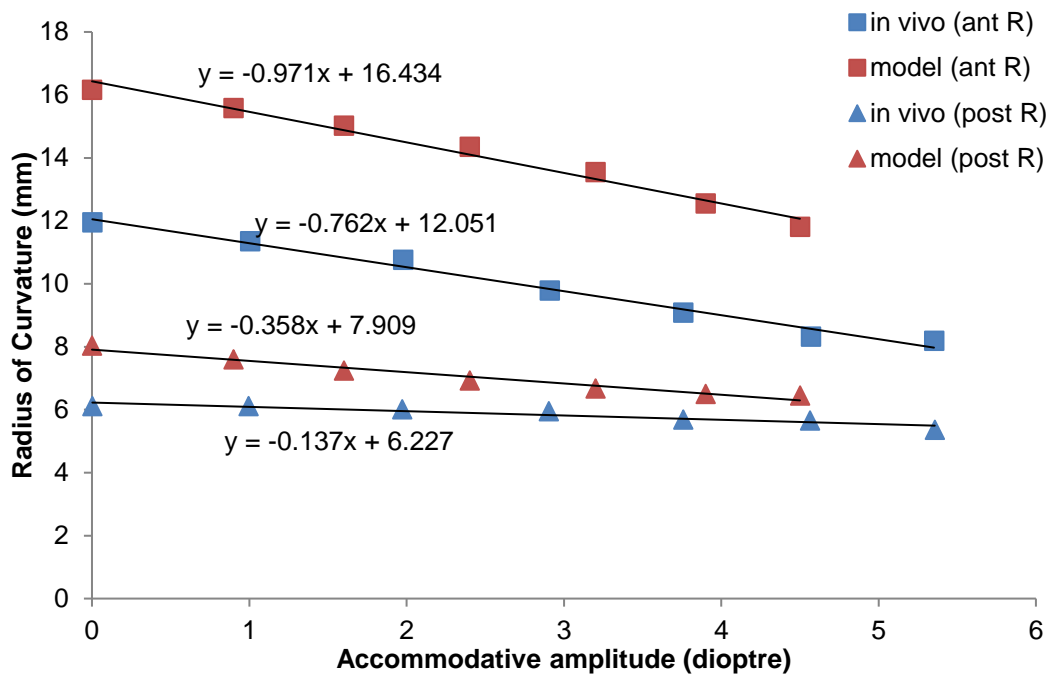


Figure 4.6 The change in anterior and posterior radii of curvature plotted against accommodative amplitude for a selective 35-year-old model with 20° anterior, 15° equatorial and 40° posterior zonular angles.

Good fits to the *in vivo* data²⁷ for both surfaces simultaneously could not be found by altering the applied displacements with the proposed zonular angle triplets. There is a

balance between the resultant anterior and posterior slopes: when one slope moves closer to the *in vivo* data, the other slope deviates further. The first and the last case listed in Table 4.6 demonstrates the minimal differences of less than 0.221 to the *in vivo* measurement²⁷ for both the anterior and posterior surfaces, but the accommodative change provided by the former case is less than 4 dioptres. In Figure 4.6 the changes in radii of curvature were plotted against accommodative amplitude for the model with a combination of displacements of 0.696mm, 0.6mm and 0.504mm.

4.5 Comparison between models with different sets of material properties

The material properties of Wilde *et al.*⁶⁵ were simulated for: (i) the model with three zonular fibres bound to a single endpoint and applied with stretching along horizontal direction as shown in Figure 4.1a, (ii) the model with zonular fibres shifted anteriorly by 15 degrees as shown in Figure 4.1b and (iii) a selected model with split zonules of 20 degrees anterior zonular angle, 15 degrees equatorial zonular angle and 40 degrees posterior zonular angle. The resultant changes in radius of curvature plotted against accommodative amplitude for these three models in comparison to their counterpart models using the material properties of Fisher⁶² and the *in vivo* data²⁷ are shown in Figures 4.7 – 4.9.

Models using the material properties of Wilde *et al.*⁶⁵ demonstrate similar changes in radii of curvature to models using the material properties of Fisher⁶², but the resultant changes in accommodative amplitude are slightly lower (Figure 4.7-4.9). Using the material properties of Wilde *et al.*⁶⁵, the model with horizontal stretching demonstrates a good anterior fitting ($p = 0.917$) but poor posterior fitting ($p \ll 0.01$) as plotted in Figure 4.7; the model with zonular fibres shifted anteriorly by 15 degrees demonstrates good posterior fitting ($p = 0.183$) but poor anterior fitting ($p \ll 0.01$) as plotted in Figure 4.8. In Figure 4.9 the balanced fits between anterior and posterior slopes are plotted for the model with split zonular fibres with displacements of 6.96mm, 6mm and 5.04mm applied to the three endpoints of the anterior, equatorial and posterior zonular fibre, respectively. For this split zonular model using the material properties of Wilde *et al.*⁶⁵, significant difference is found with *in vivo* measurements²⁷ for the posterior slope ($p \ll 0.01$) but not for the anterior slope ($p = 0.651$). As shown in section 4.4 for the split zonular models using the material properties of Fisher⁶², there appears to be a balance of the fits between the anterior and posterior curvatures.

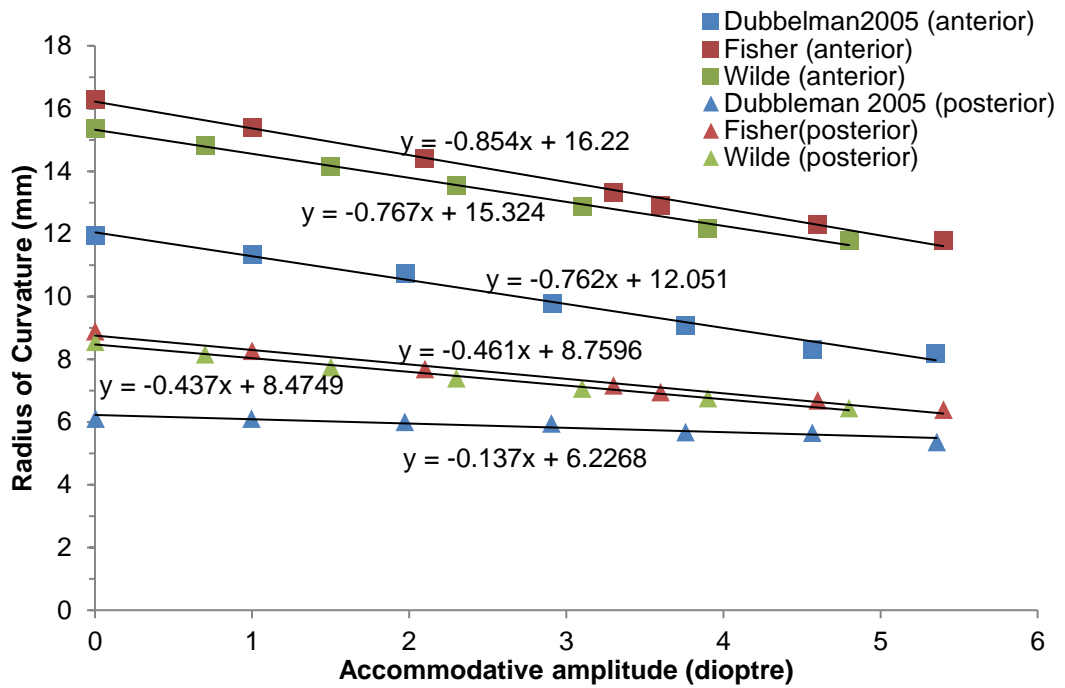


Figure 4.7 The change in anterior and posterior radii of curvature plotted against accommodative amplitude for the 35-year-old model with horizontal zonular stretching using both sets of material properties.

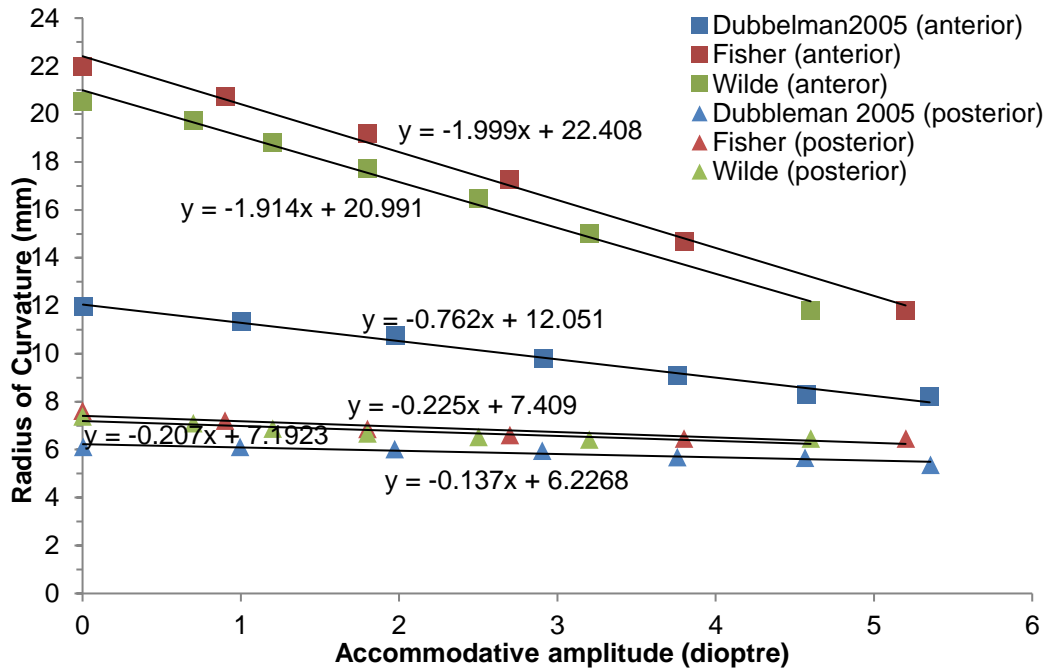


Figure 4.8 The change in anterior and posterior radii of curvature plotted against accommodative amplitude for the 35-year-old model with zonular fibres shifted anteriorly by 15 degrees using both sets of material properties.

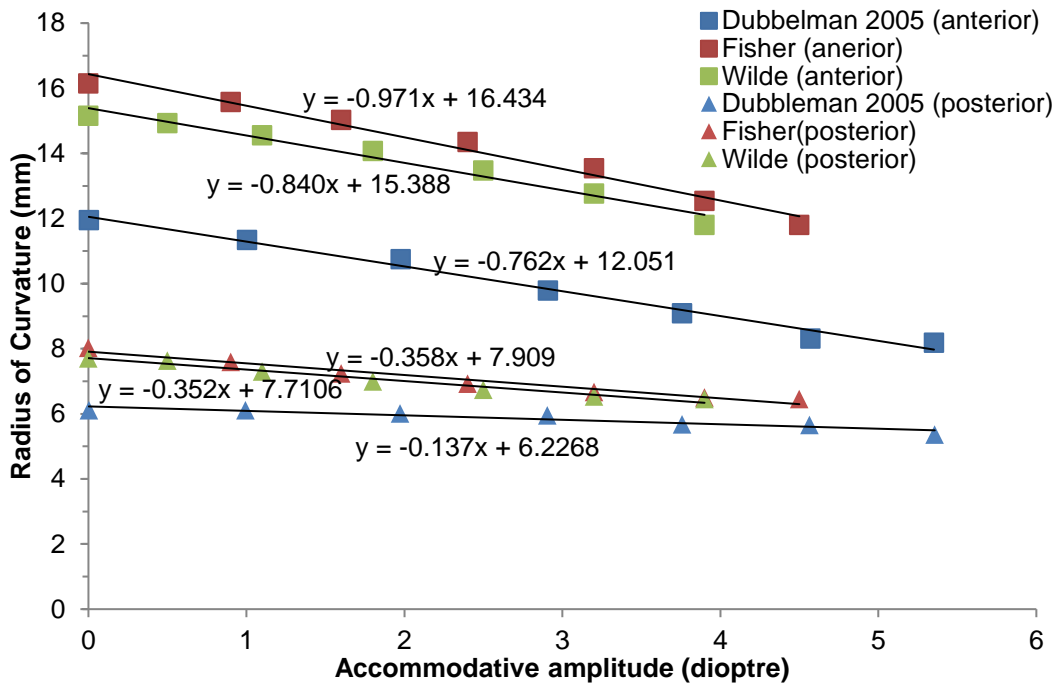


Figure 4.9 The change in anterior and posterior radii of curvature plotted against accommodative amplitude for a selective 35-year-old model with 20° anterior, 15° equatorial and 40° posterior zonular angles using both sets of material properties .

4.6 Discussion

Using FEA modelling, Stach *et al.*¹⁴¹ compared the simplified arrangement of the zonules with three zonular fibres attached to a single stretching point and a complex zonular arrangement with 10 sets of fibres. Stach *et al.*¹⁴¹ concluded that there is no significant influence on lens accommodation between models with the two different forms of zonules such that a model with the simplified version of zonular fibres is sufficient for numerical modelling. However, the analyses shown in the present chapter demonstrate the opposite: the changes in lens surface curvatures vary significantly depending on the configuration of zonular fibres and the selection of zonular angles. The zonular fibres in a real eye are more complicated than those considered for the current models displayed in Figure 4.1, they criss-cross each other and there is a distribution of anchorage points on the ciliary muscle. The models proposed here were used to determine the influence of altering the angles of the three major zonular groups. Simplification is usually needed when constructing computational models and more sophisticated forms should be considered in the future upon more available computational resources.

When the anterior, equatorial and posterior zonular fibres are attached to the same endpoint, the modelled response from the 35-year-old lens can demonstrate good fits to the clinical measurement of a 29-year-old living lens²⁷ for only one side of the lens surfaces: with horizontal stretching the anterior lens surface fits well; with stretching shifted anteriorly by 15 degrees the posterior lens surface fits well. When the three zonular fibres are split and attached to three different endpoints and different amounts of displacement are applied along different directions, a balanced fit between the anterior and posterior surface is demonstrated, although the comparison to the clinical data²⁷ for the posterior surface is quite weak.

A difference in the interceptions and small variations in the slopes of the linear regression lines from clinical measurements²⁷, for both the models with a single stretching point and the models with three stretching points can be observed. These differences may arise from a number of sources. The geometric data adopted for the present models are from measurements on *post-mortem* lenses³⁷ so that the whole lens is in a stress-free state. The clinical measurements were conducted on *in vivo* lenses²⁷ which are under a small amount of tension even in fully accommodated states. Factors like gravity, pressure and buoyancy from the vitreous and aqueous humours are excluded in *post-mortem* lenses measurements. Individual variations in lens geometry and insertion regions of zonular fibres in the lens peripheral region can also influence the curvature changes during accommodation.

4.7 Summary

The present chapter investigates three different forms of zonular configurations based on the 35-year-old lens model developed in Chapter 3. Each model was applied with higher levels of stretching forces and the simulated changes of curvature with accommodation were compared to the response obtained from a living lens. The alterations in zonular angles are examined to determine how they affect the comparison between modelled results and the living lens.

The work described in present chapter is based on a ‘trial and error’ method conducted on models with the same lens geometry and was aimed to demonstrate that the different zonular forms make a difference to the changes in radii of curvature of lens surfaces during accommodation. The changing pattern or trend of the model performances was not captured. The contributions of different lens geometries and material properties are

Chapter 4. Zonular structures: influence on lens optical performance

investigated in a more extensive analysis in chapter 5, which considers a wider range of zonular angle triplets.

5 ZONULAR ANGLES: EXHAUSTIVE SEARCH SCHEME

Theories that explain accommodation and its loss remain controversial⁵, and relate to how the zonular forces are exerted on the lens and how the lens surface curvatures change during accommodation^{34, 52, 53, 56}. Greater insights into the effect of the zonular angles, notably the directions of the zonular forces, on the accommodated state of the human lens are required. The present chapter investigates the correlations between zonular angles as well as their effects on the performance of FE lens models and presents the results of an *in silico* parametric study conducted on a range of different axisymmetric models. The correlations between a range of combinations of zonular angles, as well as the effect of these angles on the performance of lens models using different material properties are shown.

5.1 Model development

The basic design parameters used in the developed models were the following:

- (i) Age: two different cases were used, namely a 16-year-old lens and a 35-year-old lens.
- (ii) Capsular thickness: two different approaches were used, namely with uniform thickness and with varying thickness⁹.

(iii) Material properties: two different considerations were used, namely material properties according to Fisher⁶² and according to Wilde *et al.*⁶⁵

(iv) Angles of the zonular fibres: the domain for the anterior zonular angle θ_a , was between 10° and 30° towards the posterior of the eye (represented as $[10^\circ, 30^\circ]$); the domain for the equatorial zonular angle θ_e , was $[-14^\circ, 14^\circ]$ (the negative sign denoting the posterior direction and the positive sign denoting the anterior direction for θ_e only) and the domain for the posterior zonular angle θ_p , was $[24^\circ, 44^\circ]$ towards the anterior of the eye. In order to carry out a systematic investigation within the parameter space defined by these domains, a step size of 2 degrees was used for each zonular angle, giving a total of 1815 different zonular angle triplets per examined model.

The combination of the aforementioned design parameters yielded a total of eight different models. To these, the following two models were also examined. The rationale for the additional models was to examine the influence of the geometry from a 16-year-old and a 35-year-old lens for comparison with clinical data, which pertain to a 29-year-old *in vivo* lens undertaking up to 6 dioptres accommodative change as measured by Dubbelman *et al.*²⁷.

Additional model 1: Geometry from the 16-year-old lens in combination with material properties by Fisher⁶² and for the 35-year-old lens.

Additional model 2: Geometry from the 35-year-old lens in combination with material properties by Fisher⁶² and for the 16-year-old lens.

In total, ten different axisymmetric models were developed in ANSYS Mechanical version 16.0, using the intrinsic APDL programming language. The geometries were obtained from optical measurements by Bahrami *et al.*³⁷. Each model consisted of six parts, namely (i) the nucleus, (ii) the cortex, (iii) the capsule, (iv) an anterior zonular fibre, (v) an equatorial zonular fibre and (vi) a posterior zonular fibre. The lens nucleus and cortex were meshed using 8-node plane elements with the axisymmetric option enabled (ANSYS element type: PLANE 183), the capsule was modelled as a membrane and was meshed with 3-node axisymmetric shell elements (ANSYS element type: SHELL 209), the zonular fibres were treated with 2-node shell elements with the axisymmetric option enabled and the torsional capability disabled (ANSYS element type: SHELL 208). The total number of elements was 1131 and the total number of nodes was 5500 for all models. The capsular thickness was modelled either as being

uniform, equal to $13\mu\text{m}$ for the 16-year-old lens and $15\mu\text{m}$ for the 35-year-old lens¹¹⁹, or as being spatially varying with the corresponding values being retrieved from Barraquer *et al.*⁹ for comparable ages. The thickness profile of a 12-year-old lens⁹ was used for the 16-year-old lens model of the present chapter and the thickness profile of a 33-year-old lens⁹ was used for the 35-year-old lens model of the present chapter. Nonlinear geometrical analyses were conducted for all models.

5.2 Applied procedure: exhaustive search

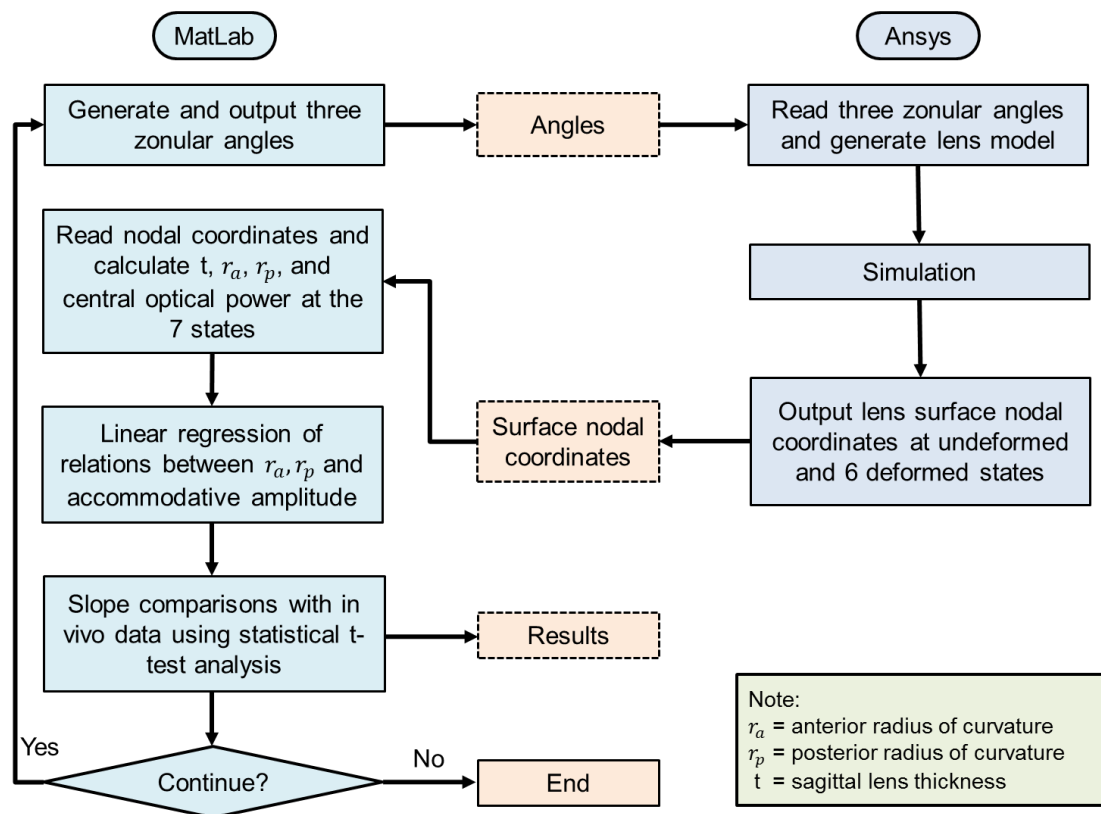


Figure 5.1 The flow diagram of the applied methodology.

The applied procedure is shown in Figure 5.1. In total, two codes were developed, one in MatLab (Ver.2015b) and one in ANSYS/Mechanical APDL (Ver.16). The MatLab code was firstly used to generate zonular angle triplets and call ANSYS, in batch mode, as an external solver for the respective Finite Element Analysis. The ANSYS program then read zonular angle triplets generated with the MatLab code and built the respective axisymmetric CAD model of the human lens, based on a predefined input file containing all the information for the lens geometry and all material properties. The ANSYS/APDL code was used to setup the FE model (i.e. define finite element types, material properties, boundary conditions), run the simulation and output results from the

FEA simulations. The MatLab code was then used to retrieve results from the FE analysis and calculate the necessary quantities for the comparison between the clinical²⁷ and the obtained numerical results as well as conduct a statistical t-test between the clinical²⁷ and the obtained numerical results. To this end, one cycle as shown in Figure 5.1 was completed and the MatLab code will enter the next cycle and generate a new zonular angle triplet. The whole simulation stops when all the 1815 triplets were simulated. For each simulation, the lens was adequately supported so that in-plane rigid body motions were restrained. Furthermore, a predefined displacement was imposed on the endpoint of each zonular fibre anchored at the ciliary body. More specifically, the orientation of the imposed displacement was defined by the respective zonular angle, while the magnitude of the displacement was 0.5mm for the equatorial zonular fibre and 0.6mm for both the anterior and the posterior zonular fibres. The aforementioned total displacements were introduced in six even sub-steps and applied to the lens model sequentially.

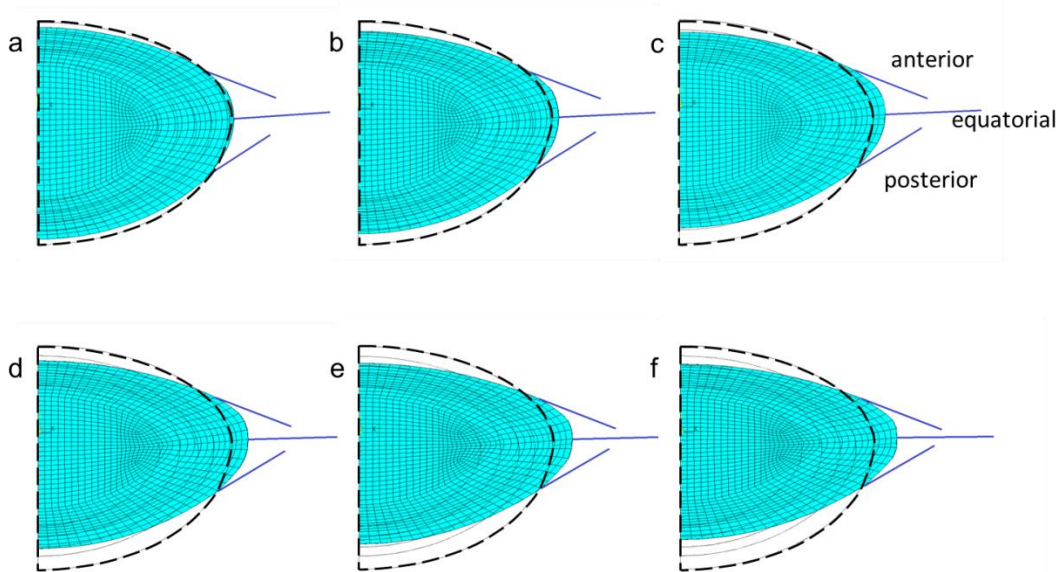


Figure 5.2 The 16-year-old lens model with -20 degree anterior, 4 degree equatorial and 34 degree posterior zonular angles at six deformed states (dashed line: undeformed shape).

Figure 5.2 shows a representative case with the deformed shapes from a set of six such sub-steps. Upon successful completion of each sub-step, four quantities were calculated as per¹⁵¹, namely (i) the radius of curvature of the lens anterior surface (r_a), (ii) the radius of curvature of the lens posterior surface (r_p), (iii) the sagittal thickness of the lens (t) and (iv) the Central Optical Power (COP) of the lens. These calculations were

based on nodal coordinates taken from the undeformed and deformed shapes of the lens anterior and posterior outer surfaces and within the lens central 3mm zone. The calculation of COP was based on equation 4.1.

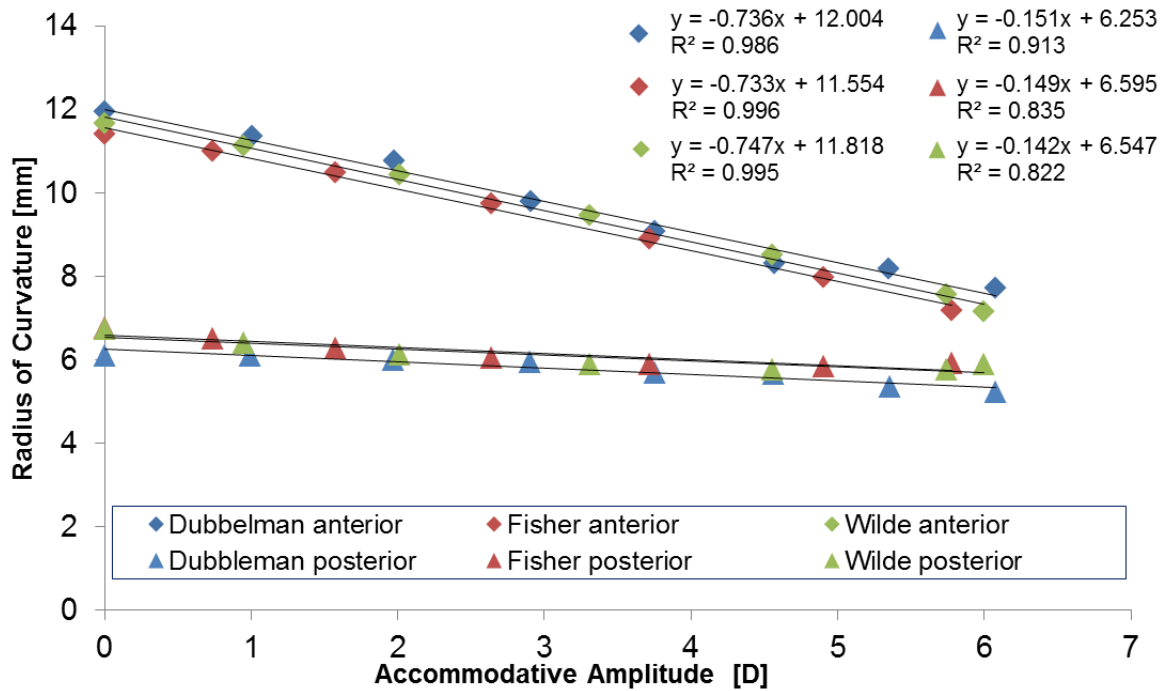


Figure 5.3 The optimum fittings provided by the 16-year-old lens model using both sets of material properties.

The slopes of the linear regression lines were then calculated depicting the relationships between the radius of curvature, for both anterior and posterior lens surfaces, and changes in COPs, namely the accommodative amplitude. The maximal deformed state (Figure 5.2f) is defined as the state with 0 dioptre of accommodation which is the accommodative demand for an eye focused on distant objects; the difference in COPs between other states and this 0 dioptre state represents the incremental change of the accommodative amplitude, corresponding to the horizontal axis shown in Figure 5.3. These slopes were compared to those from a 29-year-old *in vivo* lens which underwent up to 6 dioptres accommodative change as measured by Dubbelman *et al.*²⁷. To this end, the standard statistical t-test for comparing two slopes of independent samples were applied and two p-values per model were calculated (i.e. one p-value for the curvature of the anterior and one p-value for the curvature of the posterior part of the lens, respectively). If both p-values were greater than 0.05 then the corresponding triplet $[\theta_a, \theta_e, \theta_p]$ was considered as an acceptable combination of zonular angles because the *in silico* values obtained were found to be statistically similar to the clinical ones²⁷.

Otherwise this triplet was rejected as an unfeasible solution. The aforementioned procedure was repeated for all models and examined triplets, hence for 1815 combinations in total. The exhaustive search stops when the simulations of all the zonular angle triplets were finished.

5.3 Fits to clinical values

The relative contributions of θ_a , θ_e and θ_p on accommodation were investigated by fixing θ_e for eight different angles (-14° , -10° , -6° , -2° , 2° , 6° , 10° , 14°) and plotting contours of the p-values corresponding to θ_a , and θ_p , as shown in Figures 5.4 to 5.11. The magnitude of the p-value is indicated in the contour colours with the colour bar shown on the left hand side, the black border shows the given combination of angles.

5.3.1 Models with uniform capsular thickness

The p-value contours shown in Figure 5.4 and Figure 5.5, respectively, are for the 16-year-old and 35-year-old lens models with uniform capsular thickness using the material properties of Fisher⁶²; Figure 5.6 and Figure 5.7 show the counterparts of these models using material properties of Wilde *et al.*⁶⁵. For the 16-year-old lens (Figure 5.4 and Figure 5.6) using both sets of material properties, the p-values are displayed as contours with those that are close to 1 (contours shown in red), defining the best matches to *in vivo* data²⁷. For the anterior lens surface, these p-values lie in the regions: $\theta_a < 26^\circ$ and $\theta_p > 28^\circ$ when using the material properties of Fisher⁶²; $\theta_a < 26^\circ$ when using the material properties of Wilde *et al.*⁶⁵. For the posterior lens surface the regions are: $\theta_p > 18^\circ$ when using the material properties of Fisher⁶²; $26^\circ < \theta_p < 42^\circ$ when using the material properties of Wilde *et al.*⁶⁵. The optimal fitting range for both surfaces occurs when $\theta_a < 26^\circ$ and $\theta_p > 28^\circ$ using the material properties of Fisher⁶², $\theta_a < 26^\circ$ and $26^\circ < \theta_p < 42^\circ$ using the material properties of Wilde *et al.*⁶⁵. For the 16-year-old lens model with the material properties of Fisher⁶², the bands of p-values are relatively distinct and this is particularly so for the anterior surface. For both surfaces there is little change with varying θ_e indicating that for these models whatever angle is chosen for the equatorial zonular fibre makes very little difference to the outcome (Figure 5.4). There

is less distinction in the p-value range for the 16-year-old model using the material properties of Wilde *et al.*⁶⁵ and there is also more variation as θ_e is changed (Figure 5.6).

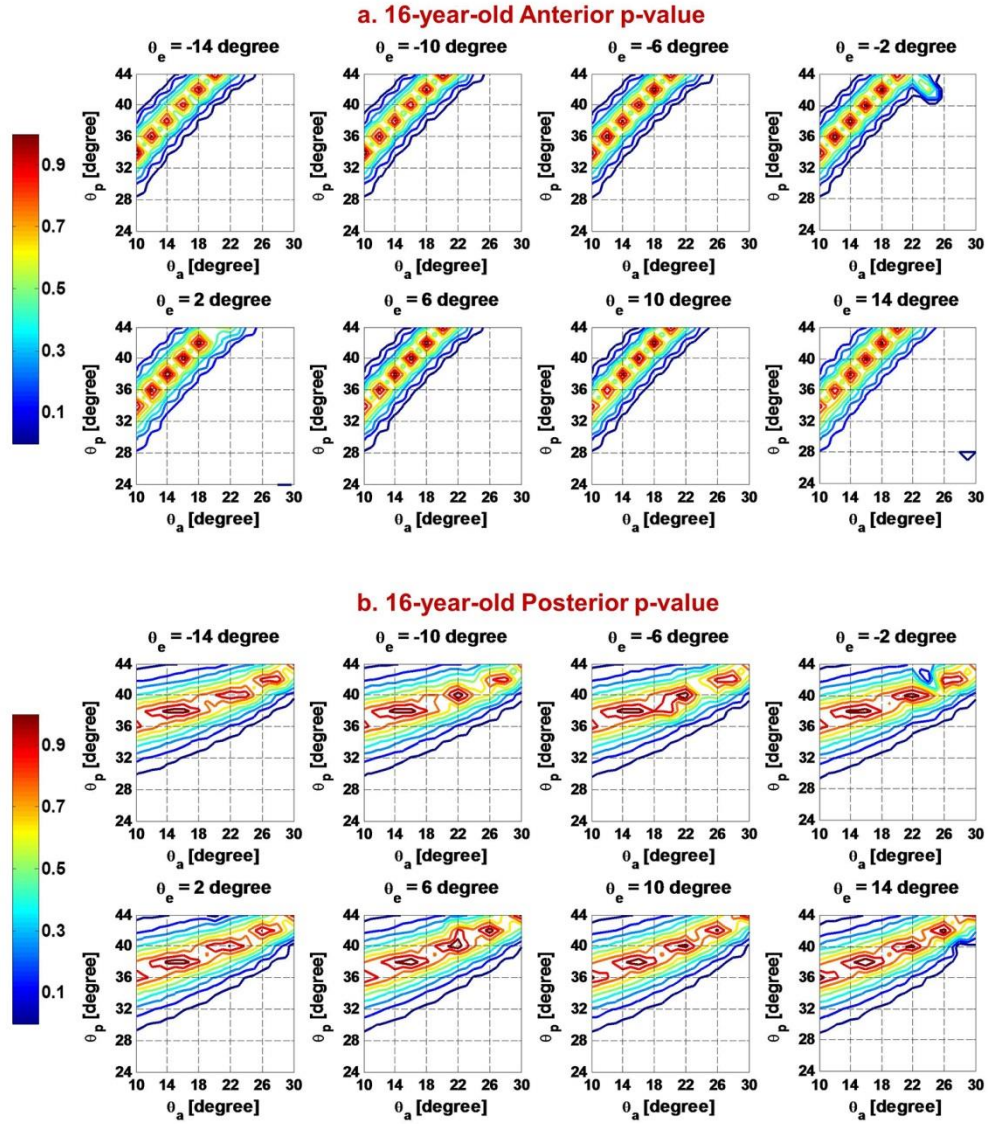


Figure 5.4 The p-value contours of (a) anterior lens surface and (b) posterior lens surface of the 16-year-old lens model with uniform capsular thickness using the material properties of Fisher⁶².

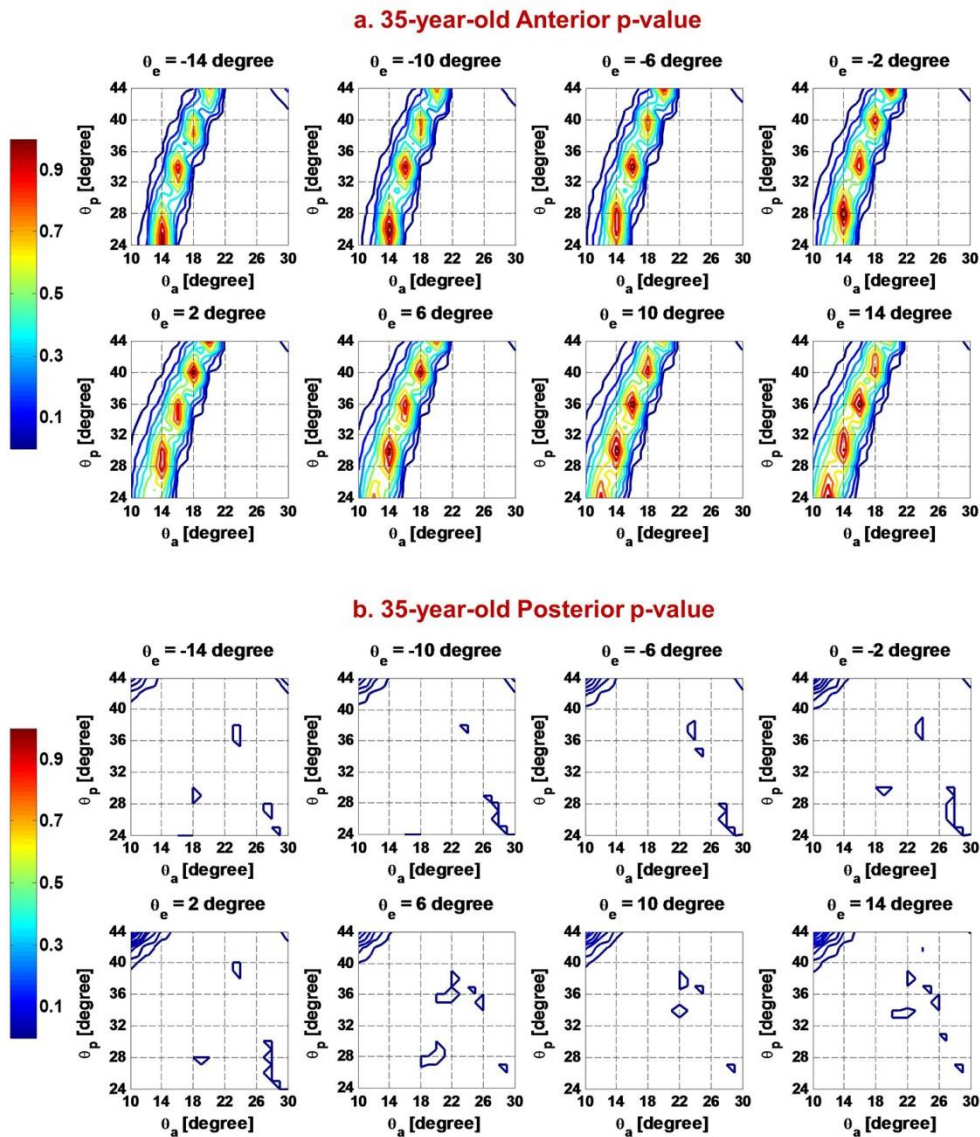


Figure 5.5 The p-value contours of (a) anterior lens surface and (b) posterior lens surface of the 35-year-old lens model with uniform capsular thickness using the material properties of Fisher⁶².

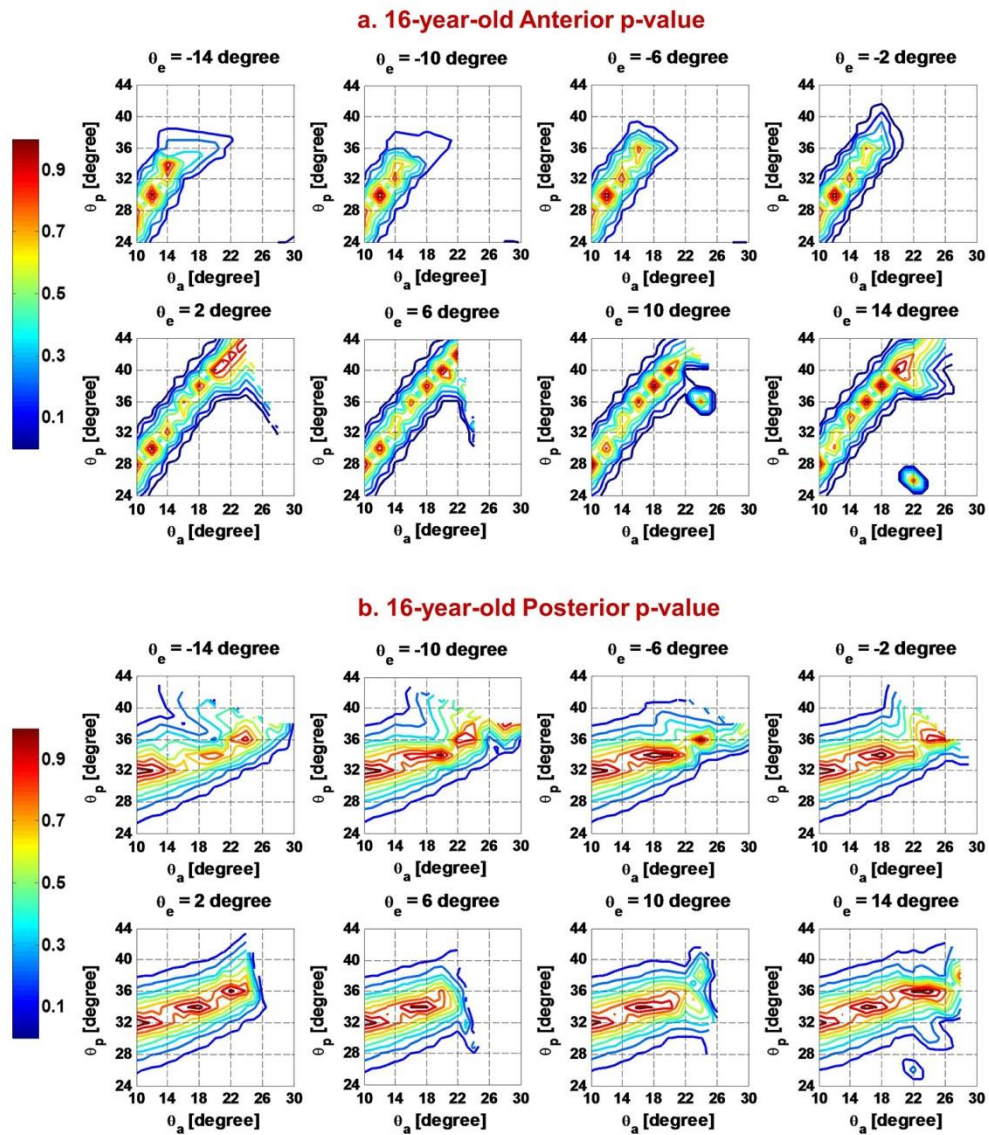


Figure 5.6 The p-value contours of (a) anterior lens surface and (b) posterior lens surface of the 16-year-old lens model with uniform capsular thickness using the material properties of Wilde *et al.*⁶⁵.

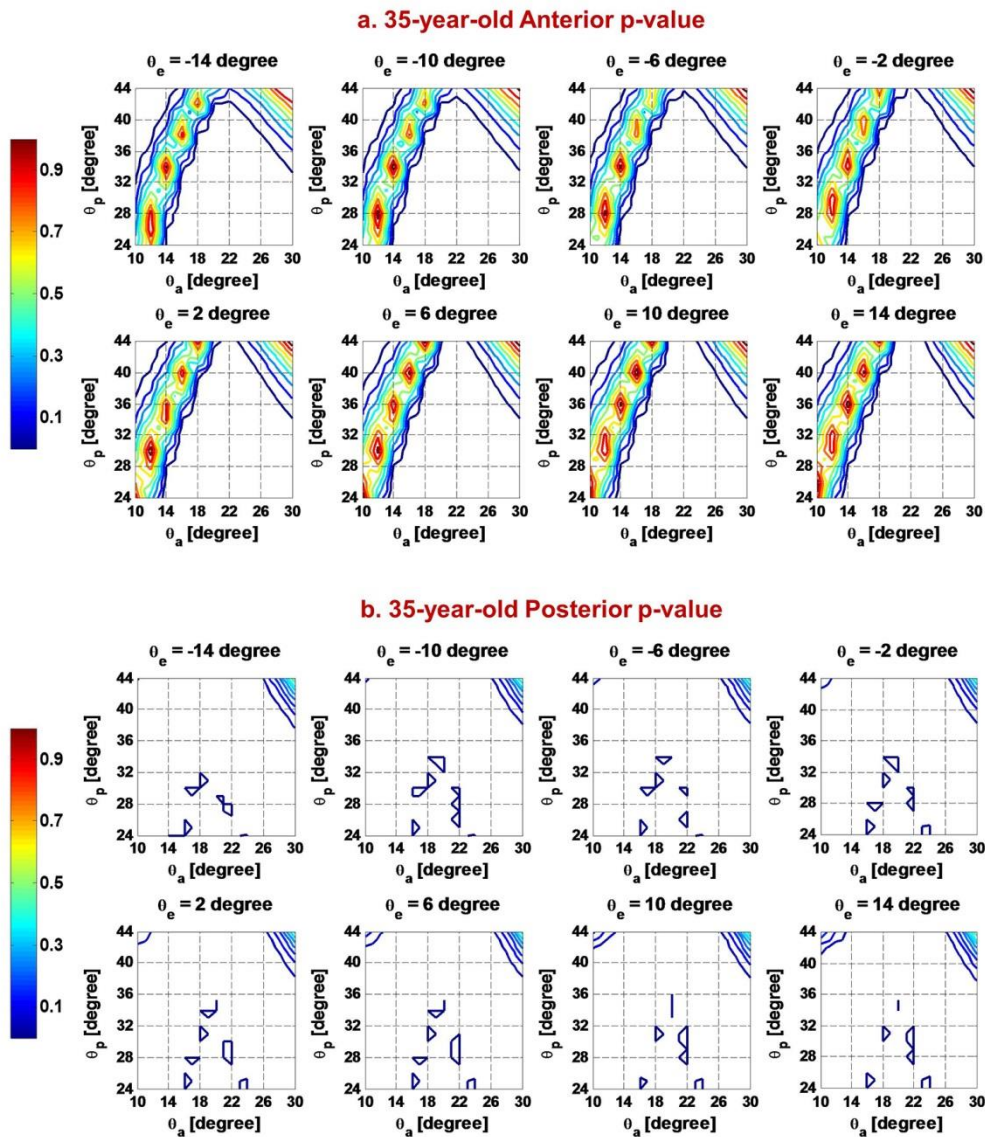


Figure 5.7 The p-value contours of (a) anterior lens surface and (b) posterior lens surface of the 35-year-old lens model with uniform capsular thickness using the material properties of Wilde *et al.*⁶⁵.

For the 35-year-old model, the anterior lens surface demonstrates a substantially improved fit to *in vivo* data²⁷ than the posterior surface with the maximal p-value for the

anterior surface almost ten times greater than its counterpart for the posterior surface. For this age, no angle combination within the tested ranges could be found to fit both surfaces using either set of material properties, and this is evidenced by the lack of overlapping contour regions in Figures 5.5a and b, or Figures 5.7a and b.

The range of p-values for comparison of the 35-year-old lens model using the material properties of Fisher⁶² to *in vivo* data²⁷ are shown in Figure 5.5. The contours are slightly less crisp for the anterior surface of the 35-year-old model (Figure 5.5a) than those seen for the anterior surface for the 16-year-old model (Figure 5.4a) with the material properties of Fisher⁶² but are nevertheless relatively well defined and again there is little variation with changing θ_e . Good fits to *in vivo* data²⁷ for the anterior lens surface only occur when $\theta_a < 22^\circ$. There are no clear bands of p-values for the posterior surface of this model (Figure 5.5b). The posterior p-value contours are only seen in dark blue (the lower range of p-values) and are mainly concentrated where $\theta_p > 38^\circ$ and $\theta_a < 16^\circ$. This applies to all θ_e tested. The 35-year-old model with material properties measured by Wilde *et al.*⁶⁵ (Figure 5.7) is similar for the anterior surface (Figure 5.7a) of the 35-year-old model constructed using the material properties of Fisher⁶² (Figure 5.5a) with some additional bands of p-values seen for higher θ_a and θ_p . Negligible difference in the results was found with varying θ_e . Good fits to *in vivo* data for the anterior lens surface occur when $\theta_a < 22^\circ$ or $\theta_a > 22^\circ$ and $\theta_p > 32^\circ$. For the posterior surface of this model (Figure 5.7b) there are a few distinct p-values, concentrated in the top right-hand corner where $\theta_p > 38^\circ$ and $\theta_a > 26^\circ$, as seen with the counterpart model constructed using the material properties of Fisher⁶² (Figure 5.5b).

5.3.2 Models with spatially varying capsular thickness

The corresponding models using varying capsular thicknesses are shown in Figures 5.8 to Figure 5.11. For both age models with the material properties of Fisher⁶² and the 35-year-old model using the material properties of Wilde *et al.*⁶⁵ the patterns of p-values are very similar to the respective models with uniform capsular thickness. The exception to this is the 16-year-old model with the material properties of Wilde *et al.*⁶⁵ for which, in the varying capsule model (Figure 5.10) there are more defined p-value bands that span a greater range of θ_a and θ_p particularly for the anterior surface (Figure 5.10a) than for the corresponding model with uniform capsular thickness (Figure 5.6a).

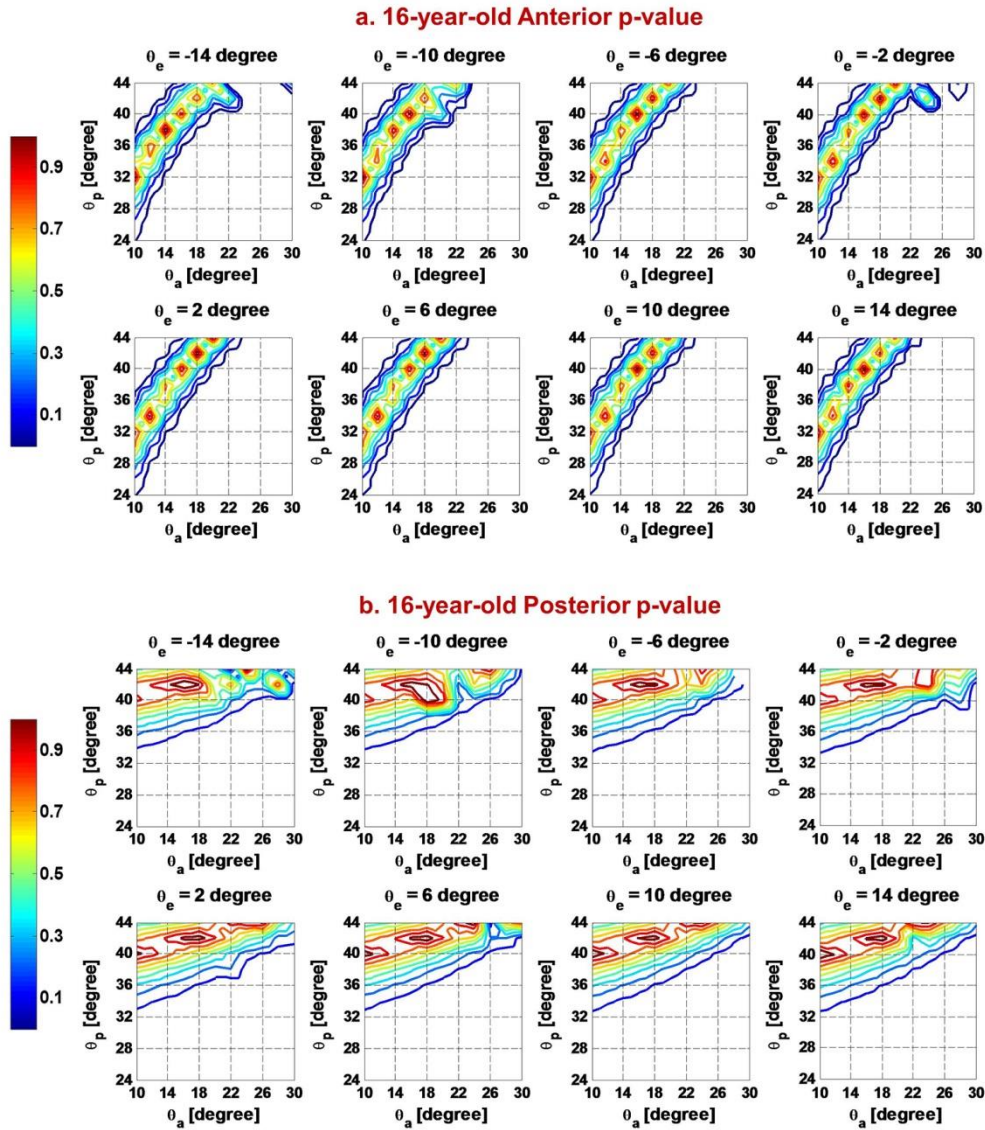


Figure 5.8 The p-value contours of (a) anterior lens surface and (b) posterior lens surface of the 16-year-old lens model with spatially varying capsular thickness using the material properties of Fisher⁶².

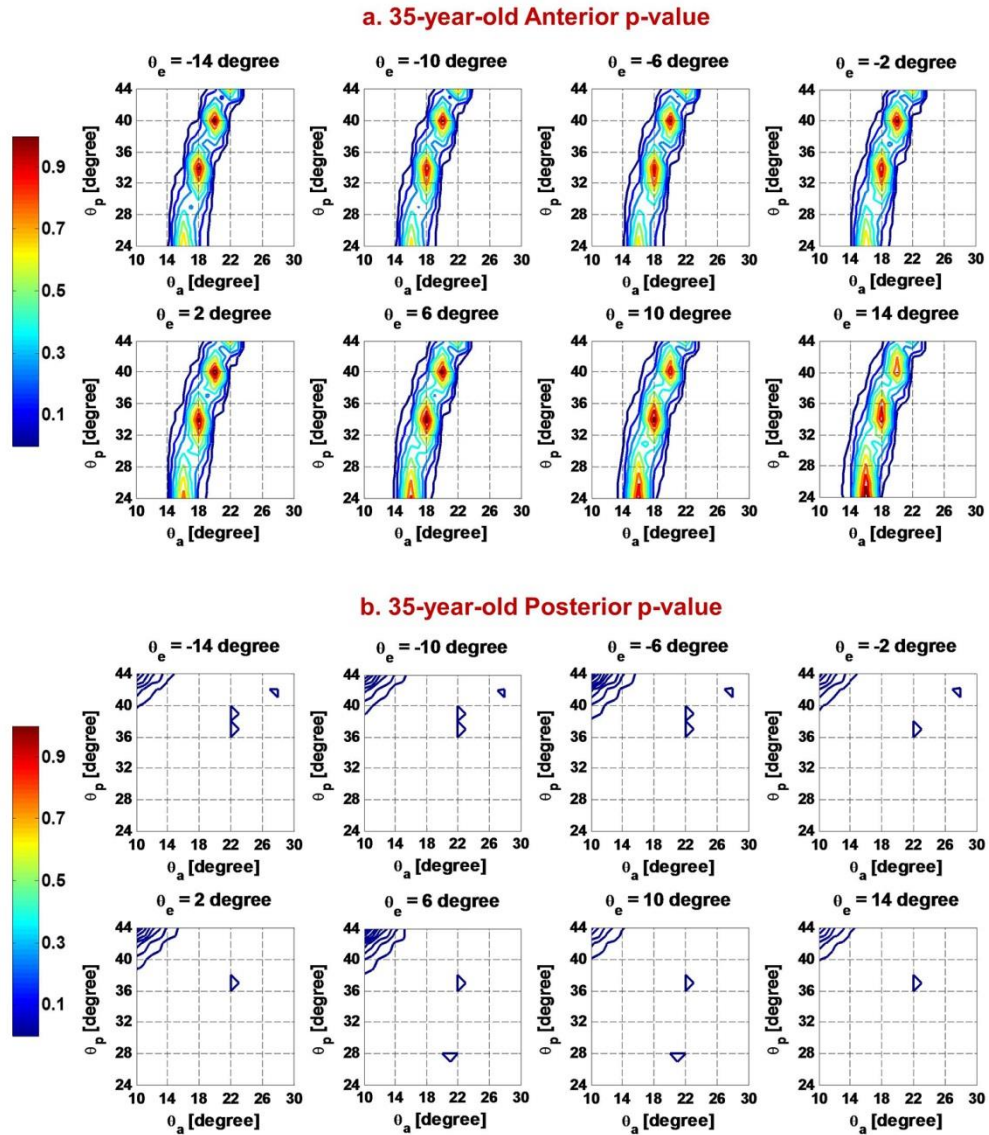


Figure 5.9 The p-value contours of (a) anterior lens surface and (b) posterior lens surface of the 35-year-old lens model with spatially varying capsular thickness using the material properties of Fisher⁶².

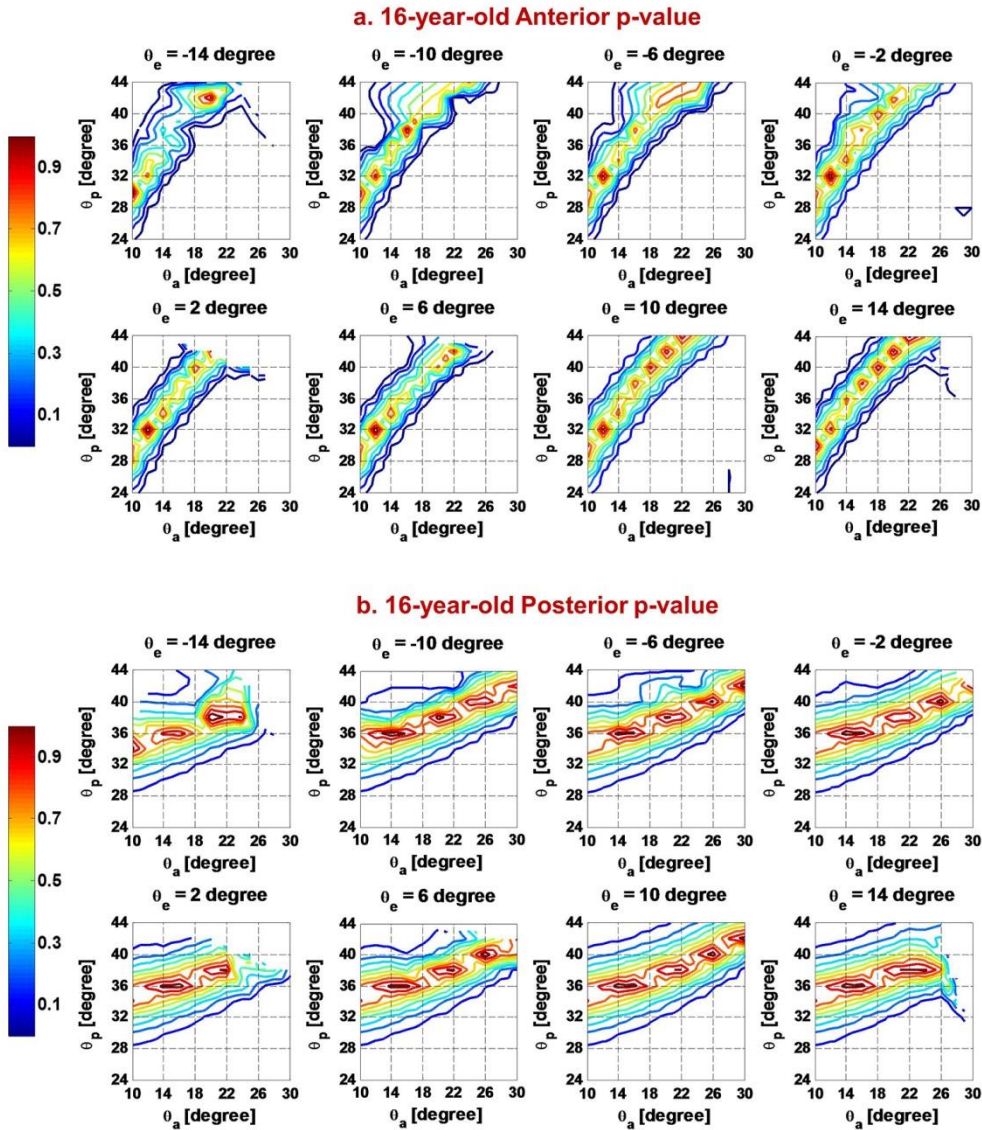


Figure 5.10 The p-value contours of (a) anterior lens surface and (b) posterior lens surface of the 16-year-old lens model with spatially varying capsular thickness using the material properties of Wilde *et al.*⁶⁵.

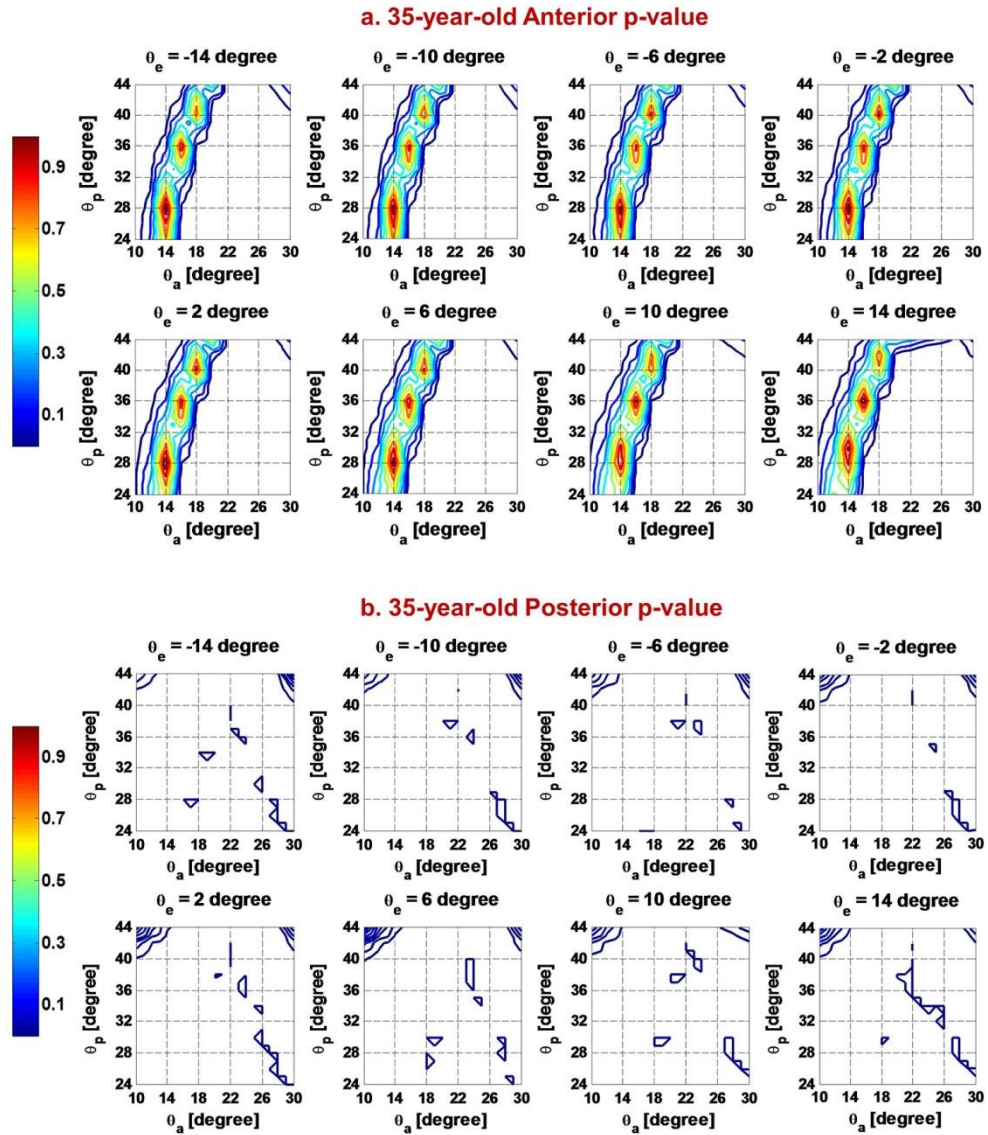


Figure 5.11 The p-value contours of (a) anterior lens surface and (b) posterior lens surface of the 35-year-old lens model with spatially varying capsular thickness using the material properties of Wilde *et al.*⁶⁵.

5.3.3 Zonular angle triplets providing the optimal fits

The zonular angle triplets providing the optimal fits for both anterior and posterior surfaces for models using both the material properties of Fisher⁶² and Wilde *et al.*⁶⁵ are listed in Table 5.1. These only refer to 16-year-old models as no 35-year-old model with adequate fits to *in vivo* data²⁷ of the posterior surface could be found. Apart from the case with the varying capsular thickness using the material properties of Fisher⁶² θ_a being 18 degrees, in the remaining three cases, the θ_a values are all equal to 14 degrees. There is less consistency for θ_p , which varies between 34 to 42 degrees. Both anterior and posterior p-values are higher when using the material properties of Fisher⁶² than when using the material properties of Wilde *et al.*⁶⁵ but the accommodative amplitudes are similar. As can be seen in Figure 5.3, the changes of radii of curvature against the accommodative amplitudes were plotted for the 16-year-old models using both the material properties of Fisher⁶² and of Wilde *et al.*⁶⁵. Both the anterior and posterior surfaces fit well to the *in vivo* measured slopes.

Table 5.1 Zonular angle triplets resulting in the optimal fittings to *in vivo* data²⁷ for 16 year old geometries and material properties.

		$[\theta_a, \theta_e, \theta_p]$	Anterior p-value	Posterior p-value	Accommodative Amplitude (D)
Fisher ⁶²	16yo model uniform capsule	14°, -6°, 38°	0.942	0.939	5.8
	16yo model varying capsule	18°, 6°, 42°	0.962	0.956	5.9
Wilde <i>et al.</i> ⁶⁵	35yo model uniform capsule	14°, 14°, 34°	0.810	0.801	6.0
	35yo model varying capsule	14°, 14°, 36°	0.730	0.937	6.0

Table 5.2 The anterior and posterior zonular angles that provide the top three highest accommodative amplitudes for each model.

	$[\theta_a, \theta_p]$	16yo model uniform capsule (D)	16yo model varying capsule (D)	35yo model uniform capsule (D)	35yo model varying capsule (D)
Fisher ⁶²	(10°, 24°)	8.7	10.6	5.8	7.2
	(12°, 24°)	8.5	10.3	5.6	7.0
	(10°, 26°)	8.4	10.2	5.5	6.9
Wilde <i>et al.</i> ⁶⁵	(10°, 24°)	8.8	9.6	5.1	6.3
	(12°, 24°)	8.5	9.2	4.9	6.1
	(10°, 26°)	8.3	9.1	4.8	6.0

The accommodative amplitude was calculated for all tested zonular angle triplets for both models of different ages with both configurations of capsular thickness using both sets of material properties. The top three highest accommodative amplitudes, among all 1815 tested zonular angle triplets, are the same for each model (listed in Table 5.2). For each combination of θ_e and θ_p the resultant accommodative amplitudes are the same for all tested θ_e within the tested range of [-14, 14] hence θ_e was not listed in Table 5.2. Varying capsular thickness models produce 0.7-1.9 dioptres of accommodative amplitudes that are higher than uniform capsular thickness models; 16-year-old lens models produce 2.9-3.7 dioptres more accommodative amplitude than 35-year-old lens models. The zonular angle triplets (Table 5.2) demonstrating the highest accommodative amplitudes are different from those (Table 5.1) providing the optimal fittings to *in vivo* lens²⁷.

5.3.4 Models with mixed geometry and material properties

The model combining the geometry of the 16-year-old lens with the material properties of the 35-year-old lens shows a better fit to *in vivo* lens²⁷ (Figure 5.12) than the two mixed models and demonstrates similar p-value contours to the original 16-year-old lens model (Figure 5.4) as both lens surfaces fit well to *in vivo* data. The model incorporating the geometry of the 35-year-old lens with the material properties of the 16-year-old lens demonstrates p-value contours (Figure 5.13) similar to those produced by the original 35-year-old lens model (Figure 5.5) and only the anterior lens surface fits well to *in vivo* data.

The zonular angle triplets providing the optimal fitting of the former model are with a 16 degree anterior zonular angle, -10 degrees equatorial zonular angle and 42 degrees posterior zonular angle, which result in p-values of 0.892 and 0.873 for the anterior and posterior surfaces respectively. The accommodative amplitude produced by this model of 5.9 dioptres is of a similar magnitude to those listed in Table 5.1.

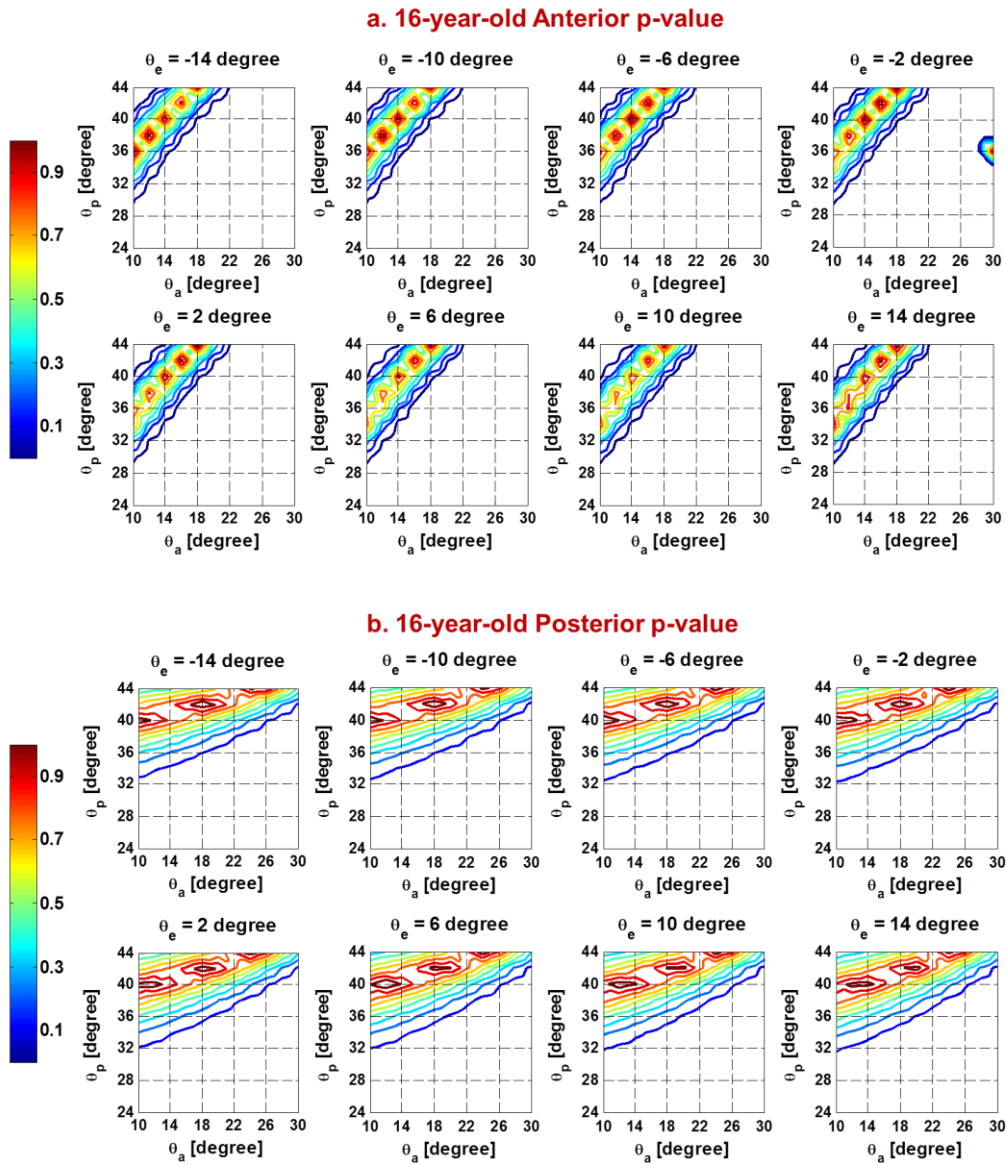


Figure 5.12 The p-value contours of (a) anterior lens surface and (b) posterior lens surface of the model with uniform capsular thickness mixing the 16-year-old geometry and 35-year-old material properties of Fisher⁶².

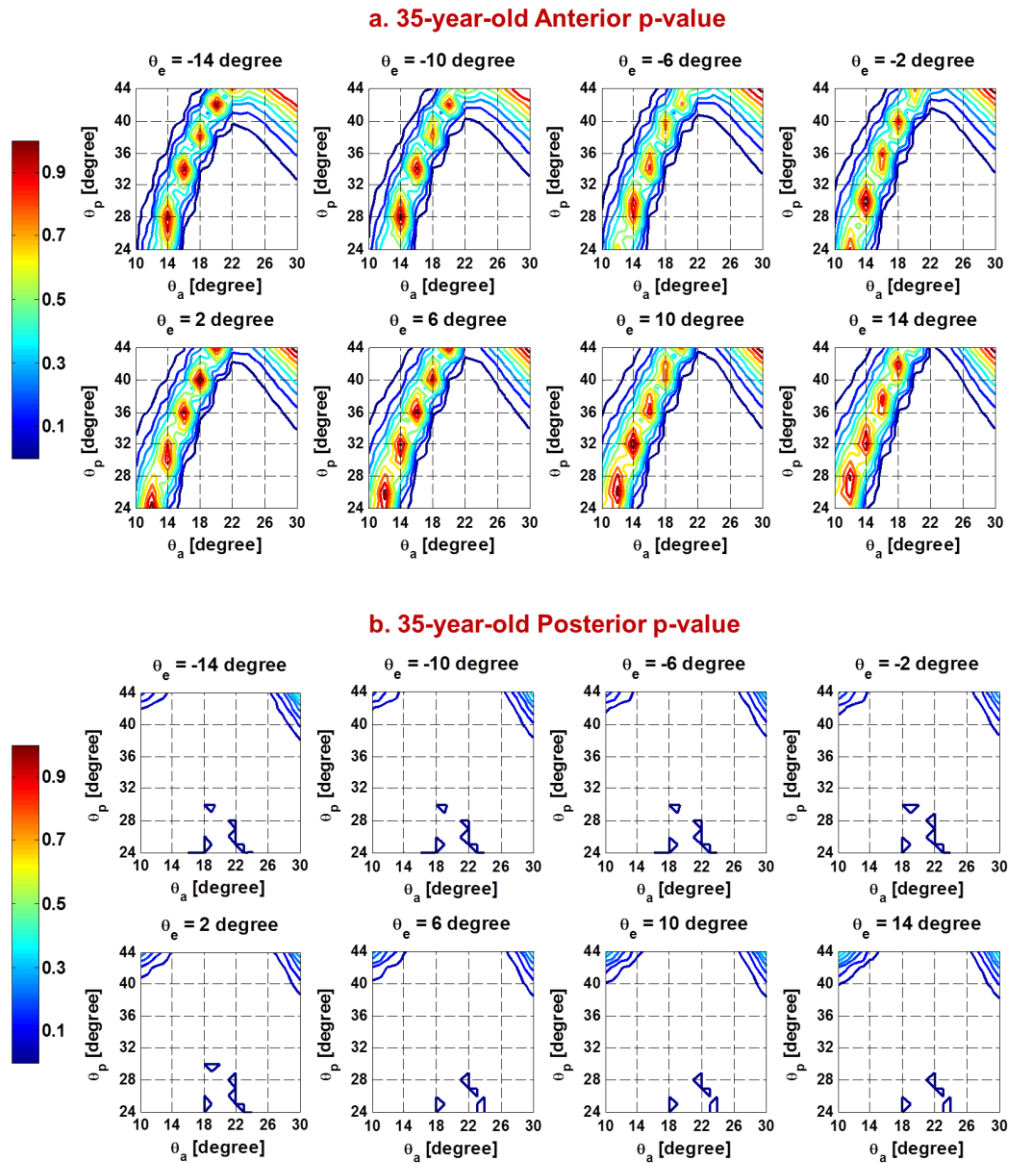


Figure 5.13 The p-value contours of (a) anterior lens surface and (b) posterior lens surface of the model with uniform capsular thickness mixing the 35-year-old geometry and 16-year-old material properties of Fisher⁶².

5.4 Optical Performances

The accommodative amplitudes, of all the tested zonular angle triplets were calculated and the values are plotted in Figures 5.14-5.17 at eight selected θ_e for both models of different ages using both sets of materials. The magnitude of the accommodative amplitude for each dot (zonular angle triplet) is indicated using colours with the colour bar shown on the right side. The missing dots in Figures 5.14, 5.16 and 5.17 correspond to zonular angle triplets for which numerical correlations, between zonular angles and the lens geometry, could not be found during the exhaustive search.

For all the models, from the top right corner all the way down to the bottom left corner, the colour becomes warmer and the value of accommodative amplitude increases. In all models, the general distributions of the colours are the same for all selected θ_e . The zonular angle triplet producing the maximal accommodative amplitude for all models is with 10 degrees θ_a and 24 degrees θ_p , corresponding to the dot located at the bottom left corner of each graph. This zonular angle triplet is different from those demonstrating optimal fits with the *in vivo* lens (Table 5.1). The histograms indicating the distributions of accommodative amplitude produced from all the tested zonular angle triplets for each model are plotted in Figure 5.18.

In Figure 5.14 to Figure 5.17, the model with uniform capsular thickness and the model with varying capsular thickness are compared. Varying capsular thickness models demonstrate warmer colours (Figures 5.14-5.17) and produces accommodative amplitudes 1 to 2 dioptres higher than uniform capsular thickness models (Figure 5.18), for both ages using both sets of materials. The plots of the 16-year-old lens models are mostly in red and yellow (Figures 5.14 and 5.16) indicating higher accommodative amplitudes than those of the 35-year-old lens models the scatter plots of which are mostly seen in green and blue (Figures 5.15 and 5.17). The highest accommodative amplitude provided by the 16-year-old uniform capsular thickness model is 8 dioptres and by 35-year-old uniform capsular thickness model is 5 dioptres using both sets materials (Figure 5.18). For varying capsular thickness models this value is 10 and 9 dioptres respectively using the material properties of Fisher⁶² and Wilde *et al.*⁶⁵ for the 16-year-old lens, and 7 and 6 dioptres for the 35-year-old lens (Figure 5.18).

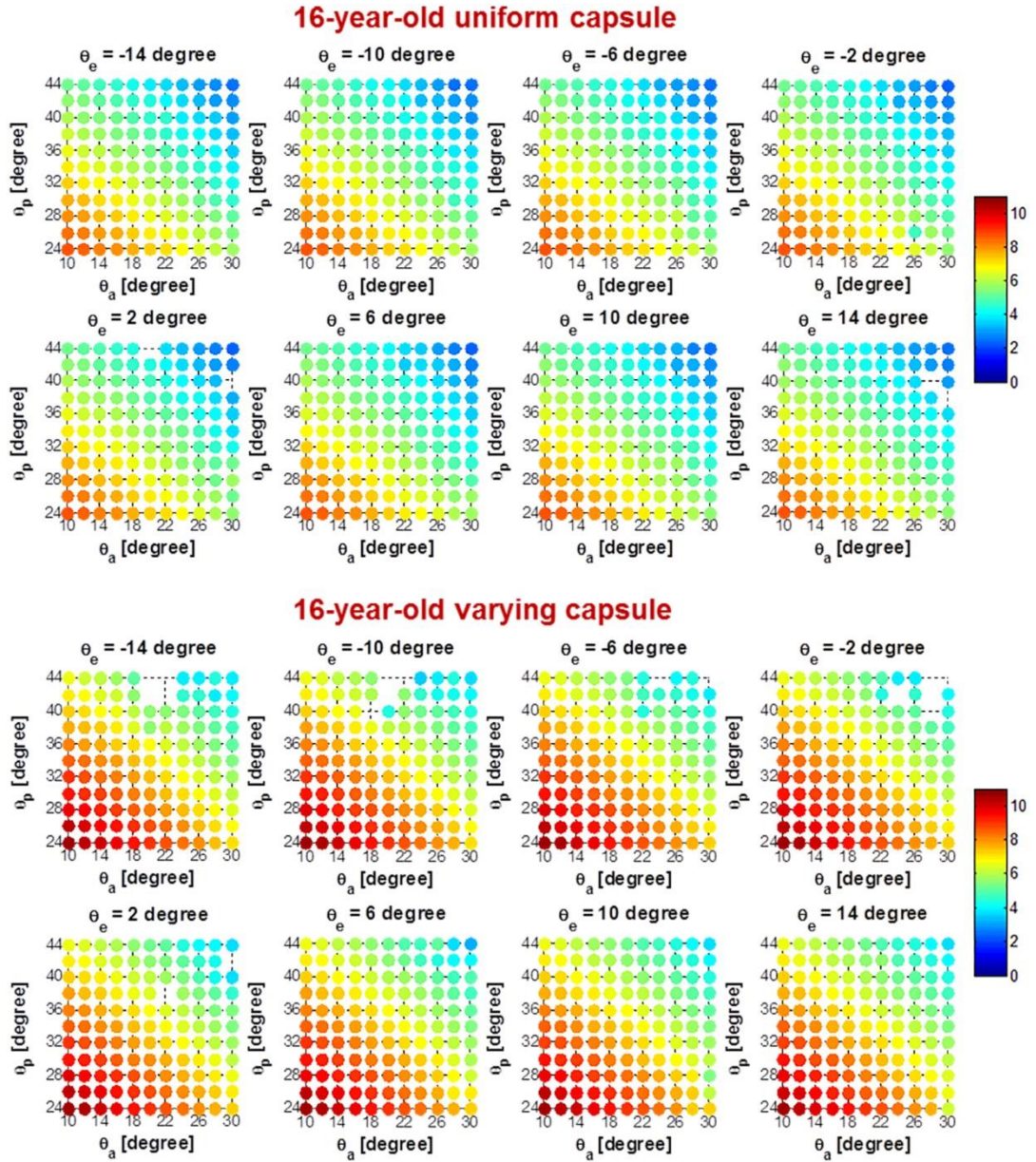


Figure 5.14 Scatter plots of Accommodative Amplitude provided by the 16-year-old model using the material properties of Fisher⁶².

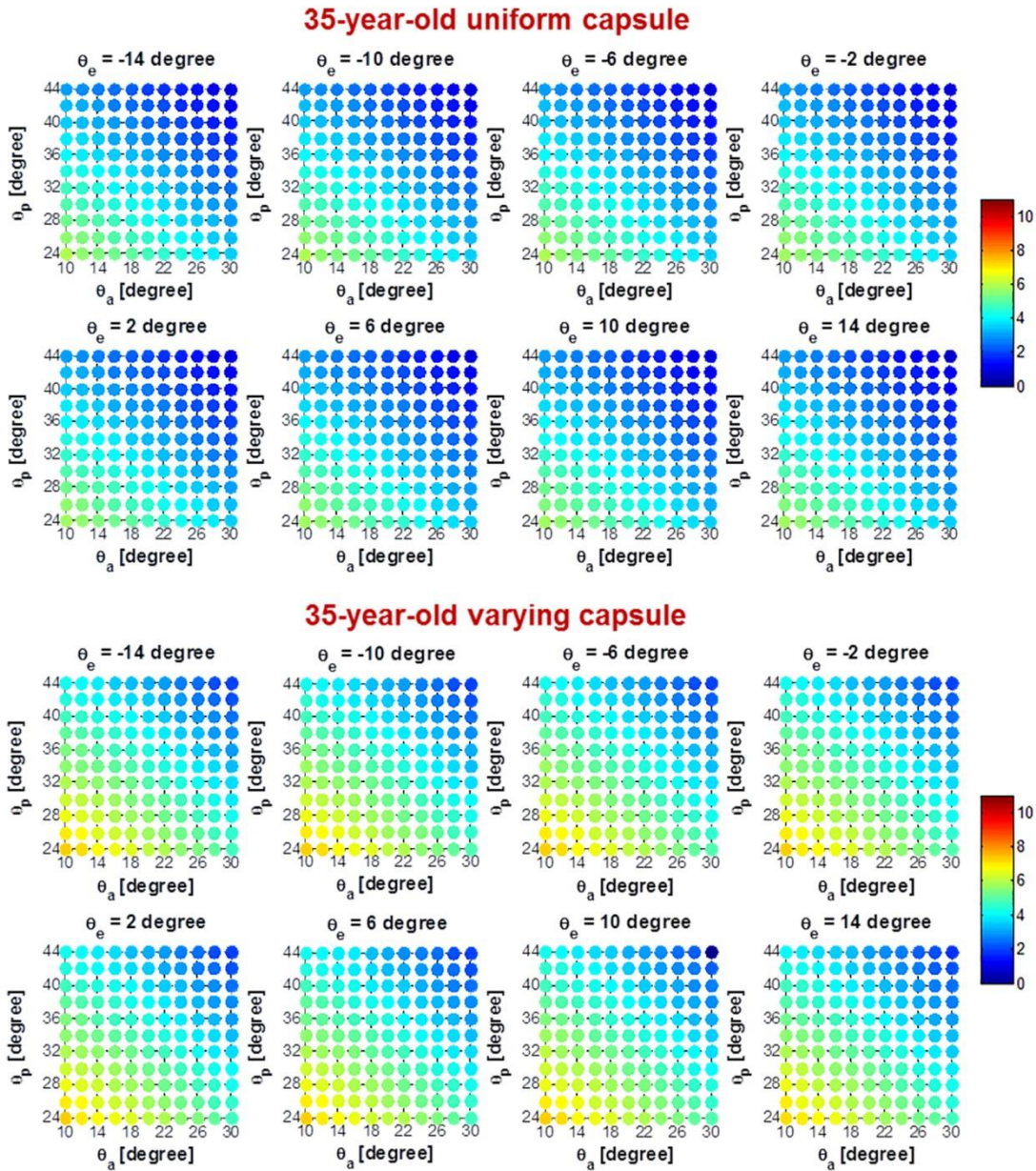


Figure 5.15 Scatter plots of Accommodative Amplitude provided by the 35-year-old model using the material properties of Fisher⁶².

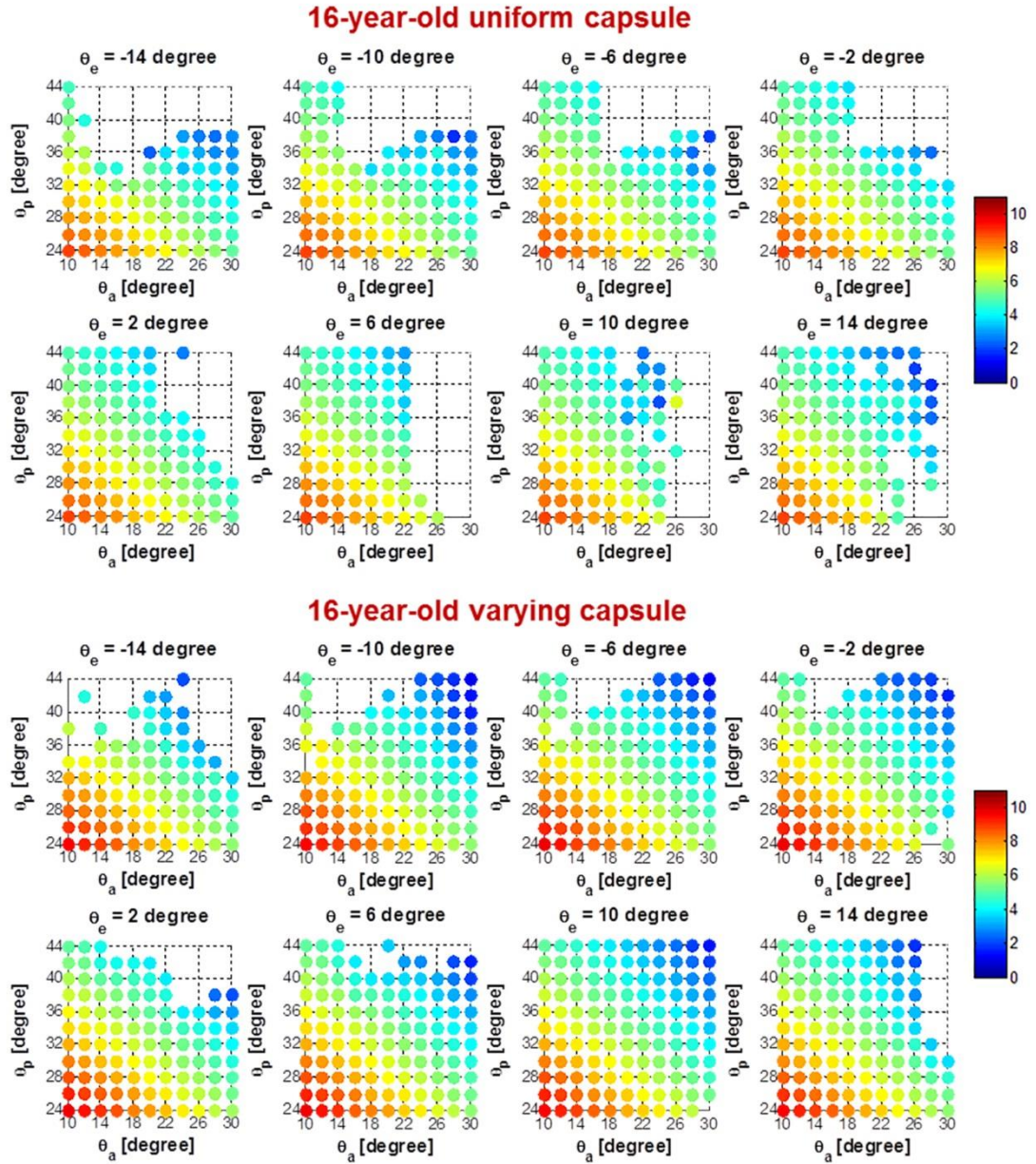


Figure 5.16 Scatter plots of Accommodative Amplitude provided by the 16-year-old model using the material properties of Wilde *et al.*⁶⁵.

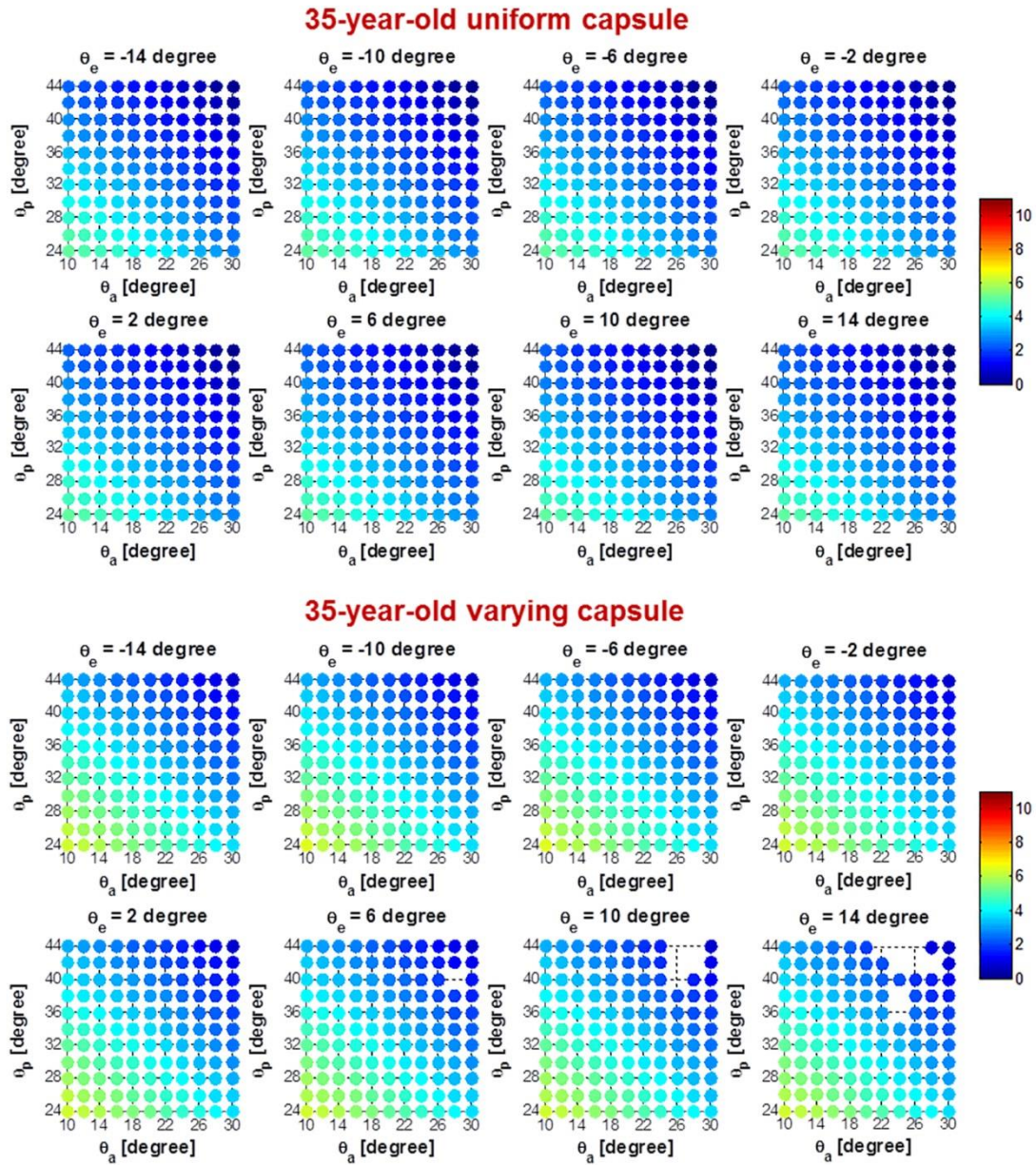


Figure 5.17 Scatter plots of Accommodative Amplitude provided by the 35-year-old model using the material properties of Wilde *et al.*⁶⁵.

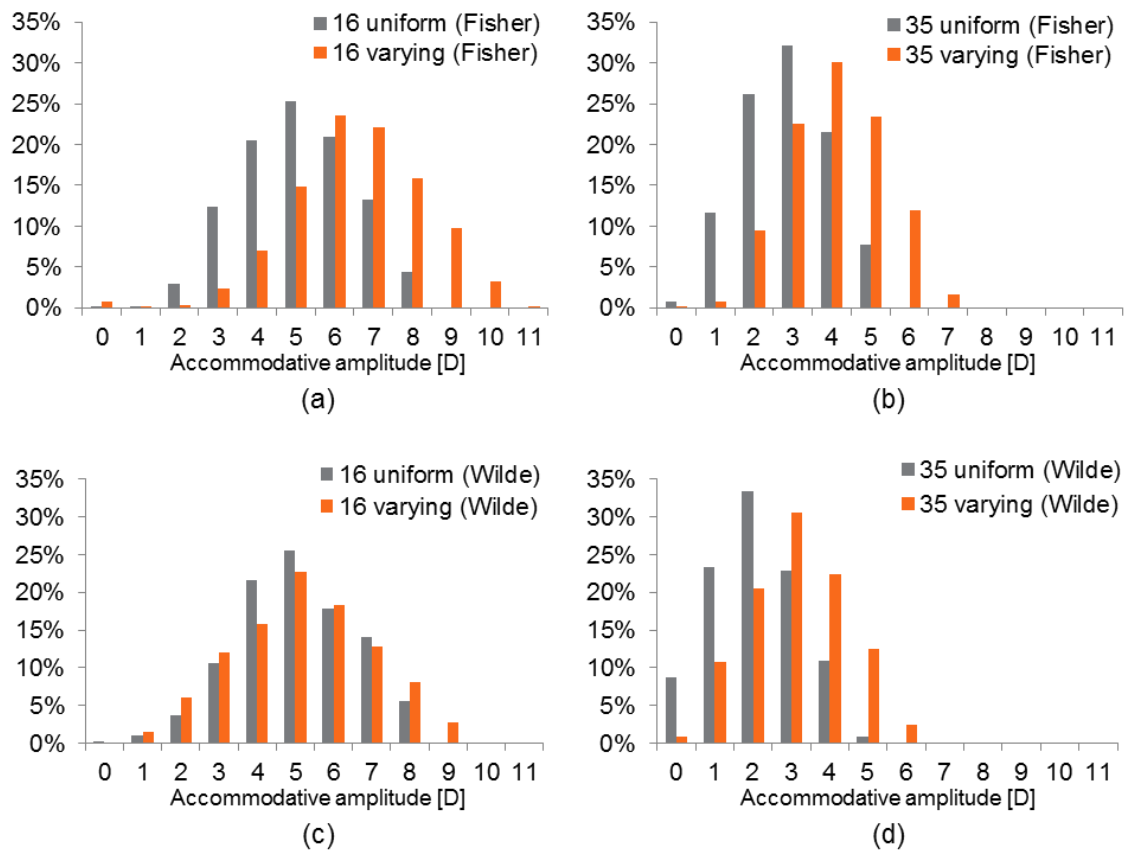


Figure 5.18 Histograms of accommodative amplitude compared between the uniform capsular thickness model and the spatially varying capsular thickness model for (a) 16-year-old lens and (b) 35-year-old lens using the material properties of Fisher⁶², (c) 16-year-old lens and (d) 35-year-old lens using the material properties of Wilde *et al.*⁶⁵.

5.5 Changes in radius of curvature

For the 16-year-old lens model using the values of Wilde *et al.*⁶⁵ and the 35-year-old lens models using both sets of values, the increase in the central radius of curvature with stretching was not observed for all of the simulated zonular angle triplets. Figure 5.19 shows changes in the radii of curvature of the anterior and posterior lens surfaces and in COP with progressive increments of simulated stretching for the 16 and 35 year old models using the two sets of material properties^{62, 65} and a uniform capsular thickness. In Figure 5.19a representing the 16-year-old lens with the material properties of Fisher⁶², the COP decreases steadily as r_a increases with very little change in r_p . For the 16-year-old lens model using the material properties of Wilde *et al.*⁶⁵ (Figure 5.19b) and the 35-year-old lens models using both sets of material properties (Figures 5.19c, d), the increase in r_a is not immediate with the first stretching increment but rather showing a

slight decrease followed by an increase but along a shallower slope than is seen in Figure 5.19a; the COP behaves in a reciprocal way (Figures 5.19b, c and d). There is a greater rate of increase with stretching in r_p for these models (Figures 5.19b, c and d) than for that seen in Figure 5.19a.

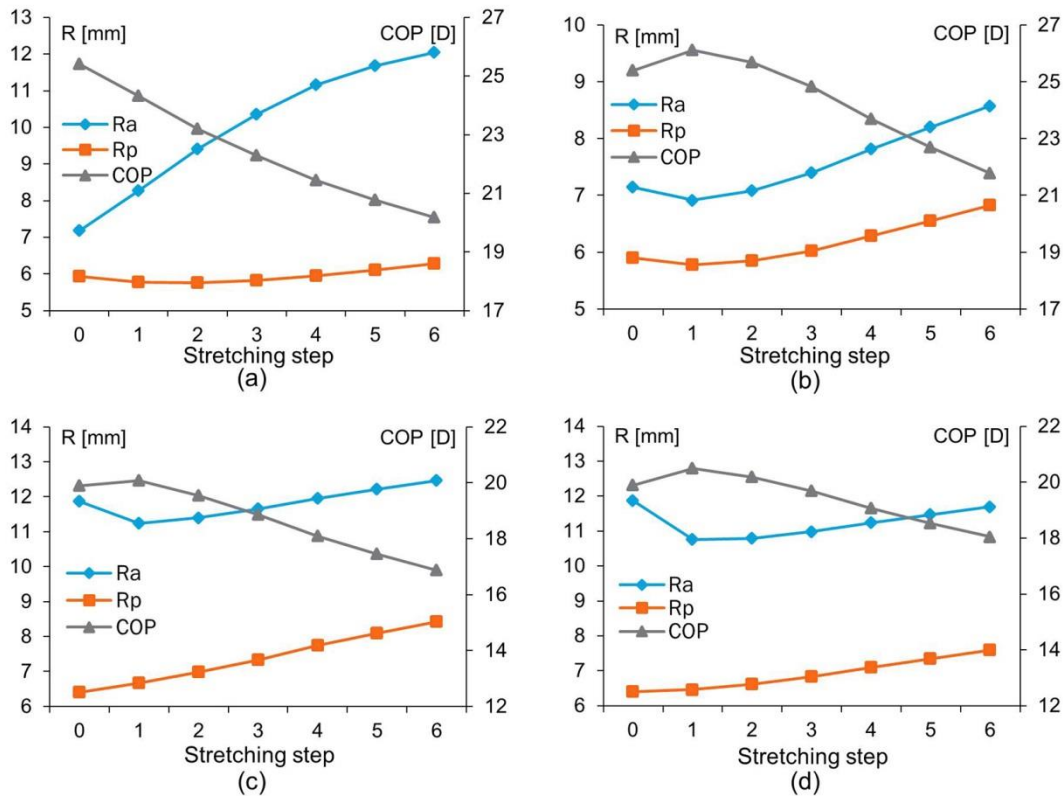


Figure 5.19 The changes in radii of curvature (R) in mm and Central Optical Power (COP) in dioptries (D) for progressive stretching steps of the 16-year-old lens model using the material properties of (a) Fisher⁶² and of (b) Wilde *et al.*⁶⁵ and of the 35-year-old lens model using the material properties of (c) Fisher⁶² and of (d) Wilde *et al.*⁶⁵.

5.6 Discussion and conclusion

5.6.1 The geometry and material properties of the lens models

The results in the present study indicate the integral importance of the zonular angles, especially those of the anterior and posterior sections, on lens shape changes as the quality of the fits to clinical data vary greatly with different zonular angle triplets (Figure 5.4 to Figure 5.11). The values of the anterior and posterior zonular angles both have specific regions within which good fits were found (Figures 5.4 to Figure 5.11). The optical performance of the lens models are also affected by the zonular angles and

the values of the accommodative amplitude vary with different zonular angle triplets (Figure 5.14 to Figure 5.17). The same zonular angle triplets were found to provide the top three highest accommodative amplitudes for all the models irrespective of age, material properties or capsular thickness (Table 5.2).

The clinical measurement was conducted on an *in vivo* human lens aged 29 years²⁷ which is an age comparable with regard to accommodative amplitude to the 35-year-old model. This model, however, only fitted well with the *in vivo* lens for the anterior lens surface. The 16-year-old lens model provided good fits to the *in vivo* lens for both the anterior and posterior surfaces. The models described in this study were based on geometries measured on *post-mortem* lenses freed from zonular attachments³⁷ which differ from the state of the lens *in vivo*. Given the breath of individual variations that can mask ageing trends^{12, 15}, in addition to differences between the *in vivo* lens and the *in vitro* lens, the modelling is not aimed to be specifically associated with age. When considering the fit of both surfaces simultaneously, however, only the 16-year-old lens model provided both p-values above the significance level for certain zonular angle triplets (Figure 5.4 and Figure 5.6). The results from the two mixed models demonstrated that the geometry has a predominant effect compared with the material properties. The model with the geometry of the younger (16 years old) lens provided a better fits than the model with the geometry of the older lens (35 years old), which conceded to a previous modelling study¹⁴⁴.

5.6.2 The influence of zonular angles

Models offer a perspective that is not currently possible from *in vivo* studies and this is particularly pertinent with respect to the zonule. The zonular fibres are crucial for determining the lens shape changes during accommodation¹⁵⁵. The current theories of accommodation have differing explanations for how the zonular fibres alter lens shape^{52, 56, 57}. It is not possible to visualize the *in vivo* behaviour of zonular fibres using biomicroscopy as the equatorial region is blocked by the iris. *In vitro* studies rely on an intact lens but it remains uncertain whether stretching such lenses is a close simulation of what happens in the living eye^{25, 147, 156, 157}.

Anatomical studies using scanning electron microscopy have revealed that the majority of the anterior and posterior zonular fibres originate from the pars plana of the ciliary body and link forward to the posterior pars plicata where they are fixed to the walls and

valleys of the ciliary process through small strands of fibre bundles⁴⁴. From there they split into two strands connecting respectively to the anterior and posterior lens capsule^{44, 158}. The equatorial fibres, which mainly originate from the pars plicata, are sparse and poorly developed compared with the anterior and posterior fibres¹⁵⁵. The angles of the anterior and posterior zonular sections that exert tension on the lens are controlled by the morphology of the ciliary body and their relative location to the lens equator. The increase in lens dimensions^{16, 18, 19}, the decrease in the inner ciliary body diameter^{6, 156} as well as the anterior movement of the zonular insertions⁴⁸ with age could all contribute to a shift in zonular angles. This results in zonular forces becoming more tangential to the lens surface with age and therefore less able to exert tension on the lens capsule^{72, 77}.

The models show ranges of anterior and posterior zonular angles for which good fits to *in vivo* data were found. The optical performance of the lens models were also affected by the zonular angles and it is seen in the scatter plots that the values of the accommodative amplitude vary with different zonular angle triplets (Figure 5.6-5.9). Similar patterns are seen for all the models irrespective of age, materials or the capsular thickness. The zonular angle triplet resulting in the maximal accommodative amplitude, occurs for an anterior angle of 10 degrees and a posterior zonular angle of 24 degrees (Figure 5.14-5.17), which is different from the values that provide the optimal fits to *in vivo* data (Table 5.1). This difference may demonstrate that changing zonular angles with age contributes to the decline of lens accommodative ability. This suggests that the 29 year old *in vivo* lens may be suspended by zonular fibres that are at angles that are not optimised for achieving maximum optical performance of that lens. It is likely the change of zonular angle could be one of the reasons for the gradual decline in accommodative capacity with age^{1, 2}.

5.6.3 The importance of spatially varying capsular thickness

The capsular thickness varies spatially and changes with age^{9, 60}. The lens capsule is the thickest basement membrane in the body and it envelops the lens completely as well as providing anchorage for the zonule^{10, 155}. The capsule is under considerable stress and plays an important role during accommodation¹¹⁹. The thickness of the anterior portion is five to ten times thicker than the posterior portion^{9, 123, 137} and the effect of age on thickness is greater for the anterior portion^{60, 137}. The capsule of an accommodative lens is thickest at the anterior and posterior periphery coinciding with the two regions of

zonular insertion^{9, 34, 60}. The strain energy stored within the capsule during deformation is directly related to the capsular thickness^{123, 150} and is therefore considered able to influence lens shape change during accommodation.

The accommodative amplitudes seen in lens models with varying capsular thickness were higher than those from the uniform capsular thickness models, for both ages using both sets of material properties (Figures 5.14-5.19). It is not definitively known whether the varying capsular thickness is a consequence of stress-induced modelling of the capsule¹²³, whether it serves a functional purpose in contributing to changes in the curvature of the accommodated lens^{34, 76, 119, 150, 159} or whether it acts only as a distributor of force¹¹⁴. The results of this work support the suggestion that varying capsular thickness may help increase the optical performance of the lens and therefore have a physiological function.

5.6.4 Comparing between accommodative theories

Modelling can offer perspectives on accommodation that test theories and provide insights into how models with different parameters align with theoretical predictions. The accommodative theory of Schachar^{56, 57}, which challenges the long-existing theory of Helmholtz⁵³, postulates that as the lens accommodates there is a steepening of the central lens surface and a flattening of the lens peripheral surface together with an increase in sagittal thickness. Similar accommodated lens shapes were described by earlier work^{13, 34}. By measuring the radius of curvature and calculating the central optical powers of thirty *post-mortem* human lenses, Schachar concluded that the lens free of zonular tensions is actually in an unaccommodated state¹⁶⁰, contradicting the conventional thinking from Helmholtz⁵³, that *post-mortem* lenses are in an accommodative state. According to Schachar^{56, 57}, the anterior and posterior zonular fibres should be relaxed whilst the equatorial zonular fibre remains taut during accommodation. The models in Figure 5.19 b, c and d show consistency with the theory of Schachar who demonstrated a similar trend in two lenses aged 19 and 29 years using FEA¹³⁵. The model in Figure 5.19a supports the theory of Helmholtz⁵³. It should be noted that whilst both Fisher and Wilde *et al.*⁶⁵ used centrifugal force to obtain material properties, the former spun lenses that were capsulated, the latter used decapsulated samples and the results did not therefore have any contribution from the capsule on lens shape.

From the optimum p-values indicating the fit of the lens models to *in vivo* measurements, as well as from the plots of accommodative amplitudes, the equatorial zonular angle does not appear to have a significant influence on shape change (Figures 5.4-5.11, Table 5.1). This tends to concur with the theory of Schachar^{56, 57}. All the zonular angle triplets tested with the 16-year-old model using the material properties of Fisher⁶² show support for the theory of Helmholtz⁵³. Previous modelling indicated that both theories can find support depending on the lens shapes, materials and applied forces used¹²⁹. It is possible that the two accommodative theories are not completely contradictory. Models must be carefully constructed if they are to provide correct insights into accommodation as this study demonstrates that even sophisticated models that compare to *in vivo* measurements, and are therefore physiologically plausible, can respond in different ways to simulated stretching.

5.7 Summary

Lens models using geometries and material properties from previous *in vitro* studies were compared to *in vivo* results to select zonular configurations that would be physiologically relevant. The equatorial zonular fibre does not appear to play as significant a role on lens shape change as do the anterior and posterior zonular fibres. Changing zonular angles with age can account for a gradual accommodative loss as zonular angle triplets that provide the optimal fits to *in vivo* data give lower accommodative amplitudes than those that produce the highest optical performance. A spatially varying capsular thickness has a greater effect on lens optical performance by increasing the resulting accommodative amplitude. Interrelations may exist between the two current alternative theories of accommodation as both find support depending on the different lens geometries, material properties and displacements that are applied.

6 MODELS WITH LINEARLY VARYING MODULI

The models with gradient elastic moduli presented in Chapter 3 are with stepped changes of material properties in the lens cortex using elastic moduli taken from studies that have spun the lenses^{62, 65}. Recent measurements using Brillouin light scattering analyses were able to map the spatially changing moduli of *in vivo* human lenses^{71, 107}. The profile of the measured longitudinal modulus along the lens central axis shows linear variation that decreases from a central stiff plateau region, the sagittal thickness of which is roughly about two thirds of the whole lens, toward the lens surface⁷¹. The magnitude of the modulus in the central plateau region shows no age dependence but its width increases with age. The present chapter investigates the linear variation of the elastic modulus in the lens cortical regions by creating lens models using geometries taken from a more recent interferometric analysis over a wider age range¹⁴⁹. The general shapes and the ageing trends of the refractive index profiles measured in the interferometric analysis¹⁴⁹ are similar to those of the longitudinal modulus measured in the Brillouin light scattering analysis⁷¹.

6.1 Geometry of the lens models

The geometries of eight lenses spanning the age range of 16 to 91 years of age, were created in SOLIDWORKS (ver.2015) based on the images with iso-indicial contours of refractive index as reported by Pierscionek *et al.*¹⁴⁹. The profiles of refractive index in

Chapter 6. Models with linearly varying moduli

the sagittal planes along the central optical axes of the eight lenses all demonstrate a central plateau region with maximum refractive index. The exception to this is the 35-year-old lens, the index profile of which is rounder in the centre than seen in the other lenses¹⁴⁹ (Figure 6.1). Although age is one variable linked to change in refractive index, there are individual variations¹⁴⁹. The contour on each image corresponding to the central plateau region of the refractive index profile was taken as the nuclear boundary for each lens, as represented in Figure 6.1. The rest of each image was treated as the lens cortex. The cortical layers were modelled as decreasing linearly from the cortico-nuclear boundary toward the outer lens surface.

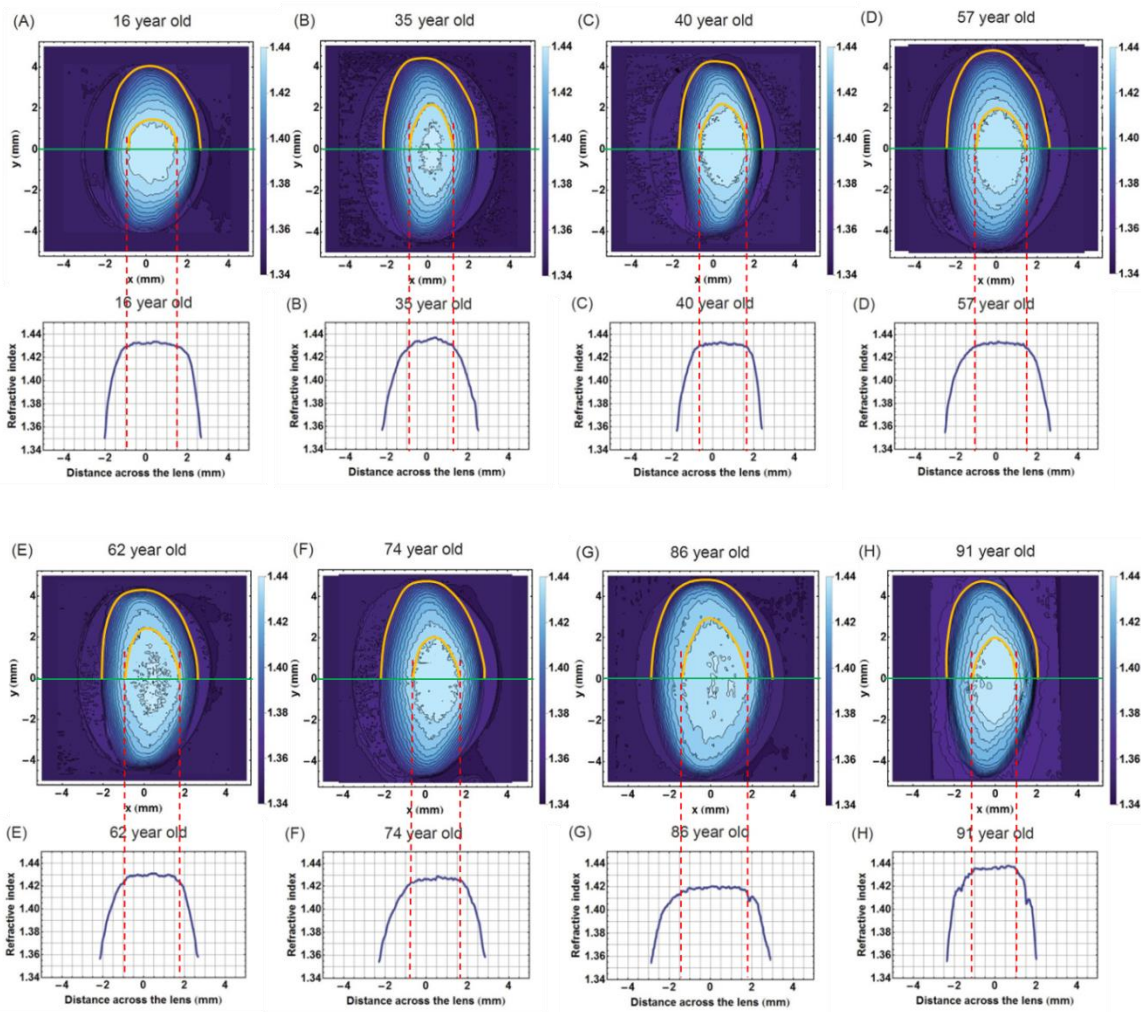


Figure 6.1 Dimensions of the lenses with the nuclear sizes fitted from corresponding refractive index profile measured by Pierscionek *et al.*¹⁴⁹.

To allow a more intuitive characterisation of the changes in lens dimensions with age, the sagittal thicknesses and the equatorial diameters of the lenses and the nuclei of the eight representative lenses are listed in Table 6.1. In general, older lenses have larger sagittal thicknesses and equatorial diameters than younger lenses. These are particularly

obvious in the 62 and 91 year old lenses. The aspect ratio, defined as the ratio of the thickness to diameter, of the whole lens and the nucleus are within the range of 0.45 to 0.65 except for the nucleus of the 16-year-old lens. This youngest lens has a rounder nucleus compared to the other lenses, giving an aspect ratio of 0.76.

Table 6.1 Dimensions of the lenses.

Unit/mm	16yr	35yr	40yr	57yr	62yr	74yr	86yr	91yr	
Nucleus	thickness	2.40	2.11	2.24	2.53	2.69	2.40	3.25	2.14
	diameter	3.15	4.45	4.05	3.97	5.08	4.10	5.76	4.00
	aspect ratio	0.76	0.47	0.55	0.64	0.53	0.58	0.56	0.54
Whole lens	thickness	4.61	4.65	4.13	5.14	4.69	5.11	5.89	4.40
	diameter	8.06	8.83	8.52	9.69	8.79	9.62	9.71	9.47
	aspect ratio	0.57	0.53	0.48	0.53	0.53	0.53	0.61	0.46

6.2 Model development

6.2.1 Element selection and mesh generation

Axisymmetric models were created in ANSYS mechanical APDL (ver.160) for all eight lenses. The components of each lens model are similar to those presented in Chapter 5, which contain six different parts: (i) the lens nucleus, (ii) the lens cortex, (iii) the capsule, (iv) an anterior zonular fibre, (v) an equatorial zonular fibre and (vi) a posterior zonular fibre. The lens nucleus and cortex were meshed using 8-node axisymmetric elements (ANSYS element type: PLANE 183), the lens capsule was modelled using 3-node membrane elements (ANSYS element type: SHELL 209), the zonular fibres were considered with 2-node spar elements carrying tensions only (ANSYS element type SHELL 208). For each model, the total number of elements was 1515 and the total number of nodes was 7436. The meshed FE lens models of all eight lenses are shown in Figure 6.2 with different colours used to distinguish the nucleus and the cortex.

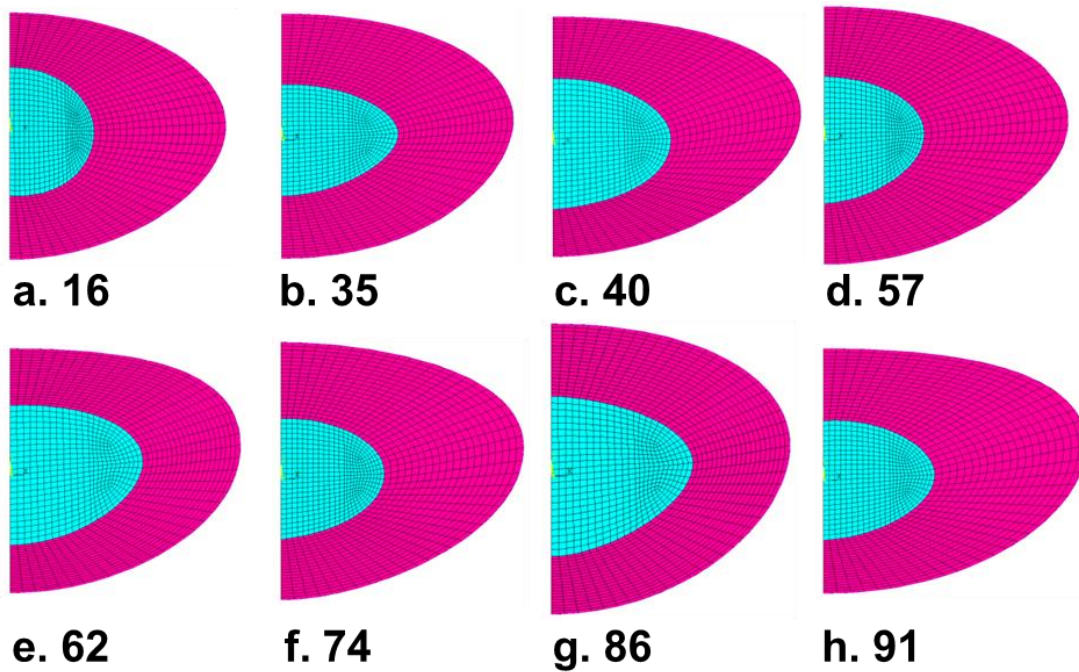


Figure 6.2 The FE lens model aged (a) 16, (b) 35, (c) 40, (d) 57, (e) 62, (f) 74, (g) 86 and (h) 91 years of age.

6.2.2 Modelling the capsule and the zonule

The lens capsule was modelled either with a uniform thickness according to Fisher¹¹⁹ or with a spatially varying thickness according to Barraquer *et al.*⁹. The uniform capsular thicknesses of each age taken from Fisher¹¹⁹ are listed in Table 6.2. The lens models aged 86 and 91 years were treated with values taken from a lens aged 80 years, which is the oldest age reported by Fisher¹¹⁹. The Young's moduli used for the lens capsule at each age are listed in Table 6.2 and the Poisson's ratio of the capsule is 0.47¹¹⁹.

Table 6.2 The capsular thickness taken from Fisher¹¹⁹ for uniform capsular thickness models.

	16yr	35yr	40yr	57yr	62yr	74yr	86yr	91yr
Capsular thickness (μm)	13	15	16	19	20	19	18	18
Capsular modulus (MPa)	5.87	4.90	4.71	3.34	2.85	1.71	1.50	1.50

The three zonular fibres were modelled either as connecting to a single endpoint (Figure 6.3a) or as connected to three different points (Figure 6.3b). When the three zonular fibres were attached to a single endpoint, the distance from the endpoint to the central axis, namely the radius of the ciliary body (R_{cb}) as illustrated in Figure 6.3a, was set to 6.5mm for all eight models. When the three zonular fibres were modelled as split in three different directions, the zonular angle triplets were kept the same as those providing the optimal optical performances demonstrated in Chapter 5: 10, 0 and 24 degrees for the anterior, equatorial and posterior zonular angle, respectively (Figure 6.3b). The coupling mechanism of the zonular-capsular attaching points with surrounding nodes, shown in purple in Figure 6.3, was the same as that introduced in Chapter 3: a number of neighbouring nodes were coupled to the zonular anchorage points on capsule. The Young's modulus for the zonular fibres is 0.35MPa^{124} for all models and the Poisson's ratio is 0.47^{126} .

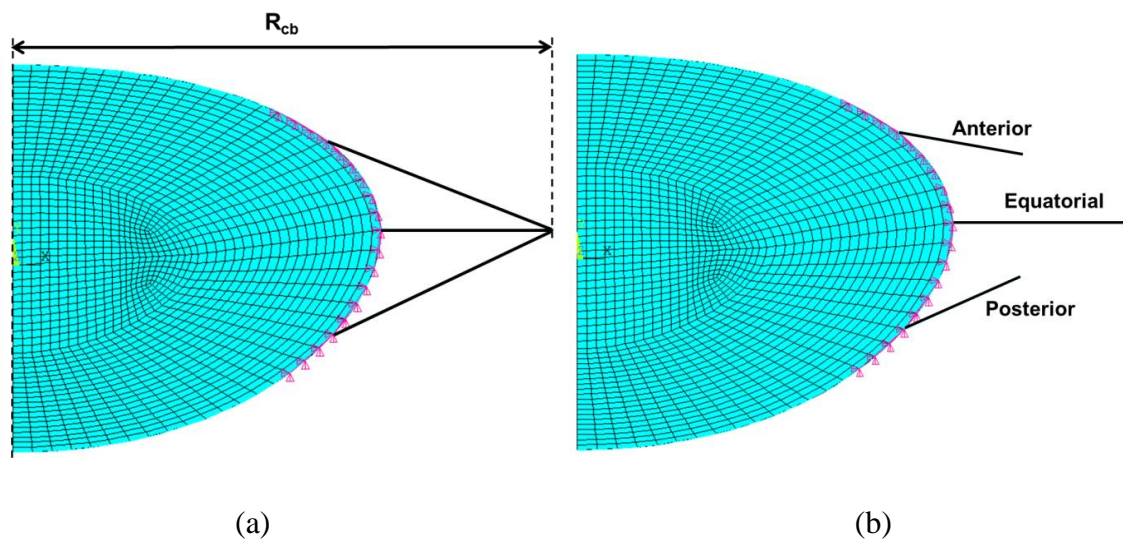


Figure 6.3 Illustration of the model (a) with three zonular fibres attached to a single endpoint showing the radius of ciliary body and (b) with three zonular fibres attached to three different endpoints.

6.2.3 Modelling the linearly changing moduli

According to the profiles of the longitudinal modulus along the lens central axis reported by Besner *et al.*⁷¹, all measured lenses demonstrate central plateau regions with peak moduli which decrease outward to the external lens surfaces. The peak longitudinal modulus of the central plateau region has no age dependence and its value presents 5% variation within the range of 3.197GPa to 3.359GPa^{71} . The averaged peak

longitudinal moduli measured at the lens centre and the averaged minimal longitudinal modulus measured at lens periphery for the 56 human lenses, reanalysed from the profiles in supplementary figures by Besner *et al.*⁷¹, was calculated to be 3.286GPa and 2.471GPa, respectively⁷¹. Poisson's ratio for the nucleus and the cortex were 0.499999 and 0.4999999 respectively when reanalysing the data from the research work by Besner *et al.*⁷¹. Young's modulus E is related to the longitudinal modulus using equation 6.1:

$$E = \frac{M(1+\nu)(1-2\nu)}{(1-\nu)} \quad (6.1)$$

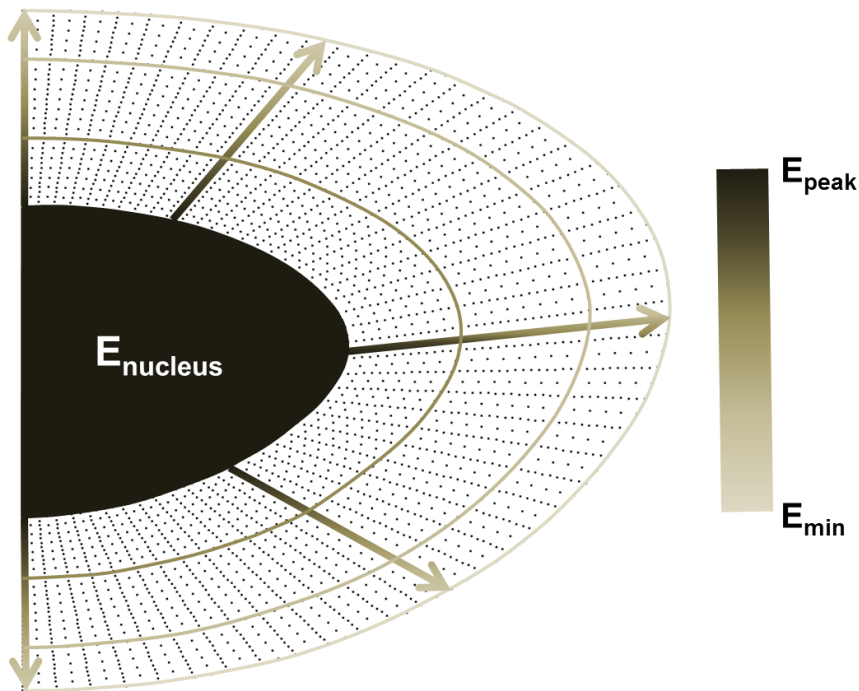


Figure 6.4 Illustration of the linearly varying moduli within the lens cortex with colour bar shown on the right side demonstrating the decreasing moduli from the nuclear boundary to the outer lens surface.

The nucleus of the models developed at each age was assigned with a uniform distribution of material properties using a single Young's modulus of 19.716kPa, which was calculated based on equation 6.1 using the averaged peak longitudinal modulus of 3.286GPa and a Poisson's ratio of 0.499999 (reanalysed from Besner *et al.*⁷¹). The lens cortex was incorporated with a linearly changing Young's modulus, which decreases from the nuclear boundary to the external lens surface. The nuclear boundary was assigned with a maximal Young's modulus of 19.716kPa. The minimal Young's modulus allocated to the external lens surface is 1.483kPa, which was calculated based

on equation 6.1 using the averaged minimal longitudinal modulus of 2.471GPa and a Poisson's ratio of 0.4999999 (reanalysed from Besner *et al.*⁷¹).

The linearly decreasing moduli within the lens cortical region were illustrated in Figure 6.4. Young's moduli were assigned to the meshed FE models directly to nodes, which were displayed in Figure 6.4 for the 35-year-old model as shown in Figure 6.2b. The lens model discretized using a mapped mesh (Figure 6.2) contributes to the well-aligned pattern of the nodes in the cortex: the number of nodes on the cortico-nuclear boundary and on the lens external boundary are both equal to 97. Starting from the anterior pole all the way to the posterior pole, each node on the external lens surface can be paired with a node on the cortico-nuclear boundary. Connecting two paired nodes using a virtual straight line will identify a group of nodes aligned to this line. In such a way all cortical nodes could be sorted into 97 groups. For each group, a linear interpolation was performed by the ANSYS program allocating a decreasing Young's modulus to nodes along each virtual line from the one attached to the cortico-nuclear boundary to the one attached to the external lens surface. The decreasing trends of Young's modulus are indicated using arrows with changing colour for five representative groups of nodes in Figure 6.4. Such distributions of material properties form iso-indicial contours of elastic moduli in the developed lens model (Figure 6.4).

6.2.4 Boundary conditions

The applied boundary conditions are: the nodes on the central axis were constrained in the horizontal direction and were allowed to have translational degrees of freedom only in the vertical direction. All models with the zonular configuration shown in Figure 6.3a were applied with a radial stretching force of 0.08N in the horizontal direction, which is the same as the forces used for models presented in Chapter 3. All models with the zonular configuration shown in Figure 6.3b were applied with displacements of 0.2mm to three endpoints and the directions of the displacements are along the orientation of the corresponding zonular fibre. The free endpoint of the zonular fibres was provided with in-plane translational degrees of freedom.

6.3 Stress distributions of models with a single stretching point

For each model, Young's modulus in the lens cortex was either modelled as a uniform distribution of 1.948kPa, or as a linearly decreasing distribution as introduced in section 6.2.3. The stress patterns for all simulated models are shown in Figures 6.5 to 6.8. The corresponding stress values (as von Mises stress in MPa) are indicated using colour bar on the left side of each figure. The stress contours for models with two different distributions of cortical moduli and with a uniform capsular thickness according to Fisher¹⁹ are displayed in the first and second column of each figure. The third column in each figure shows the stress contours of the linear-cortical moduli model with spatially varying capsular thicknesses according to the thickness profiles of similar ages as reported by Barraquer *et al.*⁹.

Stress contours of the models with a uniform cortical modulus, displayed in the first column of each figure in Figures 6.5 to 6.8, demonstrate clear boundaries between the nucleus and the cortex. The highest stresses appear in the nucleus close to the nuclear equator; for the youngest model, the red region in the nucleus extends over a wider region to the lens central axis (Figure 6.5a). A second high stress concentration region appears at the equatorial region of the cortex for all eight models. The high stress region in the cortex has similar magnitudes of stress values as the high stress region in the nucleus, for the oldest lens model aged 91 years (Figure 6.8d).

When the cortex was modelled with linearly changing Young's moduli, all eight models, (displayed in the second column of each figure in Figures 6.5-6.8) show only one high stress concentration region which covers a broader area in the equatorial region. In each model, the high stresses decrease radially outward to the lens central axis and to the lens external surface. Unlike the models with a uniform cortical modulus, there are no clear borders in the stress pattern distinguishing the nucleus from the cortex.

For models with linearly changing cortical moduli and spatially varying capsular thicknesses displayed in the third column of each figure (Figures 6.5-6.8), the stress patterns become more asymmetric and the high stresses shift anteriorly compared to their counterpart models with a uniform capsular thickness as displayed in the second column of each figure. The 16-year-old model developed in the present work shows more symmetric stress patterns compared to the rest of the lens cohort. The 16-year-old model was coupled with a capsular thickness profile from a lens aged 11 years

measured by Barraquer *et al.*⁹, which demonstrates a relatively more uniform thickness distribution compared to other lenses.

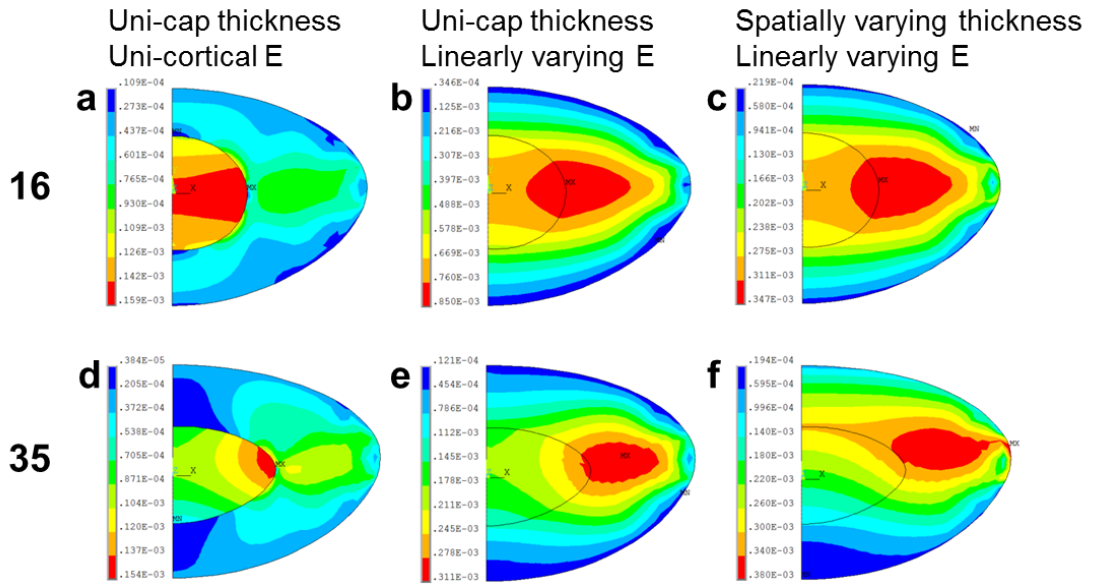


Figure 6.5 Stress distributions of the models aged 16 and 35 years of age for models with a single stretching point under a stretching force of 0.08N.

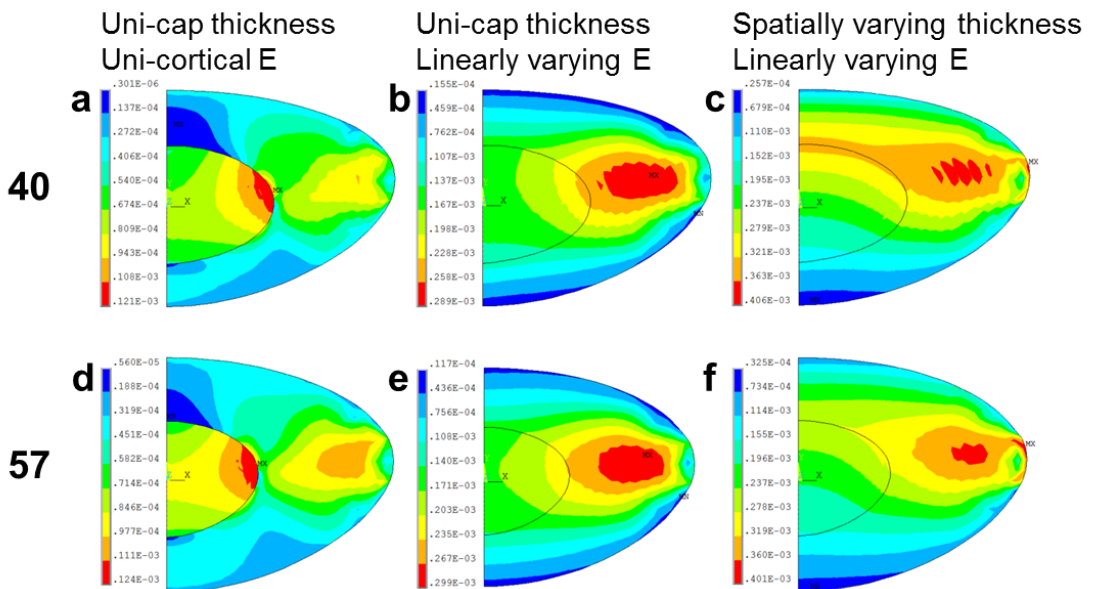


Figure 6.6 Stress distributions of the models aged 40 and 57 years of age for models with a single stretching point under a stretching force of 0.08N.

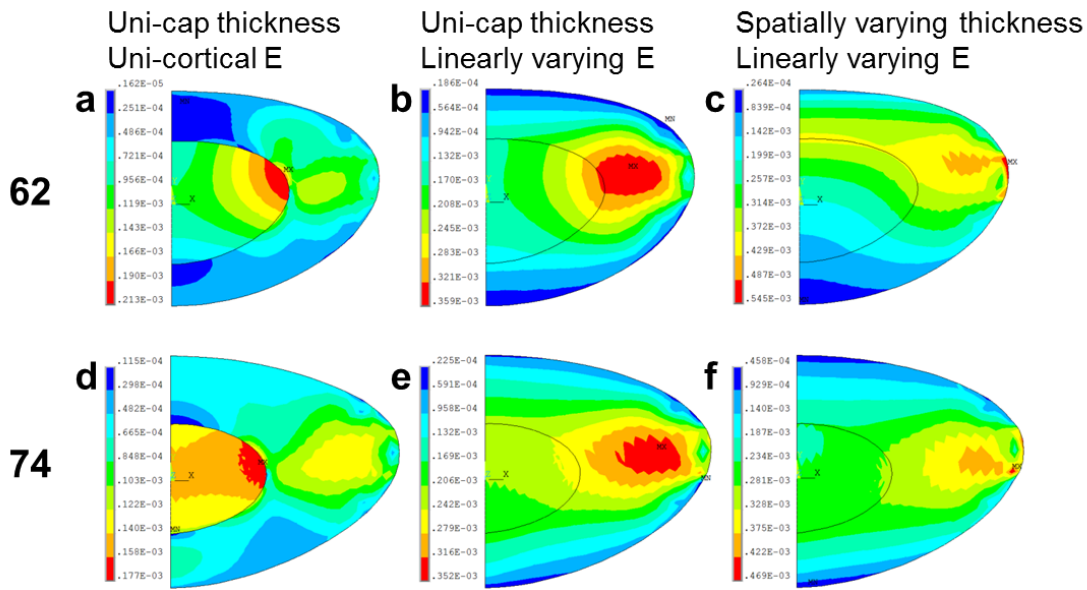


Figure 6.7 Stress distributions of the models aged 62 and 74 years of age for models with a single stretching point under a stretching force of 0.08N.

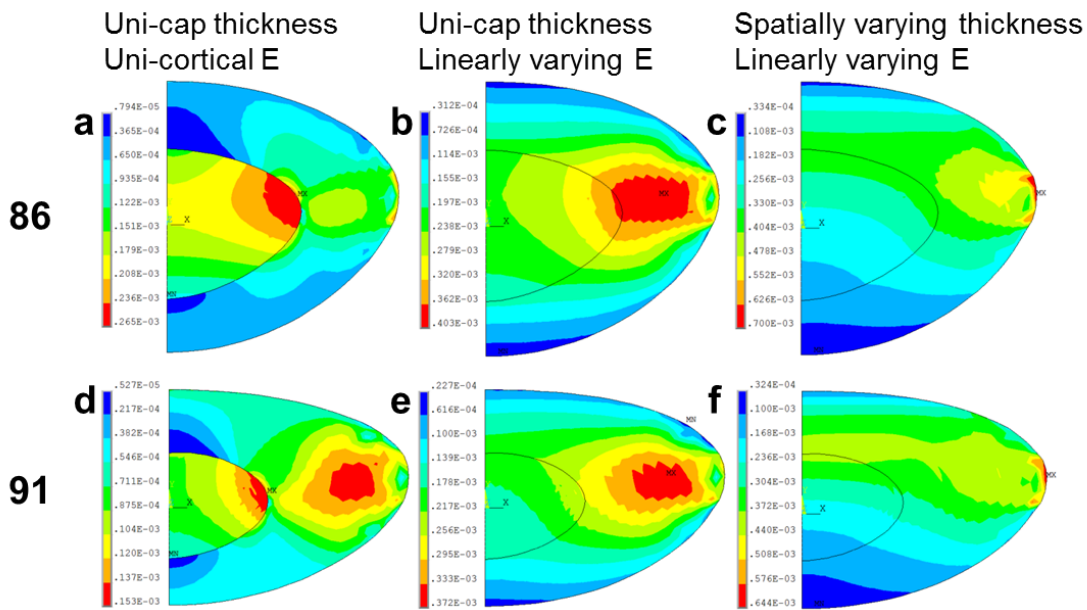
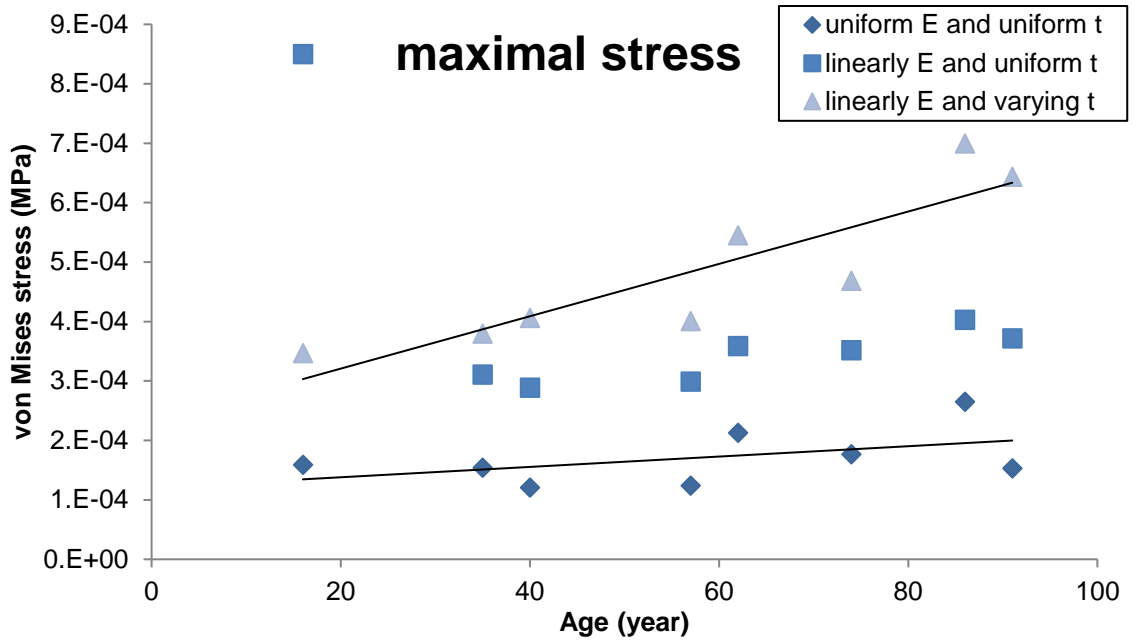
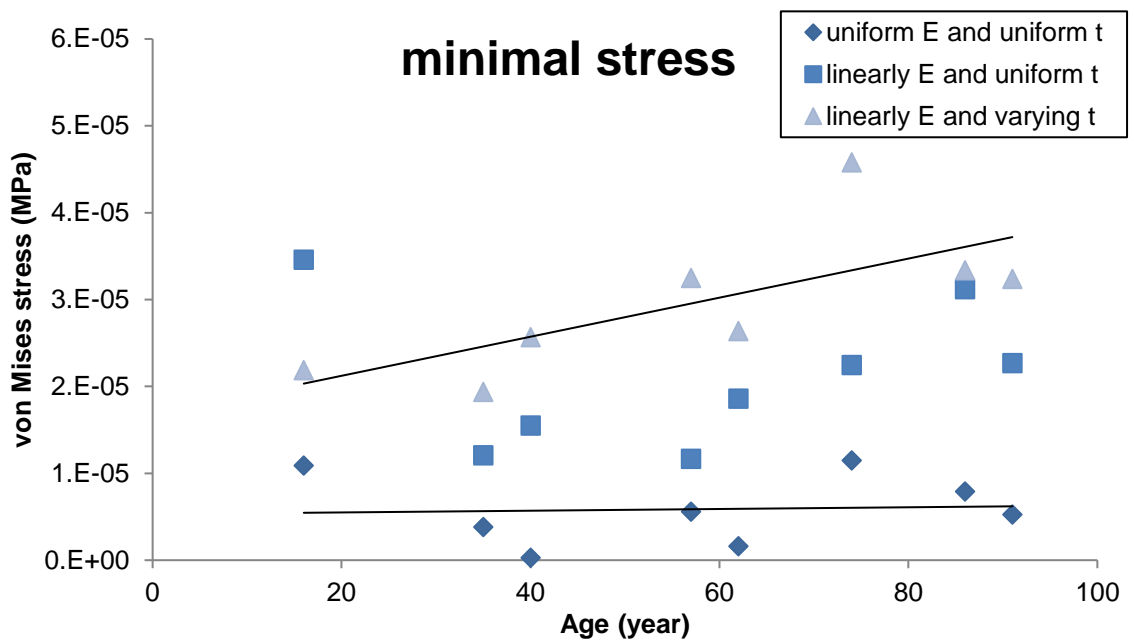


Figure 6.8 Stress distributions of the models aged 86 and 91 years of age for models with a single stretching point under a stretching force of 0.08N.



(a)



(b)

Figure 6.9 The (a) maximal and (b) minimal von Mises stresses of all lens models with a single stretching point plotted against age.

The maximal and minimal stresses are plotted as a function of age in Figure 6.9 for all three types of model. The models with a uniform cortical modulus and a uniform capsular thickness demonstrate the lowest maximal and minimal stresses; the maximal stress increases slightly with age but the minimal stress show little change (Figure 6.9). The models with linearly changing cortical moduli and spatially varying capsular thicknesses demonstrate the highest maximal and minimal stresses and both increase with age (Figure 6.9). For models with linearly changing cortical moduli and a uniform capsular thickness, increasing trends with age for both the maximal and minimal stresses can be seen if the 16-year-old lens is excluded, which demonstrate much higher stresses than all the other models.

6.4 Models with three different stretching points

6.4.1 Stress distributions

The stress distributions of models with zonular fibres stretched in three different directions and with displacements of 0.2mm applied to each zonular fibre, are displayed in Figures 6.10 to 6.13. In general, the high stress regions in these models extend to larger areas compared to the models displayed in Figures 6.5 to 6.8.

For models with a uniform cortical modulus and a uniform capsular thickness displayed in the first column of Figures 6.10 to 6.13, the highest stresses shown in red appear in the central nucleus in all ages. Similar to the models with a single stretching point (Figures 6.5-6.8), the stress patterns form clear boundaries that distinguish the nucleus and the cortex.

For models displayed in the second column of each figure, which were assigned with linearly varying cortical moduli and uniform capsular thicknesses, the regions shown in red cover the equatorial regions of both the nucleus and the cortex. No boundaries are seen on the stress patterns that separate the two regions. The stresses decrease radially toward the lens external surfaces.

For models displayed in the third column with linearly varying cortical moduli and spatially varying capsular thicknesses, the layered stress patterns are similar to those displayed in the second column but the high stresses shift anteriorly except for the youngest lens model.

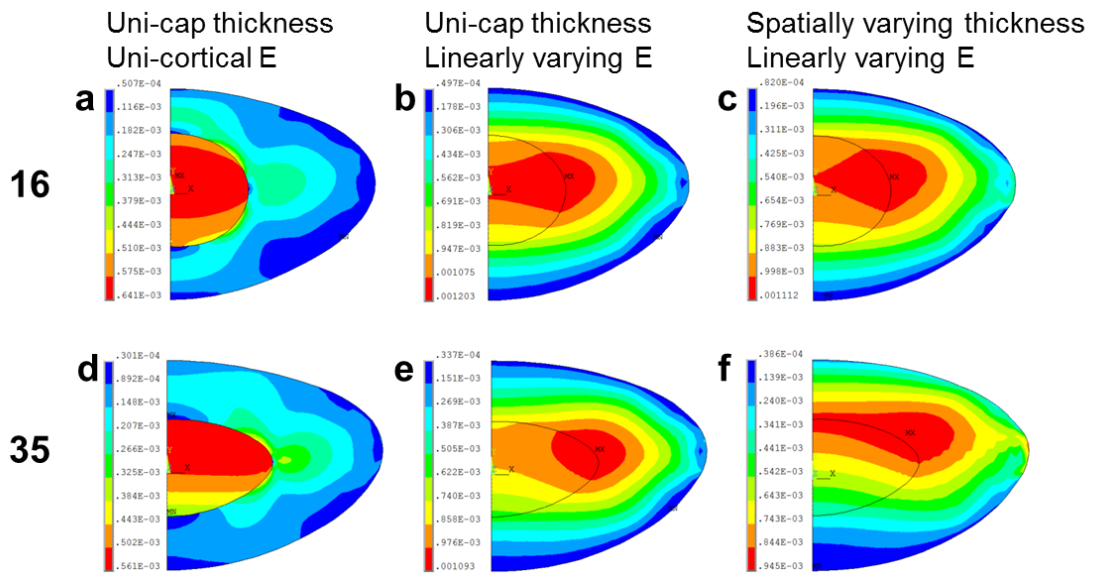


Figure 6.10 Stress distributions of the models aged 16 and 35 years of age for models with three stretching points under a displacement of 0.2mm applied to each zonular fibre.

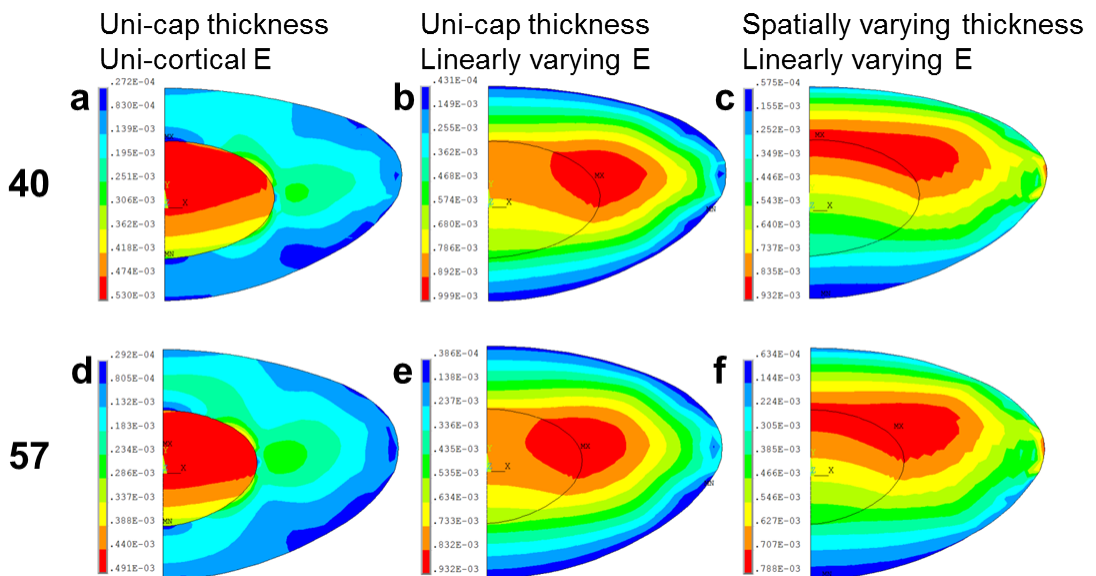


Figure 6.11 Stress distributions of the models aged 40 and 57 years of age for models with three stretching points under a displacement of 0.2mm applied to each zonular fibre.

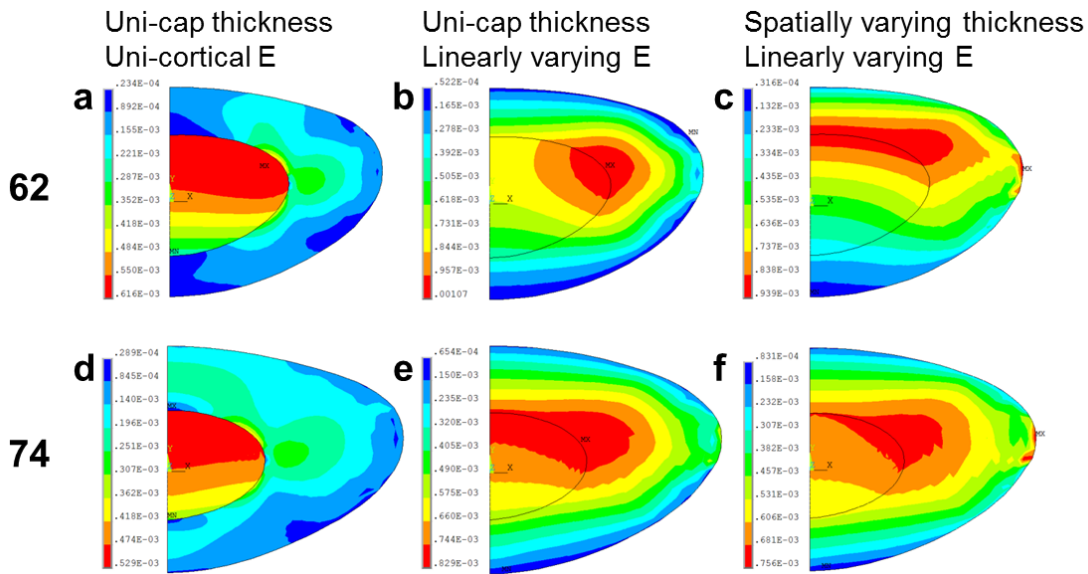


Figure 6.12 Stress distributions of the models aged 62 and 74 years of age for models with three stretching points under a displacement of 0.2mm applied to each zonular fibre.

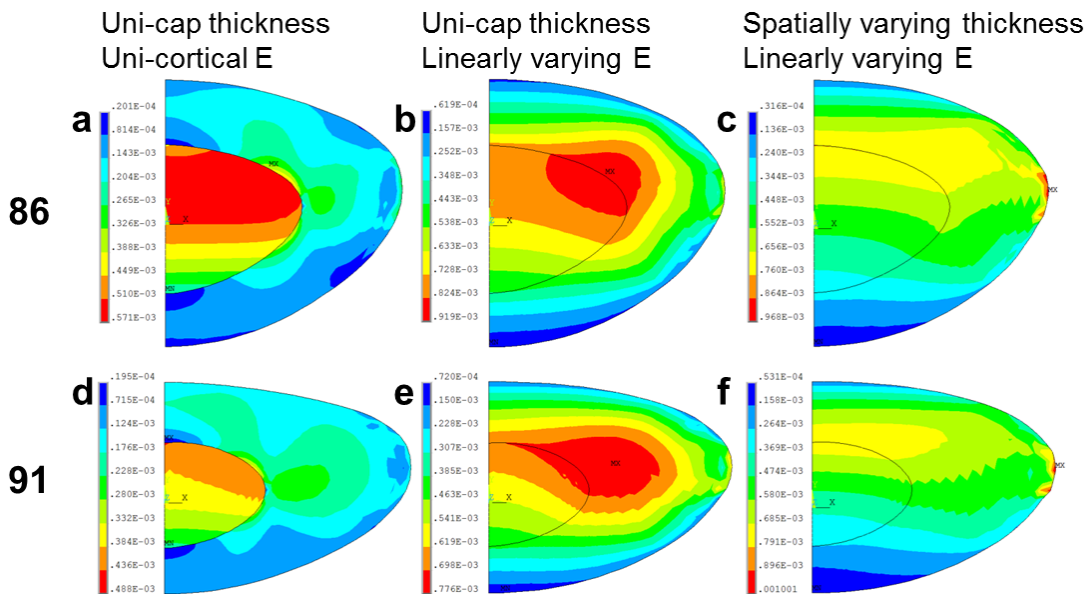
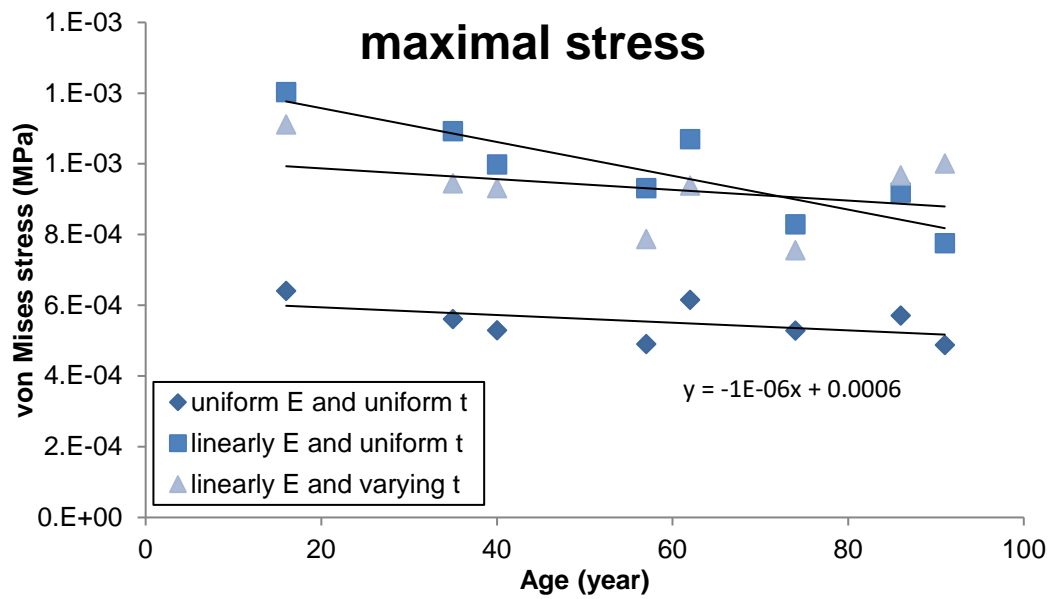
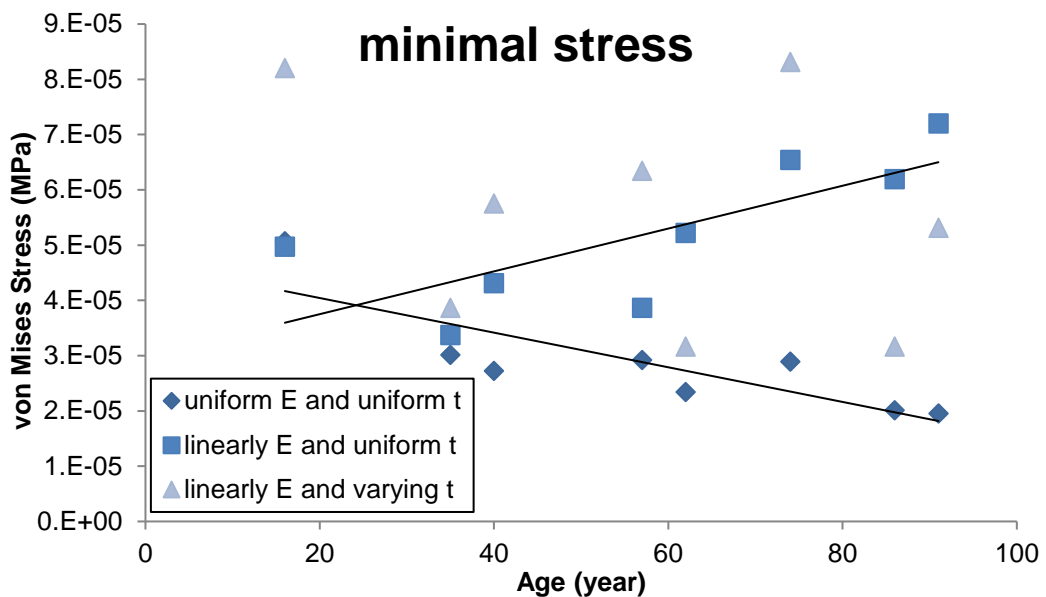


Figure 6.13 Stress distributions of the models aged 86 and 91 years of age for models with three stretching points under a displacement of 0.2mm applied to each zonular fibre.



(a)



(b)

Figure 6.14 The (a) maximal and (b) minimal von Mises stresses of all lens models with three stretching points plotted against age.

The maximal and minimal stresses are plotted against age in Figure 6.14 for models displayed in Figures 6.10 to 6.13. The maximal stresses decrease with age for all three types of models, which appear to be almost negligible for the model with a uniform cortical modulus and a uniform thickness as well as the model with linearly changing cortical moduli and spatially varying capsular thicknesses. The minimal stress in models

Chapter 6. Models with linearly varying moduli

with a uniform cortical modulus and a uniform capsular thickness decreases with age, but increases with age for models with linearly varying moduli and a uniform capsular thickness. For models with linearly varying cortical moduli and spatially varying capsular thicknesses, the minimal stress shows a wide range of scatter. The maximal stresses of the models with three stretching points applied with displacements of 0.2mm (Figure 6.14a) are three to four times higher than those of the models with a single stretching point under a stretching force of 0.08N (Figure 6.9a). The minimal stresses of the two types of models are of a similar magnitude.

6.4.2 Change in radii of curvature

The central radii of curvature, taken at the 3mm diameter zone of the lens, are listed in Table 6.3 for the external lens and the nuclear surfaces of each lens model in the undeformed state. The radii of curvature of deformed lens models with a uniform cortical modulus and a uniform capsular thickness are listed in Tables 6.4; of models with linearly changing cortical moduli and a uniform capsular thickness are listed in Table 6.5; of models with linearly changing cortical moduli and spatially varying capsular thickness are listed in Table 6.6.

Table 6.3 The central radii of curvature of undeformed models.

		16	35	40	57	62	74	86	91
Whole lens	Anterior R	7.14	10.72	13.13	11.42	17.01	11.53	10.88	18.89
	Posterior R	5.34	6.91	5.78	6.56	6.03	5.90	5.86	7.67
Nucleus	anterior R	1.58	3.59	2.80	3.46	4.92	2.97	6.01	2.64
	posterior R	1.40	3.25	3.57	2.36	3.27	3.49	3.59	3.03

Table 6.4 The central radii of curvature of models with a uniform cortical modulus and a uniform capsular thickness.

		16	35	40	57	62	74	86	91
Whole lens	Anterior R	7.03	9.19	10.29	9.81	11.09	10.01	8.97	12.88
	Posterior R	5.24	6.34	5.63	6.34	5.70	5.68	5.61	6.91
Nucleus	anterior R	1.62	3.79	2.91	3.12	5.10	3.09	6.28	2.73
	posterior R	1.46	3.38	3.73	2.77	3.42	3.61	3.72	3.12

Table 6.5 The central radii of curvature of models with linearly varying cortical moduli and a uniform capsular thickness.

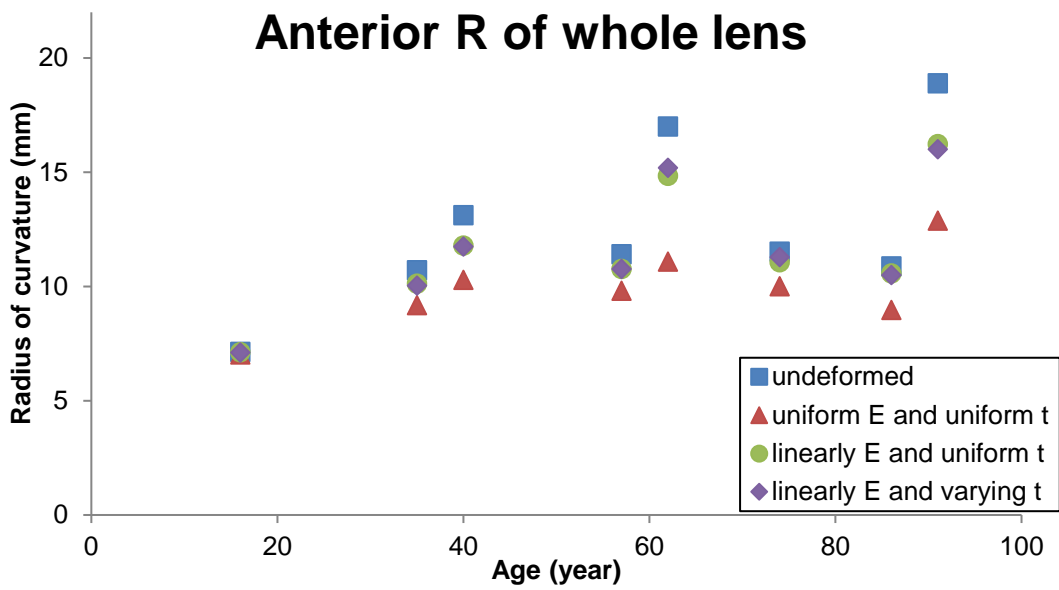
		16	35	40	57	62	74	86	91
Whole lens	Anterior R	7.12	10.13	11.79	10.77	14.84	11.07	10.58	16.24
	Posterior R	5.41	6.88	5.94	6.66	6.19	6.00	5.98	7.79
Nucleus	anterior R	1.72	3.91	2.99	3.22	5.12	3.16	6.36	2.80
	posterior R	1.53	3.47	3.80	2.84	3.46	3.68	3.77	3.18

Table 6.6 The central radii of curvature of models with linearly varying cortical moduli and a spatially varying capsular thickness.

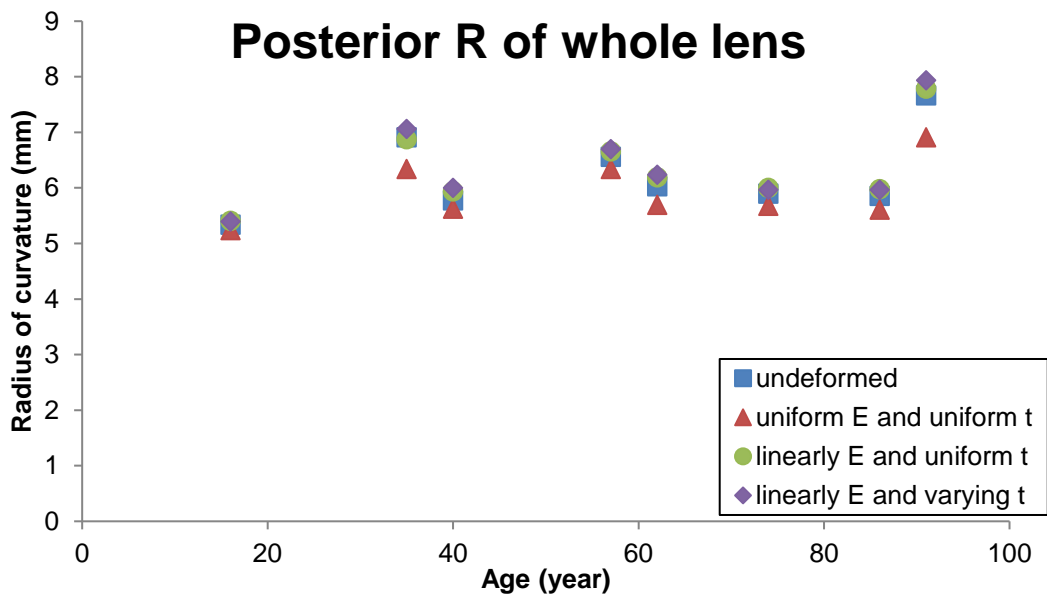
		16	35	40	57	62	74	86	91
Whole lens	Anterior R	7.11	10.04	11.75	10.77	15.20	11.29	10.51	16.01
	Posterior R	5.40	7.06	6.00	6.70	6.24	5.97	5.97	7.94
Nucleus	anterior R	1.70	3.81	2.95	3.16	5.11	3.15	6.26	2.78
	posterior R	1.52	3.46	3.80	2.81	3.44	3.65	3.74	3.17

The changes in radius of curvature of both the anterior and posterior surfaces are plotted against age in Figures 6.15 and 6.16, respectively. The anterior radii of curvature of undeformed lens shapes are higher than those of the deformed lens shapes for all three types of models at eight different ages (Figure 6.15a), which suggest that the anterior surface of the lens becomes steeper with stretching. The steepening of the anterior central lens surface is most pronounced in models with a uniform cortical modulus and a uniform capsular thickness, compared to the other two types of models. Either with a uniform capsular thickness or with spatially varying capsular thicknesses, the changes in anterior radii of curvature are similar when models were simulated with linearly changing cortical moduli (Figure 6.15a).

Steeper posterior surfaces with stretching are seen for models with a uniform cortical modulus and a uniform capsular thickness. The other two types of models with linearly changing cortical moduli, on the contrary, demonstrate flatter posterior surfaces and the results for these two types of models at all eight ages are similar (Figure 6.15b). The magnitudes of the change in the radius of curvature of the posterior surfaces are substantially lower than that of the anterior surfaces and show almost no change from undeformed to deformed states.

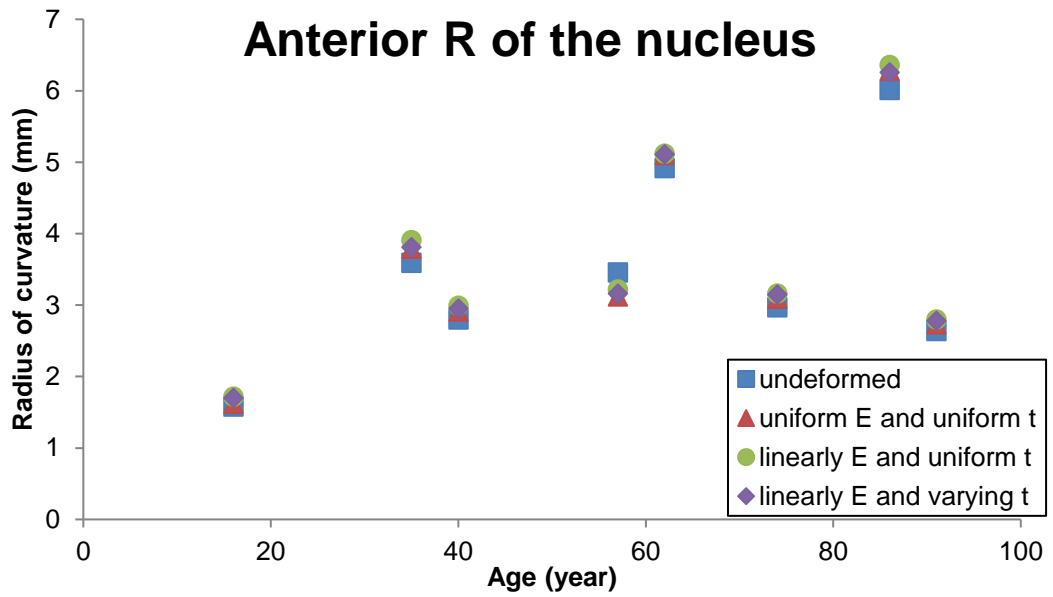


(a)

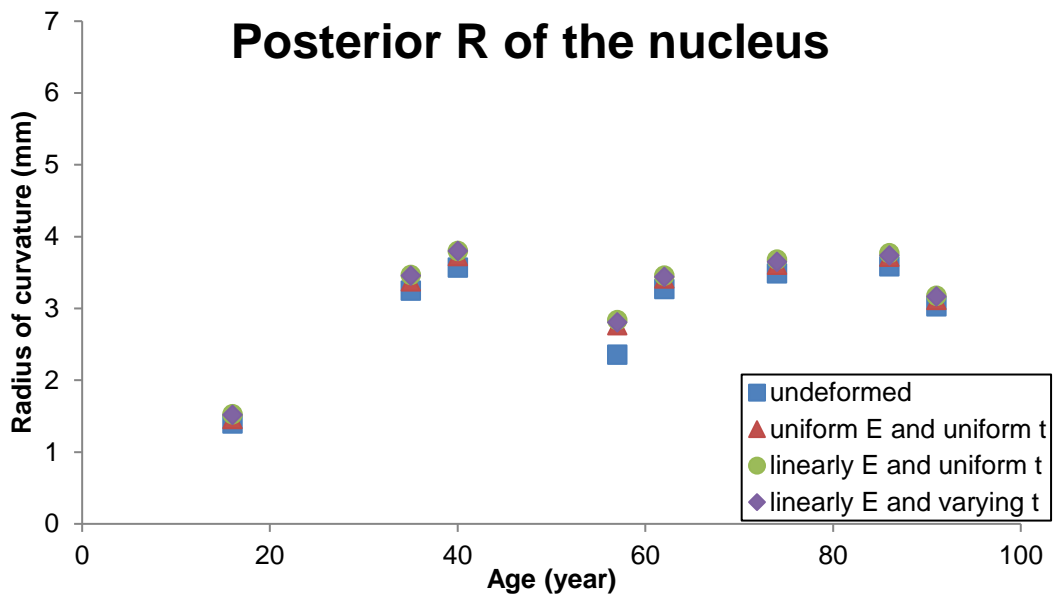


(b)

Figure 6.15 The central radius of curvature of the (a) anterior and (b) posterior lens surfaces plotted against age for all three types of models.



(a)



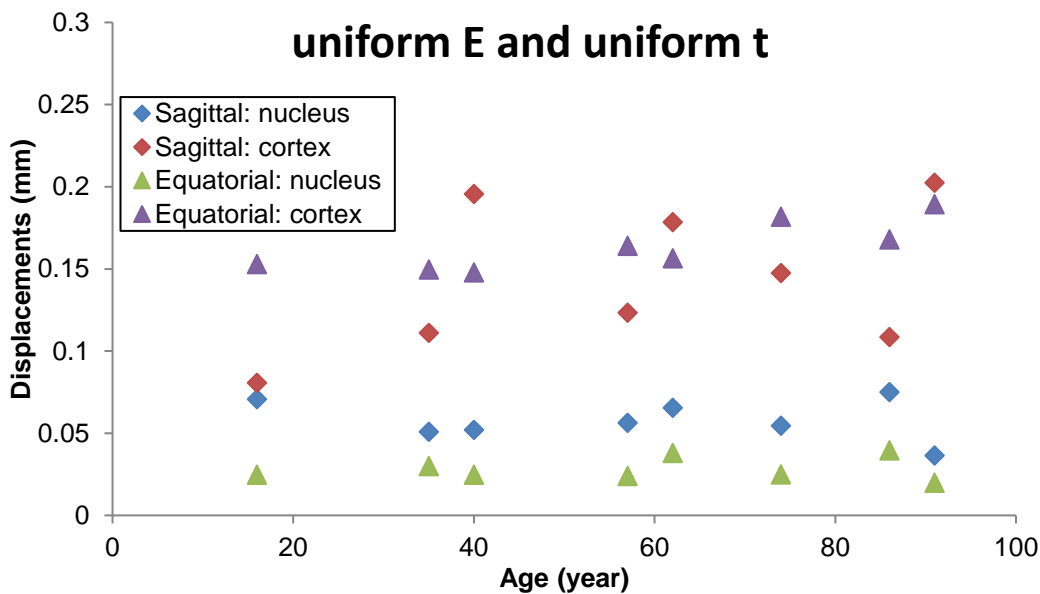
(b)

Figure 6.16 The central radius of curvature of the (a) anterior and (b) posterior nuclear surfaces plotted against age for all three types of models.

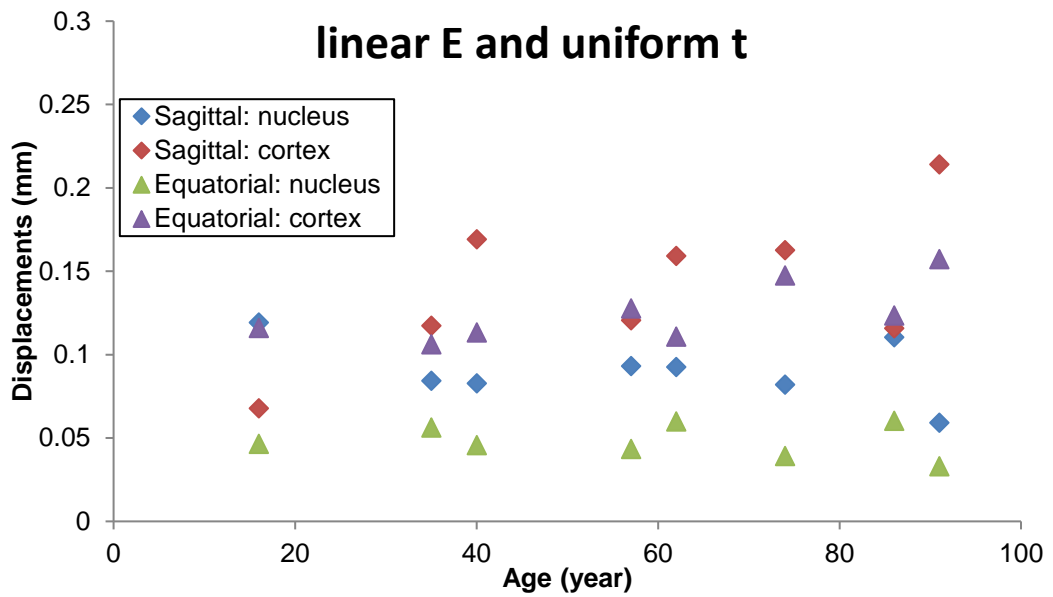
Both the anterior and posterior nuclear surfaces become very slightly flatter with stretching for all three types of models except for the 57 year old lens, in which the anterior surface of the nucleus become slightly steeper for all three types of models (Figure 6.16a). The changes between deformed and undeformed states are much less than those seen for the whole lens curvatures. The magnitudes of change in radii of curvature are similar for the two linear cortical moduli models with two different distributions of capsular thickness.

6.4.3 Deformations of the model in sagittal and equatorial directions

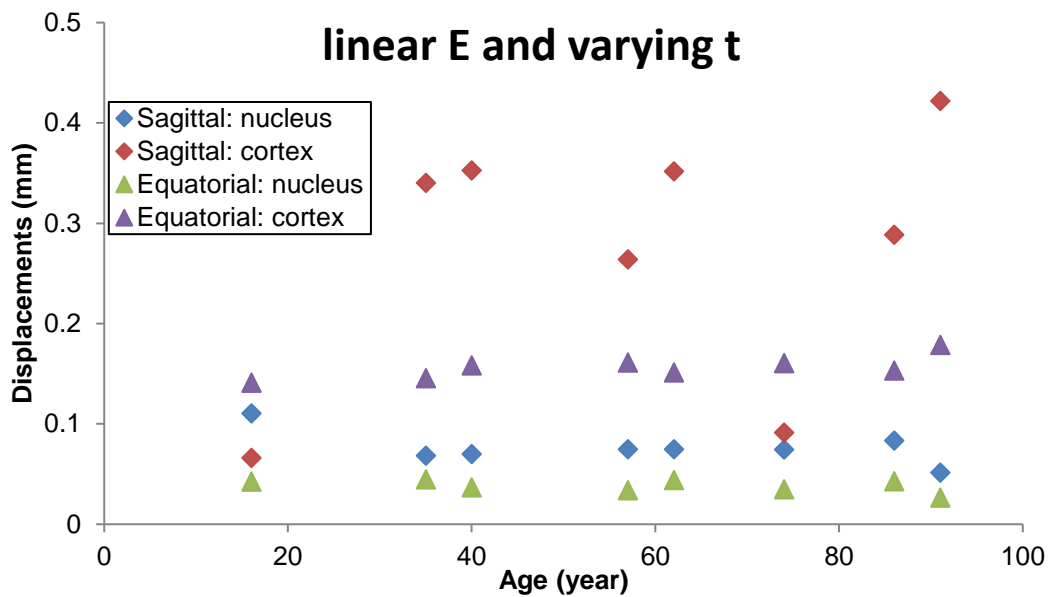
The deformations of the nucleus and the cortex in both the sagittal and equatorial directions are compared and plotted against age in Figure 6.17 a, b and c for all three types of models. The two 16-year-old models with linearly changing cortical moduli demonstrate higher sagittal deformations in the nucleus than in the cortex (Figure 6.17b and c); for all other models, the cortex shows higher deformations than the nucleus in the sagittal direction. In the equatorial direction, the deformations of the nucleus are lower than those of the cortex for three types of models at all eight ages.



(a)



(b)



(c)

Figure 6.17 The sagittal and equatorial deformations of the nucleus and the cortex plotted against age for models with (a) a uniform cortical modulus and a uniform capsular thickness, (b) linearly changing cortical moduli and a uniform capsular thickness and (c) linearly changing cortical moduli and spatially varying capsular thickness.

6.5 Discussion

The models were developed using material properties of similar distributions to the refractive index profiles according to *in vivo* measurements¹⁴⁹. The material properties provided by Besner *et al.*⁷¹ are in the format of a longitudinal modulus. The Young's moduli used for the models were converted from the longitudinal moduli using equation 6.1, and it is noted that the calculated Young's moduli are very sensitive to the selection of Poisson's ratio for a nearly incompressible material (Appendix II). A mathematical analysis of Poisson's ratio of incompressible materials showed the conflict between the classical theory of elasticity and experimental results¹⁶¹ based on the relationship between the bulk modulus and the shear modulus. A similar outcome can be obtained between longitudinal modulus and Young's modulus as well (shown in Appendix II): as Poisson's ratio approaches 0.5, the longitudinal modulus is nearly constant. However, according to equation 6.1, the longitudinal modulus becomes infinitely large as Poisson's ratio is nearly 0.5. There is a paucity of data on Poisson's ratio for biological tissues demonstrating viscoelastic behaviour¹⁶² and this requires further investigation.

The internal stress distributions are presented for models with different types of zonular fibres, distributions of material properties and capsular thickness. A horizontal stretching force of 0.08N was firstly applied to models with a single stretching point allowing a direct comparison to the models shown in Chapter 3. With a uniform cortical modulus all eight models demonstrate the highest stresses in the nucleus close to the nuclear equator, which is similar to the stress patterns of the 48-year-old model using the material properties of Wilde *et al.*⁶⁵ presented in Chapter 3. In both situations, the nucleus is stiffer than the surrounding cortex. When the models are stretched by zonular fibres separately into three different directions, the second highest stresses concentrated in the equatorial regions of the cortex, seen in Figures 6.5 to 6.8, were eliminated (Figures 6.10-6.13).

The stress pattern changes greatly when the lens cortex was replaced with linearly changing moduli; borders between the nucleus and the cortex are erased, allowing for the high stresses at the equatorial region to decrease more gradually towards the lens surface. Varying the capsular thickness, in general, only shifts the high stresses anteriorly. This could be attributed to the capsules being much thicker at the anterior periphery than the posterior periphery as seen in the profiles reported by Barraquer *et al.*⁹. Supporting evidence for this is seen in the more symmetric stress patterns of the

16-year-old model, which was incorporated with a relatively uniform distribution of capsular thickness from an 11-year-old lens⁹.

Direct comparisons between the stress values shown in Figures 6.5 to 6.8 and Figures 6.10 to 6.13 are inappropriate as the magnitude of lens deformations differ greatly. In the former scenario when models were applied with a stretching force of 0.08N, the deformations in all positions are less than 0.01mm, which are not able to provide discernible accommodative change and are hence not presented. Ageing trends, although in opposite ways, are found for the stresses in both the models with a single stretching point and with three stretching directions.

In all models with three zonular endpoints, the anterior surfaces of the whole lens become steeper (Figure 6.15) while the nuclear surfaces become flatter with stretching (Figure 6.16). The models at eight different ages were applied with Young's moduli at the same magnitudes and the nucleus is about ten times stiffer than the cortex. The stiffer nucleus is more resistant to external forces. The more flexible cortex shows higher deformations than the nucleus in both the sagittal and equatorial directions (Figure 6.17). In the 16-year-old lens having a more curved nucleus, the sagittal deformations of the nucleus are higher than that of the cortex for the two models with linearly changing cortical moduli (Figure 6.17b, c).

The models present further support for the conclusions drawn in Chapter 3 that a much stiffer nucleus contributes to steeper lens surfaces at the poles with stretching, and are in accordance with the accommodative theory of Schachar⁵⁶.

6.6 Summary

The models developed in the present chapter spread over a wide age range from teenage to extreme old age and were developed based material properties that vary linearly in the cortical region. The changes in the stress and displacement fields of each model were analysed. The models presented in this chapter are based on data from different aged lenses and the differing modelling parameters are related to the lens geometries, capsular thickness and capsular elasticity. It is evident that the zonular fibres, the distributions of material properties, and the geometrical parameters i.e. the nuclear shape, all influence the deformation of the lens model. Future studies are needed to investigate the sensitivities of a much wider range of modelling parameters.

7 DISCUSSION AND FUTURE WORK

7.1 Discussion

The work presented in this dissertation includes the development of FE models of human lenses that can closely represent the anatomy and mimic the physiological process of accommodation. Demonstrated models were created based on geometries of intact *post-mortem* lenses^{37, 149} and material properties taken from both *post-mortem* lenses^{62, 65} and *in vivo* lenses⁷¹. The modelled results were compared to clinical studies. The influence of different parameters to accommodative process and the contributions of different ocular components to the accommodative loss with age were investigated.

FEA serves as an excellent approach for seeking correlation between *in vivo* and *in vitro* measurements and proves useful for investigating biological problems that are not tractable by experimental work. Various forms of experimental work using optical approaches that study the accommodative process can at best indicate changes in lens surfaces profiles, but only in central regions of the lens because light is blocked by the iris. Numerical modelling, as shown in the present work, can provide detailed information about mechanical changes in the internal lens, i.e. the deformations of different cortical layers and the internal stress distributions. Furthermore, the proposed methods could facilitate the design and optimize the performance of IOLs for restoring the lenticular accommodative ability. In addition, the developed models have added new innovative elements to the methodologies for developing lens models, elements related

Chapter 7. Summary and future work

to simulating the biological structure and the physiological function of the human lens in the following aspects:

Firstly, the distributions of the modulus of elasticity were considered to be linearly correlated to the profile of the respective refractive index across the lens. Such a consideration has not been conducted before. Models presented in Chapter 3 were developed with the elastic modulus being altered incrementally in different cortical layers, while models presented in Chapter 6 had a linearly varying cortical modulus, which decreases from the nuclear boundary to the external lens surfaces. In both Chapters, the nucleus of each model was assumed to have a constant value of elastic modulus, corresponding to the central plateau region of the respective refractive index profile and in accordance with previous work using Brillouin scatter analysis.

Secondly, the anchorage mechanism of the zonular fibres on the lens capsule was improved so that the discontinuities in curvatures of deformed lens shapes seen in several previous modelling studies were avoided. Furthermore, due to this newly introduced mechanism, artefact local excessive deformations around the location of anchorage were avoided. Maintaining the smooth curvature of lens shapes, especially in the equatorial region, is essential as this greatly influences the deformation of lens models in the equatorial regions, from which insights into the different accommodative theories will emanate.

Thirdly, the geometries of the developed lens models, including their internal layers, are taken from real and intact lens samples. On the contrary, the majority of the lens models in the literature are based on geometries assembled from various sources and compound uncertainties in model performance.

Finally and most pertinent from a kinematics perspective, the three zonular bands (anterior, equatorial and posterior) were constructed to be able to move in different and uncoupled directions, thus more accurately replicate the anatomy and physiology of the accommodative system. The conventional approach of binding the three zonular bands to a single stretching point on the ciliary muscle is less accurate as the zonular bands exhibit a coupled kinematic behaviour.

The outcomes of the present work have added to the understanding of the importance of the mechanical properties of the lens and the capsule, the biometric parameters, such as lens geometry and capsular thickness, and the role that zonular insertions have in the

accommodative process and the development of presbyopia. These findings can be summarised under the following points:

1. Lens models with a stiffer cortex than nucleus demonstrate minimal stresses in the nucleus; lens models with a stiffer nucleus than cortex demonstrate the maximal stresses in the nucleus. Stresses change more uniformly and more gradually in models where the material property distribution is in accordance with profiles found for the respective refractive index. Clear borders of stress patterns that separate the nucleus and the cortex can be seen in models with a constant modulus of elasticity for the nucleus and a different but constant modulus of elasticity for the cortex, as shown in Chapters 3 and 6. It is commonly believed that biological tissues cannot undertake sharp changes of stress as this would cause damage to the metabolic bodies. Therefore most mechanical measurements reported in the literature assumed the homogeneity of the nucleus and cortex which was inaccurate for characterizing the true mechanical behaviour of lenses. Models with varying elastic moduli in the cortex such as those reported by Besner *et al.*⁷¹ are closer to the physiological condition. The inhomogeneity of the lens material properties requires further investigation.

2. According to the results from the lens models presented in Chapters 3, 5 and 6, the central radii of curvature of the external lens surfaces can either increase or decrease with stretching, dependent on the lens geometry, material properties and different zonular angles. Lenses with a much stiffer nucleus than the cortex tend to show steeper central surfaces in deformed lens shapes supporting the accommodative theory by Schachar⁵⁶, which is the case for the 48-year-old model using the material properties of Wilde *et al.*⁶⁵ and all eight lens models presented in Chapter 6. Together with the results of changes in Central Optical Powers, it was demonstrated that both accommodative theories by Helmholtz⁵² and by Schachar⁵⁶ can be supported with different modelling parameters. Interrelations existed between the two seemingly opposing theories and further efforts are required to seek a possible solution that reconciles the two.

3. The fitting of simulated results of lens models to *in vivo* data was conducted in Chapter 4 for both the models with three zonular fibre bands bound to a single stretching point and the models with three zonular fibre bands stretched in different and uncoupled directions. The importance of the zonular configurations was shown as the two types of models provided different fits. A further parametric analysis was shown in Chapter 5, which demonstrated the significant influence of zonular angles to the optical performances of lens models as well as the quality of fits to *in vivo* data.

4. Varying the capsular thickness spatially, according to the thickness profiles measured by Barraquer *et al.*⁹, improves the accommodative change of each lens model by 1 or 2 dioptres compared to models with a uniform distribution of capsular thickness, as shown in Chapter 5. This outcome demonstrates the crucial role of the spatially varying capsular thickness in enhancing the accommodative abilities.

7.2 Future directions

The capabilities of FEA in characterising the fundamental behaviour of human lenses during accommodation and examining the relative contributions of different ocular components to the physiological process were demonstrated by the present work. The research has opened avenues for future work:

1. The models developed here contain the lens and the zonular fibres. The ciliary body was simplified as a system of single or multiple stretching points. Future modelling should consider developing these models into whole eye models.

2. It is not yet known how the lens capsule interacts with the inner lens substance, as well as between different layers of lens fibres. The contact between the lens capsule and the cortex, the cortex and the nucleus were assumed to be fully bonded in the present work. It would be valuable to investigate the interactions between these components in future studies.

3. Over a third of the lens consists of water, the concentration of which varies spatially. The water and the protein contents together contribute to the viscoelastic properties of the lens substance. More knowledge from biochemical studies on the changes in water-protein interactions and how this alters viscoelastic behaviour would, if available, enhance the development of future models.

4. Considering the existence of individual variations between different lenses, it would be greatly beneficial to conduct simulations on a larger number of lens models covering ages that span over the complete lifetime of human beings. In such a way the general ageing trend and normal variations of key features that can reflect the ageing process could be explored.

5. The present modelling work demonstrated the important role played by the capsule during the deformation of lens models. The lens capsule, modelled as an elastic

membrane, carries a certain amount of residual stress even in the fully accommodated state. It would be interesting to investigate the nature of the capsule using experimental findings on the degree of inhomogeneity and anisotropic behaviour.

6. Another aspect that the present work has highlighted is the importance of stating and solving the coupled opto-elastostatic problem. More particularly, experimentally measured refractive indices were used as input and in order to define a distribution of the modulus of elasticity inside the lens, which was then used for solving the respective elastostatic problem. It would be of interest to solve the inverse problem, which is to find such a distribution of the material properties, the viscosity being included, so that the optical performance (i.e. the refractive index) of a lens model matches the experimentally measured ones.

Knowledge of the biological lens and accommodative system is vital for the development of IOLs, which are commonly used for replacement of the clouded crystalline lens during cataract surgery. The alterations in focusing distances of an eye with accommodative IOLs rely on the effective coupling of the implant with the lens capsule, zonules and the ciliary muscle. The correct zonular force directions and nature of capsular material properties are particularly pertinent to this. More efforts are expected to improve the design of IOLs using FE models as these simulations can help promote better personalised implants and optimize the device prior to prototyping and physical testing.

The present work also sheds light on an interesting new research direction related to the lenses. Due to the high concentration of water, which contributes to the nearly incompressible behaviour of lenses, the Poisson's ratio used for modelling the lens nucleus and lens cortex was generally treated as 0.49. The selection of 0.49 was made to approach Poisson's ratio of 0.5 for an incompressible material in accordance with the theory of elasticity. Young's modulus is very sensitive to Poisson's ratio. Given that Poisson's ratio for the eye lens has not been measured or determined, it may depend on the frequency of the measurement and may vary spatially due to the viscoelastic and inhomogeneous nature of the lens substance, such a topic requires further investigation.

APPENDIX I

Young's modulus of multi-layered lens models

Table I.1. Young's moduli of each cortical layer for multi-layered models using the material properties of Fisher⁶².

		16-year-old (kPa)	35-year-old (kPa)	48-year-old (kPa)
Multi-cortex 1	Layer 1	1.5	2.5	2.8
	Layer 2	2.1	3.1	3.4
	Layer 3	2.7	3.7	4.0
	Layer 4	3.3	4.3	4.6
	Layer 5	-	4.9	5.2
Multi-cortex 2	Layer 1	1.5	2.500	2.80
	Layer 2	1.7	2.715	3.04
	Layer 3	1.9	2.930	3.28
	Layer 4	2.1	3.150	3.52
	Layer 5	2.3	3.370	3.76
	Layer 6	2.5	3.588	4.00
	Layer 7	2.7	3.806	4.24
	Layer 8	2.9	4.026	4.48
	Layer 9	3.1	4.246	4.72
	Layer 10	3.3	4.464	4.96
	Layer 11	-	4.682	5.20
	Layer 12	-	4.900	-

Table I.2. Young's moduli of each cortical layer for flipped multi-layered models using the material properties of Fisher⁶².

		16-year-old (kPa)	35-year-old (kPa)	48-year-old (kPa)
Multi-cortex 1	Layer 1	0.8	1.0	1.5
	Layer 2	0.6	0.8	1.3
	Layer 3	0.4	0.6	1.1
	Layer 4	0.2	0.4	0.9
	Layer 5	-	0.2	0.7
Multi-cortex 2	Layer 1	0.95	1.15	1.6
	Layer 2	0.85	1.05	1.5
	Layer 3	0.75	0.95	1.4
	Layer 4	0.65	0.85	1.3
	Layer 5	0.55	0.75	1.2
	Layer 6	0.45	0.65	1.1
	Layer 7	0.35	0.55	1.0
	Layer 8	0.25	0.45	0.9
	Layer 9	0.15	0.35	0.8
	Layer 10	0.05	0.25	0.7
	Layer 11	-	0.15	0.6
	Layer 12	-	0.05	-

Table I.3. Young's moduli of each cortical layer for multi-layered models using the material properties of Wilde *et al.*⁶⁵.

		16-year-old (kPa)	35-year-old (kPa)	48-year-old (kPa)
Multi-cortex 1	Layer 1	0.5	1.44	4.8
	Layer 2	0.8	2.04	4.2
	Layer 3	1.1	2.64	3.6
	Layer 4	1.4	3.24	3.0
	Layer 5	-	3.84	2.4
Multi-cortex 2	Layer 1	0.5	1.44	4.8
	Layer 2	0.6	1.658	4.56
	Layer 3	0.7	1.876	4.32
	Layer 4	0.8	2.094	4.08
	Layer 5	0.9	2.312	3.84
	Layer 6	1.0	2.532	3.6
	Layer 7	1.1	2.75	3.36
	Layer 8	1.2	2.968	3.12
	Layer 9	1.3	3.186	2.88
	Layer 10	1.4	3.404	2.64
	Layer 11	-	3.622	2.40
	Layer 12	-	3.84	-

APPENDIX II

The longitudinal modulus of incompressible materials

The ratio of Young's modulus E to the longitudinal modulus M , according to classical elasticity¹⁶¹, is

$$\frac{E}{M} = \frac{(1+\nu)(1-2\nu)}{1-\nu} \quad (\text{II.1})$$

Eq. (II.1) yields $\left(\frac{E}{M}\right) = 0$ for $\nu = 0.5$. Differentiation of Eq. (II.1) gives

$$\frac{d}{d\nu} \left(\frac{E}{M}\right) = \frac{1}{M^2} \left[M \frac{dE}{d\nu} - E \frac{dM}{d\nu} \right] = \frac{d}{d\nu} \left(\frac{1-\nu-2\nu^2}{1-\nu} \right) \quad (\text{II.2})$$

Rearranging Eq. (II.2) yields:

$$\frac{dE}{d\nu} - \frac{E}{M} \frac{dM}{d\nu} = \frac{2\nu(\nu-2)M}{(1-\nu)^2} \quad (\text{II.3})$$

As $\nu \rightarrow 0.5$ and $E \rightarrow 0$, this gives

$$\lim_{\nu \rightarrow \frac{1}{2}} \left(\frac{dE}{d\nu} \right) = -6M \quad (\text{II.4})$$

$$\lim_{\nu \rightarrow 1/2} \left(\frac{dM}{d\nu} \right) = \lim_{\nu \rightarrow 1/2} \left[\frac{M}{E} \frac{dE}{d\nu} - \frac{M^2}{E} \frac{2\nu(\nu-2)}{(1-\nu)^2} \right] = \lim_{\nu \rightarrow 1/2} \left[\frac{M}{E} (-6M) - \frac{M^2}{E} 6 \right] = 0 \quad (\text{II.5})$$

The above analysis follows the procedure proposed by Mott *et al.*¹⁶¹ between the bulk modulus and shear modulus. Similar conclusions were drawn:

1. The longitudinal modulus is nearly constant as Poisson's ratio approaches 0.5 according to Eq.(II.5), which is contrary to the classical theory of elasticity assuming the longitudinal modulus is infinitely large when $\nu \rightarrow 0.5$.
2. Young's modulus E is a very sensitive function of Poisson's ratio ν according to Eq.(II.4).

References

1. Donders, F. C. & Moore, W. D. in *On the anomalies of accommodation and refraction of the eye: With a preliminary essay on physiological dioptrics* (The New Sydenham Society, 1864).
2. Duane, A. Normal values of the accommodation at all ages. *J. Am. Med. Assoc.* **59**, 1010-1013 (1912).
3. Borja, D., Manns, F., Ho, A., Ziebarth, N., Rosen, A. M., Jain, R., Amelinckx, A., Arrieta, E., Augusteyn, R. C., Parel, J. M. Optical power of the isolated human crystalline lens. *Invest. Ophthalmol. Vis. Sci.* **49**, 2541-2548 (2008).
4. Glasser, A. & Campbell, M. C. Presbyopia and the optical changes in the human crystalline lens with age. *Vision Res.* **38**, 209-229 (1998).
5. Werner, L., Trindade, F., Pereira, F. & Werner, L. Physiology of accommodation and presbyopia. *Arq. Bras. Oftalmol.* **63**, 487-493 (2000).
6. Strenk, S. A., Strenk, L. M. & Koretz, J. F. The mechanism of presbyopia. *Prog. Retin. Eye Res.* **24**, 379-393 (2005).
7. Charman, W. N. The eye in focus: accommodation and presbyopia. *Clinical and experimental optometry* **91**, 207-225 (2008).
8. Schachar, R. A. in *The mechanism of accommodation and presbyopia*. 21-48 (Kugler Publications, 2012).
9. Barraquer, R. I., Michael, R., Abreu, R., Lamarca, J. & Tresserra, F. Human lens capsule thickness as a function of age and location along the sagittal lens perimeter. *Invest. Ophthalmol. Vis. Sci.* **47**, 2053-2060 (2006).
10. Bron, A. J. Wolff's Anatomy of the Eye and Orbit. 411-442 (1997).
11. Burd, H., Montenegro, G., Cortés, L. P., Barraquer, R. & Michael, R. Equatorial wrinkles in the human lens capsule. *Exp. Eye Res.* **159**, 77-86 (2017).
12. Augusteyn, R. C. On the growth and internal structure of the human lens. *Exp. Eye Res.* **90**, 643-654 (2010).
13. Brown, N. The change in shape and internal form of the lens of the eye on accommodation. *Exp. Eye Res.* **15**, 441-459 (1973).
14. Dubbelman, M., Van der Heijde, G., Weeber, H. & Vrensen, G. Changes in the internal structure of the human crystalline lens with age and accommodation. *Vision Res.* **43**, 2363-2375 (2003).
15. Bron, A. J., Vrensen, G. F., Koretz, J., Maraini, G. & Harding, J. J. The ageing lens. *Ophthalmologica* **214**, 86-104 (2000).

References

16. Rosen, A. M., Deham, D. B., Fernandez, V., Borja, D., Ho, A., Manns, F., Parel, J. M., Augusteyn, R. C. In vitro dimensions and curvatures of human lenses. *Vision Res.* **46**, 1002-1009 (2006).
17. Pierscionek, B. K. & Augusteyn, R. C. Shapes and dimensions of in vitro human lenses. *Clinical and Experimental Optometry* **74**, 223-228 (1991).
18. Jones, C. E., Atchison, D. A. & Pope, J. M. Changes in lens dimensions and refractive index with age and accommodation. *Optom. Vis. Sci.* **84**, 990-995 (2007).
19. Strenk, S. A. *et al.* Age-related changes in human ciliary muscle and lens: a magnetic resonance imaging study. *Invest. Ophthalmol. Visual Sci.* **40**, 1162-1169 (1999).
20. Koretz, J. F., Kaufman, P. L., Neider, M. W. & Goeckner, P. A. Accommodation and presbyopia in the human eye—aging of the anterior segment. *Vision Res.* **29**, 1685-1692 (1989).
21. Cook, C. A., Koretz, J. F., Pfahnl, A., Hyun, J. & Kaufman, P. L. Aging of the human crystalline lens and anterior segment. *Vision Res.* **34**, 2945-2954 (1994).
22. Dubbelman, M. & Van der Heijde, G. The shape of the aging human lens: curvature, equivalent refractive index and the lens paradox. *Vision Res.* **41**, 1867-1877 (2001).
23. Koretz, J. F., Strenk, S. A., Strenk, L. M. & Semmlow, J. L. Scheimpflug and high-resolution magnetic resonance imaging of the anterior segment: a comparative study. *JOSA A* **21**, 346-354 (2004).
24. Brown, N. The change in lens curvature with age. *Exp. Eye Res.* **19**, 175-183 (1974).
25. Pierscionek, B. K. Age-related response of human lenses to stretching forces. *Exp. Eye Res.* **60**, 325-332 (1995).
26. Koretz, J. F., Cook, C. A. & Kaufman, P. L. Accommodation and presbyopia in the human eye. *Invest. Ophthalmol. Vis. Sci.* **38**, 569-578 (1997).
27. Dubbelman, M., Van der Heijde, G. & Weeber, H. Change in shape of the aging human crystalline lens with accommodation. *Vision Res.* **45**, 117-132 (2005).
28. Strenk, S. A., Strenk, L. M., Semmlow, J. L. & DeMarco, J. K. Magnetic resonance imaging study of the effects of age and accommodation on the human lens cross-sectional area. *Invest. Ophthalmol. Vis. Sci.* **45**, 539-545 (2004).
29. Hermans, E. A., Pouwels, P. J., Dubbelman, M., Kuijer, J. P., van der Heijde, R. G., Heethaar, R. M. Constant volume of the human lens and decrease in surface area of the capsular bag during accommodation: an MRI and Scheimpflug study. *Invest. Ophthalmol. Vis. Sci.* **50**, 281-289 (2009).
30. Hermans, E., Dubbelman, M., van der Heijde, R. & Heethaar, R. The shape of the human lens nucleus with accommodation. *J. Vis.* **7**, 16.1-16.10 (2007).

31. Patnaik, B. A photographic study of accommodative mechanisms: changes in the lens nucleus during accommodation. *Invest. Ophthalmol. Vis. Sci.* **6**, 601-611 (1967).
32. Koretz, J. F., Cook, C. A. & Kaufman, P. L. Aging of the human lens: changes in lens shape upon accommodation and with accommodative loss. *JOSA A* **19**, 144-151 (2002).
33. Garner, L. F. & Yap, M. K. Changes in ocular dimensions and refraction with accommodation. *Ophthalmic and Physiological Optics* **17**, 12-17 (1997).
34. Fincham, E. The Mechanism of Accommodation. *Br. J. Ophthalmol. Monograph Suppl.* **VIII**, 1-80 (1937).
35. Pierscionek, B. K. & Regini, J. W. The gradient index lens of the eye: an opto-biological synchrony. *Prog. Retin. Eye Res.* **31**, 332-349 (2012).
36. Pierscionek B, A. R. Species variations in optical parameters of the eye lens. *Clin Exp Optom* **76**, 22-26 (1993).
37. Bahrami, M., Hoshino, M., Pierscionek, B., Yagi, N., Regini, J., Uesugi, K. Optical properties of the lens: An explanation for the zones of discontinuity. *Exp. Eye Res.* **124**, 93-99 (2014).
38. Jones, C. E., Atchison, D. A., Meder, R. & Pope, J. M. Refractive index distribution and optical properties of the isolated human lens measured using magnetic resonance imaging (MRI). *Vision Res.* **45**, 2352-2366 (2005).
39. Gladstone, J. H. & Dale, T. Researches on the refraction, dispersion, and sensitiveness of liquids. *Philosophical Transactions of the Royal Society of London* **153**, 317-343 (1863).
40. Koretz, J. F., Handelman, G. H. & Brown, N. P. Analysis of human crystalline lens curvature as a function of accommodative state and age. *Vision Res.* **24**, 1141-1151 (1984).
41. Sparrow, J., Bron, A., Brown, N., Ayliffe, W. & Hill, A. The Oxford clinical cataract classification and grading system. *Int. Ophthalmol.* **9**, 207-225 (1986).
42. Brown, N. & Tripathi, R. Loss of anterior sub-capsular clear zone of lens-prognostic significance in cataract formation. *Trans. Ophthalmol. Soc. U. K.* **94**, 29-45 (1974).
43. Streeten, B. W. The zonular insertion: A scanning electron microscopic study. *Invest Ophthalmol Vis Sci.* **16**, 364 (1977)
44. Rohen, J. W. Scanning electron microscopic studies of the zonular apparatus in human and monkey eyes. *Invest. Ophthalmol. Vis. Sci.* **18**, 133-144 (1979).
45. Bergua, A. & Kuchle, M. Visualization of the hyalo-capsular ligament in the living eye. *Graefe's archive for clinical and experimental ophthalmology* **240**, 503-505 (2002).
46. Bernal, A., Parel, J. & Manns, F. Evidence for posterior zonular fiber attachment on the anterior hyaloid membrane. *Invest. Ophthalmol. Vis. Sci.* **47**, 4708-4713 (2006).

References

47. Weale, R. A. Human ocular aging and ambient temperature. *Br J Ophthalmol.* **65**, 869-870 (1981).
48. Farnsworth, P. & Shyne, S. Anterior zonular shifts with age. *Exp. Eye Res.* **28**, 291-297 (1979).
49. Scheiner, C. Oculus, hoc est fundamentum opticum. Oeniponti. p37 (Daniel Agricola, 1619).
50. Daxecker, F. in *Christopher Scheiner's eye studies.* **81**, 27-35 (Doc Ophthalmol, 1992).
51. Descartes, R. Traite' de l'homme. Translated as Treatise on Man, by Hall TS (Cambridge: Harvard Univ Press, 1677).
52. Helmholtz, H. The accommodation of the eyes. *Alb. Graefe's Arch. Klin. Exp. Ophthalmol* **1**, 1-74 (1855).
53. Tscherning, M. H. v. Helmholtz et la theorie de l'accommodation. *Paris.* (1909).
54. Coleman, D. J. Unified model for accommodative mechanism. *Am. J. Ophthalmol.* **69**, 1063-1079 (1970).
55. Schachar, R. A. Cause and treatment of presbyopia with a method for increasing the amplitude of accommodation. *Ann. Ophthalmol.* **24**, 445-7, 452 (1992).
56. Schachar, R. A. Zonular function: a new hypothesis with clinical implications. *Ann. Ophthalmol.* **26**, 36-38 (1994).
57. Schachar, R. A. Is Helmholtz's theory of accommodation correct? *Annals of ophthalmology.Glaucoma* **31**, 10-17 (1999).
58. Tscherning, M. Recherchers sur les changement optiques des l'oeil pendant accommodation. *Arch de Physiol Norm et Pathol* **7**, 158-180 (1895).
59. Tscherning, M. Physiologic Optics (translated by C Weiland). *Keystone: Philadelphia* (1924).
60. Salzmann, M. & Brown, E. V. L. in *The anatomy and histology of the human eyeball in the normal state: its development and senescence.* 164-167 (The University of Chicago Press, 1912).
61. Coleman, D. J. & Fish, S. K. Presbyopia, accommodation, and the mature catenary. *Ophthalmology* **108**, 1544-1551 (2001).
62. Fisher, R. The elastic constants of the human lens. *J. Physiol. (Lond.)* **212**, 147-180 (1971).
63. Heys, K. R., Cram, S. L. & Truscott, R. J. Massive increase in the stiffness of the human lens nucleus with age: the basis for presbyopia? *Mol Vis* **10**, 956-963 (2004).

64. Weeber, H. A., Eckert, G., Pechhold, W. & van der Heijde, Rob GL. Stiffness gradient in the crystalline lens. *Graefe's Archive for Clinical and Experimental Ophthalmology* **245**, 1357-1366 (2007).
65. Wilde, G., Burd, H. & Judge, S. Shear modulus data for the human lens determined from a spinning lens test. *Exp. Eye Res.* **97**, 36-48 (2012).
66. Pau, H. & Kranz, J. The increasing sclerosis of the human lens with age and its relevance to accommodation and presbyopia. *Graefe's archive for clinical and experimental ophthalmology* **229**, 294-296 (1991).
67. Weeber, H. A., Eckert, G., Soergel, F., Meyer, C. H., Pechhold, W., van der Heijde, R. G. Dynamic mechanical properties of human lenses. *Exp. Eye Res.* **80**, 425-434 (2005).
68. Hollman, K. W., O'Donnell, M. & Erpelding, T. N. Mapping elasticity in human lenses using bubble-based acoustic radiation force. *Exp. Eye Res.* **85**, 890-893 (2007).
69. Glasser, A. & Campbell, M. C. Biometric, optical and physical changes in the isolated human crystalline lens with age in relation to presbyopia. *Vision Res.* **39**, 1991-2015 (1999).
70. Fisher, R. F. Presbyopia and the changes with age in the human crystalline lens. *J. Physiol.* **228**, 765-779 (1973).
71. Besner, S., Scarcelli, G., Pineda, R. & Yun, S. In Vivo Brillouin Analysis of the Aging Crystalline Lens. *Invest. Ophthalmol. Vis. Sci.* **57**, 5093-5100 (2016).
72. Koretz, J. F. & Handelman, G. H. How the human eye focuses. *Sci. Am.* **259**, 92-99 (1988).
73. Strenk, S. A., Strenk, L. M. & Semmlow, J. L. High resolution MRI study of circumlental space in the aging eye. *Journal of Refractive Surgery* **16**, S659-S660 (2000).
74. Sheppard, A. L. & Davies, L. N. The effect of ageing on in vivo human ciliary muscle morphology and contractility. *Invest. Ophthalmol. Vis. Sci.* **52**, 1809-1816 (2011).
75. Schachar, R. A., Black, T. D., Kash, R. L., Cudmore, D. P. & Schanzlin, D. J. The mechanism of accommodation and presbyopia in the primate. *Ann. Ophthalmol.* **27**, 58-67 (1995).
76. Weale, R. A. Presbyopia. *Br. J. Ophthalmol.* **46**, 660-668 (1962).
77. Koretz, J. F. & Handelman, G. H. Modeling age-related accommodative loss in the human eye. *Mathematical Modelling* **7**, 1003-1014 (1986).
78. Duane, A. Are the current theories of accommodation correct? *Am. J. Ophthalmol.* **8**, 196-202 (1925).

References

79. Balazs EQA, D. J. The vitreous. In: Davson H, ed. *The Eye*, Vol 1A, 3rd ed. *London: Academic Press*, 533-588.
80. Strenk, S. A., Strenk, L. M. & Guo, S. Magnetic resonance imaging of the anteroposterior position and thickness of the aging, accommodating, phakic, and pseudophakic ciliary muscle. *Journal of Cataract & Refractive Surgery* **36**, 235-241 (2010).
81. Park, K., Yun, J. & Kee, C. The effect of cataract extraction on the contractility of ciliary muscle. *Am. J. Ophthalmol.* **146**, 8-14. e2 (2008).
82. Glasser, A. Restoration of accommodation: surgical options for correction of presbyopia. *Clinical and experimental optometry* **91**, 279-295 (2008).
83. Mathews, S. Scleral expansion surgery does not restore accommodation in human presbyopia. *Ophthalmology* **106**, 873-877 (1999).
84. Malecaze, F. J., Gazagne, C. S., Tarroux, M. C. & Gorrand, J. Scleral expansion bands for presbyopia. *Ophthalmology* **108**, 2165-2171 (2001).
85. Qazi, M., Pepose, J. & Shuster, J. Implantation of Scleral Expansion Band Segments for the Treatment of Presbyopia. *Evidence-Based Ophthalmology* **4**, 130-131 (2003).
86. Singh, G. & Chalfin, S. A complication of scleral expansion surgery for treatment of presbyopia. *Am. J. Ophthalmol.* **130**, 521-523 (2000).
87. Renna, A., Alió, J. L. & Vejarano, L. F. Pharmacological treatments of presbyopia: a review of modern perspectives. *Eye and Vision* **4**, 3 (2017).
88. Crawford, K. S., Garner, W. H. & Burns, W. Dioptin™: a novel pharmaceutical formulation for restoration of accommodation in presbyopes. *Invest. Ophthalmol. Vis. Sci.* **55**, 3765-3765 (2014).
89. Blum, M., Kunert, K., Nolte, S., Riehemann, S., Palme, M., Peschel, T., Dick, M., Dick, H. B. Presbyopia treatment using a femtosecond laser. *Ophthalmologe* **103**, 1014-1019 (2006).
90. Myers, R. I. & Krueger, R. R. Novel approaches to correction of presbyopia with laser modification of the crystalline lens. *Journal of refractive surgery* **14**, 136-139 (1998).
91. Krueger, R. R. *et al.* First safety study of femtosecond laser photodisruption in animal lenses: tissue morphology and cataractogenesis. *Journal of Cataract & Refractive Surgery* **31**, 2386-2394 (2005).
92. Bellucci, R. in *Cataract* 38-55 (Karger Publishers, 2013).
93. Sheppard, A. L., Bashir, A., Wolffsohn, J. S. & Davies, L. N. Accommodating intraocular lenses: a review of design concepts, usage and assessment methods. *Clinical and Experimental Optometry* **93**, 441-452 (2010).

94. Koopmans, S. A. *et al.* Accommodative lens refilling in rhesus monkeys. *Invest. Ophthalmol. Vis. Sci.* **47**, 2976-2984 (2006).
95. Nishi, O. & Nishi, K. Accommodation amplitude after lens refilling with injectable silicone by sealing the capsule with a plug in primates. *Arch. Ophthalmol.* **116**, 1358-1361 (1998).
96. Moaveni, S. in *Finite element analysis: theory and application with ANSYS*. p6 (Harlow : Prentice Hall, Harlow, 2007).
97. Logan, D. L. in *First course in finite element method, si* (Mason, OH: South-Western, Cengage Learning, Mason, OH, 2011).
98. Ripken, T., Breitenfel, P., Fromm, M., Oberheide, U., Gerten, G., Lubatschowski, H. *FEM simulation of the human lens compared to ex vivo porcine lens cutting pattern: a possible treatment of presbyopia* Ser. 6138, Ophthalmic Technologies XVI, 2006).
99. Burd, H., Judge, S. & Cross, J. Numerical modelling of the accommodating lens. *Vision Res.* **42**, 2235-2251 (2002).
100. Hermans, E., Dubbelman, M., Van der Heijde, G. & Heethaar, R. Estimating the external force acting on the human eye lens during accommodation by finite element modelling. *Vision Res.* **46**, 3642-3650 (2006).
101. Martin, H., Guthoff, R., Terwee, T. & Schmitz, K. Comparison of the accommodation theories of Coleman and of Helmholtz by finite element simulations. *Vision Res.* **45**, 2910-2915 (2005).
102. Liu, Z., Wang, B., Xu, X. & Wang, C. A study for accommodating the human crystalline lens by finite element simulation. *Comput. Med. Imaging Graphics* **30**, 371-376 (2006).
103. Bailey, S. T., Twa, M. D., Gump, J. C., Venkiteshwar, M., Bullimore, M. A., Sooryakumar, R. Light-scattering study of the normal human eye lens: elastic properties and age dependence. *Biomedical Engineering, IEEE Transactions on* **57**, 2910-2917 (2010).
104. Burd, H., Wilde, G. & Judge, S. Can reliable values of Young's modulus be deduced from Fisher's (1971) spinning lens measurements? *Vision Res.* **46**, 1346-1360 (2006).
105. Heys, K. R., Friedrich, M. G. & Truscott, R. J. Presbyopia and heat: changes associated with aging of the human lens suggest a functional role for the small heat shock protein, α -crystallin, in maintaining lens flexibility. *Aging Cell* **6**, 807-815 (2007).
106. Erpelding, T. N., Hollman, K. W. & O'Donnell, M. Mapping age-related elasticity changes in porcine lenses using bubble-based acoustic radiation force. *Exp. Eye Res.* **84**, 332-341 (2007).
107. Scarcelli, G. & Yun, S. H. In vivo Brillouin optical microscopy of the human eye. *Optics express* **20**, 9197-9202 (2012).

References

108. Okuno, T., Kojima, M., Hata, I. & Sliney, D. H. Temperature rises in the crystalline lens from focal irradiation. *Health Phys.* **88**, 214-222 (2005).
109. Sliney, D., Aron-Rosa, D., DeLori, F., Frankhauser, F., Landry, R., Mainster, M., Marshall, J., Rassow, B., Stuck, B., Trokel, S., West, T. M., Wolffe, M. Adjustment of guidelines for exposure of the eye to optical radiation from ocular instruments: statement from a task group of the International Commission on Non-Ionizing Radiation Protection (ICNIRP). *Appl. Opt.* **44**, 2162-2176 (2005).
110. Itoi, M., Ito, N. & Kaneko, H. Visco-elastic properties of the lens. *Exp. Eye Res.* **4**, 168-173 (1965).
111. Kikkawa, Y. & Sato, T. Elastic properties of the lens. *Exp. Eye Res.* **2**, 210-215 (1963).
112. Beers, A. & Van Der Heijde, G. In vivo determination of the biomechanical properties of the component elements of the accommodation mechanism. *Vision Res.* **34**, 2897-2905 (1994).
113. Alcala, J. & Maisel, H. in *The ocular lens* 169-222 (Marcel Dekker New York, 1985).
114. Koretz, J. F. & Handelman, G. H. Model of the accommodative mechanism in the human eye. *Vision Res.* **22**, 917-927 (1982).
115. Beers, A. & Van der Heijde, G. Age-related changes in the accommodation mechanism. *Optometry & Vision Science* **73**, 235-242 (1996).
116. Schachar, R. A., Chan, R. W. & Fu, M. Viscoelastic properties of fresh human lenses under 40 years of age: implications for the aetiology of presbyopia. *Br. J. Ophthalmol.* **95**, 1010-1013 (2011).
117. Ejiri, M., Thompson, H. E. & O'Neill, W. D. Dynamic visco-elastic properties of the lens. *Vision Res.* **9**, 233-244 (1969).
118. Krag, S. & Andreassen, T. T. Mechanical properties of the human lens capsule. *Prog. Retin. Eye Res.* **22**, 749-767 (2003).
119. Fisher, R. Elastic constants of the human lens capsule. *J. Physiol. (Lond.)* **201**, 1-19 (1969).
120. Danielsen, C. C. Tensile mechanical and creep properties of Descemet's membrane and lens capsule. *Exp. Eye Res.* **79**, 343-350 (2004).
121. Pedrighi, R., David, G., Dziezyc, J. & Humphrey, J. Regional mechanical properties and stress analysis of the human anterior lens capsule. *Vision Res.* **47**, 1781-1789 (2007).
122. Krag, S., Olsen, T. & Andreassen, T. T. Biomechanical characteristics of the human anterior lens capsule in relation to age. *Invest. Ophthalmol. Vis. Sci.* **38**, 357-363 (1997).

123. Krag, S. & Andreassen, T. T. Mechanical properties of the human posterior lens capsule. *Invest. Ophthalmol. Vis. Sci.* **44**, 691-696 (2003).
124. Fisher, R. F. The ciliary body in accommodation. *Trans. Ophthalmol. Soc. U. K.* **105**, 208-219 (1986).
125. Fisher, R. The force of contraction of the human ciliary muscle during accommodation. *J. Physiol. (Lond.)* **270**, 51-74 (1977).
126. Van Alphen, G. & Graebel, W. P. Elasticity of tissues involved in accommodation. *Vision Res.* **31**, 1417-1438 (1991).
127. Michael, R. *et al.* Elastic Properties of Human Lens Zonules as a Function of Age in Presbyopes. Elasticity of Human Lens Zonules in Presbyopia. *Invest. Ophthalmol. Vis. Sci.* **53**, 6109-6114 (2012).
128. Weeber, H. A. & van der Heijde, Rob GL. On the relationship between lens stiffness and accommodative amplitude. *Exp. Eye Res.* **85**, 602-607 (2007).
129. Belaidi, A. & Pierscionek, B. K. Modeling internal stress distributions in the human lens: can opponent theories coexist? *J. Vis.* **7**, 1.1-12 (2007).
130. Weeber, H. A. & Van Der Heijde, Rob GL. Internal deformation of the human crystalline lens during accommodation. *Acta Ophthalmol.* **86**, 642-647 (2008).
131. Abolmaali, A., Schachar, R. & Le, T. Sensitivity study of human crystalline lens accommodation. *Comput. Methods Programs Biomed.* **85**, 77-90 (2007).
132. Schachar, R. A., Abolmaali, A. & Le, T. Insights into the age-related decline in the amplitude of accommodation of the human lens using a non-linear finite-element model. *Br. J. Ophthalmol.* **90**, 1304-1309 (2006).
133. Burd, H. J., Judge, S. J. & Flavell, M. J. Mechanics of accommodation of the human eye. *Vision Res.* **39**, 1591-1595 (1999).
134. Schachar, R. A., Huang, T. & Huang, X. Mathematic proof of Schachar's hypothesis of accommodation. *Ann. Ophthalmol.* **25**, 5-9 (1993).
135. Schachar, R. A. & Bax, A. J. Mechanism of human accommodation as analyzed by nonlinear finite element analysis. *Ann. Ophthalmol.* **33**, 103-112 (2001).
136. McCulloch, C. The zonule of Zinn: its origin, course, and insertion, and its relation to neighboring structures. *Trans. Am. Ophthalmol. Soc.* **52**, 525-585 (1954).
137. Fisher, R. F. & Pettet, B. E. The postnatal growth of the capsule of the human crystalline lens. *J. Anat.* **112**, 207-214 (1972).
138. Krag, S., Andreassen, T. & Olsen, T. *Elastic properties of the lens capsule in relation to accommodation and presbyopia.* (Investigative Ophthalmology & Visual Science Ser. 37, LIPPINCOTT-RAVEN PUBL 227 EAST WASHINGTON SQ, PHILADELPHIA, PA 19106, 1996).

References

139. Ljubimova, D., Eriksson, A. & Bauer, S. Aspects of eye accommodation evaluated by finite elements. *Biomechanics and modeling in mechanobiology* **7**, 139-150 (2008).
140. Weeber, H. A. Influence of the Stress-free Shape of the Lens on Accommodation . *Applied Research Pharmacia Groningen Netherlands* **43** (2002).
141. Stachs, O., Martin, H., Behrend, D., Schmitz, K. & Guthoff, R. Three-dimensional ultrasound biomicroscopy, environmental and conventional scanning electron microscopy investigations of the human zonula ciliaris for numerical modelling of accommodation. *Graefe's Archive for Clinical and Experimental Ophthalmology* **244**, 836-844 (2006).
142. Schachar, R. A., Abolmaali, A. & Kamangar, F. Comment on the publication" Three-dimensional ultrasound, biomicroscopy environmental and conventional scanning electron microscopy investigations of the human zonula ciliaris for numerical modelling of accommodation" by O. Stachs et al. *Graefe's Archive for Clinical and Experimental Ophthalmology* **244**, 1062-1063 (2006).
143. Lizak, M. J., Datiles, M. B., Aletras, A. H., Kador, P. F. & Balaban, R. S. MRI of the human eye using magnetization transfer contrast enhancement. *Invest. Ophthalmol. Vis. Sci.* **41**, 3878-3881 (2000).
144. Van de Sompel, D., Kunkel, G. J., Hersh, P. S. & Smits, A. J. Model of accommodation: Contributions of lens geometry and mechanical properties to the development of presbyopia. *Journal of Cataract & Refractive Surgery* **36**, 1960-1971 (2010).
145. Hermans, E., Dubbelman, M., Van der Heijde, G. & Heethaar, R. Change in the accommodative force on the lens of the human eye with age. *Vision Res.* **48**, 119-126 (2008).
146. Duane, A. Studies in monocular and binocular accommodation with their clinical applications. *Am. J. Ophthalmol.* **5**, 865-877 (1922).
147. Pierscionek, B. K. In vitro alteration of human lens curvatures by radial stretching. *Exp. Eye Res.* **57**, 629-635 (1993).
148. Brown, B. H., Smallwood, R., Barber, D., Lawford, P. & Hose, D. in *Medical physics and biomedical engineering* (CRC Press, 1998).
149. Pierscionek, B., Bahrami, M., Hoshino, M., Uesuqi, K., Regini, J., Yaqi, N. The eye lens: age-related trends and individual variations in refractive index and shape parameters. *Oncotarget* **6**, 30532-30544 (2015).
150. Fisher, R. F. The significance of the shape of the lens and capsular energy changes in accommodation. *J. Physiol.* **201**, 21-47 (1969).
151. Taubin, G. Estimation of planar curves, surfaces, and nonplanar space curves defined by implicit equations with applications to edge and range image segmentation. *IEEE Transactions on Pattern Analysis & Machine Intelligence* **11**, 1115-1138 (1991).

152. Scarcelli, G., Kim, P. & Yun, S. H. In vivo measurement of age-related stiffening in the crystalline lens by Brillouin optical microscopy. *Biophys. J.* **101**, 1539-1545 (2011).
153. Dubbelman, M., Van der Heijde, G. & Weeber, H. A. The thickness of the aging human lens obtained from corrected Scheimpflug images. *Optometry & Vision Science* **78**, 411-416 (2001).
154. Koretz, J. F., Cook, C. A. & Kuszak, J. R. The zones of discontinuity in the human lens: development and distribution with age. *Vision Res.* **34**, 2955-2962 (1994).
155. Marshall, J., Beaconsfield, M. & Rothery, S. The anatomy and development of the human lens and zonules. *Trans Ophthalmol Soc UK* **102**, 423-440 (1982).
156. Augusteyn, R. C., Mohamed, A., Nankivil, D., Veerendranath, P., Arrieta, E., Taneja, M., Manns, F., Ho, A., Parel, J. M. Age-dependence of the optomechanical responses of ex vivo human lenses from India and the USA, and the force required to produce these in a lens stretcher: the similarity to in vivo disaccommodation. *Vision Res.* **51**, 1667-1678 (2011).
157. Manns, F., Parel, J. M., Deham, D., Billotte, C., Ziebarth, N., Borja, D., Fernandez, V., Aly, M., Arrieta, E., Ho, A., Holden, B. Optomechanical response of human and monkey lenses in a lens stretcher. *Invest. Ophthalmol. Vis. Sci.* **48**, 3260-3268 (2007).
158. Farnsworth, P. N. & Burke, P. Three-dimensional architecture of the suspensory apparatus of the lens of the rhesus monkey. *Exp. Eye Res.* **25**, 563-576 (1977).
159. O'Neill, W. D. & Doyle, J. A thin shell deformation analysis of the human lens. *Vision Res.* **8**, 193-206 (1968).
160. Schachar, R. A. Central surface curvatures of postmortem-extracted intact human crystalline lenses: implications for understanding the mechanism of accommodation. *Ophthalmology* **111**, 1699-1704 (2004).
161. Mott, P., Dorgan, J. & Roland, C. The bulk modulus and Poisson's ratio of "incompressible" materials. *J. Sound Vibrat.* **312**, 572-575 (2008).
162. Tschoegl, N. W., Knauss, W. G. & Emri, I. Poisson's ratio in linear viscoelasticity—a critical review. *Mechanics of Time-Dependent Materials* **6**, 3-51 (2002).

References

LIST OF PUBLICATIONS

Journal Papers

1. Wang, K., Venetsanos, DT., Wang, J., Pierscionek BK. Gradient moduli lens models: how material properties and application of forces can affect deformation and distributions of stress. *Sci. Rep.* **6**, 31171; doi: 10.1038/srep31171 (2016).
2. Wang, K., Venetsanos, DT., Wang, J., Augousti, AT., Pierscionek BK. The importance of parameter choice in modelling dynamics of the eye lens. *Sci. Rep.* **7**, 16688; doi: 10.1038/s41598-017-16854-9 (2017)
3. Wang, K., Venetsanos, DT., Wang, J., Pierscionek BK. Parametric analysis of zonular angles using lens models with linearly varying elastic moduli. (*to be submitted_Oncotarget*).

Conference Proceedings and Abstracts

1. Wang, K., Venetsanos, DT., Wang, J., Pierscionek BK. Investigation on accommodative mechanism of human lens using FEA. CEESRC, Kingston University, London, Feb (2016).
2. Wang, K., Venetsanos, DT., Wang, J., Pierscionek BK. The application of FEA in the study of human lens accommodation. 3rd IhSHA, Kingston University, London, Jun (2015).
3. Pierscionek BK., Wang, K., Venetsanos, DT., Wang, J. Modelling material properties in eye lenses: stress distributions and deformation. EMPVOVIII Topical Meeting on Visual and Physiological Optics, Antwerp, Belgium, Aug (2016)
4. Pierscionek BK., Wang, K., Venetsanos, DT., Wang, J. Models of zonular forces for presbyopia correction. (Keynote) International Society of Presbyopia. Copenhagen, Denmark, Sept (2016)
5. Pierscionek BK., Wang, K., Venetsanos, DT., Wang, J. Modelling the physiological optics of the eye. ARVO ASIA Brisbane, Australia February (2017)

References

6. Wang, K., Venetsanos, DT., Wang, J., Pierscionek BK. Finite Element modelling of the human lens for the investigation of accommodative theories. STEM for Britain, House of Parliament, London, UK, Mar (2017)
7. Wang, K., Venetsanos, DT., Wang, J., Pierscionek BK. Finite Element models of human crystalline lens for the investigations of presbyopia, 23rd Congress European Society of Biomechanics, Seville, Spain, Jul (2017)